



**ایران مواد**

Iran-mavad.com



**@iranmavad**



شبکه آزمایشگاهی ایران مواد

**FESEM, SEM, TEM, XRD**

XRF, SPS, TGA, DTA, DSC, FTIR, BET

[www.IMlabsnet.ir](http://www.IMlabsnet.ir)

مرکز آموزش تخصصی ایران مواد

**Iran Mavad Education Professional Center**

آموزش های تخصصی و نرم افزاری مهندسی مواد و متالورژی

[www.IMpec.ir](http://www.IMpec.ir)

گروه فنی پژوهش ایران مواد

ویراستاری، ترجمه تخصصی مقالات و کتب مهندسی مواد

مشاوره پژوهشی تا چاپ مقاله **ISI**

[www.IMpaper.ir](http://www.IMpaper.ir)

Materials Forming, Machining and Tribology

Bekir Sami Yilbas  
Iyad Al-Zaharnah  
Ahmet Sahin

# Flexural Testing of Weld Site and HVOF Coating Characteristics

 Springer

[www.iran-mavad.com](http://www.iran-mavad.com)  
ایران مواد

# **Materials Forming, Machining and Tribology**

*Series editor*

J. Paulo Davim, Aveiro, Portugal

For further volumes:

<http://www.springer.com/series/11181>

Bekir Sami Yilbas · Iyad Al-Zaharnah  
Ahmet Sahin

# Flexural Testing of Weld Site and HVOF Coating Characteristics

 Springer

Bekir Sami Yilbas  
Department of Mechanical Engineering  
King Fahd University of Petroleum  
and Minerals  
Dhahran  
Saudi Arabia

Iyad Al-Zaharnah  
Ahmet Sahin  
KFUPM  
Dhahran  
Saudi Arabia

ISSN 2195-0911                      ISSN 2195-092X (electronic)  
ISBN 978-3-642-54976-2            ISBN 978-3-642-54977-9 (eBook)  
DOI 10.1007/978-3-642-54977-9  
Springer Heidelberg New York Dordrecht London

Library of Congress Control Number: 2014942065

© Springer-Verlag Berlin Heidelberg 2014

This work is subject to copyright. All rights are reserved by the Publisher, whether the whole or part of the material is concerned, specifically the rights of translation, reprinting, reuse of illustrations, recitation, broadcasting, reproduction on microfilms or in any other physical way, and transmission or information storage and retrieval, electronic adaptation, computer software, or by similar or dissimilar methodology now known or hereafter developed. Exempted from this legal reservation are brief excerpts in connection with reviews or scholarly analysis or material supplied specifically for the purpose of being entered and executed on a computer system, for exclusive use by the purchaser of the work. Duplication of this publication or parts thereof is permitted only under the provisions of the Copyright Law of the Publisher's location, in its current version, and permission for use must always be obtained from Springer. Permissions for use may be obtained through RightsLink at the Copyright Clearance Center. Violations are liable to prosecution under the respective Copyright Law. The use of general descriptive names, registered names, trademarks, service marks, etc. in this publication does not imply, even in the absence of a specific statement, that such names are exempt from the relevant protective laws and regulations and therefore free for general use.

While the advice and information in this book are believed to be true and accurate at the date of publication, neither the authors nor the editors nor the publisher can accept any legal responsibility for any errors or omissions that may be made. The publisher makes no warranty, express or implied, with respect to the material contained herein.

Printed on acid-free paper

Springer is part of Springer Science+Business Media ([www.springer.com](http://www.springer.com))

# Preface

Defect sites can be created in solid substrates when subjected to a deformation or a thermal distortion and the property variation occurs in defected regions, such as elastic module, density, Poisson's ratio variations in the heat affected zone of the welded, or locally heat treated sites in the solid substrates. In addition, during thermal processing, the properties of the substrate material change because of the temperature dependence. Flexural motion of the substrate material, subjected to thermal processing, provides useful information about the level distortion in the substrate material, which is more pronounced as the temperature in the substrate material increases. However, nonlinear response of the elastic modulus, due to the temperature filed, changes amplitude and time shift of amplitudes due to residual thermal distortions. Determining magnitude and phase lagging of the maximum amplitude provides information about the heating rate, heat source speed, size of heat affected zone, etc. Therefore, flexural characteristics of the substrate material can be associated with the source of distortion, which in turn enables to control the process for improved performance and the end product quality. Nondestructive testing of coat layer thickness is very fruitful to assess characteristics of thermal spray coating process. Monitoring the flexural motion enables to correlate amplitude and frequency of the wave with geometric configuration of coating, such as coating thickness, coating uniformity, tapering, etc.

High velocity oxy-fuel (HVOF) spraying technique finds wide application in industry because of low cost and operational easiness. Although HVOF coating protects the substrate surfaces from high temperature and wear environments, presence of porous and oxide inclusions in the coating reduces mechanical strength of the resulting coating. Thermal integration of coating is possible by introducing control melting using high energy beams, in which case, pores and voids can be eliminated in the coating. Mechanical, metallurgical, and morphological characteristics of coating are highly affected by melting rates and cooling periods of the coating. In thermal processing, such as welding, property changes in the welded regions are important to secure sound and quality welds for the practical applications. Optimization of welding process, utilizing flexural characteristics of the welded material improves mechanical and metallurgical properties and assists to produce desirable welds for the particular applications.

In this book, thermal analysis and flexural motion of weld joints and thermally processed parts are presented. Analytical and numerical simulations of flexural

characteristics of cantilever beams are provided in detail. Several heating situations and flexural behavior of the thermally treated beams are included. Various studies for high velocity oxy-fuel coating are introduced and coating characteristics prior and after controlled melting by a laser beam are discussed. Changes in metallurgical, mechanical, and morphological characteristics of coating are described for various types of coating powders. However, some cases related to modeling of flexural characteristics and coating properties are not presented in this book due to space limitations and, therefore, these cases are left for the future treatments.

# Acknowledgments

We would like to acknowledge the role of King Fahd University of Petroleum and Minerals in extending strong support from beginning to end facilitating every means during the preparation of the book. The author wishes to thank the colleagues who contributed to the work presented in the book through previous cooperation of the authors. In particular, thanks to all our graduate students.

# Contents

<b>1</b>	<b>Introduction</b> . . . . .	1
1.1	Flexural Characteristics . . . . .	1
1.2	High Velocity Oxy-Fuel Coating and Characterization . . . . .	5
1.3	Analytical Formulation of a Beam Subjected to a Flexural Motion . . . . .	7
	References . . . . .	12
<b>2</b>	<b>Flexural Motion Due to Laser Heating Applications</b> . . . . .	15
2.1	Laser Induced Evaporation Process . . . . .	15
2.1.1	Temperature and Pressure . . . . .	15
2.1.2	Wave Analysis . . . . .	18
2.1.3	Results and Discussions . . . . .	21
2.2	Laser Evaporative Heating of Steel . . . . .	24
2.2.1	Heat Transfer Analysis . . . . .	24
2.2.2	Flexural Wave Analysis . . . . .	28
2.2.3	Results and Discussion . . . . .	32
2.3	Laser Pulse Heating of Steel Surface . . . . .	35
2.3.1	The Mathematical Model . . . . .	37
2.3.2	Wave Analysis . . . . .	42
2.3.3	Results and Discussions . . . . .	43
2.4	Laser Pulse Heat Treatment of Metallic Surfaces . . . . .	44
2.4.1	Heat Transfer Analysis . . . . .	45
2.4.2	Wave Analysis . . . . .	47
2.4.3	Results and Discussion . . . . .	47
2.5	Laser Ablation: Influence of Force Location . . . . .	48
2.5.1	Heat Transfer Analysis . . . . .	48
2.5.2	Flexural Wave Analysis . . . . .	51
2.5.3	Results and Discussions . . . . .	51
2.6	Laser Ablation in Multilayer Assembly . . . . .	52
2.6.1	Heat Transfer Model . . . . .	54
2.6.2	Flexural Wave Analysis . . . . .	55
2.6.3	Results and Discussions . . . . .	55

2.7	Cantilever Plate Heated at Fixed End . . . . .	59
2.7.1	Mathematical Modeling Numerical Solution . . . . .	60
2.7.2	Heat Transfer Analysis . . . . .	60
2.7.3	Flexural Wave Analysis . . . . .	63
2.7.4	Results and Discussion . . . . .	65
2.8	Welding of Bar to Rigid Body . . . . .	67
2.8.1	Heat Transfer Analysis . . . . .	68
2.8.2	Results and Analysis . . . . .	70
2.9	Local Heating of a Bar: Effect of Heat Source Location . . . . .	72
2.9.1	Mathematical Modeling Numerical Solution . . . . .	74
2.9.2	Results and Discussion . . . . .	77
2.10	Laser Welding of Cantilever Plate: Influence of Speed of the Heating Source . . . . .	81
2.10.1	Mathematical Modeling and Numerical Solution . . . . .	81
2.10.2	Results and Discussion . . . . .	83
2.11	Laser Pulse Heating of Two-Layer Assembly . . . . .	87
2.11.1	Heat Transfer Analysis . . . . .	87
2.11.2	Flexural Wave Analysis . . . . .	88
2.11.3	Results and Discussions . . . . .	93
2.12	3D Analysis of Laser Evaporative Heated Cantilever Workpiece . . . . .	94
2.12.1	Heat Transfer Analysis . . . . .	94
2.12.2	Flexural Wave Analysis . . . . .	96
2.12.3	Results and Discussions . . . . .	96
2.13	Laser Induced Flexural Wave: Aluminum in Steel Substrate . . . . .	97
2.13.1	Heat Transfer Analysis . . . . .	98
2.13.2	Flexural Wave Analysis . . . . .	99
2.13.3	Results and Discussions . . . . .	99
	References . . . . .	100
<b>3</b>	<b>HVOF Coating and Characterization . . . . .</b>	<b>103</b>
3.1	Single Layer HVOF Coating and Characterization . . . . .	103
3.1.1	The Point Bending Tests . . . . .	104
3.1.2	Fatigue Tests . . . . .	107
3.1.3	Tensile Tests . . . . .	113
3.1.4	Fracture Toughness Measurement . . . . .	117
3.2	Two Layer HVOF Coating and Characterization . . . . .	119
3.3	Residual Stress Analysis HVOF Coating . . . . .	125
3.3.1	Experimental . . . . .	125
3.3.2	Heat Transfer Analysis . . . . .	126
3.3.3	Modeling of Thermal Stresses . . . . .	127
3.3.4	Residual Stress Measurements . . . . .	128
3.3.5	Findings and Discussion . . . . .	129

3.4	Laser Re-melting of Inconel HVOF Coating . . . . .	136
3.4.1	Mathematical Analysis . . . . .	136
3.4.2	Experimental . . . . .	140
3.4.3	Findings and Discussion . . . . .	140
3.4.4	Laser Control Melting HVOF Coating . . . . .	145
3.4.5	Experimental . . . . .	146
3.4.6	Findings and Discussion . . . . .	147
3.5	Nanoparticles Blended Wires Deposition . . . . .	151
3.5.1	Experimental . . . . .	151
3.5.2	Results and Findings . . . . .	152
	References . . . . .	155
<b>4</b>	<b>Concluding Remarks . . . . .</b>	<b>157</b>
4.1	Findings from the Flexural Analysis . . . . .	157
4.2	Findings from High Velocity Oxy-Fuel Coating Characterization . . . . .	162
	References . . . . .	166

# Chapter 1

## Introduction

**Abstract** Flexural behavior of mechanical systems can be used to identify the system characteristics including parts and system failure. In this chapter, the basics of flexural characteristics of a simple system are presented and the formations associated with the flexural behavior of the system are presented. Heating effects and thermal deflection in terms of flexural motion are also included.

**Keywords** Flexural motion • Mechanical parts • Thermal analysis

The flexural motion of the mechanical parts provides physical insight into the structural disintegrations and enables to assess the presence of defect sites in the parts. On the other hand, thermal spray coating is a widely used in industry to protect the metallic surfaces from the high temperature, wear, and corrosive environments. The flexural characteristics of the beams, due to structural changes and heating, and mechanical, morphological and metallurgical properties of the high velocity oxy-fuel coatings are presented under the appropriate sub-headings in in line with the previous studies [1–57].

### 1.1 Flexural Characteristics

The flexural characteristics of a solid plate depend on the mechanical properties of the plate material, such as density, stiffness, and damping factor, external applied force, such as duration and amplitude, and geometric arrangement of the plate, such as tapered, parallel plate geometry with presence of holes, etc. Modification of any one of these properties results in alteration of the wave characteristics of the motion. This situation is often resulted when the flat solid is heated at one side during the welding or heat treatment process. In this case, the bar resembles the cantilever assembly with non-uniform mechanical properties due to heating. However, the size of the heat affected zone in the treated bar may be correlated with the wave characteristics of the flexural motion of the bar when the impact force is introduced from the free end of the bar. In addition, the characteristics of

flexural motion for a cantilever plate can be used to identify the size of the heated zone of the cantilever plate subjected to the heating process. This is because of the temperature dependent properties of the substrate material such as temperature dependent modulus of elasticity. This situation is more pronounced as the temperature in the plate increases. The nonlinear response of the elastic modulus, due to the temperature field, changes the amplitude of the oscillation during the flexural motion and the time shift in the amplitudes because of heating and no heating situations can provide useful information on the heating rate. Therefore, determining the amplitude difference and the time shift between the maximum amplitudes provide the data on the heating rate, particularly heat source speed and size of the heat affected zone when the source moves along one side of the plate.

The flexural characteristics including the time period of oscillation and the maximum amplitude of motion, can lead to improving quality of heated products, which are affected by the thermal distortion generated and the residual stresses. Investigating the oscillation characteristics of heated structures, and relating the resulting temperatures fields with the flexural characteristics, is an increasingly spreading approach by researchers to demonstrate the influence of heating parameters. The flexural wave generated in the substrate material is modified with the irregularities within the substrate material and the temperature dependent mechanical properties. Therefore, the local heating in the substrate material alters the mechanical properties as well as the resulting flexural characteristics when the substrate material is subjected to the flexural load. Consequently, measurement or prediction of the flexural characteristics enables to predict the heating location and the size of the heat affected zone in the substrate material. In addition, the structural irregularity generated at the workpiece surface through coating can be analyzed from the flexural characteristics of the coated substrate. In this case, coating thickness and its variation can be identified from the amplitude and frequency of the flexural motion of the coated specimen.

Considerable research studies were carried out to examine the flexural characteristics of the solid parts subjected to the various heating and process conditions. The propagation of flexural wave along a clamped supported beam was studied by Shim et al. [9]. They showed that the fringe pattern produced was the loci of constant out-of-plane displacement derivatives with respect to the direction of image shear, which were integrated to yield the instantaneous out-of-plane displacement induced by the flexural wave. The sub-ablation optical excitation of flexural vibration in cantilevers and suspended truck-wheel rim due the laser pulse were investigated by Philp et al. [10]. The results indicated that the technique employed could be used as non-destructive tool for mechanical testing of cantilever beams. The elastic properties of the solid substrates due to laser beam excitation were investigated by Bardenstein et al. [11]. They showed that the amplitude of thermoelastic flexural wave as well as the amplitude of longitudinal pulse was proportional to the energy absorbed by the beam, which in turn enabled to determine elastic constants of the beam. A theoretical study of laser generated transient Lamb waves in orthotropic plates was carried out by Cheng and Berthelot [12]. They introduced quantitative analysis for non-contact and non-destructive

detection of the elastic stiffness properties of machine-made paper by a laser generated Lamb wave technique. Flexural waves transmitted by rectangular piezoceramic transducers were examined by Veidt et al. [13]. They showed that the assumption of a uniform contact pressure distribution between the transducer and the plate could accurately predict the frequency spectrum and time domain response signals of the propagating waves along the main axes of the transmitter element. The defective bonding areas within the brazed adjoining contact surfaces of composite ceramic-metal plates were studied by Conrod and Sayir [14] using a flexural waves and holography. They indicated that the experimental interferograms were matched precisely with analytic results derived from Mindlin's plate equations. An investigation into flexural waves generated on silicon nitride thin films was carried out by Hang and Amit [15] using piezoelectric plates attached to silicon bulk substrate. They demonstrated that the predictions agreed well with the experimental results. Laser generated flexural acoustic waves traveling along the tip of a wedge were studied by Jia et al. [16]. They made the comparison between the laser-generated antisymmetrical flexural model and the flexural Lamb wave propagating along the edge of the plate. Yilbas et al. [17] studied the stress generation and flexural motion during the laser heating process. They showed that the stress level is higher once the displacement of the surface is high.

The flexural characteristics can be associated with the thermal process parameters of the solid parts when subjected to the heating such as laser heating. Considerable research studies were carried out on wave generation in solids due to laser irradiating pulse. A theoretical investigation of the dynamic thermoelastic response of various thickness workpieces due to Q-switched laser pulses was done by Cheng et al. [18] They showed that as the laser pulse duration decreased or workpiece thickness increased, the dynamic wave behavior gradually became apparent. Ultrasound radiation into water by a Lamb wave device using a piezoelectric ceramic with spatially varying thickness was investigated by Motegi [19] He indicated that there was a small velocity gap deriving from the inhomogeneity, but radiation efficiency was much higher than that in the case of a flat plate. A hybrid elastic wave method was employed by Wo and Lui [20] to determine the anisotropic constants of a thin fiber-reinforced composite plate. They noted that with the hybrid method, some of anisotropic constants could be measured accurately with well-developed bulk wave ultrasonics. The propagation velocities of laser generated ultrasonic plate waves were measured by Ridgway et al. [21]. They compared the laser-ultrasonic measurements of phase velocities for the fast-propagating vibration mode with contact transducer based measurements. The propagation of Lamb waves in multilayered plates was examined by Grondal et al. [22]. They indicated that the Lamb waves and particularly their velocities were very sensitive to defects in solids. Laser generation of Lamb waves in copy paper was investigated by Johnson et al. [23]. They observed the significant statistical variations of the wave forms and quantified the variations by means of cross-relation techniques. Propagation characteristics of plate-mode waves on a wedge shaped substrate were investigated by Wakatsuki et al. [24]. They indicated that

the process in which two wave modes were reflected from the front end of the substrate was degenerated into the Rayleigh mode.

The thermal stresses generated during the laser quenching were investigated by Wang et al. [25]. They indicated that the residual stress developed in the surface vicinity resulted in the hardening of the surface. The experimental and numerical studies of fracture initiation in thin aluminum oxide ceramics during laser cutting were carried out by Li and Sheng [26]. They introduced plane stress model when predicting the stresses along the cut edges. They showed that low cutting speed reduces the stress level and minimizes the possible fracture initiation at the cut edges. An analytical solution of a two-dimensional thin coating attached to a substrate was obtained by Elperin and Rudin [27]. They indicated that the temperature difference across the coating generated excessive stress levels, which in turn caused inelastic deformation of the coating. Modest [28] investigated the elastic and viscoelastic stresses during laser drilling of ceramics. He indicated that the material softened in the region closer to the melt zone.

The laser-induced waves in solids received considerable attention, since it served as a nondestructive tool for materials evaluation. Several analytical methods were introduced when modelling the thermoelastic process that took place during the laser heating pulse. Some of these include Green function method, and Laplace and Henkel transformations. However, the thermal stresses developed in the substrate vary with time and it is, in general, difficult to present in a simple mathematical function. Therefore, the analytical solution to the transient problem with nonordered input load becomes very difficult to obtain. Consequently, the general trend is to solve the governing equations numerically. Dubois et al. [29] investigated numerically the laser thermoelastic generation of ultrasound in an orthotropic medium. They compared the predictions with the experimental results and indicated that their predictions agreed well with the experimental findings. They further argued that the model developed could be used to optimize the laser generation of ultrasound in various materials. Cheng et al. [30] studied the dynamic thermoelastic response of pulsed photothermal deformation deflection detection for Q-switched laser pulses. They indicated that when the laser pulse rise time decreases in the order of 10 ns or less, the pulsed photothermal deformation deflection signal reflected a totally dynamic wave behavior. The laser-induced waves such as Lamb waves can also be used to determine the properties of the substrate material. The Lamb wave is generated due to normal and shear loads applied to the surface of the half-space. Dewhurst et al. [31] introduced a Lamb wave technique to describe the measurement of the film thickness on the substrate material.

When a high-intensity laser beam interacts with a solid phase, change occurs in the surface region of the substrate material which, in turn, results in a vapour pressure acting on the surface. This generates flexural waves in the substrate material. Consequently, a stress field due to flexural motion of the workpiece is developed. Considerable research has been carried out to explore the flexural motion generated in the workpiece by laser pulse operation. The propagation of Lamb waves in a multilayer assembly was investigated by Sebastian et al. [32]. They showed that Lamb wave characteristics were very sensitive to any defects in

the substrate material. Yilbas and Faisal [33] investigated laser-induced flexural waves in steel. They indicated that the flexural wave motion was affected by end reflections of the waves.

The change of direction of flexural ultrasonic waves, propagating due to modulating excitation frequency, was investigated by Loh and Ro [34]. They showed that modulation of excited frequency changed the direction of wave propagation. The wave decomposition technique was introduced by Szwerc et al. [35] to separate longitudinal and flexural wave intensities. They indicated that the method could be implemented to determine the power flow fields on structures, which were vibrating with these two wave types.

## 1.2 High Velocity Oxy-Fuel Coating and Characterization

Thermal barrier coating of parts subjected to the high-temperature is necessary for preventing the surface of the parts from excessive heating, erosion, and corrosion during the operation. The coating material selected for such an application must have the properties that resistant to harsh environments as well as the coating process must be efficient, low cost, and fast. One of the coating methods fulfilling these conditions is High Velocity Oxy-Fuel coating (HVOF). Although the process is fast, effective, and low cost, due to the irregularities associated within the resulting coating, investigation into the process is necessary for further improvements of the coating quality. The mechanical properties of the coating, particularly at coating-base material interface, are important to secure the sound coating. The powder emerging from the spray gun reaches almost the melting temperature of the constituting substrate material. Since the stand-off-distance between the gun exit and the base material surface is short, the splats changes from the round shape to the oval shape upon impacting onto the surface due to their elevated temperatures. Once the coating is formed on to the base material surface, the coating temperature remains high while the substrate bulk temperature is low. This, in turn, modifies the stress levels in the coating and at the coating-base material interface. However, depending on the coating thickness, the residual stresses can be compressive or tensile. The residual stress in the coating influences the mechanical performance of the coating.

Considerable research studies were carried out to examine the residual stress development in the coating. The residual stress measurement using the curvature method was carried out by Liao et al. [36]. They showed that temperature history of a part was of paramount importance in stress generation and distribution. The evolution of the residual stress in thermal barrier coatings using the modified layer removal method was carried out by Lima et al. [37]. They showed that the residual stresses were mainly influenced by the thermal history regarding the plastic deformation and the quenching of individual splats. The residual stress generation during thermal spraying was examined by Gill and Clyne [38]. They showed that the continuous curvature measurement technique was potentially a reliable and

accurate method with a minimum measurement error. The measurement of the residual stress in plasma-sprayed coatings was carried out by Kesler et al. [39]. They indicated that the respective thermal expansion coefficients and the mechanical properties were the most important factors determining the stress level and the magnitude. The residual stress measurement using the curvature interferometer was carried out by Wang et al. [40]. They showed that the existence of sub-surface tensile layer was expected to play an important role in the wear process associated with the normal contact loading. The residual stress development in thermal spray coatings was investigated by Ghafouri-Azar et al. [41]. They indicated that the magnitude of residual stress increased significantly with increasing the coating thickness. The residual stress development in the HVOF carbide coatings was studied by Pejryd et al. [42]. They evaluated the coating crack resistance due to bending and low cycle fatigue loads. The residual stress distribution in thermally sprayed coatings was carried out by Otsubo et al. [43]. They indicated that the residual stress remained almost the same in the coating, except at interface, which reduced from the mean value. The residual stress in HVOF tungsten carbide coating and its effect on the fatigue life were studied by McGrann et al. [44]. They showed that the fatigue life of the tungsten carbide coating could be determined using the modified layer removal method. The fracture behavior of the brittle coatings was investigated by Bansal et al. [45]. They showed that the development of the finite element code made it possible to study the effect of various coating parameters in isolation, which was difficult to achieve in an experimental study.

The electron beam re-melting of HVOF coating was studied by Hamatani and Miyazaki [46]. They showed that low melting speed and homogeneous heating reduced the unevenness of the surface of the number of pores in the coating. The laser surface treatment of HVOF coating was carried out by Oksa et al. [47]. They successfully sealed the coating surface for corrosion prevention. HVOF coating and the laser treatment were investigated by Suutala et al. [48]. They observed that the cracks occurred in the coating after the laser treatment and the crack orientation was perpendicular to the laser processing direction. Adhesion testing of coatings produced via arc spray, HVOF, and laser cladding was carried out by Hjornhede and Nylund [49]. They indicated that the coatings deposited with the laser technique did not show the de-lamination. The effect of laser glazing on the microstructure of the HVOF coating was examined by Kumari et al. [50]. They showed that laser glazing of coatings affected the surface roughness in either way depending on the coating composition as well on the treatment parameters. Laser produced functionally graded coatings was examined by Riabkina-Fishman et al. [51]. They showed that the laser treatment resulted the coating, which had wear resistance five times higher than that of untreated coatings.

The thermal process pertinent to the formation of a WC-Ni coating on low alloy steel by HVOF spraying was studied by Sobolev et al. [52]. They indicated that the second and subsequent layers of the coating did not have practical influence on the thermal state of the substrate-coating interface. Moreover, the substrate coatings thermal interactions were completely determined by interactions between substrate

and the first layer of the coatings. The influence WC-Cr was examined by Zhao et al. [53]. They indicated that the spray distance had less influence on the wear resistance of coating as compared to those corresponding to the total gas flow rate and the powder feed rate.

The microstructure of multilayer coatings produced by thermal spray process was examined by Fagoaga et al. [54]. They showed that the multilayer coatings presented a microstructure composed of alternate phases of chromium carbide cermet and oxides, which were resulted from preferential oxidation of chromium compounds. The mechanical properties of mono and multilayered coatings were examined by David et al. [55]. They observed that WC-CoCr deposited by HVOF spraying onto P91 steel presented on high fatigue resistance. The bond strength and thermal shock behavior of HVOF sprayed multi-layered coating was examined by Wilden et al. [56]. They showed that HVOF coatings had higher contact of oxygen and higher density than that produced by plasma sprayed coatings. The microstructure and wear resistance of WC-Co coatings thermally sprayed onto tool steel were studied by Pepe et al. [57]. They introduced the neural network to classify the wear performance of the coatings and indicated that the neural network would be used as an effective tool to classify the wear behavior of the resulting coatings.

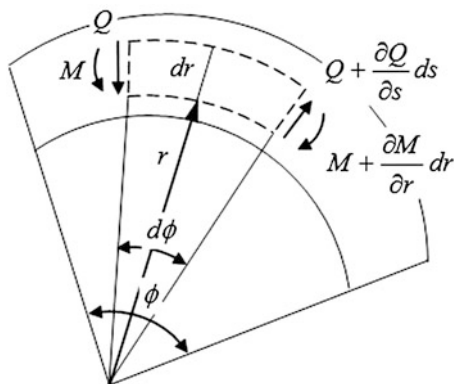
### 1.3 Analytical Formulation of a Beam Subjected to a Flexural Motion

The mathematical analysis associated with the flexural characteristics of a cantilever beam is given below in line with the previous study [33]. Therefore, the following assumptions are made in the analysis:

1. Beam is initially straight and unstressed.
2. The material of the beam is perfectly elastic, homogeneous and isotropic.
3. Every cross-section of the beam is symmetrical about the plane of bending i.e. about an axis perpendicular to the neutral axis.
4. There is no resultant force perpendicular to any cross-section.
5. Plane sections remain plain during bending, but no longer perpendicular to the centroidal plane. Accordingly, warping of the cross-section is no longer present. Thus shear deformation will be considered.
6. Relationship between moment and curvature as assumed in elementary theory still exists.
7. The effects of rotary inertia are included.
8. The deflections are small compared to the beam thickness.
9. Material properties are kept constant in the analysis.

Consider an element of beam subjected to shear force, bending moment and distributed load as can be seen in Fig. 1.1.

**Fig. 1.1** Beam element subjected to bending moment and shear force



The transverse displacement is measured by  $y \equiv y(x, t)$  and the slope of the centroidal axis is given by  $\frac{\partial y}{\partial x}$ . This slope is considered to be made of two contributions. The first is  $\phi \equiv \phi(x, t)$  due to the effects of bending. An additional contribution is  $\gamma_0$  which defines the shear strain due to shearing effects. Thus one has:

$$\frac{\partial y}{\partial x} = \phi + \gamma_0 \quad (1.1)$$

Now one can relate the above kinematic expression to the applied load using assumption 2 in terms of present parameters:

$$\frac{M}{EI} = \frac{-1}{R} \quad (1.2)$$

where  $R$  is the radius of curvature,  $M$  is the bending moment at the cross-section under consideration and  $E$  is the modulus of elasticity of the substrate material. For small curvature:

$$Rd\phi = dx \quad (1.3)$$

or

$$\frac{1}{R} = \frac{d\phi}{dx} \quad (1.4)$$

From Eq. (1.2) one can get:

$$\frac{M}{EI} = \frac{-\partial\phi}{\partial x} \quad (1.5)$$

The shear force  $Q$  as the cross-section is given in terms of the shear stress  $\tau$  or shear strain  $\gamma$  as

$$Q = \int_A \tau dA = G \int_A \gamma dA \quad (1.6)$$

where  $G$  defines the material modulus of rigidity, which is assumed to be constant and  $A$  is the area of cross-section.

As  $\gamma_0$  is defined as the shear strain at the centroidal axis, then  $G\gamma_0 A$  will give a shear force. To account for the fact that shear is not constant across the thickness a correction factor,  $\kappa$  (Timoshenko shear factor) is introduced such that:

$$Q = G \int_A \gamma dA = G\gamma_0 \kappa A \quad (1.7)$$

The value of  $\kappa$  will depend on the shape of the cross-section and must be determined, usually by stress analysis means, for each cross-section. It can be taken to be equal to  $2/3$ . By substituting Eq. (1.1) into Eq. (1.7) one can obtain:

$$Q = AG\kappa \left( \frac{\partial y}{\partial x} - \phi \right) \quad (1.8)$$

Now writing the equation of motion in vertical direction, one can obtain:

$$-Q + \left( Q + \frac{\partial Q}{\partial x} dx \right) + q dx = \rho A dx \frac{\partial^2 y}{\partial t^2} \quad (1.9)$$

where  $q \equiv q(x, t)$  is the distributed force. Simplifying Eq. (1.9), one can get:

$$\frac{\partial Q}{\partial x} + q = \rho A \frac{\partial^2 y}{\partial t^2} \quad (1.10)$$

Summing moments about an axis perpendicular to  $x$ - $y$  plane and passing through the center of element, one can get:

$$M - \left( M + \frac{\partial M}{\partial x} dx \right) + \frac{1}{2} Q dx + \frac{1}{2} \left( Q + \frac{\partial Q}{\partial x} dx \right) dx = J \frac{\partial^2 \phi}{\partial t^2} \quad (1.11)$$

where  $J \equiv J(x)$  is the polar moment of inertia and is equal to  $\rho I dx$ , where  $I \equiv I(x)$  is second moment of area.

From Eq. (1.11), it can be observed that:

$$Q - \frac{\partial M}{\partial x} = \rho I \frac{\partial^2 \phi}{\partial t^2} \quad (1.12)$$

Substituting Eqs. (1.5) and (1.8) into the Eqs. (1.10) and (1.12) gives:

$$G\kappa \left[ \frac{\partial A}{\partial x} \left( \phi - \frac{\partial y}{\partial x} \right) + A \left( \frac{\partial \phi}{\partial x} - \frac{\partial^2 y}{\partial x^2} \right) \right] + \rho A \frac{\partial^2 y}{\partial t^2} = q(x, t) \quad (1.13)$$

and

$$GA\kappa \left( \frac{\partial y}{\partial x} - \phi \right) + E \left( \frac{\partial I}{\partial x} \frac{\partial \phi}{\partial x} + I \frac{\partial^2 \phi}{\partial x^2} \right) = \rho I \frac{\partial^2 \phi}{\partial t^2} \quad (1.14)$$

Equations (1.13) and (1.14) are the governing equations of motion of Timoshenko beam of varying thickness.

Dispersion relation shows the relation between the phase velocity and the frequency of the harmonic wave. It determines the change of shape of the travelling wave. For constant thickness, Timoshenko beam, the equations of motion [Eqs. (1.13) and (1.14)] can be written as, after setting  $q = 0$ :

$$GA\kappa \left[ \frac{\partial^2 y}{\partial x^2} - \frac{\partial \phi}{\partial x} \right] = \rho A \frac{\partial^2 y}{\partial t^2} \quad (1.15)$$

and

$$EI \frac{\partial^2 \phi}{\partial x^2} + GA\kappa \left( \frac{\partial y}{\partial x} - \phi \right) = \rho I \frac{\partial^2 \phi}{\partial t^2} \quad (1.16)$$

There are two dependent variables  $y$ ,  $\phi$  and the remaining coefficients are constants.

Assuming harmonic waves, the solution can be written as:

$$y = y_0 e^{-i(kx - \omega t)} \quad (1.17)$$

$$\phi = \phi_0 e^{-i(kx - \omega t)} \quad (1.18)$$

where  $\phi_0$  and  $y_0$  are the amplitudes.

Substituting Eqs. (1.17) and (1.18) into Eqs. (1.15) and (1.16) one can get:

$$\begin{bmatrix} GA\kappa k^2 & -ikGA\kappa \\ ikGA\kappa & EI k^2 + GA\kappa - \rho I \omega^2 \end{bmatrix} \begin{bmatrix} y_0 \\ \phi_0 \end{bmatrix} = 0 \quad (1.19)$$

Defining:

$$c_1 \equiv \sqrt{\frac{EI}{\rho A}} \quad c_2 \equiv \sqrt{\frac{GA\kappa}{\rho A}} \quad c_3 \equiv \sqrt{\frac{\rho I}{\rho A}}$$

Therefore one can have from Eq. (1.19):

$$\begin{bmatrix} \left(k^2 - \frac{\omega^2}{c_2^2}\right) & -ik \\ ik & \left(\frac{k^2 c_1^2}{c_2^2} + 1 - \frac{\omega^2 c_3^2}{c_2^2}\right) \end{bmatrix} \begin{bmatrix} y_0 \\ \phi_0 \end{bmatrix} = 0 \quad (1.20)$$

For nontrivial solution determinant must be zero, so one can obtain from Eq. (1.20):

$$k^4 - k^2 \omega^2 \left[ \left(\frac{1}{c_2}\right)^2 + \left(\frac{c_3}{c_1}\right)^2 \right] - \left[ \left(\frac{\omega}{c_2}\right)^2 + \left(\frac{c_3}{c_2 c_1}\right)^2 \omega^4 \right] = 0 \quad (1.21)$$

Solving for  $k$ , one can get:

$$k^2 = \frac{1}{2} \left[ \left(\frac{1}{c_2}\right)^2 + \left(\frac{c_3}{c_1}\right)^2 \right] \omega^2 \pm \sqrt{\left(\frac{\omega}{c_1}\right)^2 + \frac{1}{4} \left[ \left(\frac{1}{c_2}\right)^2 - \left(\frac{c_3}{c_1}\right)^2 \right]^2 \omega^4} = 0 \quad (1.22)$$

Therefore, there are four modes of wave propagation. Equation (1.22) is the dispersion equation for constant thickness Timoshenko beam.

At very small frequency, in comparison with the cut off frequency of second mode:

$$k_1 \approx \pm \sqrt{\frac{\omega}{c_1}} \quad k_2 \approx \pm i \sqrt{\frac{\omega}{c_1}}$$

So modes are independent of  $GA\kappa$  and  $\rho I$  and that is why this high-order theory does not introduce additional modes. On the other hand, as the frequency becomes very large then:

At high frequency:

$$k_1 \Rightarrow \frac{\omega}{c_2} \quad k_2 \Rightarrow \frac{c_3}{c_1} \omega$$

$k_1$  and  $k_2$  are the propagating modes, hence imaginary branch must have turned real. Cut-off frequency of the second mode,  $\omega_0$  is obtained where  $k$  is zero and this is found to be where

$$\omega_0 = \frac{c_2}{c_3} = \sqrt{\frac{GA\kappa}{\rho I}}$$

To eliminate the rotational inertia, it is necessary to let  $c_3 = 0$  and to eliminate the shear deformation to let  $c_2 = \infty$ . In both cases the cut-off frequency goes to infinity giving the second mode only evanescent.

## References

1. D. Al-Anazi, M.S.J. Hashmi, B.S. Yilbas, M. Sunar, Three-point bend testing of HVOF AMDRY 9954 coating on Ti-6Al-4 V alloy. *J. Mater. Process. Technol.* **174**(1-3), 204-210 (2006)
2. D. Al-Anazi, M.S.J. Hashmi, B.S. Yilbas, HVOF thermally sprayed CoNiCrAlY coatings on Ti-6Al-4 V alloy: high cycle fatigue properties of coating. *Proc. Inst. Mech. Eng. Part B J. Eng. Manuf.* **221**(4), 647-654 (2007)
3. D. Al-Anazi, M.S.J. Hashmi, B.S. Yilbas, HVOF coating of AMDRY 9954 onto Ti-6Al-4 V alloy: fracture toughness measurement. *Proc. Inst. Mech. Eng. Part B J. Eng. Manuf.* **221**(4), 617-623 (2007)
4. D. Al-Anazi, M.S.J. Hashmi, B.S. Yilbas, M. Sunar, in *HVOF sprayed AMDRY 995 powders onto Ti-6 Al-4 V alloy: tensile properties*, Conference on Advances in Material Processing Technology, AMPT06, Las Vegas, July 30-Aug 2 2006
5. D.M. Al-Anazi, Study of the mechanical and metallurgical properties of AMDRY 9954 HVOF coated Ti-6Al-4 V alloy. Ph.D. Thesis, School of Mechanical and Manufacturing Engineering, Dublin City University, Ireland, 2007
6. A.F.M. Arif, B.S. Yilbas, Laser treatment of HVOF coating: modeling and measurement of residual stress in coating. *J. Mater. Eng. Perform.* **17**(5), 644-650 (2008)
7. Z.Y. Taha-al, M.S.J. Hashmi, B.S. Yilbas, Effect of WC on the residual stress in the laser treated HVOF coating. *J. Mater. Process. Technol.* **209**(7), 3172-3181 (2009)
8. Y.A. Al-Shehri, M.S.J. Hashmi, B.S. Yilbas, HVOF coating of metallic surfaces using different powders: fracture toughness measurement of resulting surfaces. *Adv. Mater. Res.* **445**, 621-626 (2012)
9. V.P.W. Shim, S.L. Toh, S.E. Quah, Impact-induced flexural waves in a Timoshenko beam-shearographic detection and analysis. *Exp. Mech.* **34**, 340-348 (1994)
10. W.R. Philp, D.J. Booth, N.D. Perry, Single laser excitation of structural vibration using power densities below the surface ablation threshold. *J. Sound Vib.* **185**, 643-654 (1995)
11. A.L. Bardenstein, V.I. Bykov, D.I. Vaisburd, in *Pulsed power electron and ion beams diagnostics based on simultaneous detection of acoustic longitudinal and flexural waves*, IEEE International Pulsed Power Conference, Piscataway, NJ, vol. 1, pp. 390-395, 1995
12. J. Cheng, Y. Berthelot, Theory of laser generated transient Lamb waves in orthotropic plates. *J. Phys. D Appl. Phys.* **29**(7), 1857-1867 (1996)
13. M. Veidt, T. Liu, S. Kitipornchai, Flexural waves transmitted by a rectangular piezoceramic transducers. *Smart Mater. Struct.* **10**, 681-688 (2001)
14. M. Conrad, M. Sayir, Composite ceramic-metal plates tested with flexural waves and holography. *Exp. Mech.* **41**, 412-420 (2001)
15. G. Hang, L. Amit, in *Flexural plate wave excitation using bulk modes*, *Proceedings of Ultrasonics Symposium*, Atlanta, GA, vol. 1, pp. 799-802 (2001)
16. X. Jia, D. Auribault, M. de Billy, G. Quentin, in *Laser generated flexural acoustic waves traveling along the tip of a wedge*, *Proceedings of IEEE Ultrasonics Symposium*, Piscataway, NJ, vol. 2, pp. 637-640 (1993)
17. B.S. Yilbas, S.J. Hyder, S.Z. Shuja, Flexural wave generation and stress analysis during laser evaporative heating of steel. *Proc. ImechE Part C J. Eng. Sci.* **216**, 531-542 (2002)
18. J. Cheng, L. Wu, S. Zong, Thermoelastic response of pulsed photo thermal deformation of thin plates. *J. Appl. Phys.* **76**, 716-722 (1994)
19. K. Moteqi, Ultrasound radiation into water by a Lamb wave device using a piezoelectric ceramic plate with spatially varying thickness. *Ultrasonics* **37**, 405-412 (1999)
20. T.T. Wu, Y.H. Lui, On the measurement of anisotropic elastic constants of fiber-reinforced composite plate using ultrasonic bulk wave and laser generated Lamb wave. *Ultrasonics* **37**, 505-510 (1999)
21. P.L. Ridgway, A.J. Hunt, M. Quinby-Hunt, R.E. Russo, Laser ultrasonics on moving paper. *Ultrasonics* **37**, 395-403 (1999)

22. S. Grondal, J. Assad, C. Delebarre, P. Blabquet, E. Moulin, Propagation of Lamb waves in multilayered plates: phase-velocity measurement. *Meas. Sci. Technol.* **10**, 348–353 (1999)
23. M.A. Johnson, Y.H. Berhelot, P.H. Brodeur, L.A. Jacobs, Investigation of laser generation of Lamb waves in copy paper. *Ultrasonics* **34**, 703–710 (1999)
24. N. Wakatsuki, K. Muzitani, K. Nagai, Propagation characteristics of plate-mode waves on wedge-shaped substrate. *Jpn. J. Appl. Phys.* **34**(1), 2561–2564 (1995)
25. H.G. Wang, Y.H. Guan, T.L. Chen, J.T. Zhang, A study of thermal stresses during laser quenching. *J. Mater. Process. Technol.* **63**, 550–553 (1997)
26. K. Li, P. Sheng, Plane stress model for fracture of ceramics during laser cutting. *Int. J. Mach. Tools Manuf* **35**, 1493–1506 (1995)
27. T. Elperin, G. Rudin, Thermo-elasticity problem for a multilayer coating-substrate assembly irradiated by a laser beam. *Int. Commun. Heat Mass Trans.* **23**, 133–142 (1996)
28. M.F. Modest, Transient elastic and viscoelastic thermal stresses during laser drilling of ceramics. *ASME J. Heat Trans.* **120**, 892–898 (1998)
29. M. Dubois, F. Enguehard, L. Bertland, Modeling of laser thermoelastic generation of ultrasound in an orthotropic medium. *Appl. Phys. Lett.* **65**, 554–556 (1994)
30. J. Cheng, L. Wu, S. Zong, Thermoelastic response of pulsed photothermal deformation of thin plates. *J. Appl. Phys.* **76**, 716–722 (1994)
31. R.J. Dewhurst, C. Edwards, A.D.W. Mckie, S.B. Palmer, Estimation of thin metal sheet using laser generated ultrasound. *Appl. Phys. Lett.* **51**(14), 1066–1068 (1987)
32. G. Sebastian, A. Jamal, D. Christophe, B. Pierrick, P. Emmanuel, Propagation of Lamb waves in multilayered plates: phase-velocity measurement. *Measure. Sci. Technol.* **10**(5), 348–353 (1999)
33. B.S. Yilbas, M. Faisal, Flexural waves generated due to pressure force during laser induced evaporation process. *Laser Appl.* **13**, 118–124 (2001)
34. B.G. Loh, P.I. Ro, Changing the propagation direction of flexural ultrasonic progressive waves by modulating excitation frequency. *J. Sound Vibr.* **238**, 171–178 (2000)
35. R.P. Szwerc, C.B. Burroughs, T.E. McDevitt, in Wave decomposition technique to separate longitudinal and flexural wave intensities. *Proceedings of the National Conference on Noise Control Engineering*, vol. 1, pp. 215–220 (1997)
36. H. Liao, P. Vaslin, Y. Yang, C. Coddet, Determination of residual stress distribution from in situ curvature measurements for thermally sprayed WC/Co coatings. *J. Therm. Spray Technol.* **6**(2), 235–412 (1998)
37. C.R.C. Lima, J. Nin, J.M. Guilemany, Evaluation of residual stresses of thermal barrier coatings with HVOF thermally sprayed bond coats using the modified layer removal method (MLRM). *Surf. Coat. Technol.* **200**(12–13), 5963–5972 (2006)
38. S.C. Gill, T.W. Clyne, Investigation of residual stress generation during thermal spraying by continuous curvature measurement. *Thin Solid Films* **250**, 172–180 (1994)
39. O. Kesler, J. Matejcek, S. Sampath, S. Suresh, T. Gnaeupel-Herold, P.C. Brand, H.J. Prask, Measurement of residual stress in plasma-sprayed metallic, ceramic and composite coatings. *Mater. Sci. Eng. A Struct. Mater. Prop. Microstruct. Process.* **257**(2), 215–224 (1998)
40. J. Wang, P. Shortriya, K.S. Kim, Surface residual stress measurement using curvature interferometry. *Exp. Mech.* **46**, 39–46 (2006)
41. R. Ghafouri-Azar, J. Mostaghimi, S. Chandra, Modeling development of residual stresses in thermal spray coatings. *Comput. Mater. Sci.* **35**, 13–26 (2006)
42. L. Pejryd, J. Wigren, D.J. Greving, J.R. Shadley, E.F. Rybicki, Residual stresses as a factor in the selection of tungsten carbide coatings for a jet engine application. *J. Therm. Spray Technol.* **4**(3), 268–274 (1995)
43. F. Otsubo, K. Kishitake, T. Terasaki, Residual stress distribution in thermally sprayed self-fluxing alloy coatings. *Mater. Trans.* **46**(11), 2473–2477 (2005)
44. R.T.F. McGrann, D.J. Greving, J.R. Rybicki, B.E. Bodger, D.A. Somerville, Effect of residual stress in HVOF tungsten carbide coatings on the fatigue life in bending of thermal spray coated aluminum. *J. Therm. Spray Technol.* **7**(4), 546–552 (1998)

45. P. Bansal, P.H. Shipway, S.B. Leen, Finite element modeling of the fracture behavior of brittle coatings. *Surf. Coat. Technol.* **200**(12–13), 5318–5327 (2006)
46. H. Hamatani, Y. Miyazaki, Optimization of an electron beam remelting of HVOF sprayed alloys and carbides. *Surf. Coat. Technol.* **154**, 176–181 (2002)
47. M. Oksa, E. Turunen, T. Varis, Sealing of thermally sprayed coatings. *Surf. Eng.* **20**(4), 251–254 (2004)
48. J. Suutala, J. Tuominen, P. Vuorisio, Laser-assisted spraying and laser treatment of thermally sprayed coatings. *Surf. Coat. Technol.* **201**, 1981–1987 (2006)
49. A. Hjornhede, A. Nylund, Adhesion testing of thermally sprayed and laser deposited coatings. *Surf. Coat. Technol.* **184**, 208–218 (2004)
50. S. Kumari, A.S. Khanna, and A. Gasser, in *The influence of laser glazing on morphology, composition and microhardness of thermal sprayed Ni-WC coatings*, 4th International Surface Engineering Conference, St. Paul, MN, USA, 2005
51. M. Riabkina-Fishman, E. Rabkin, P. Levin, N. Frage, M.P. Dariel, A. Weisheit, R. Galun, B.L. Mordike, Laser produced functionally graded tungsten carbide coatings on M2 high-speed tool steel. *Mater. Sci. Eng.* **302**, 106–114 (2001)
52. V.V. Sobolev, J.M. Guilemany, J.R. Miguel, J.A. Calero, Influence of thermal processes on coating formation during high velocity oxy-fuel (HVOF) spraying of WC-Ni powder particles. *Surf. Coat. Technol.* **82**, 121–129 (1996)
53. L. Zhao, M. Maurer, F. Fischer, R. Dicks, E. Lugscheider, Influence of spray parameters on the particle in-flight properties and the properties of HVOF coating of WC-CoCr. *Wear* **257**, 41–46 (2004)
54. I. Fagoaga, J.L. Vivienta, P. Gavin, J.M. Bronte, J. Garcia, J.A. Tagle, Multilayer coatings by continuous detonation system spray technique. *Thin Solid Films* **317**, 259–265 (1998)
55. C. David, K. Anthymidis, P. Agrianidis, D. Tsipas, Determination of the fatigue resistance of HVOF thermal spray WC-CoCr coatings by means of impact testing. *J. Test. Eval.* **35**, 630–633 (2007)
56. J. Wilden, M. Wank, H.D. Steffens, M. Brune, in *New thermal barrier coating system for high temperature applications, proceedings of the 15th International Thermal Spray Conference*, vol. 2, pp. 1669–1673 (1998)
57. G. Pepe, L. Looney, M.S.J. Hashmi, Predicting the wear resistance of WC-Co coatings using neural networks. *Int. J. Model. Simul.* **19**, 410–417 (1999)

## Chapter 2

# Flexural Motion Due to Laser Heating Applications

**Abstract** Laser evaporative heating of solid surfaces involves phase change process and recoil pressure generation in between the vapor and liquid phases. Recoil pressure remains high during a short period of time, which in turn causes mechanical vibration of the body irradiated by a laser beam. When the body resembles a cantilever arrangement and if the laser radiation takes place at the free end of the cantilever beam, the body undergoes a flexural motion. Depending on the laser pulse intensity and duration, the displacement characteristics of the cantilever beam provide information on the mechanical properties of the irradiated beam. In this chapter, laser pulse heating is formulated and thermal stress developed in the heated region is analyzed. In addition, flexural behavior of the cantilever beam is presented in detail.

**Keywords** Laser heating • Temperature • Stress • Flexural motion

## 2.1 Laser Induced Evaporation Process

In the analysis of the flexural characteristics of the beam, the formulation and findings of the previous study [1] are considered.

Consider the flexural wave generated during the laser ablation of steel surface. The pressure rise at the interface zone can be translated into a force acting normal to the surface of the substrate. The resulting force is then considered to generate flexural waves along the substrate. In the following, the pressure rise at the surface during the laser-workpiece interaction is formulated and wave equations are solved numerically to obtain the flexural wave characteristics due to the normal pressure force.

### 2.1.1 Temperature and Pressure

The analytical solution is limited to the temperature range where the plasma formation is negligible as compared to vapor emission from the surface.

### 2.1.1.1 Surface Temperature

The surface temperature of the evaporating surface can be written as [2]

$$T_s = \frac{I_0 \alpha}{k V} - \frac{\alpha \rho L_v}{k} \quad (2.1)$$

where  $I_0$  is the peak power intensity and  $V$  is the velocity of the surface, which is

$$V = \left( \frac{k_B T_s}{2\pi m} \right)^{1/2} \exp\left( -\frac{m L_v}{k_B T_s} \right) \quad (2.2)$$

where  $m$  is the mass of an atom,  $k_B$  is Boltzmann's constant, and  $L_v$  is latent heat of evaporation.

### 2.1.1.2 Interface Pressure

The pressure acting on the surface is taken as the time averaged rate of momentum change which, although it might appear dubious in view of the small periods of time over which the surface ablates, correlates reasonably well with measured results [3]. When omitting the aggregation of substrate vapor above the target surface and the expulsion of liquid globules, the recoil pressure (which is the pressure that was generated in the interface of evaporated surface and acted onto the substrate) can be formulated through the conservation of momentum. Denoting the surface recession velocity as  $V_s$  (Fig. 2.1a), mass continuity requires

$$\rho_s V_s = \rho_v (V_v + V_s), \quad (2.3)$$

where  $v$  and  $s$  refer to the vapor and the liquid phases at interface, respectively. The momentum equation across the interface is

$$P_s + \rho_s V_s^2 = P_v + \rho_s V_s (V_v + V_s). \quad (2.4)$$

The recoil pressure ( $P_s$ ) can be calculated after knowing the vapor pressure, vapor density (the value is taken from the previous study [4]), recession velocity, and the liquid density (taken as the density of the substrate at the melting temperature). Consequently, determination of vapor pressure and recession velocity are necessary to determine the recoil pressure. The recoil pressure is determined from Eq. (2.4) and it is validated using the equation derived from the previous study [5] which is

$$P_s = \frac{I_v V_v}{[L_v + \frac{1}{2} V_v^2]}, \quad (2.5)$$

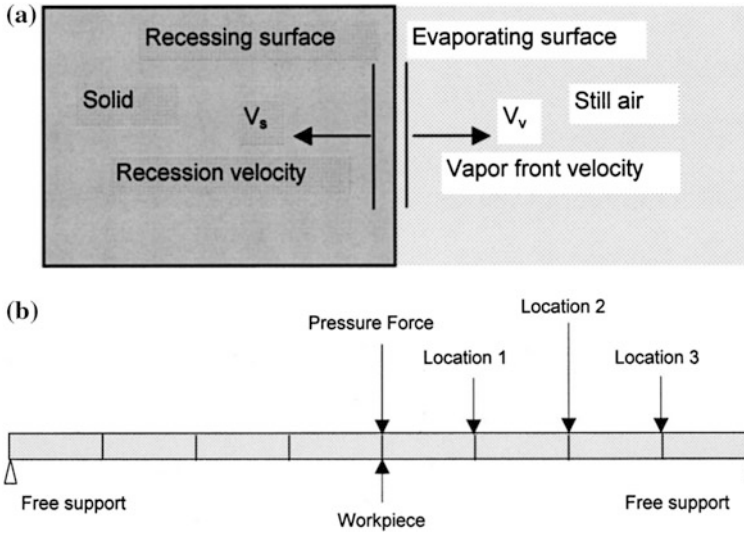


**Fig. 2.1** a Schematic view of interface. b Schematic view of workpiece and elements used in the analysis [1]

where  $I_v$  is the energy consumed during the evaporation process and it is given by

$$I_v = \int_{T_1}^T C_p dT + L_v \quad (2.6)$$

### 2.1.1.3 Vapor Pressure

The vapor expands into the still air, where the gauge pressure is zero. Hence, the vapor pressure can be written after considering the momentum equation across the vapor front and the still air as

$$P_v = \rho_s V_s V_v, \quad (2.7)$$

where  $\rho_s V_s$  is the mass flow rate. The vapor pressure predicted from Eq. (2.7) is validated using the equation given in the previous study, [6] i.e.,

$$P_v = 1.82 \times 10^{-3} \frac{\sqrt{C_p T_v I_0}}{[C_p (T_v - T_0) + L_v]} \quad (2.8)$$

The unit of Eq. (2.8) is in bar.

### 2.1.2 Wave Analysis

The solution in the wave problem is in general a function of space and time. If the time variation of the solution is focused on at a particular point in space, then it can be presented by a spectral function. The spectral formulation starts with the equations of motion of the workpiece (as free supported beam) including inertia terms.

After dividing the workpiece into a number of elements, cross-sectional area and second moment of area at the midpoint of each element can be considered as constant over the entire element. Therefore, the equation of motion can be written as [7]

$$GA\kappa \left[ \frac{\partial^2 y}{\partial x^2} - \frac{\partial \phi}{\partial x} \right] = \rho A \frac{\partial^2 y}{\partial t^2} - q \quad (2.9)$$

and

$$\frac{\partial^2 \phi}{\partial x^2} + GA\kappa \left[ \frac{\partial y}{\partial x} - \phi \right] = \rho I \frac{\partial^2 \phi}{\partial t^2} \quad (2.10)$$

The displacement and the bending slope can be written in the spectral form as [8]

$$y(x, t) = \sum_n \hat{y}_n(x, \omega_n) e^{i\omega_n t} \quad (2.11)$$

and

$$\phi(x, t) = \sum_n \hat{\phi}_n(x, \omega_n) e^{i\omega_n t} \quad (2.12)$$

The spectral component  $\hat{y}_n$  and  $\hat{\phi}_n$  have the solution as

$$\hat{y}_n = A_1 e^{-ik_1 x} + B_1 e^{-ik_2 x} + C_1 e^{ik_1 x} + D_1 e^{ik_2 x} \quad (2.13)$$

and

$$\hat{\phi}_n = A_2 e^{-ik_1 x} + B_2 e^{-ik_2 x} + C_2 e^{ik_1 x} + D_2 e^{ik_2 x} \quad (2.14)$$

where  $k_1$  and  $k_2$  are the wave numbers and  $A_1, A_2, B_1, B_2, C_1, C_2$  and  $D_1, D_2$  are the frequency dependent coefficients, which are complex in nature. The first term in Eqs. (2.13) and (2.14) represent the waves moving in the forward direction while the last two describe the backward moving waves.

Substituting  $\hat{y}_n$  and  $\hat{\phi}_n$  in Eqs. (2.9) and (2.10), and considering the load to be applied at the modes, yields

$$\begin{aligned}
GA\kappa(-k_1^2 A_1 + ik_1 A_2) &= -\omega^2 \rho A (-A_1) \\
GA\kappa(-k_1^2 B_1 + ik_1 B_2) &= -\omega^2 \rho A (-B_1) \\
GA\kappa(-k_1^2 C_1 + ik_1 C_2) &= -\omega^2 \rho A (-C_1) \\
GA\kappa(-k_1^2 D_1 + ik_1 D_2) &= -\omega^2 \rho A (-D_1)
\end{aligned} \tag{2.15}$$

where the coefficients

$$\begin{aligned}
A_2 &= \left[ \frac{-\omega^2 \rho A + k_1^2 GA\kappa}{ik_1 GA\kappa} \right] A_1, & B_2 &= \left[ \frac{-\omega^2 \rho A + k_1^2 GA\kappa}{ik_1 GA\kappa} \right] B_1, \\
C_2 &= \left[ \frac{\omega^2 \rho A - k_1^2 GA\kappa}{ik_1 GA\kappa} \right] C_1, & D_2 &= \left[ \frac{\omega^2 \rho A - k_1^2 GA\kappa}{ik_1 GA\kappa} \right] D_1.
\end{aligned}$$

The shear force and momentum equations can be written as

$$\dot{Q} = -EI \frac{\partial^2 \hat{\phi}}{\partial x^2} - \omega^2 \rho I \hat{\phi} \tag{2.16}$$

and

$$\dot{M} = -EI \frac{\partial \hat{\phi}}{\partial x} \tag{2.17}$$

The dynamic stiffness is obtained by first relating the coefficients to the nodal displacement as

$$[A, B, C, D] = \hat{\alpha} [\hat{y}_1, \hat{\phi}_1, \hat{y}_2, \hat{\phi}_2], \tag{2.18}$$

where  $[\hat{\alpha}] = [\beta]$  and  $[\beta]^{-1}$  are given in [8].

The nodal loads are obtained by using the shear force and momentum Eqs. (2.16) and (2.17) i.e.,

$$[\hat{F}]^T = [\hat{k}][d]^T$$

where

$$[\hat{F}]^T = [\hat{Q}_1 \hat{M}_1 \dots \hat{Q}_n \hat{M}_n]$$

and

$$[d]^T = [\hat{y}_1 \hat{\phi}_1 \dots \hat{y}_n \hat{\phi}_n]$$

where n is the number of nodes.

### 2.1.2.1 Initial and Boundary Conditions

Initially the displacements and velocities are set to zero. The free supported boundary condition at the workpiece ends is considered. In this case, at free ends of the workpiece ( $x = 0$  and  $x = 1$ ), the bending moment is set to zero at all frequencies, i.e.,

$$\frac{d\hat{\phi}(I, \omega)}{dx} = 0.$$

In order to observe the effect of reflecting waves from the free ends of the workpiece, one end of the workpiece is assumed to be at infinity. This boundary condition (element extends to infinity) requires that the element behaves as a radiating beam which acts as a conduit for energy out of the system.

### 2.1.2.2 Method of Solution

In the analysis, the workpiece is divided into eight elements and each element can be treated as uniform (Fig. 2.1b). The displacement vector is then transformed from time domain into frequency domain using fast Fourier transformation (FFT). The transform response is fed back into the governing differential equations, which is solved at each frequency component using the finite element method. The transient response is recovered by using the inverse FFT. The input excitation signal, which is the load generated due to the normal component of the thermal stress, at discrete time steps needs to be converted into frequency domain by FFT. The sampling rate  $\Delta t$  must be in accordance with Nyquist frequency of the signal. The frequency step is obtained from

$$\Delta f = \frac{1}{N\Delta t}$$

where  $N$  is the number of data points in the power spectrum. The signal is bound limited between the minimum frequency ( $f_{\min}$ ) and the maximum frequency ( $f_{\max}$ ).

Beginning from the minimum frequency, the assembled dynamic stiffness matrix and the assembled load vector in frequency domain are obtained by the finite element method, i.e.,

$$[\hat{F}] = [\hat{K}][\hat{d}] \quad (2.19)$$

or

$$[\hat{d}] = [\hat{K}]^{-1}[\hat{F}]$$

**Table 2.1** Properties of steel used in the simulation and number of elements employed

E (GPa)	G (GPa)	$\rho$ (kg/m <sup>3</sup> )	$\kappa$	$\nu$	$\eta$
207	77.6	7,836	0.67	0.3	0.025

**Table 2.2** Workpiece size and number of elements used in simulations

Length (m)	Width (m)	Thickness (m)	Number of elements
1	0.2	0.002	8

After applying the boundary conditions to Eq. (2.19),  $[K]$  is inverted by the Gauss reduction method. Consequently, the response is obtained at  $f_{\min}$ . This procedure is repeated for other frequencies up to  $f_{\max}$ . Hence, the displacement vector  $[\hat{d}]$  is obtained at the desired element. The frequency dependent response is reconstructed with time domain by using the inverse Fourier transformation method. In order to improve the stability of the computation, damping is introduced through the wave number  $k$  in the form of

$$k = k_0(1 - i\eta),$$

where  $k_0$  is the undamped value and  $\eta$  is taken as 0.025. The material properties are given in Table 2.1 while workpiece size and number of elements used in the simulation are given in Table 2.2.

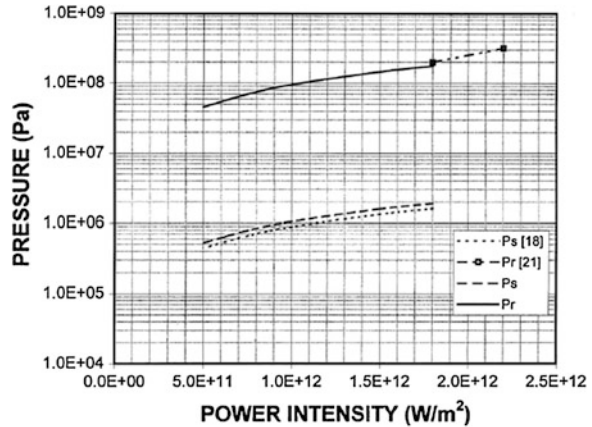
### 2.1.3 Results and Discussions

The pressure increase in the interface zone due to laser heating of the steel surface is determined. The force normal to the workpiece surface resulting from the pressure rise at the workpiece surface interface is considered to be an impulsive force generating the flexural wave motion in the workpiece. To observe the wave amplitude and frequency, three equally spaced locations in the plane of the workpiece surface are considered. In the analysis, the reflection of the traveling waves from the free ends of the workpiece is also considered. To investigate the effect of reflected waves on the traveling wave characteristics a radiating element at one end of the workpiece is considered.

Figure 2.2 shows the pressure predicted from the present study and the previous studies [4, 5]. The equation derived previously predicts the interface zone pressure to be as high as 300 MPa. The values of the pressure predicted from the present study agree well with the previous results. The small discrepancies between the findings are negligibly small.

Figure 2.3 shows the model of the temporal variation of the impulsive pressure force and the corresponding power spectrum density curve. The value of the force

**Fig. 2.2** Vapor and recoil pressures with power intensity [1]



is obtained by multiplying the pressure by the ablated surface area. It should be noted that the pressure distribution across the ablated surface is not known; therefore, it is assumed that it is uniform across the ablated surface. In the present study, the maximum frequency (Nyquist frequency) is taken as 2,000 (Fig. 2.3b). The flexural wave propagates in two modes provided that the second mode propagates faster than the first mode. In addition, the workpiece is a dispersive media, which modifies the wave characteristics during the wave propagation. Consequently, the propagating wave characteristics are modified due to dispersive media, interference of reflected waves, and overlapping of the wave modes.

Figure 2.4 shows the relative displacement of the flexural waves at the center of the workpiece. The amplitude of the displacement dies as the time progresses. This is because of the damping factor of the workpiece. The irregular wave pattern with time is due to one or all of the following facts: (i) overlapping of two modes of the wave, since the second mode propagates faster than the first mode, (ii) the reflected waves from the free ends of the workpiece modifies the wave amplitude, and (iii) the dispersive nature of the workpiece alters the wave characteristics. Moreover, as the time progresses, the wave displays a regular pattern provided that the effect of the reflected wave is evident in the tail of the wave pattern.

Figure 2.5 shows the flexural waves at three different locations at the workpiece surface. The locations are equally spaced and 12.5 cm apart. The wave amplitude is higher and has a spikey appearance in the first location at the workpiece surface, which is closer to the workpiece center where the pressure force is applied. No certain pattern is observed in the wave. In this case, the traveling wave amplitude and frequency are modified by the reflected waves from the free ends of the workpiece and by the dispersive nature of the workpiece material. As the location from the workpiece center moves toward the workpiece end, the amplitude of the wave reduces due to the damping effect of the workpiece material. The wave patterns changes, i.e., an almost regular pattern is observed after 2 ms of the propagation period at location 2. However, this time is shifted to 4 ms at location 3

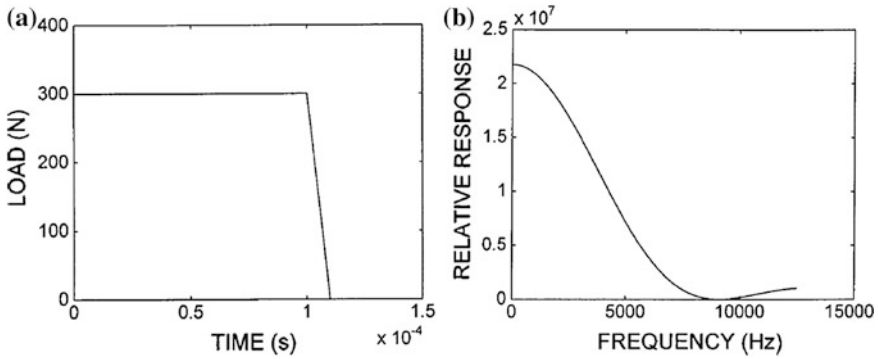


Fig. 2.3 a Temporal variation of pressure force. b Power spectrum density of pressure force [1]

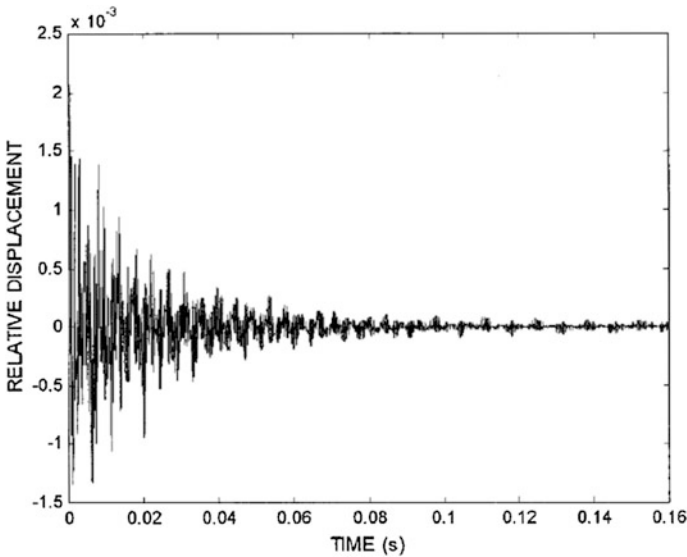


Fig. 2.4 Flexural wave motion generated at the center of the workpiece [1]

at the workpiece surface. In this case, the reflected wave interferes with the traveling wave resulting in the wave amplitude modification in the early period of wave propagation. Consequently, a common pattern in the traveling wave moves forward in time as the location at the surface moves towards the workpiece free end.

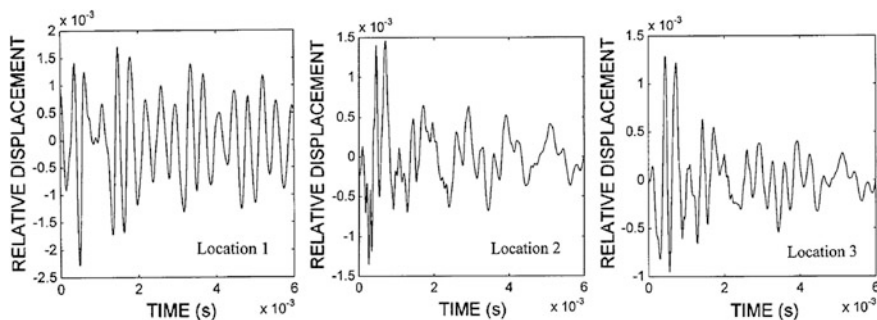


Fig. 2.5 Flexural waves at different locations at the workpiece surface [1]

## 2.2 Laser Evaporative Heating of Steel

The mathematical analysis and the findings are presented below in line with the previous study [9].

A stress field is developed during the flexural motion of workpieces when ablated by a laser beam. Consequently, when modeling the laser evaporative heating process, flexural wave motions and stress levels in the substrate material need to be included. In the following, laser evaporative heating of steel is modeled analytically. The vapor pressure generated during the evaporation process is obtained. The flexural motion and stress field in the substrate material are formulated. Consequently, the normal pressure force, the amplitude and frequency of the flexural waves and the stress levels in the substrate material are computed using the finite element method (FEM). The study is extended to include two geometric arrangements of the substrate material: a cantilever arrangement and a beam simply supported with both ends. Aluminum is introduced as an additional element in the steel in order to investigate the effect of an additional element, different to the substrate material, on displacement and on the stress field.

### 2.2.1 Heat Transfer Analysis

The Fourier heat transfer equation for a laser heating pulse can be written as

$$k \frac{\partial^2 T(x, t)}{\partial x^2} + \rho C_p V \frac{\partial T}{\partial x} + I_o (1 - r_f) \delta \exp(-\delta x) = \frac{\partial}{\partial t} [\rho C_p T(x, t)] \quad (2.20)$$

where  $r_f$  is the surface reflectivity,  $I_o$  is the power intensity of the step input pulse,  $\delta$  is the absorption depth,  $\rho$  is the density,  $C_p$  is the specific heat capacity,  $k$  is the

thermal conductivity, and  $V$  is the recession velocity of the surface, which can be determined from the energy balance at the surface [2], i.e.,

$$V = \frac{I_o}{\rho(CpT + L_{ev})} \quad (2.21)$$

where  $L_{ev}$  is the latent heat of evaporation. It should be noted that in Eq. (2.20), a laser step-input intensity pulse is considered, i.e. intensity does not vary with time, and therefore,  $I_o$  is constant. The initial and boundary conditions are as follows:

At

$$t = 0 \quad T(x, 0) = 0$$

and at the surface

$$\left. \frac{\partial T(x, t)}{\partial x} \right|_{x=0} = \frac{\rho}{k} VL_{ev}$$

and at  $x = \infty$

$$T(\infty, t) = 0.$$

where  $L_{ev}$  is the latent heat of evaporation.

Laplace transformation of Eq. (2.20) with respect to time allows the resultant second-order differential equation to be solved in the transformed plane. The mathematical derivation of the closed-form solution can be found in Ref. [10]. The resulting closed-form solution is

$$T(x, t) = \frac{I_o \delta \sqrt{\alpha}}{2\rho Cp(\alpha\delta - V)} \left( \begin{aligned} & 4ierfc\left(\frac{x}{2\sqrt{\alpha t}} + b\sqrt{t}\right) + \frac{3b^2 + c^2}{2b(b^2 - c^2)} erfc\left(\frac{x}{2\sqrt{\alpha t}} + b\sqrt{t}\right) \\ & + \frac{1}{2b} \exp\left(-\frac{2bx}{\alpha}\right) erfc\left(\frac{x}{2\sqrt{\alpha t}} - b\sqrt{t}\right) \\ & + \frac{1}{(b-c)} \exp[-[\delta x + (b^2 - c^2)]t] erfc\left[-\left(\frac{x}{2\sqrt{\alpha t}} + c\sqrt{t}\right)\right] \\ & + \frac{1}{(b+c)} \exp\left[\frac{x}{\sqrt{\alpha}}(b+c) + (b^2 - c^2)t\right] erfc\left[\left(\frac{x}{2\sqrt{\alpha t}} - c\sqrt{t}\right)\right] \\ & - \frac{2}{(b-c)} \exp(-\delta x) \end{aligned} \right) \\ - \frac{\rho VL_{ev}}{4bk} \left( \begin{aligned} & 4b\sqrt{\alpha t} erfc\left(\frac{x}{2\sqrt{\alpha t}} + b\sqrt{t}\right) \\ & - \sqrt{\left(\frac{x}{2\sqrt{\alpha t}} + b\sqrt{t}\right)} + \sqrt{\alpha} \exp\left(\frac{2bx}{\sqrt{\alpha}}\right) erfc\left(\frac{x}{2\sqrt{\alpha t}} - b\sqrt{t}\right) \end{aligned} \right) \quad (2.22)$$

where  $b = \frac{V}{2\sqrt{\alpha}}$  and  $c = b - \delta\sqrt{\alpha}$ .

The quasi-steady solution for the temperature [Eq. (2.22)] can be obtained by an iterative procedure, i.e., setting the velocity and calculating the temperature, later correcting the velocity by inserting the temperature calculated in the velocity equation [Eq. (2.21)], and then repeating this procedure until Eqs. (2.21) and

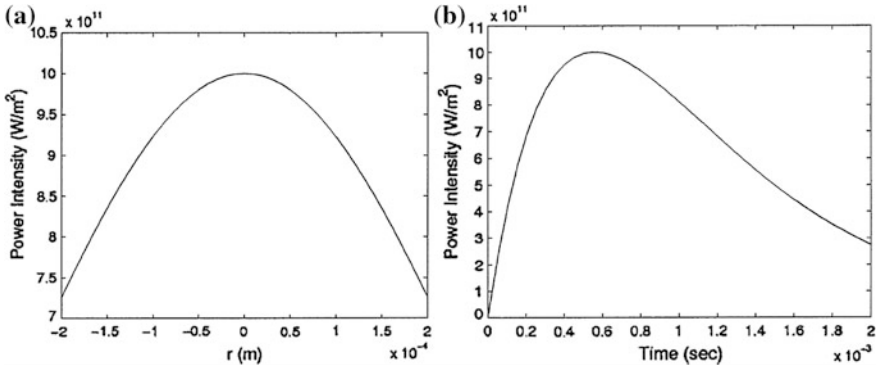


Fig. 2.6 a Spatial variation, and b temporal variation in the laser power intensity distribution [9]

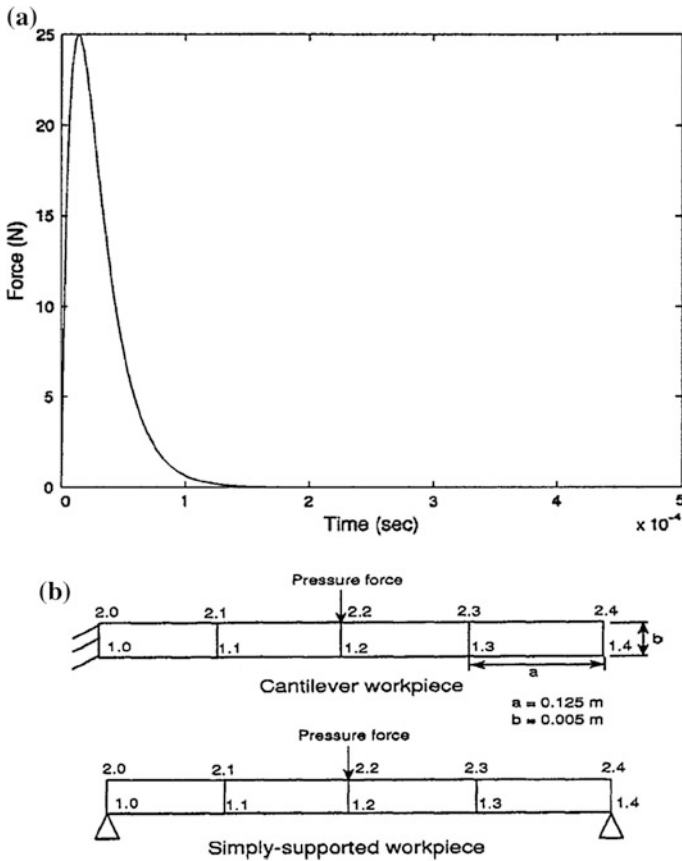


Fig. 2.7 a Force input applied to the workpiece, and b layout of the workpiece [9]

(2.22) are satisfied. Figure 2.6a, b shows the spatial and temporal variation in the laser power intensity distribution.

The recoil pressure can be calculated after considering the rate of momentum change across the receding surface [4]. The rate of momentum at the irradiated surface owing to the receding surface, as shown in Fig. 2.7a, is

$$AP_r = \dot{m}V_{ev}$$

where A is the area of the irradiated surface,  $P_r$  is the recoil pressure,  $\dot{m}$  is the rate of mass flow and  $V_{ev}$  is the evaporating front velocity, which can be formulated from Maxwell's law for the velocity distribution of molecules [11], i.e.,

$$V_{ev} = \sqrt{\frac{k_B T_s}{2\pi m}} \exp\left(-\frac{mL_{ev}(T)}{k_B T_s}\right)$$

where m is the mass of an atom,  $T_s$  is the surface temperature and  $k_B$  is the Boltzmann's constant.

The recoil pressure can be written as

$$P_r = \frac{\dot{m}}{A} V_{ev} \quad (2.23)$$

The energy dissipated by evaporation is the sum of the latent heat of evaporation and the kinetic energy of the evaporated molecules, i.e.

$$I_{ev} = \frac{\dot{m}\left(\frac{1}{2}V_{ev}^2 + L_{ev}\right)}{A}$$

Substitution of  $\dot{m}/A$  in the above equation yields

$$I_{ev} = \frac{P_r}{V_{ev}} \left(\frac{1}{2}V_{ev}^2 + L_{ev}\right)$$

Therefore, the recoil pressure can be written as

$$P_r = \frac{I_{ev}L_{ev}}{\left(\frac{1}{2}V_{ev}^2 + L_{ev}\right)} \quad (2.24)$$

The recoil pressure is computed from Eq. (2.24). The laser power intensity dissipated by evaporation is

$$I_{ev} \cong I_0 - \dot{q}_{solid}$$

where  $\dot{q}_{solid}$  is the energy dissipated in the solid phase. It should be noted that the energy dissipated by melting is considerably smaller than the energy dissipated during evaporation and can be neglected.

The pressure force acting normal to the substrate surface can be written as

$$F_o = \int_0^{r_e} 2\pi r_e P dr \quad (2.25)$$

where  $r_e$  is the radius of the evaporated surface ( $r_e = 0.4$  mm). The variation in normal pressure force with time is assumed to be exponential, i.e.,

$$F(t) = F_o(\exp(-\beta t) - \exp(-\gamma t))$$

where  $\beta$  and  $\gamma$  are constants. Figure 2.7a shows the normal pressure force.

### 2.2.2 Flexural Wave Analysis

The finite element method (FEM) is applied as a numerical tool for the analysis of flexural wave behavior for a workpiece as shown in Fig. 2.7b. The rectangular finite elements for the workpieces contain pseudo-internal degrees of freedom (DOF). The size of each element is schematically illustrated in Fig. 2.7b. The internal DOF are for better representation of bending moments generated by the external actuators and are condensed into the physical DOF using the Guyan reduction technique [12].

Hamilton's principle is given by

$$\delta \int_{t_1}^{t_2} (K_i - \Pi) dt = 0$$

where  $\Pi$  is the potential energy while  $K_i$  is the kinetic energy defined as

$$K_i = \frac{1}{2} \int_V \rho \dot{\mathbf{u}}^T \dot{\mathbf{u}} dV \quad (2.26)$$

where  $\dot{\mathbf{u}}$  is velocity vector and  $\mathbf{T}$  is the tensor notation. In Eq. (2.26), the potential energy  $\Pi$  is given by

$$\Pi = - \int_V \mathbf{u}^T \mathbf{P}_b dV - \int_S \mathbf{u}^T \mathbf{P}_s dS - \mathbf{u}^T \mathbf{P}_c$$

where  $\mathbf{P}_b$  is the vector of body forces applied to volume  $V$ ,  $\mathbf{P}_s$  is the vector of surface force and  $\mathbf{P}_c$  is the concentrated load vector.

The following relations are defined for the finite element formulation:

$$\mathbf{u}_e = N_u \mathbf{u}_i$$

where  $N_u$  is the shape function matrix and  $\mathbf{u}_i$  is the vector of nodal displacement. The subscript 'e' in the equations stands for the element. Relating strain to displacement

$$S_e = L_u \mathbf{u}_e = [L_u N_u] \mathbf{u}_i = B_u \mathbf{u}_i$$

where  $S_e$  is the elemental strain and  $L_u$  is the differential operator which is given by

$$L_u = \begin{bmatrix} \frac{\partial}{\partial x} & 0 \\ 0 & \frac{\partial}{\partial y} \\ \frac{\partial}{\partial y} & \frac{\partial}{\partial x} \end{bmatrix} \quad (2.27)$$

Substituting the above equations in (2.26) gives

$$M_{uu} \ddot{\mathbf{u}} + K_{uu} \mathbf{u} = \mathbf{F} \quad (2.28)$$

where  $\ddot{\mathbf{u}}$  is the acceleration vector and the element matrices and vectors are given by

$$M_{uu} = \int_{V_e} \rho N_u^T N_u dV : K_{uu} = \int_{V_e} B_u^T c B_u dV$$

$$\mathbf{F}_e = \int_{V_e} N_u^T \mathbf{P}_b dV + \int_{S_e} N_u^T \mathbf{P}_s dS + N_u^T \mathbf{P}_c$$

For a rectangular element of size  $(2a \times 2b)$  with  $W_s$  as the width, the shape functions are given as

$$N_1 = \frac{1}{4} \left(1 - \frac{x}{a}\right) \left(1 - \frac{y}{b}\right) \quad N_2 = \frac{1}{4} \left(1 + \frac{x}{a}\right) \left(1 - \frac{y}{b}\right)$$

$$N_3 = \frac{1}{4} \left(1 + \frac{x}{a}\right) \left(1 + \frac{y}{b}\right) \quad N_4 = \frac{1}{4} \left(1 - \frac{x}{a}\right) \left(1 + \frac{y}{b}\right) \quad (2.29)$$

Internal DOF are added to the element to give a better representation to the bending moments caused by the piezoelectric effects. Two shape functions are defined for this purpose, which are given as follows:

$$N_5 = \frac{a^2 - x^2}{a^2} \quad N_6 = \frac{b^2 - y^2}{b^2}$$

The shape functions vanish at the element boundaries when  $x = \pm a$  and  $y = \pm b$ . The displacement vector,  $\mathbf{u}_e$ , is now expressed as

$$\mathbf{u}_e = N_u \mathbf{u}_i + X \mathbf{a}_j \quad (2.30)$$

The strain vector,  $\mathbf{S}_e$ , is now written as

$$\mathbf{S}_e = B_u \mathbf{u}_i + Y \mathbf{a}_j \quad (2.31)$$

where  $\mathbf{a}_j$  is the added generalized coordinate vector and X and Y in the above equations are given by

$$X = \begin{bmatrix} 0 & 0 \\ N_5 & N_6 \end{bmatrix} \quad \text{and} \quad Y = L_u X = -2 \begin{bmatrix} 0 & 0 \\ 0 & y \\ x & 0 \end{bmatrix} \quad (2.32)$$

The new matrix,  $K_{uu}^*$  is the global elastic stiffness matrix which is composed of  $[K_{uu}]_e^*$  and given by

$$[K_{uu}]_e^* = [K_{uu}]_e - [K_{ua}]_e [K_{aa}]_e^{-1} [K_{au}]_e \quad (2.33)$$

where  $[K_{ua}]_e$  and  $[K_{aa}]_e$  are partitioned stiffness matrices given by

$$[K_{ua}]_e = \int_V B_u^T c Y dV \quad \text{and} \quad [K_{aa}]_e = \int_V Y_u^T c Y dV \quad (2.34)$$

where C is a constant matrix. Hence the final equation becomes

$$M_{uu} \ddot{\mathbf{u}} + K_{uu} \mathbf{u} = \mathbf{F} \quad (2.35)$$

### 2.2.2.1 Initial and Boundary Conditions

Initially, the displacements are set to zero for the cantilever and simply supported cases. Also, at  $x = 0$ , i.e. at the fixed end, the displacement is always zero, which is given as follows: at  $x = 0$ ,  $u = 0$ ; for the simply supported case, at  $x = 1$ ,  $u = 0$ .

### 2.2.2.2 Method of Solution

In the finite element analysis, the workpiece is divided into four elements where the number of divisions is uniform in the x direction and the thickness is considered to be uniform. The elemental stiffness and mass matrices are determined, which are then assembled to yield the global matrices.

### 2.2.2.3 State-Space Method

The equation of motion is converted into state-space form and for a deterministic system and is given as

$$\dot{z} = Az + BF \quad (2.36)$$

where  $\dot{z}$  is the velocity vector in the steady space and

$$\mathbf{u} = Cz \quad (2.37)$$

where  $z$  is the complete state vector,  $u$  is the required displacement.  $C$  is a matrix defining the location where displacement is required,  $A$ , and  $B$  are the system and input matrices, respectively, given as

$$A = \begin{bmatrix} 0 & I \\ -M_{uu}^{-1}K_{uu} & -M_{uu}^{-1}C_{uu} \end{bmatrix} \text{ and } B = \begin{bmatrix} 0 \\ -M_{uu}^{-1}F \end{bmatrix} \quad (2.38)$$

where  $C_{uu}$  is the proportional damping introduced through the following equations:

$$C_{uu} = \alpha M_{uu} + \beta K_{uu}$$

$\alpha$  and  $\beta$  being the damping coefficients. Matrix  $C$  in Eq. (2.37) defines the location where displacement is required. These matrices are introduced through Matlab code and simulated for a given force and time interval to obtain the displacement  $u$  at various locations.

### 2.2.2.4 Determination of Stresses

The strain for a given element is given by  $\mathbf{S}_e = B_u \mathbf{u}_e$ , where  $B_u = L_u N_u$  and  $N_u$  is given by

$$N_u = \begin{bmatrix} N_1 & 0 & N_2 & 0 & N_3 & 0 & N_4 & 0 \\ 0 & N_1 & 0 & N_2 & 0 & N_3 & 0 & N_4 \end{bmatrix}$$

The stress is then obtained by using the stress–strain relationship which is given by  $\sigma_e = E\mathbf{S}_e$ . These elemental stresses are properly mapped with respect to global node numbering to obtain the global stress. The global stress  $s$  obtained in this way is given by

$$\sigma = \begin{bmatrix} \sigma_x \\ \sigma_y \\ \tau_{xy} \end{bmatrix} \quad (2.39)$$

Hence, the equivalent stress is given by

$$\sigma_{eq} = \sqrt{\sigma_x^2 + \sigma_y^2} \quad (2.40)$$

### 2.2.3 Results and Discussion

The stress field due to flexural motion of the substrate material is determined by using FEM in the simulations. In order to examine the effect of an additional element, aluminum is introduced as the third element in Fig. 2.7b. It should be noted that no discontinuity of stress and displacement boundaries at the interface between aluminum and steel elements is considered; i.e. the continuity in the stress and displacement fields with change in the mechanical properties of the substrate is taken into account for the aluminum. The displacement and equivalent stress differences due to the additional element are computed. Two different arrangements of the workpiece are taken into account, namely a cantilever arrangement and with both ends simply supported.

Figure 2.8a shows the surface displacement of the workpiece for these two geometric arrangements of the substrate material. Displacement of the surface at the central position of the workpiece (Fig. 2.7b) is higher for the cantilever case than for the case where both ends are freely supported. This is because of the cantilever arrangement, in which case the workpiece moves freely from one end. This, in turn, enhances the amplitude of the surface displacement. Moreover, the amplitude of the surface displacement oscillates in the early period  $t \leq 40,006$  s, increases gradually, reaching its maximum at  $t \approx 0.085$  s, and then decreases; i.e. the temporal behavior of displacement does not show a regular pattern for the cantilever case. In the case of the workpiece with both ends simply supported, the amplitude of displacement damps out as time progresses. This is because of the simply supported system, which forces the displacement to decay with time. A peak amplitude of surface displacement of the order of  $2 \mu\text{m}$  occurs.

Figure 2.8b shows the temporal variation in the displacement difference at different locations (Fig. 2.7b). The displacement difference is obtained by subtracting the displacements corresponding to cases with and without additional aluminum. The displacement corresponding to the additional element is lower than that corresponding to a steel substrate. Moreover, the displacement difference decays with time for the cantilever arrangement and when both ends are simply supported. This indicates that the influence of the additional element on the displacement is significant in the early period, but that the effect decreases with time.

Figure 2.9a shows the temporal variation in the equivalent stress at four locations on the workpiece, as shown in Fig. 2.7b, for a cantilever arrangement. The equivalent stress level attains high values in the early period and decreases to zero before reaching its second peak. Moreover, as the location moves away from the

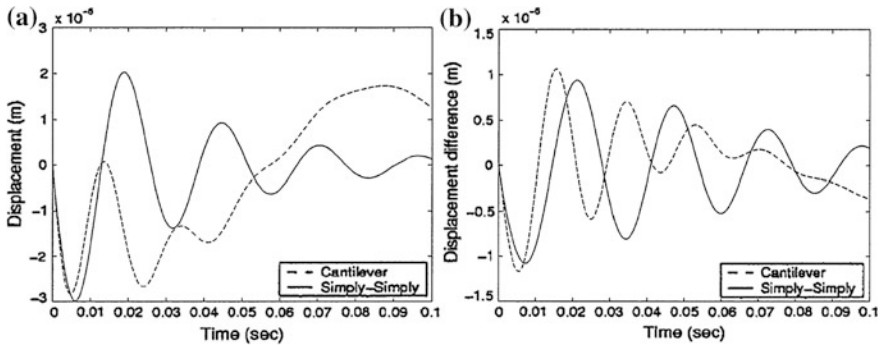


**Fig. 2.8** **a** Displacement of the flexural waves obtained at the center of the beam, and **b** displacement difference in the flexural waves obtained at the centre of the beam (the displacement difference corresponds to the displacement difference due to an additional element and no additional element) [9]

fixed end (locations 1.3 and 1.4), the magnitude of the equivalent stress decreases. This is because of the flexural motion of the workpiece, i.e. the stress levels drop as the displacement decreases. The zero equivalent stress indicates zero stress components. Zero stress components occur when the displacement decreases to zero, i.e. when the workpiece straightens. This corresponds to 0.0057 s for both Figs. 2.8a and 2.9a. The maximum equivalent stress is of the order of  $10^4$  Pa, which is considerably less than the yield stress of the substrate material (215 MPa).

Figure 2.4b shows the equivalent stress difference at different locations in the workpiece for the cantilever arrangement. The equivalent stress difference is obtained from the equivalent stress corresponding to steel and that corresponding to steel with additional aluminum. The equivalent stress attains high values at location 1.1 in the workpiece (Fig. 2.7b). This occurs because location 1.1 is close to the fixed end of the workpiece. The equivalent stress difference oscillates and damps out with time. The frequency of the oscillation appears to be regular; i.e., at all locations the stress level oscillates with almost the same frequency. Moreover, the stress level oscillations are out of phase at locations 1.2 and 1.3. Consequently, the additional element in the workpiece modifies the equivalent stress levels, in which case the magnitude of the stress levels decreases.

The bending of the workpiece during flexural motion results in shear stress development in the substrate material. This is shown in Fig. 2.10 at different locations (Fig. 2.7b). The magnitude of shear stress is almost twice the equivalent stress. The level of shear stress is negative in the region close to the fixed end. As the location moves towards the free end, the shear stress becomes positive. Moreover, the stress level oscillates with time. The level of the shear stress decreases to zero at 0.057 s, at which the displacement is also zero. The stress level decreases with time at a location close to the free end. The temporal behavior of the shear stress at locations 1.2 and 1.3 (Fig. 2.7b) is almost identical with opposite signs.

**Fig. 2.9** **a** Equivalent stress distribution, and **b** equivalent stress difference for a cantilever beam. Curves correspond to nodal points shown in Fig. 2.7b [9]

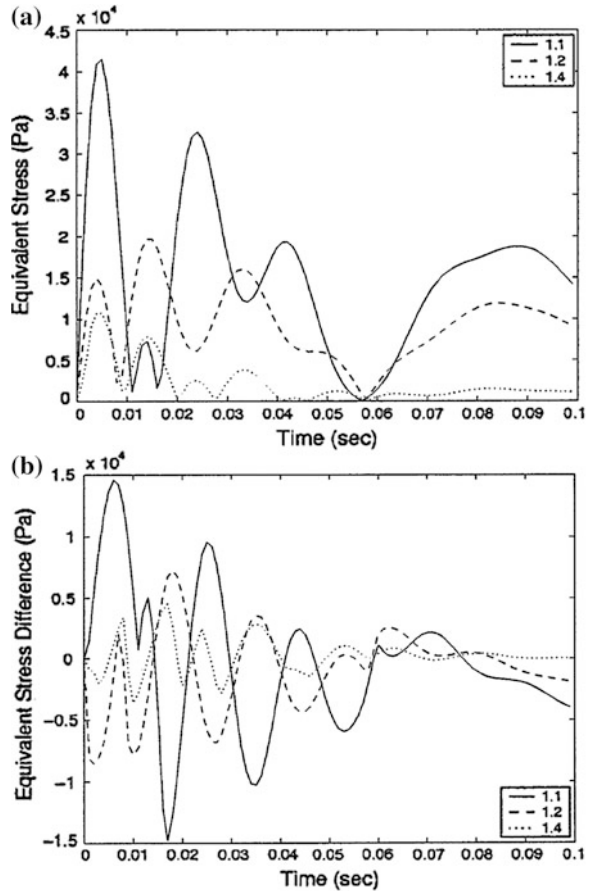
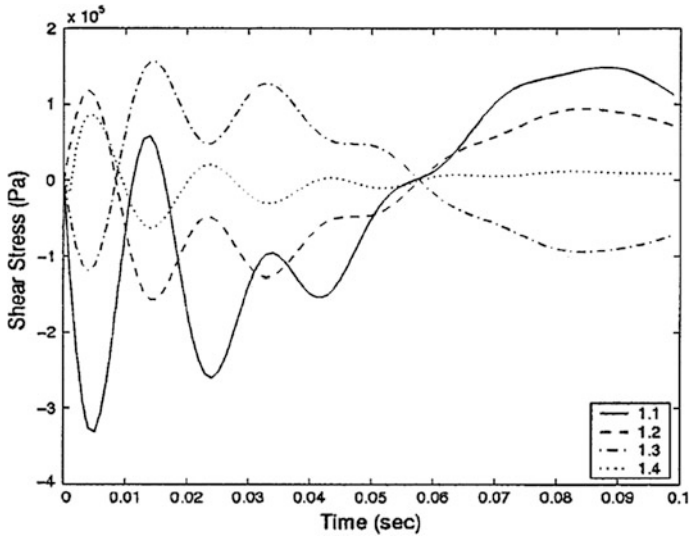


Figure 2.11a shows the temporal variation in the equivalent stress at different locations in the workpiece (Fig. 2.7b) for the case where both ends are simply supported. The equivalent stress decreases as time increases. This is because of the dying of the flexural motion of the workpiece. The equivalent stress decreases to zero at points where the displacement is zero. The equivalent stress decreases in the region close to the center of the workpiece (location 1.3). This occurs because of surface displacement in this region, which is small. Consequently, a small displacement gives low stress components, which, in turn, results in a low equivalent stress in this region.

Figure 2.11b shows the equivalent stress difference at different locations in the workpiece for the case where both ends are simply supported. The equivalent stress difference decreases with time for all locations. In general, the additional element reduces the equivalent stress levels, since the magnitude of the equivalent stress difference is positive. Moreover, the stress level difference is almost steady at points 1.1, 1.2 and 1.3 during the period  $0.01 \leq t \leq 0.07$  s. This indicates that



**Fig. 2.10** Shear stress distribution for a cantilever beam. Curves correspond to nodal points in Fig. 2.7b [9]

the temporal response of the workpiece is almost the same for these points during this period, provided that the equivalent stress corresponding to steel with additional aluminum results in lower equivalent stress levels. The frequency of oscillation of the stress difference is almost the same for each location. This indicates that flexural motions of the workpiece with and without additional aluminum are the same, but their amplitude varies, which, in turn, results in different stress levels at each point in the workpiece.

Figure 2.12 shows the temporal variation in shear stress at four locations in the workpiece (Fig. 2.7b) for the case with both ends simply supported. The magnitude of shear stress decreases with time. This is because of the temporal behavior of the displacement, which decreases with time. Moreover, opposite behavior in shear stress is observed for two consecutive points from the free supported end. The stress level decreases to low values at the center of the workpiece, which cannot be observed in Fig. 2.12. The opposite stress behavior at points 1.1 and 1.2 is due to flexural motion of the workpiece. The stress level is higher in the early heating period owing to the high amplitude of displacement in this period.

### 2.3 Laser Pulse Heating of Steel Surface

In the analysis of the flexural characteristics of the laser pulse heating of steel surface, the formulation and findings of the previous study [13] are considered.

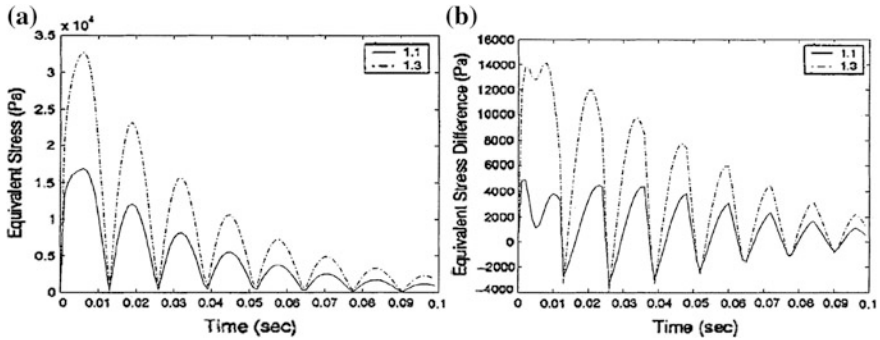


Fig. 2.11 **a** Equivalent stress distribution, and **b** equivalent stress difference for a simply supported beam. Curves correspond to nodal points shown in Fig. 2.7b [9]

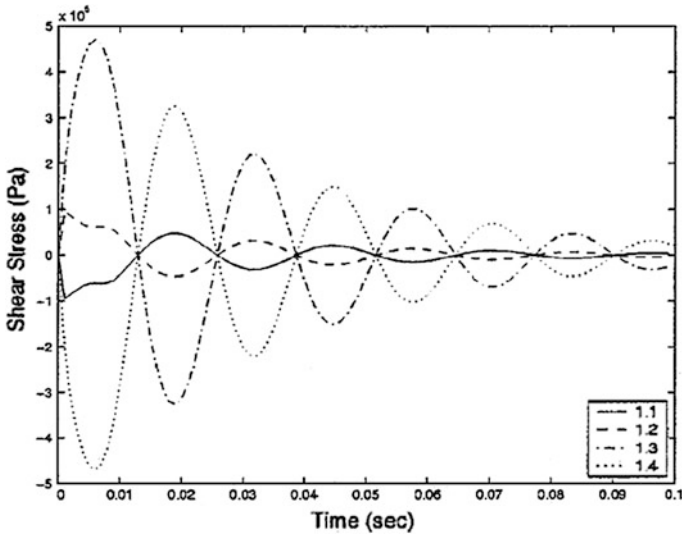


Fig. 2.12 Shear stress distribution for a simply supported beam. Curves correspond to nodal points shown in Fig. 2.7b [9]

Consider the flexural wave propagation in the substrate during the laser heating process. In this case, the thermal stresses developed in the substrate are predicted first and the wave generated due to axial stress component in the surface vicinity of the substrate is analyzed using a spectral finite element method. Since the workpiece has a certain length, the reflecting waves from the free supported ends of the workpiece are also considered in the analysis.

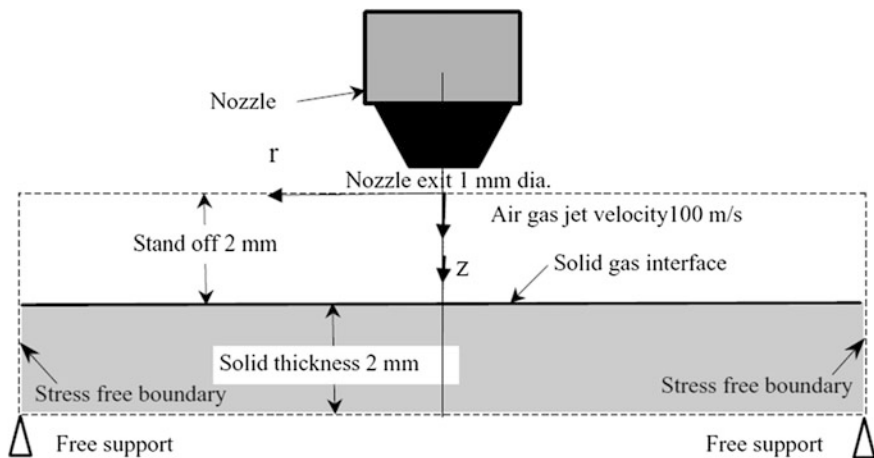


Fig. 2.13 A view of impinging gas and laser workpiece arrangement [13]

### 2.3.1 The Mathematical Model

The gas-assisted laser pulse heating process is considered when modelling the laser workpiece interaction provided that conduction limited heating case is taken into account in the present study [14]. Figure 2.13 shows the schematic view of the heating process.

#### 2.3.1.1 Flow and Heat Conduction Equations

The unsteady flow equations need to be solved to obtain the flow field due to axisymmetric gas jet impingement. The continuity and momentum equations are

$$\frac{\partial \rho}{\partial t} + \frac{\partial}{\partial x_i} (\rho U_i) = 0 \quad (2.41)$$

and

$$\frac{\partial}{\partial t} (\rho U_j) + \frac{\partial}{\partial x_i} (\rho U_i U_j) = \frac{\partial p}{\partial x_j} + \frac{\partial}{\partial x_i} \left[ (\mu_t + \mu) \frac{\partial U_j}{\partial x_i} \right], \quad (2.42)$$

where  $\mu_t$  is the eddy viscosity which has to be specified by a turbulence model. In the present study, low Reynolds number  $k$ - $\epsilon$  turbulence model is introduced to account for the turbulence effect of the impinging gas, which is air [14].

The partial differential equation governing the transport of thermal energy has the form

$$\frac{\partial T}{\partial t} + \frac{\partial}{\partial x_i} (U_i T) = \frac{\partial}{\partial x_i} \left[ \left( \frac{\mu_t}{Pr_t} + \frac{\mu}{Pr} \right) \frac{\partial T}{\partial x_i} \right]. \quad (2.43)$$

### 2.3.1.2 Boundary Conditions for Flow Equations

Laminar boundary conditions are set for the mean-flow variables, and the boundary conditions  $k = 0$  and  $d\varepsilon/dz = 0$  are applied at the wall. The low-Reynolds number extension does not employ wall functions; therefore, the grid employed normal to the main flow direction needs to be distributed so as to give a high concentration of grid cells near the wall, with the wall-adjacent node positioned at  $z^+ = \rho z u^*/\mu \leq 1.0$ .

Inlet to control volume:

$$U_i = \text{specified and } T = \text{constant}. \quad (2.44)$$

The kinetic energy of turbulence is estimated according to some fraction of the square of the average inlet velocity [15]

$$k = \lambda \bar{u}^2, \quad (2.45)$$

where  $\bar{u}$  is the average inlet velocity and  $\lambda$  is a fraction.

The dissipation is calculated according to the equation [16]

$$\varepsilon = C_\mu \frac{k^{3/2}}{bd} \quad (2.46)$$

where  $d$  is the inlet diameter. The values  $\lambda = 0.03$  and  $b = 0.005$  are commonly used and may vary slightly in the literature [15].

Outlet to control volume:

It is assumed that the flow extends over a sufficiently long domain; therefore, it is fully developed at the exit section. Thus, for any variable  $\phi$  the condition is

$$\frac{\partial(r\phi)}{\partial x} = 0 \quad (2.47)$$

where  $x$  is the arbitrary outlet direction.

Symmetry axis:

The radial derivative of the variables is set to zero at the symmetry axis, i.e.,

$$\frac{\partial\phi}{\partial r} = 0 \quad \text{and} \quad V = 0 \quad (2.48)$$

Solid fluid interface:

The temperature at the solid–gas interface is considered as the same, i.e.,

$$T_{w_{solid}} = T_{w_{gas}} \quad \text{and} \quad K_{solid} \frac{\partial T_{w_{solid}}}{\partial z} = K_{gas} \frac{\partial T_{w_{gas}}}{\partial z}.$$

The unsteady heat conduction equation:

$$\frac{\partial}{\partial t} (C_p \rho T) = \frac{\partial}{\partial x_i} \left[ K \frac{\partial T}{\partial x_i} \right] + S, \quad (2.49)$$

where  $S$  is the unsteady spatially varying laser output power intensity distribution and is considered as Gaussian with  $1/e^2$  points equal to 0.375 mm, from the center of the beam. Therefore,  $S$  is stated as follows:

$$S = \frac{I_0}{\sqrt{2\pi}a} \exp\left(-\frac{r^2}{a^2}\right) \delta \exp(-\delta z) f(t), \quad (2.50)$$

where  $\frac{I_0}{\sqrt{2\pi}a} \exp\left(-\frac{r^2}{a^2}\right)$  is the intensity distribution across the surface,  $\exp(-\delta z)$  is the absorption function, and  $f(t)$  is the function accommodating the time variation of the pulse shape. The pulse properties are given in Table 2.3.

Boundary conditions for the heat conduction equation:

Convection with a constant coefficient for still air is considered at the  $z = z_{max}$  boundary for the plate. The continuity of temperature between the solid and the gas is enforced at the interface; and a constant temperature,  $T = T_{amb}$ , is assumed for the distance far away from the laser source.

### 2.3.1.3 Variable Properties

An equation of state is used for the impinging gas and the specific heat capacity and thermal conductivity for both air and steel were considered only as a function of temperature. The temperature dependence of properties is given in [17].

### 2.3.1.4 Calculation of the Flow Field Variables

The control volume approach is used when solving the governing equations of flow and heat transfer numerically. The differential equation is integrated over the control volume to yield the discretization equation. The main reasons for choosing the control-volume formulation for flow field are its simplicity and easy physical interpretation [18]. The discretization process is not given here due to lengthy arguments, but refer to [19].

**Table 2.3** Pulse properties used in the simulation

Rise time (ms)	Fall time (ms)	Total pulse length (ms)	Peak power intensity (W/m <sup>2</sup> )
0.2	1.08	1.48	10 <sup>9</sup>

The grid used in the present calculations has  $38 \times 70$  mesh points, provided that the grid independent test is satisfied. The details of the grid orientation and grid independent test results are given in [20].

The two problems of determining the pressure and satisfying continuity are overcome by adjusting the pressure field so as to satisfy continuity. This arrangement gives a convenient way of handling the pressure linkages through the continuity equation and is known as the Semi-Implicit Method for Pressure-Linked Equations (SIMPLE) algorithm. The details of this algorithm are found in [21].

The governing equation for heat conduction in solid [Eq. (2.49)] can be written in the form of flow equations. Thus, the discretization procedure leads to algebraic equations of the form similar to flow equations with temperature  $T$  replacing the general variable.

### 2.3.1.5 Thermal Stress Modelling

The temperature field results in the thermal stresses being generated in the substrate, which can lead to the elastic–plastic displacement in the substrate material. The stress is related to strains by

$$\{\sigma\} = [D]\{\varepsilon^e\}, \quad (2.51)$$

where  $\{\sigma\}$  is the stress vector, and  $[D]$  is the elasticity matrix.

$$\{\varepsilon^e\} = \{\varepsilon\} - \{\varepsilon^{th}\}$$

where  $\{\varepsilon\}$  is the total strain vector and  $\{\varepsilon^{th}\}$  is the thermal strain vector.

Equation (2.51) may also be written as

$$\{\varepsilon\} = [D]^{-1}\{\sigma\} + \{\varepsilon^{th}\} \quad (2.52)$$

Since the present case is axially symmetric, and the material is assumed to be isotropic, the above stress–strain relations can be written in cylindrical coordinates as

$$\begin{aligned} \varepsilon_{rr} &= \frac{1}{E}[\sigma_{rr} - \nu(\sigma_{\theta\theta} + \sigma_{zz})] + \alpha\Delta T(r, z, t) \\ \varepsilon_{\theta\theta} &= \frac{1}{E}[\sigma_{\theta\theta} - \nu(\sigma_{rr} + \sigma_{zz})] + \alpha\Delta T(r, z, t) \\ \varepsilon_{zz} &= \frac{1}{E}[\sigma_{zz} - \nu(\sigma_{rr} + \sigma_{\theta\theta})] + \alpha\Delta T(r, z, t) \\ \varepsilon_{rz} &= \frac{1}{G}\sigma_{rz} \end{aligned} \quad (2.53)$$

where  $E$ ,  $\nu$ , and  $\alpha$  are the modulus of elasticity, Poisson's ratio, and coefficient of thermal expansion, respectively.  $\Delta T(r, z, t)$  represents the temperature rise at a point  $(r, z)$  at time  $t$  with respect to that at  $t = 0$  corresponding to a stress-free condition. A typical component of thermal strain from Eq. (2.53) is

$$\begin{aligned}\varepsilon^{th} &= \alpha \Delta T(r, z, t) \\ &= \alpha(T(r, z, t) - T_{ref})\end{aligned}\quad (2.54)$$

where  $T_{ref}$  is the reference temperature at  $t = 0$ .

When  $\alpha$  a function of temperature then Eq. (2.54) becomes

$$\varepsilon^{th} = \int_{T_{ref}}^T \alpha(T) dT \quad (2.55)$$

The present study uses a mean or weighted-average value of  $\alpha$ , such that

$$\varepsilon^{th} = \bar{\alpha}(T)(T - T_{ref}), \quad (2.56)$$

where  $\bar{\alpha}(T)$  is the mean value of coefficient of thermal expansion and is given by

$$\bar{\alpha}(T) = \frac{\int_{T_{ref}}^T \alpha(T) dT}{T(r, z, t) - T_{ref}} \quad (2.57)$$

To develop a finite element procedure for stress computation, the standard displacement-based finite element method is used. The basis of this approach is the principle of virtual work, which states that the equilibrium of any body under loading requires that for any compatible small virtual displacements (which are zero at the boundary points and surfaces and correspond to the components of displacements that are prescribed at those points and surfaces) imposed on the body in its state of equilibrium, the total internal virtual work or strain energy ( $\delta U$ ) is equal to the total external work due to the applied thermally induced loads ( $\delta V$ ), i.e.,  $\delta U = \delta V$ . For the static analysis of problems having linear geometry and thermoelastic material behavior, one can derive the following equation using standard procedure [22].

$$\begin{aligned}& \int_{\forall} (\{\delta \varepsilon\}^T [D] \{\varepsilon\} - \{\delta \varepsilon\}^T [D] \{\varepsilon^{th}\}) dV \\ &= \int_{\forall} \{\delta U\}^T \{f^B\} dV + \int \{\delta U_s\}^T \{P\} d\Omega + \sum \{\delta \bar{U}\}^T \{\bar{F}\}\end{aligned}\quad (2.58)$$

where  $\{f^B\}$  is the applied body force,  $\{P\}$  the applied pressure vector,  $\{\bar{F}\}$  the concentrated nodal forces to the element,  $\{\delta U\}$  the virtual displacement,  $\{\delta U_s\}$  the virtual displacement on the boundary where pressure is prescribed, and  $\{\delta \bar{U}\}$  the virtual displacement of boundary nodes where concentrated load is prescribed.

The strains may be related to the nodal displacement by

$$\{\varepsilon\} = [B]\{\bar{U}\} \quad (2.59)$$

where  $[B]$  is the strain displacement gradient matrix, and  $\{\bar{U}\}$  the nodal displacement vector.

The displacements within the elements are related to the nodal displacement by

$$\{U\} = [N]\{\bar{U}\} \quad (2.60)$$

where  $[N]$  is the matrix of shape (or interpolation) functions.

Equation (2.58) can be reduced to the following matrix form:

$$[K_e]\{\bar{U}\} - \{F^{th}\} = \{F\}^b + \{F\}^s + \{\bar{F}\} \quad (2.61)$$

where  $[K_e] = \int_V [B]^T [D] [B] dV$  is the element stiffness matrix,  $\{F^{th}\} = \int_V [B]^T [D] [\varepsilon^{th}] dV$  the element thermal load vector,  $\{F\}^b = \int_V [N]^T [f^B] dV$  the element body force vector,  $\{F\}^s = \int_V [N_n]^T [P] dV$  the element pressure vector, and  $[N_n] =$  matrix of shape functions for normal displacement at the boundary surface.

Assembly of element matrices and vectors of Eq. (2.61) yields

$$[K]\{\bar{d}\} = \{\bar{R}\},$$

where  $[K]$ ,  $\{\bar{d}\}$  and  $\{\bar{R}\}$  are the global stiffness matrix, global nodal displacement vector, and global nodal load vector, respectively. Solution of the above set of simultaneous algebraic equations gives unknown nodal displacements and reaction forces.

### 2.3.2 Wave Analysis

In the analysis, the workpiece is divided into a number of elements and each element can be treated as uniform. The displacement vector is then transformed from time domain into frequency domain using fast Fourier transformation (FFT). The transform response is fed back into the governing differential equations as solved at each frequency component using finite element method (FEM) and the transient response is recovered by using the inverse FFT. Flexural wave analysis is given above in Eqs. (2.9)–(2.19).

### 2.3.3 Results and Discussions

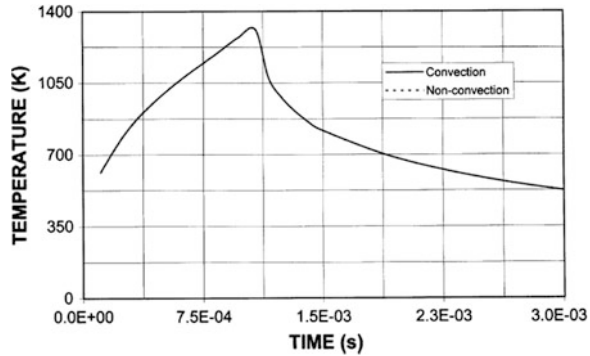
In order to investigate the wave propagation along the transverse direction in the workpiece, six locations with three located at each side from the center of the workpiece along the transverse direction are considered. This is necessary, since the workpiece material disperses the travelling waves in amplitude and frequency domain. The wave reflections from both ends of the workpiece also modify the travelling wave properties. Consequently, to analyze the influence of reflected waves emanating from the ends of the workpiece, a case in which one end of the workpiece is located at infinity is considered. This provides no reflection of the wave from one end of the workpiece.

Figure 2.14 shows the temporal variation of the surface temperature at the center of the heated spot (at  $r = 0$ ) for convective and nonconvective boundary conditions at the surface. The temperature rises rapidly in the early heating period and the rate of rise of surface temperature reduces as the heating progresses. In the cooling cycle, the decay rate of the surface temperature is faster in the beginning of the cooling cycle and the decay rate slows as the cooling period progresses. Consequently, the material response to the heating pulse changes in the cooling cycle as compared to that in the heating cycle. This is because once the laser source disappears, the rate of energy diffused from the surface vicinity of the substrate to the bulk through the conduction becomes large immediately after the laser pulse ends, i.e., the large temperature gradient attainment in the surface region during the heating cycle accelerates the conduction cooling of the surface vicinity. In the case of the long cooling period, the temperature gradient in the surface vicinity is low and the energy diffusion from the surface vicinity to the bulk of the substrate slows down. When comparing temperature profiles with and without convective boundary condition at the surface, it is evident that both temperature profiles are identical. This indicates that convective cooling of the surface is negligibly smaller than the energy input to the substrate material due to the absorption of a laser beam as consistent with the previous work [20].

Figure 2.15a shows the temporal variation of the normal (axial) component of the thermal stress while Fig. 2.15b shows the temporal variation of the equivalent strain in the surface vicinity. The equivalent strain increases as the heating progresses provided that the increase in strain is continuous even in the cooling cycle. It reduces rapidly as the cooling period progresses further. This is because the elastic response of the material is not as fast as the temperature field, i.e. the expansion is continuous for a while after the laser source vanishes. The normal component of the stress varies considerably with time. It results in two maxima; one in the heating cycle and the other in the cooling cycle. The normal component of the stress in the surface vicinity is tensile and it reaches as high as 20 MPa; which is less than the yield stress of the workpiece material.

Figure 2.16a shows the load variation with time while Fig. 2.16b shows the power spectrum density curve. The temporal variation of the load is similar to the normal stress component as shown in Fig. 2.15a, i.e. the value of the stress

**Fig. 2.14** Temporal variation of surface temperature at the center of the irradiated spot with and without convective boundary condition at the surface [13]



component is multiplied by the size of the irradiated spot to obtain the load. Since the total power in a signal is constant, the low and high frequency limits of the signal are determined from Fig. 2.16b. In the present case, Nyquist frequency ( $f_c = \frac{1}{2} \Delta t$ ; where  $\Delta t$  is the sampling rate) is selected as 2,000. It should be noted that  $f_c$  is the maximum frequency contained in the signal.

Figure 2.17 shows the flexural wave amplitude variation with time at four equally spaced locations at the workpiece surface. The first location is 12:5 cm away from the center of the heated spot and following locations are 12:5 cm away from the first location, respectively. The wave amplitude varies with time and no dominant pattern is observed in the wave. This is because the initial wave form at the center of the workpiece is modified as it travels along the workpiece due to: (i) the dispersion effect of the workpiece material, (ii) overlapping of wave modes, and (iii) the reflected waves from the free ends of the workpiece that interfere with the travelling wave. The group speed of the first wave mode is about 3,125 m/s; therefore, the reflection from the free ends takes about  $0.16 \times 10^{-3}$  s to reach the center of the workpiece. Consequently, the reflected wave modifies the travelling wave in the time and amplitude domain. As the location from the first point changes to the following point along the surface, the amplitude of the wave decreases and the travelling wave pattern changes. This indicates that the travelling wave vanishes as it travels towards the free ends of the workpiece, i.e. in the present study, damping coefficient of the workpiece material is taken as 0.025. Moreover, at locations close to the free ends of the workpiece, the wave appears as in high frequency mode. This is because the travelling wave has a low amplitude in these locations and reflected waves modify easily the travelling wave pattern.

## 2.4 Laser Pulse Heat Treatment of Metallic Surfaces

In the analysis of the flexural characteristics of the laser pulse heat treatment of metallic surfaces, the formulation and findings of the previous study [23] are considered. In this section laser induced flexural wave propagation due to recoil pressure generated at vapor–liquid interface of the evaporated surface is

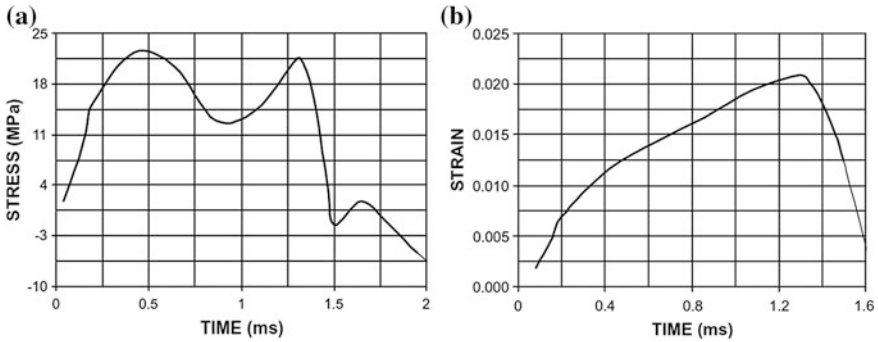


**Fig. 2.15** **a** Temporal variation of load generated in the surface vicinity of the workpiece due to normal component of the thermal stress, and **b** temporal variation of strain in the surface vicinity of the workpiece [13]

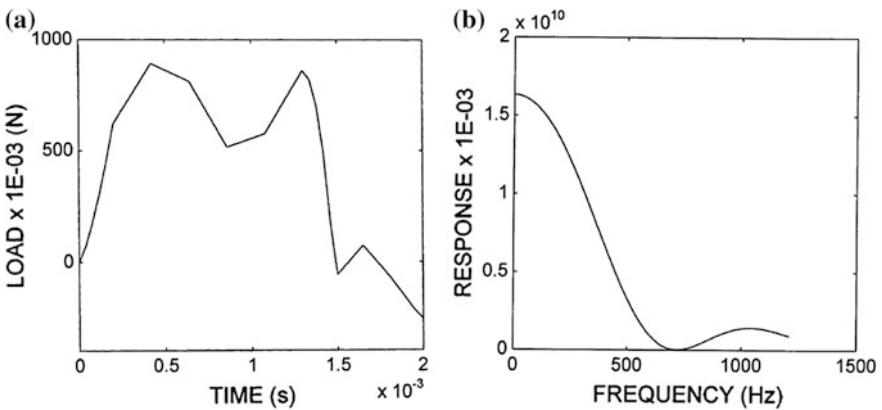


**Fig. 2.16** **a** Temporal variation of load generated due to normal component of the thermal stress, and **b** power spectrum density of thermal load [13]

investigated. The surface temperature rise during a laser heating pulse is presented analytically and recoil pressure is formulated. The flexural wave generation and propagation (due to recoil pressure) are simulated using a finite element method (FEM). The analysis is extended to include three cases of workpiece configurations; namely free-support, cantilever and fix ends.

### 2.4.1 Heat Transfer Analysis

The schematic of the interface is shown in Fig. 2.18. The heat transfer analysis is given above in Eqs. (2.20)–(2.24).

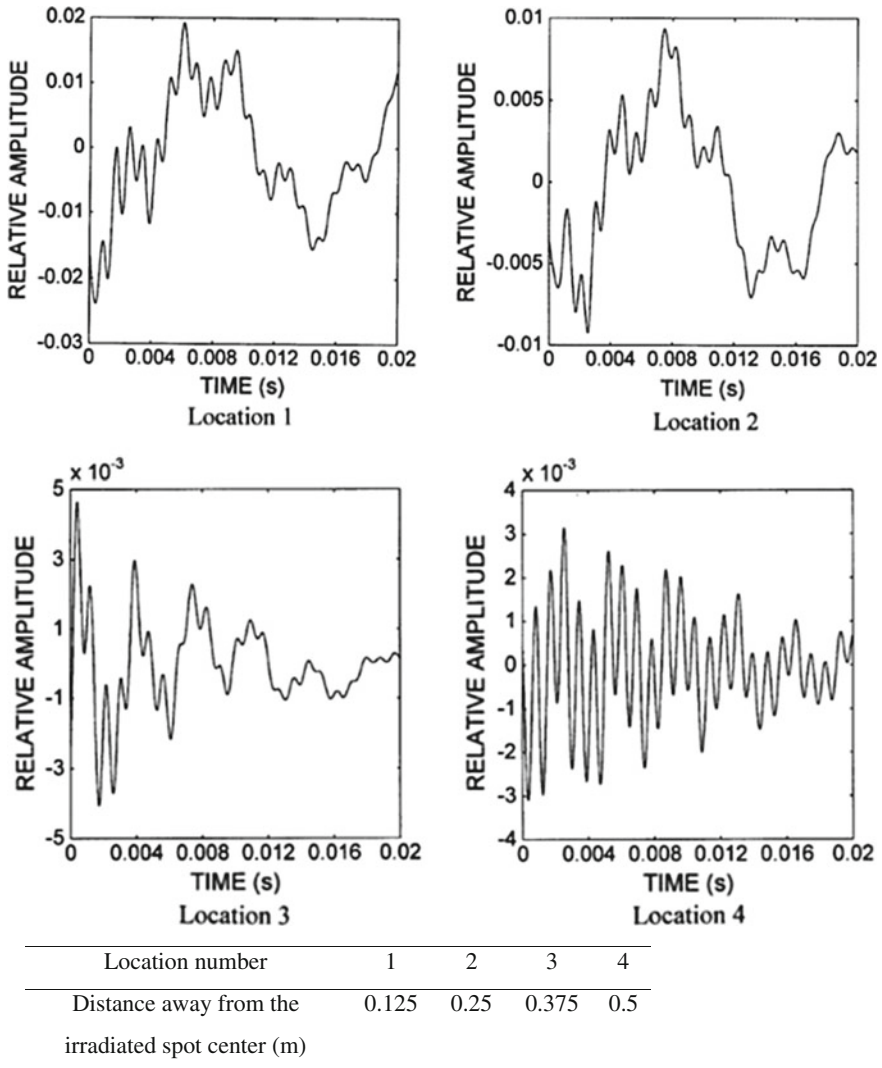


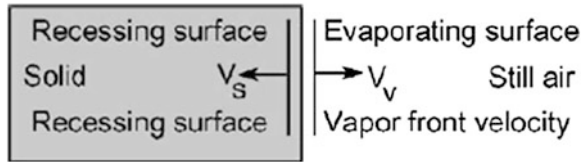
Fig. 2.17 The wave generated at different locations of the workpiece [13]

The pressure predicted is given in the previous study [6]:

$$P_v = 1.82 \times 10^{-3} \frac{\sqrt{C_p T_s I_0}}{[C_p(T_s - T_0) + L_v]} \tag{2.62}$$

The unit in Eq. (2.62) is bar.

**Fig. 2.18** Schematic view of interface [23]



### 2.4.2 Wave Analysis

In wave analysis, the workpiece is divided into a number of elements and each element can be treated as uniform (Fig. 2.19). The displacement vector is then transformed from time domain into frequency domain using fast Fourier transformation (FFT). The transform response is fed back into the governing differential equations as solved at each frequency component using FEM and the transient response is recovered by using the inverse FFT. The cross-sectional area and second moment of area at the mid of each element can be considered as constant over the entire element. Flexural wave analysis is given above in Eqs. (2.9)–(2.19).

### 2.4.3 Results and Discussion

In this case laser non-conduction heating of steel is considered. The flexural wave generation and propagation due to recoil pressure are simulated using FEM. The simulation conditions are extended to include free-supported, cantilever and fixed end workpieces. The material properties employed in the simulations are given in Table 2.4.

Figure 2.20 shows the temporal variation of recoil pressure generated during surface ablation. The pressure force calculation is based on the surface temperature predictions. Moreover, the peak values of the pressure force predicted from the present study and obtained from the previous study is in a good agreement, i.e. the difference is acceptably small which is in the order of 5 %. Moreover, the pressure force variation with time is assumed to be in exponential form.

Figure 2.21 shows the amplitude of displacement at the center of the workpiece with time for different workpiece configurations. In all workpiece configurations, displacement is negative in the early period and it becomes positive as time increases. This indicates the oscillation of the workpiece with a small amplitude. Moreover, the amplitude of the oscillation is lower for both ends fixed workpiece as compared to those corresponding to other workpiece configurations, provided that the amplitude of oscillation is maximum for the cantilever workpiece. Consequently, flexural motion of the workpiece due to a pressure force is damped for both ends fixed workpieces. The amplitude of oscillation as high as 15 mm occurs for both ends simple supported workpiece during the early oscillation period. As the time progresses, oscillation damps at the workpiece surface, except cantilever workpiece as shown in Fig. 2.22. The amplitude and frequency of oscillation is

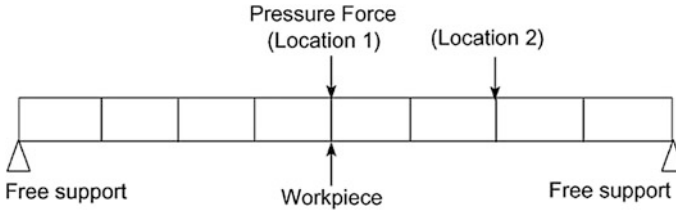


**Fig. 2.19** Schematic view of workpiece and elements used in the analysis [23]

**Table 2.4** Properties of steel and number elements used in simulations

E (GPa)	G (GPa)	$\rho$ (kg/m <sup>3</sup> )	$\kappa$	$\nu$	$\eta$	Length (m)	Width (m)	Thickness (m)	Number of elements
207	77.6	7,836	0.67	0.3	0.025	1	0.2	0.002	8

affected by the workpiece geometric configuration, i.e. both ends fixed workpiece results in small amplitude and low frequency and oscillation damps in the early period. Moreover, the maximum amplitude of oscillation is in the order of 20 mm for cantilever workpiece arrangement. The free-support arrangement results in the oscillation in the order of 10 mm at the workpiece center.

## 2.5 Laser Ablation: Influence of Force Location

In the analysis of the flexural characteristics of laser ablation process, the formulation and findings of the previous study [24] are considered.

In this section flexural waves generated during laser ablation of the three-layer assembly are considered. The assembly consists of 200  $\mu\text{m}$  Inconel 625 alloy (top layer), 2 mm stainless steel (intermediate layer), and 200  $\mu\text{m}$  Inconel 625 alloy (bottom layer). The assembly resembles the both side Inconel 625 coated stainless steel sheet. The effect of the location of the pressure force on the flexural wave characteristics is examined.

### 2.5.1 Heat Transfer Analysis

A schematic view of laser workpiece interaction due to evaporative heating is shown in Fig. 2.23. The heat transfer analysis is given above in Eqs. (2.20)–(2.24).

The vapor pressure predicted is given in the previous study [6], i.e.:

$$\text{Pr} = 1.82 \times 10^{-3} \frac{\sqrt{C_p T_{ev} I_0}}{C_p (T_{ev} - T_o) + L_{ev}} \quad (2.63)$$

Equation (2.63) is expressed in units of bar.

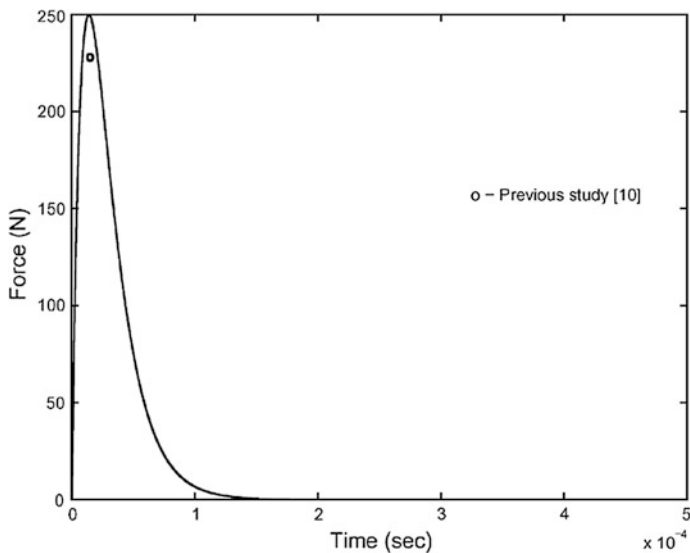


Fig. 2.20 Force response [23]

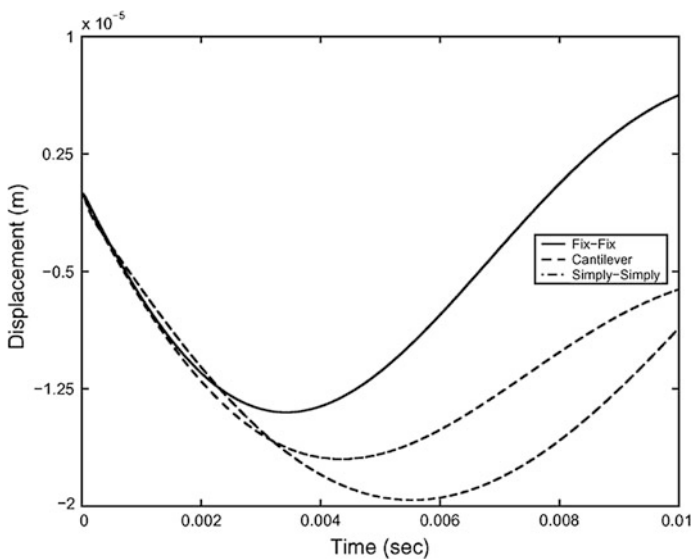


Fig. 2.21 Initial period displacement response for various configurations at the center of the beam [23]

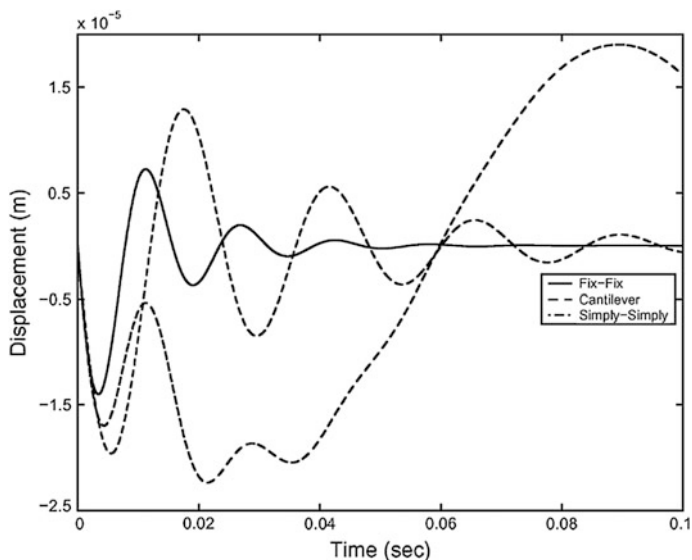


Fig. 2.22 Displacement response for various configurations at the center of the beam [23]

The recoil pressure is computed from Eq. (2.63). Moreover, the laser power intensity dissipated due to evaporation is:

$$I_{ev} \cong I_o - \dot{q}_{solid}$$

where  $\dot{q}_{solid}$  is the rate of energy dissipated in the solid phase. It should be noted that the rate of energy dissipated due to melting is considerably smaller than the rate of energy dissipated during evaporation; therefore, it is neglected.

The pressure force acting normal to the substrate surface can be written as:

$$F_o = \int_0^{r_e} Pr 2\pi r dr \quad (2.64)$$

where  $r_e$  is the radius of the evaporated surface. It should be noted that in the present study the evaporated surface, during the laser ablation, is considered as a circular shape with radius 0.4 mm, i.e.,  $r_e = 0.4$  mm. The variation of normal force with time is assumed as exponential, i.e.:

$$F(t) = F_o(\exp(-\beta t) - \exp(-\gamma t)) \quad (2.65)$$

where  $\beta$  and  $\gamma$  are constants. Figure 2.24 shows the normal pressure force.

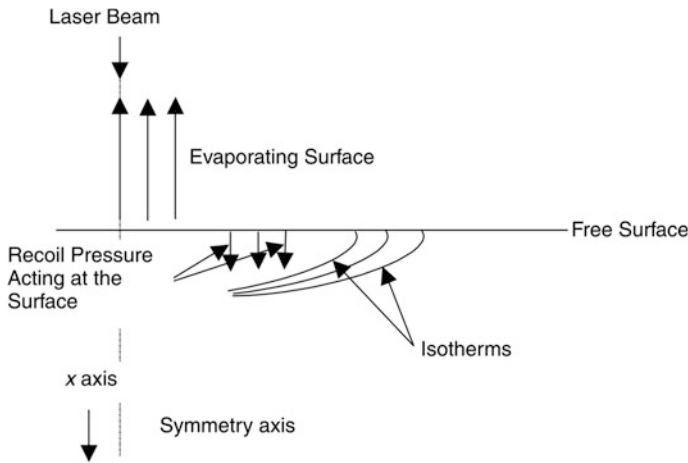


Fig. 2.23 A schematic view of laser workpiece interaction [24]

### 2.5.2 Flexural Wave Analysis

Flexural wave analysis is given above in Eqs. (2.26)–(2.40).

Initial and Boundary Conditions:

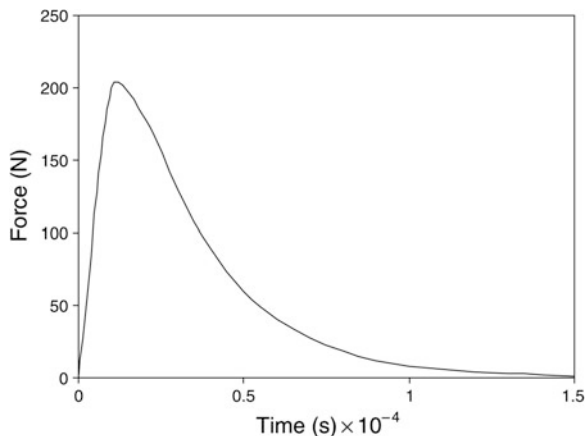
Initially the displacements are set to zero for a cantilever arrangement. At  $x = 0$  (at the fixed end), the displacement is always zero, i.e. at  $x = 0 : u = 0$ . It should be noted that in laser cutting of sheet metals, the workpiece is clamped at both ends. However, in the present situation, high magnitude flexural motion is required during the laser pulse heating process (during the cavity formation). This can be achieved by using a cantilever arrangement of the workpiece where the load due to recoil pressure should be acting at the free end of the workpiece.

### 2.5.3 Results and Discussions

In this case laser evaporative heating of three-layer assembly is considered and flexural wave generated due to the pressure force is investigated. Cantilever arrangement of the assembly is accommodated in the analysis. The location of laser evaporated spot is varied at the workpiece surface and the effect of pressure force location on the flexural wave characteristics is examined. Tables 2.5 and 2.6 give the mechanical and thermal properties of the substrate material employed in the simulations, respectively.

Figure 2.24 shows temporal variation of loading pressure force due to the recoil pressure. The magnitude of pressure force reaches as high as 200 kN. This is due to the high magnitude of recoil pressure generated during the ablation process. The

**Fig. 2.24** Temporal variation of pressure force [24]



temporal behavior of the pressure force is similar to that presented in the previous study [6].

Figure 2.25 shows the schematic view of the assembly and its geometric arrangements as well as the location of the mesh points where the flexural wave characteristics and stress levels are computed.

Figure 2.26 shows the temporal variation of the tip displacement (free end of the cantilever assembly) for different locations of the pressure force at the workpiece surface. The pressure force location is associated with the cell number as shown in Fig. 2.25. Due to high magnitude of the pressure force, the maximum flexural displacement is in order of 45  $\mu\text{m}$  at the tip of the cantilever assembly. The peak amplitude reduces sharply when the load position moves towards the fixed end of the assembly (5.1 nodal location). It should be noted that the nodal points of the elements in the assembly is shown in Fig. 2.25. The pressure force due to recoil pressure diminishes at about  $10^{-4}$  s; however, the amplitude of the flexural displacement of the assembly reaches maximum at about  $10^{-3}$  s. The time shift in the flexural displacement is due to the damping effect of the assembly arrangement and elastic and mass matrixes of the substrate material. Moreover, the location of the force does not alter the time occurrence of the peak amplitude, i.e. the peak amplitude of the flexural displacement corresponding to different locations of the pressure force occurs at the same time. Consequently, influence of pressure force on the time occurrence of the maximum displacement is insignificant.

## 2.6 Laser Ablation in Multilayer Assembly

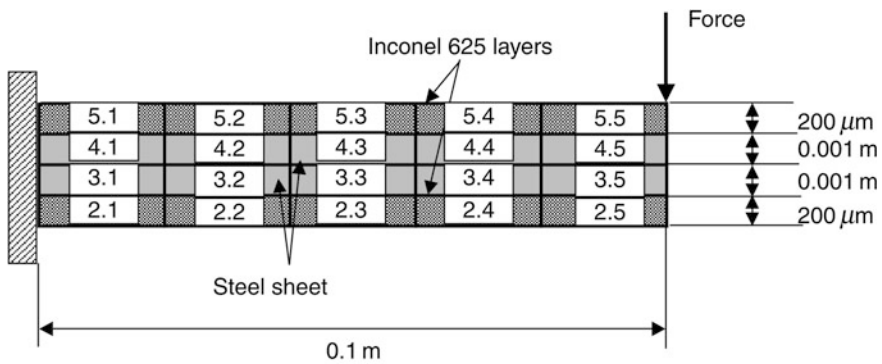
In this section the analysis of the flexural characteristics of the multilayer assembly, the formulation and findings of the previous study [25] are considered. Thus, the flexural motion of the three- and four-layer assemblies is modelled. In

**Table 2.5** Mechanical properties of steel and Inconel 617 alloy

	Poisson’s ratio $\nu$	Density ( $\text{kg/m}^3$ )	Elastic modulus (Pa)
Steel	0.3	7,830	$2.068 \times 10^{11}$
Inconel 625	0.313	8,460	$2.12 \times 10^{11}$

**Table 2.6** Thermal properties of steel and Inconel 625 alloy

	$C_p$ (J/Kg K)	$k$ (W/m K)	$\delta$ (1/m)	$\alpha$ ( $\text{m}^2/\text{s}$ )
Steel	460	80.3	$6.16 \times 10^7$	$0.22 \times 10^{-4}$
Inconel 625	425	14.4	$6.16 \times 10^7$	$0.38 \times 10^{-5}$



	Steel	Inconel
Thickness (m)	0.001	2.00E-04
Length (m)	0.1	0.1

**Fig. 2.25** Workpiece arrangement and layers. *Numbers* represent the cell number for the locations in the assembly [24]

order to generate impact load at the workpiece surface for the flexural motion, the laser ablation of the surface is considered. The laser evaporative heating of the solid surface is modelled and recoil pressure generated during the evaporation process is formulated in order to account for the impact load. The three-layer assembly consists of two layers of steel and a single layer of Inconel 617 alloy, while the four-layer assembly consists of two layers of steel and two layers of Inconel 617 alloy.

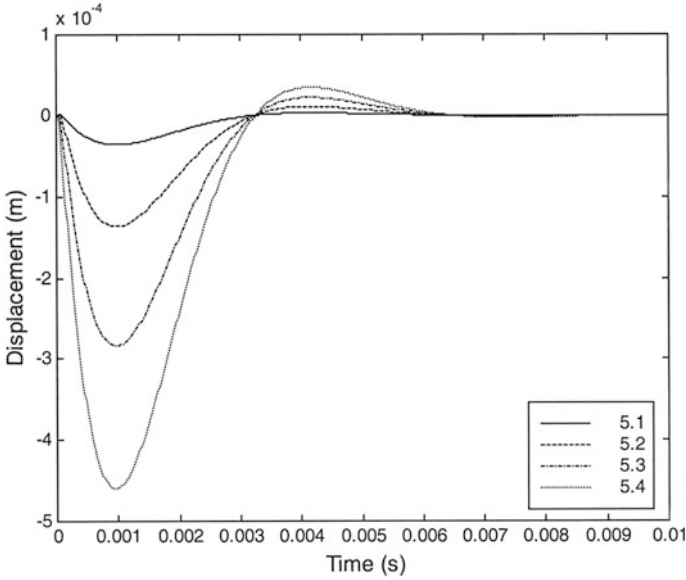


**Fig. 2.26** Temporal variation of flexural displacement for different pressure load location at the assembly surface as shown in Fig. 2.25 [24]

### 2.6.1 Heat Transfer Model

A schematic view of laser workpiece interaction for non-conduction limited heating situation is shown in Fig. 2.27. The heat transfer analysis is given above in Eqs. (2.20)–(2.24).

The pressure force acting normal to the substrate surface can be written as:

$$F_o = \int_0^{r_e} P 2\pi r dr$$

where  $r_e$  is the radius of the evaporated surface. It should be noted that in the present study the evaporated surface, during the laser ablation, is considered as a circular shape with radius 0.4 mm, i.e.,  $r_e = 0.4$  mm. The variation of normal force with time is assumed as exponential, i.e.:

$$F(t) = F_o(\exp(-\beta t) - \exp(-\gamma t))$$

where  $\beta$  and  $\gamma$  are constants. Figure 2.28 shows the normal pressure force.

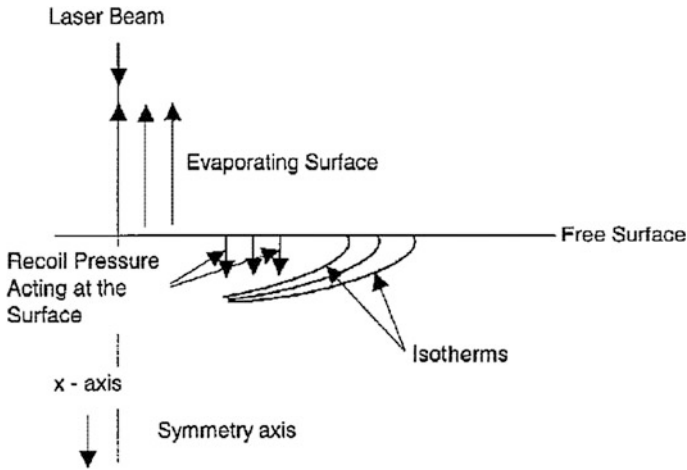


Fig. 2.27 A schematic view of laser workpiece interaction [25]

### 2.6.2 Flexural Wave Analysis

Flexural wave analysis is given above in Eqs. (2.26)–(2.40).

Initial and Boundary Conditions:

Initially the displacements are set to zero for a cantilever arrangement. At  $x = 0$  (at the fixed end), the displacement is always zero, i.e. at  $x = 0$ :  $u = 0$ . It should be noted that in laser cutting of sheet metals, the workpiece is clamped at both ends. However, in the present situation, high magnitude flexural motion is required during the laser pulse heating process (during the cavity formation). This can be achieved by using a cantilever arrangement of the workpiece where the load due to recoil pressure should be acting at the free end of the workpiece.

### 2.6.3 Results and Discussions

Laser non-conduction limited heating of multiplayer assembly is considered in this section. The recoil pressure developed at the vapor-liquid interface during the evaporation process is analyzed and the pressure force is considered as the impacting load generating the flexural motion of the workpiece. In order to obtain large amplitude flexural wave, a cantilever arrangement of the workpiece is taken into account and the impacting load is assumed to act close to the free end of the workpiece. Figure 2.29 illustrates the schematic view of the workpiece, the location of the impacting load and the elements used in the computation while Fig. 2.28 shows temporal variation of resulting pressure force (impacting load). Tables 2.7 and 2.8 give the material properties used in the simulations.

**Fig. 2.28** Temporal variation of pressure force [25]

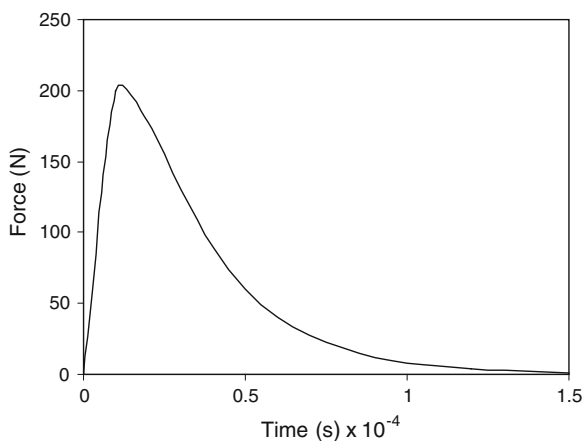
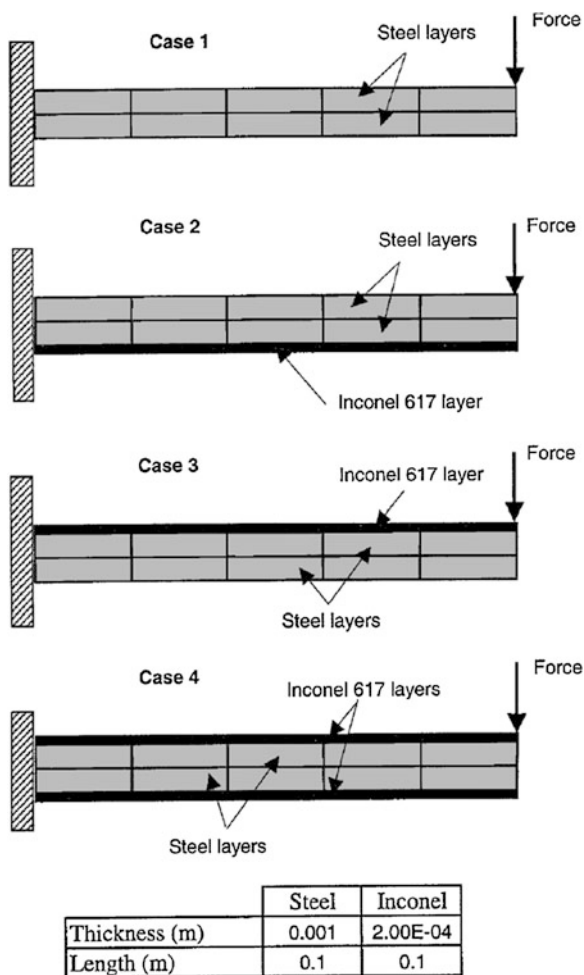


Figure 2.30 shows the displacement with time for four cases, which are illustrated in Fig. 2.29. The magnitude of displacement is higher for the case 1, and then follows the cases 2 and 3, and 4. The large displacement for case 1 is because of the number of layers in the assembly, which are 2 and the end location of cantilever arrangement of the workpiece, i.e. it results the maximum displacement of the order of 500  $\mu\text{m}$  in this region. Consequently, increasing number of layers from 2 to 4 reduces the displacement considerably despite the addition of two layers have thickness in the order of 400  $\mu\text{m}$ , i.e. each layer thickness is 200  $\mu\text{m}$  which is 1/10 of the steel layer thickness. However, thin layer of Inconel alloy reduces the amplitude of the flexural motion of the workpiece due to its properties as seen from Table 2.7, i.e. it has a high density. The cases for 2 and 3, in which the Inconel alloy layer is either at top or bottom, indicate that the location of Inconel alloy layer (whether at top or bottom) has no influence on the amplitude of the flexural motion.

Figure 2.31 shows equivalent stress (Fig. 2.29) for four cases. The maximum stress in the order of 20 MPa, which is less than the yield strength of the substrate materials. The time, at which the maximum stress occurs, corresponds to the time when the magnitude of displacement is maximum. It should be noted that although the displacement for cases 2 and 3 are almost identical, the magnitude of equivalent stress differs slightly, which is more pronounced when the stress is maximum. The stress level reduces to zero when the magnitude of displacement becomes zero.

Figure 2.32 shows shear stress with time for four cases. Shear stress behavior is similar to that corresponding to equivalent stress, provided that the maximum magnitude of shear stress is higher than that of equivalent stress. The small magnitude of shear stress is because of small displacement, which is in the order of  $10^{-4}$  m.

Figure 2.33 shows the maximum displacement for different cases. The maximum displacement is almost identical for the cases 2 and 3 and its magnitude

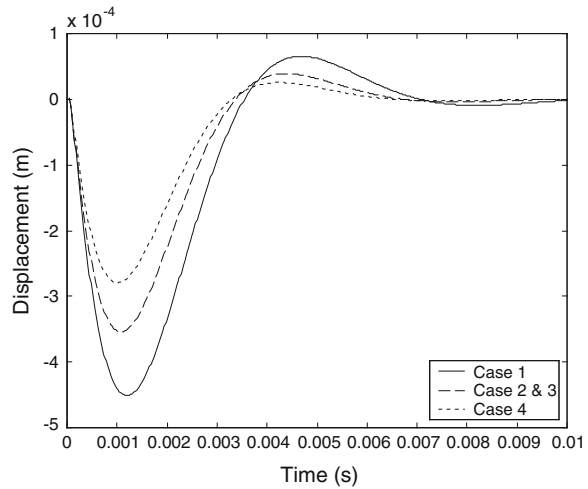
**Fig. 2.29** Workpiece arrangement and layers [25]**Table 2.7** Mechanical properties of steel and Inconel 617 alloy

	Poisson's ratio $\nu$	Density ( $\text{kg/m}^3$ )	Elastic modulus (Pa)
Steel	0.3	7,830	$2.068 \times 10^{11}$
Inconel 617	0.312	8,440	$2.11 \times 10^{11}$

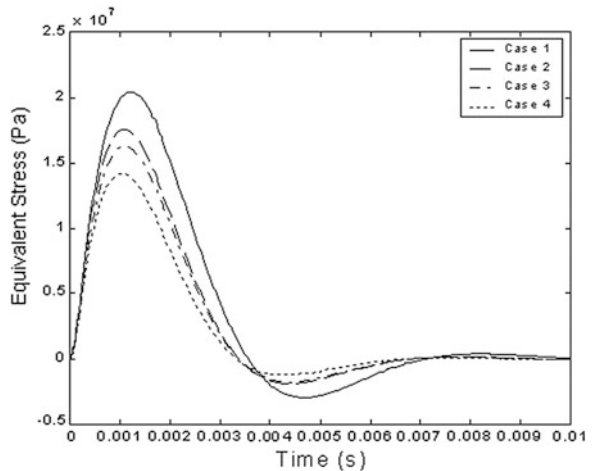
**Table 2.8** Thermal properties of steel and Inconel 617 alloy

	$C_p$ (J/Kg K)	$k$ (W/m K)	$\delta$ (1/m)	$\alpha$ ( $\text{m}^2/\text{s}$ )
Steel	460	80.3	$6.16 \times 10^7$	$0.22 \times 10^{-4}$
Inconel 617	419	13.4	$6.16 \times 10^7$	$0.38 \times 10^{-5}$

**Fig. 2.30** Temporal variation of displacement for different arrangements of workpiece layers (cases) [25]



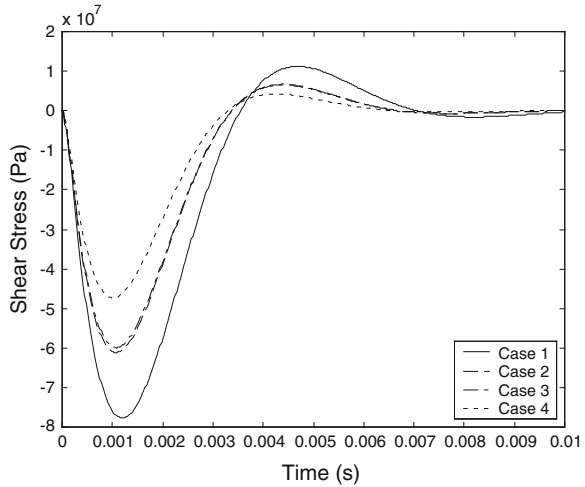
**Fig. 2.31** Temporal variation of equivalent stress for different arrangements of workpiece layers (cases) [25]



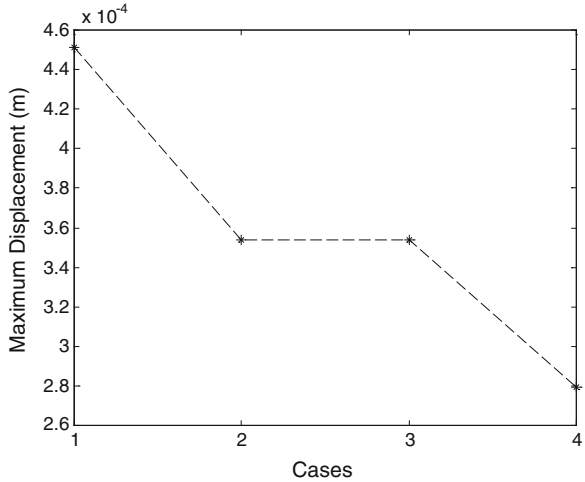
reduces more than 50 % for the case 4. Consequently, addition of thin Inconel layer influences the amplitude of the flexural motion considerably.

Figure 2.34 shows the maximum equivalent stress for different cases. The variation in equivalent stress with cases is not as considerable as the variation of maximum displacement. In this case, the magnitude of maximum equivalent stress reduces about 25 % for the case 4 while the magnitude of displacement reduces about 50 % for the same case.

**Fig. 2.32** Temporal variation of shear stress for different arrangements of workpiece layers (cases) [25]



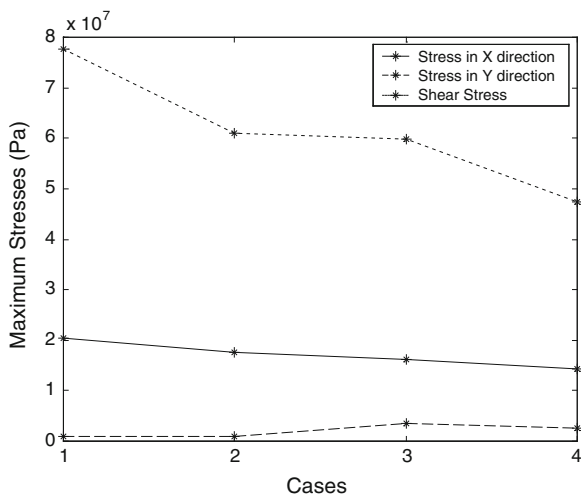
**Fig. 2.33** Maximum displacement for different arrangements of workpiece layers (cases) [25]



## 2.7 Cantilever Plate Heated at Fixed End

In the analysis of the flexural characteristics of the cantilever plate heated at fixed end, the formulation and findings of the previous study [26] are considered. In the present case, consider locally heated flat plated in a cantilever arrangement. Thus the effect of the size of the heat source on the flexural motion of the plate when subjected to the impulsive force at the free end of the plate is examined. A numerical scheme employing a Finite Element Method (FEM) is used to predict the frequency and the amplitude of the flexural motion of the plate. The influence of the size of the heat source is then correlated with the change in the frequency and the amplitude of the resulting flexural motion.

**Fig. 2.34** Temporal variation of maximum stress for different arrangements of workpiece layers (cases) [25]



### 2.7.1 Mathematical Modeling Numerical Solution

Consider a flat solid-like of finite thickness as shown in Fig. 2.35, where the geometry is defined by:

$$\bar{D} = \{(x,y,z): 0 \leq x \leq l; 0 \leq y \leq h; 0 \leq z \leq w\}$$

where  $\bar{D}$  is the space vector.

### 2.7.2 Heat Transfer Analysis

The transient diffusion equation based on the Fourier heating model can be written in the Cartesian coordinates as:

$$\rho c_p \frac{\partial T}{\partial t} = k \left( \frac{\partial^2 T}{\partial x^2} + \frac{\partial^2 T}{\partial y^2} + \frac{\partial^2 T}{\partial z^2} \right) \quad (2.66)$$

where  $\rho$  is the density,  $c_p$  is the specific heat capacity and  $k$  is the thermal conductivity. In a matrix form, Eq. (2.66) is written as:

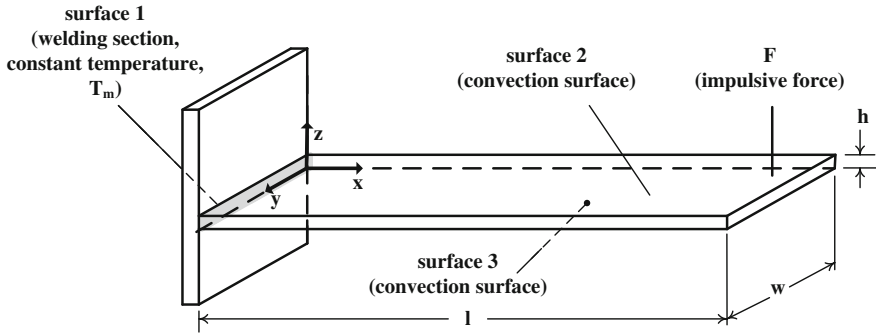


Fig. 2.35 The plate coordinate system [26]

$$\rho c_p \frac{\partial T}{\partial t} + [L]^T [q] = 0 \tag{2.67}$$

or

$$\rho c_p \frac{\partial T}{\partial t} = [L]^T ([D^t] [L] T) \tag{2.68}$$

where \$[q]\$ is the heat flux vector, \$[D^t]\$ is the thermal conductivity matrix:

$$[D^t] = \begin{bmatrix} k & 0 & 0 \\ 0 & k & 0 \\ 0 & 0 & k \end{bmatrix} \tag{2.69}$$

and \$[L]\$ is the vector operator and is defined as:

$$[L] = [\partial/\partial x \quad \partial/\partial y \quad \partial/\partial z]^T = \text{vector operator}$$

The thermal boundary conditions of the flat solid are as follows:

A constant temperature heat source is assumed at one of the following locations: surface 1 (as shown in Fig. 2.36) of the flat solid, i.e.,

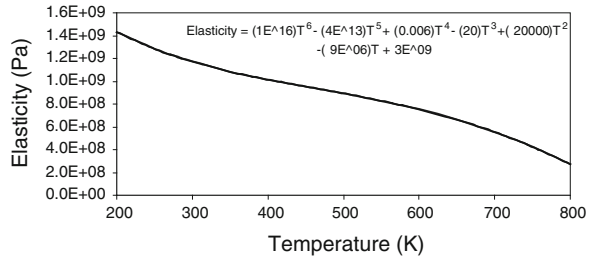
$$T = T_m \quad \text{at } x = 0, 0 \leq y \leq h, 0 \leq z \leq w$$

where \$T\_m\$ is the melting temperature of the flat solid material.

At the free surfaces (surfaces 2 and 3) (in \$x\$-\$y\$ plane at \$z = 0\$ and \$z = h\$) a convective boundary is assumed, therefore, the corresponding boundary condition is:

$$[q]^T [\eta] = h_f [T_s - T_B] \quad \text{at } z = 0 \text{ (surface 2) and } z = h \text{ (surface 3)}$$

**Fig. 2.36** Elastic modulus versus temperature curve [26]



where  $[\eta]$  is the unit outward normal vector,  $h_f$  is the heat transfer coefficient and  $T_s$  and  $T_B$  are the surface temperature and bulk temperature of adjacent fluid, respectively.

Initially the substrate material is assumed to be at a reference temperature,  $T_o$ , therefore, the initial condition becomes:

$$T = T_o \quad \text{at } t = 0$$

The thermal properties of the flat solid material used are given in Table 2.9. In finite element domain the flat solid is divided into SOLID98 ANSYS elements. The coupled-field 10-node (i, j, k, l, m, n, o, p, q and r) tetrahedral element has a quadratic displacement behavior. Each of the ten nodes has 3 structural (translations:  $u_x$ ,  $u_y$  and  $u_z$ ), and one thermal degrees of freedom at each node (temperature,  $T$ ) [27]. The heat balance equations for the finite element, in matrix form, is written as:

$$[C_e^t][\dot{T}_e] + ([K_e^{tb}] + [K_e^{tc}])[T_e] = [Q_e^c] \quad (2.70)$$

where

$$[C_e^t] = \rho \int_{\forall} c_p [N][N]^T d\forall = \text{element specific heat matrix}$$

$$[T_e] = [T_i \ T_j \ T_k \ T_l \ T_m \ T_n \ T_o \ T_p \ T_q \ T_r]^T = \text{nodal temperature vector of element}$$

$$[K_e^{tb}] = \int_{\forall} [B^t]^T [D^t] [B^t] d\forall = \text{element diffusion conductivity matrix}$$

$$[K_e^{tc}] = \int_{S_2} h_f [N][N]^T dS_2 + \int_{S_3} h_f [N][N]^T dS_3 = \text{element convection surface conductivity matrix}$$

$$[Q_e^c] = \int_{S_2} T_B h_f [N] q dS_2 + \int_{S_3} T_B h_f [N] q dS_3 = \text{element convection surface heat flow vector}$$

The element shape functions matrix,  $[N]$  relates the temperature variable,  $T$ , which is allowed to vary in both space and time, with the nodal temperature vector of element as follows:

**Table 2.9** The thermal properties of the flat solid material used in the simulations

Thermal conductivity, $k$ (W/m K)	53
Specific heat, $c_p$ (J/kg K)	520
Poisson's ratio, $\nu$	0.29
Thermal expansion coefficient, $\alpha$ (1/K)	$1.5 \times 10^{-5}$
Density, $\rho$ (kg/m <sup>3</sup> )	7,880
Damping coefficient	0.015

$$T(x,y,z,t) = [N]^T [T_e] \quad (2.71)$$

For a 10-node tetrahedral ANSYS element, the shape functions matrix (for all degrees of freedom) is written as:

$$[N] = \begin{bmatrix} (2L_1 - 1)L_1 & 0 & 0 & 0 & 0 & 0 & 0 & 0 & 0 & 0 \\ 0 & (2L_2 - 1)L_2 & 0 & 0 & 0 & 0 & 0 & 0 & 0 & 0 \\ 0 & 0 & (2L_3 - 1)L_3 & 0 & 0 & 0 & 0 & 0 & 0 & 0 \\ 0 & 0 & 0 & (2L_4 - 1)L_4 & 0 & 0 & 0 & 0 & 0 & 0 \\ 0 & 0 & 0 & 0 & 4L_1L_2 & 0 & 0 & 0 & 0 & 0 \\ 0 & 0 & 0 & 0 & 0 & L_2L_3 & 0 & 0 & 0 & 0 \\ 0 & 0 & 0 & 0 & 0 & 0 & L_1L_3 & 0 & 0 & 0 \\ 0 & 0 & 0 & 0 & 0 & 0 & 0 & L_1L_4 & 0 & 0 \\ 0 & 0 & 0 & 0 & 0 & 0 & 0 & 0 & L_2L_4 & 0 \\ 0 & 0 & 0 & 0 & 0 & 0 & 0 & 0 & 0 & L_3L_4 \end{bmatrix} \quad (2.72)$$

where  $L_1, L_2, L_3$  and  $L_4$  are the normalized coordinates going from 0.0 at a vertex to 1.0 at the opposite side. Matrix  $[B^t]$  is defined as:

$$[B^t] = [L] [N]^T \quad (2.73)$$

### 2.7.3 Flexural Wave Analysis

The finite element, in matrix form, description of the flexural motion of the flat solid is written as:

$$[M_e^s] [\ddot{U}_e] + [C_e^s] [\dot{U}_e] + [K_e^s] [U_e] = [F_e^{th}] + [F_e^{nd}] \quad (2.74)$$

where

$$[M_e^s] = \rho \int_V [N]^T [N] dV = \text{element mass matrix}$$

$$[U_e] = [u_i \ u_j \ u_k \ u_l \ u_m \ u_n \ u_o \ u_p \ u_q \ u_r]^T = \text{nodal displacement vector of element}$$

$$[C_e^s] = \text{structural damping matrix}$$

$$[K_e^s] = \int_{\forall} [B^s]^T [D^s] [B^s] d\forall = \text{element stiffness matrix}$$

$$[F_e^{th}] = \int_{\forall} [B^s]^T [D^s] [\varepsilon^{th}] d\forall = \text{element thermal load vector}$$

$$[F_e^{nd}] = \text{vector of nodal forces applied to the element}$$

where  $[B^s]$  is the strain-displacement matrix, based on the element shape factors and relates the strain displacement vector,  $[\varepsilon]$ , with the nodal displacements vector,  $[U]$  by:

$$[\varepsilon] = [B^s] [U] \quad (2.75)$$

and  $[D^s]$  is the elasticity matrix and defines the relation between stress and strain vectors as:

$$[\sigma] = [\sigma_x \ \sigma_y \ \sigma_z \ \sigma_{xy} \ \sigma_{yz} \ \sigma_{xz}]^T = [D^s] [\varepsilon^{el}] = [D^s] \left[ [\varepsilon] - [\varepsilon]^{th} \right] \quad (2.76)$$

where:

$$[\varepsilon^{el}] = \text{elastic strain vector} \quad (2.77)$$

$$[\varepsilon^{th}] = (T - T_0) [\alpha \ \alpha \ \alpha \ 0 \ 0 \ 0]^T = \text{thermal strain vector} \quad (2.78)$$

and

$$[\varepsilon] = [\varepsilon_x \ \varepsilon_y \ \varepsilon_z \ \varepsilon_{xy} \ \varepsilon_{yz} \ \varepsilon_{xz}]^T = \text{total strain vector} \quad (2.79)$$

where  $\alpha$  is the thermal expansion coefficient of the flat solid material. The structural properties of the flat solid material are given in Table 2.10, while Fig. 2.36 presents the elastic modulus (E) versus temperature (T). The elasticity matrix,  $[D^s]$ , is inversely defined as the flexibility (or compliance) matrix,  $[D^s]^{-1}$ , which is written as:

$$[D^s]^{-1} = \frac{1}{E} \begin{bmatrix} 1 & -\nu & -\nu & 0 & 0 & 0 \\ -\nu & 1 & -\nu & 0 & 0 & 0 \\ -\nu & -\nu & 1 & 0 & 0 & 0 \\ 0 & 0 & 0 & 2(1+\nu)/E & 0 & 0 \\ 0 & 0 & 0 & 0 & 2(1+\nu)/E & 0 \\ 0 & 0 & 0 & 0 & 0 & 2(1+\nu)/E \end{bmatrix} \quad (2.80)$$

where  $\nu$  is Poisson's ratio.

The structural boundary conditions of the flat solid are as follows:

At the fixed end, the displacement in all directions is always zero i.e. at  $x = 0$ :  $u_x = u_y = u_z = 0$ . It should be noted that in laser cutting of sheet metals, the workpiece is clamped at both ends. However, in the present situation, high

**Table 2.10** Description of the impulsive loads employed in the present study

Size of constant heating source (w)	Heating time at which impulsive load is applied (s)	Amplitude of impulsive load, F (N)	Duration of impulsive load (s)
0.25	2.5	1	0.001
0.50	5	1	0.001
0.75	7.5	1	0.001
1	10	1	0.001

magnitude flexural motion is required during the laser pulse heating process (during the cavity formation). This can be achieved by using a cantilever arrangement of the workpiece where the load due to recoil pressure should be acting at the free end of the workpiece. Initially the displacements are set to zero for a cantilever arrangement.

The grid size independency heat transfer and flexural studies were carried to determine the optimum grid size of the flat solid. The flat solid dimensions employed in the present study were as follows: 0.15 m for length,  $l$ , 0.05 m for width,  $w$ , and 0.0015 m for thickness,  $h$ . The impulsive force exciting the free end of plate is as described in Table 2.10. The flexural properties of the plate material are presented in Fig. 2.36.

### 2.7.4 Results and Discussion

The flexural motion of cantilever assembly heated at the fixed end is considered and the effect of the size of the heat affected zone in the flexural motion is examined. The constant temperature heat source is assumed at the fixed edge while an impulsive load is applied at the free end of the cantilever assembly. The size of the heat source is varied while the load level is kept constant in the analysis. Temperature dependent thermal and mechanical properties of steel are accommodated in the simulations.

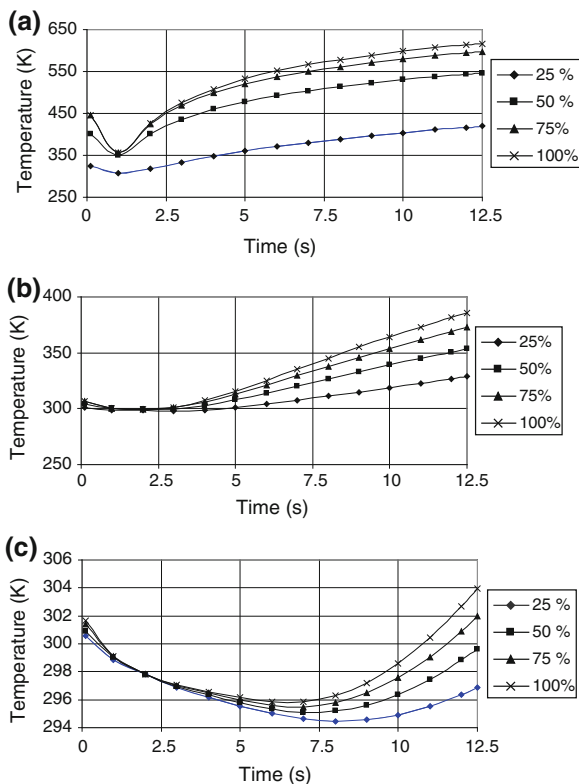
Figure 2.37 shows temporal variation of temperature at 0.5 width of the plate in the z-axis (mid-plane of the plate) and at different x-axis locations for various sizes of the constant temperature heat source at the fixed end of the cantilever assembly. Temperature rises rapidly in the early heating periods and temperature rise becomes gradual as the heating progresses with time. This is particularly true for the location  $x = L/15$  ( $L$  being the length of the plate). The rapid rise of temperature in the early heating period is associated with the conduction heat transfer in the vicinity of the heat source, since location  $x = L/15$  is close to the heat source at the fixed end. In the early heating period, temperature gradient is high in the neighborhood region of the heat source. This enhances the heat conduction from the heat source to its neighborhood. Consequently, temperature in the neighborhood of the fixed end rises rapidly. As the time progresses, the temperature gradient becomes low due to initially rapid rise of temperature in the region

**Fig. 2.37** Temporal variations of temperature at plate mid-plane ( $z = 0.5$  W) for different  $x$ -locations [26].

**a**  $x = 0.01$  m ( $x = L/15$ ).

**b**  $x = 0.03$  m ( $x = L/5$ ).

**c**  $x = 0.05$  m ( $x = L/3$ ).



next to the heat source. This results in gradual rise of temperature with progressing time. Similar arguments are true for all the sizes of the heat source, provided that magnitude of temperature increases slightly with size of the heat source at the end of 12.5 s of heating duration. However, temperature rise is low as the  $x$ -axis location increases to  $x = L/5$  for all the sizes of the heat source. This is because of the time taken for temperature rise through the heat conduction, which is long.

Figure 2.38 shows the flexural motion of the cantilever plate for different sizes of the constant temperature heat source. It should be noted that the time shift of the flexural response of the cantilever plate is obtained through subtracting the time response of the corresponding flexural motion with heating and no heating situations. Moreover, the amplitude shift is obtained through the maximum amplitude difference of the corresponding flexural motion with heating and without heating situations. When the size of the heat source increases, the changes in the amplitude of the flexural motion increases sharply and this increase becomes gradual as the size of the heat source increases further. This is associated with the temperature field in the substrate material, which modifies the elastic modulus of the substrate material (Fig. 2.36). In this case, increasing the size of the heat source enhances the high temperature region in the material through heat diffusion. This lowers the elastic modulus and modifies the displacement of the flexural motion of the

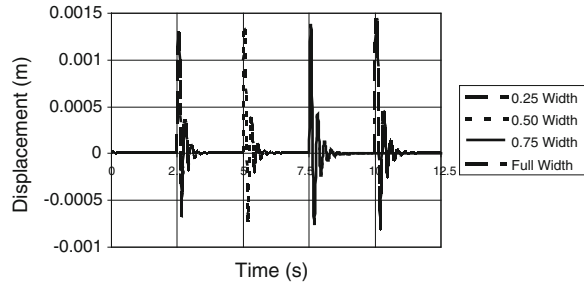
cantilever plate. Moreover, once the size of the heat source increase further, the heat diffusion enhances into the substrate material modifying the elastic modulus further, provided that the amplitude of the flexural motion is not affected significantly. This is because of the size of high temperature ( $T > 500$  K) region, which does not extend significantly as compared to the extension of the low temperature region in the plate ( $T < 500$  K). It should be noted that the elastic modulus varies in a non-linear form with temperature and the magnitude of this variation becomes high for temperatures greater than 500 K. The limited size of extension of the high temperature region in the substrate material is associated with the diffusion mechanism, which is governed by the temperature gradient. Since the constant temperature heat source has temperature less than the melting temperature of the substrate material, due to avoiding the phase change process, the temperature gradient remains low in the region next to the heat source. However, as the distance from the heat source increases further along the x-axis, the temperature gradient reduces significantly enhancing the heat diffusion (Fig. 2.38). Therefore, high temperature region is only limited with the small size in the neighborhood of the heat source. Consequently, amplitude of the flexural motion does not vary much with further increasing of the constant heat temperature source size.

In the case of the time shift, of the flexural motion (Fig. 2.38), a gradual increase in the time shift with the size of the constant temperature heat source is observed. The gradual change in the time shift is because of the temporal response of the substrate material to the constant heat source. Since, for each case, the excitation loads is applied from the free end of the plate after the 2.5 s time steps, which is also seen from Fig. 2.38, heat diffusion into the substrate material enhances with progressing time and elastic modulus is modified accordingly. Therefore, the time shift between no-heating and heating situations is affected by the heating duration prior to the excitation load is applied. Moreover, the region where the heat is diffused increases with increasing the rise of the constant temperature heat source. Consequently, by the time, at which the excitation load is applied, heat diffusion enhances with increasing heat source size. This, in turn, increases the time shift between the frequency of the flexural motion corresponding to heating and no-heating situations of the plate. It is, therefore, expected that the time shift of the flexural motion with and without heating situations enables to determine the size of the heat source at the fixed end of the cantilever plate. It is also equally true that the measuring the maximum amplitude difference between the flexural waves with heating and no-heating situations of the palate enables to determine the size of the heat source at the fixed end of the cantilever plate.

## 2.8 Welding of Bar to Rigid Body

The mathematical analysis and the findings for welding of bar to rigid body are presented below in line with the previous study [28]. Flexural motion of a bar, resembling cantilever beam, subjected to one side welding is discussed in this

**Fig. 2.38** Flexural motion of plate for different sizes of constant heat source [26]



section. The wave characteristics of the bar motion will be correlated with the size of the heat affected zone during the welding process.

The bar which has a finite thickness is shown in Fig. 2.39. The bar dimensions employed in the present study were as follows: 0.15 m for length,  $l$ , 0.05 m for width,  $s$ , and 0.0015 m for thickness,  $w$ .

### 2.8.1 Heat Transfer Analysis

The transient diffusion equation based on the Fourier heating model can be written in the Cartesian coordinates as:

$$\rho c_p \frac{\partial T}{\partial t} = k \left( \frac{\partial^2 T}{\partial x^2} + \frac{\partial^2 T}{\partial y^2} + \frac{\partial^2 T}{\partial z^2} \right) \quad (2.81)$$

where  $\rho$  is the density,  $c_p$  is the specific heat capacity and  $k$  is the thermal conductivity.

The thermal boundary conditions of the bar are as follows:

A constant temperature heat source is assumed at the fixed end (surface 1) of the bar, i.e.

$$T = T_m \quad \text{at } x = 0, 0 \leq y \leq s, 0 \leq z \leq w$$

where  $T_m$  is the melting temperature of the flat solid material.

At the free surfaces (surfaces 2 and 3) (in  $x$ - $y$  plane at  $z = 0$  and  $z = w$ ) a convective boundary is assumed, therefore, the corresponding boundary condition is:

$$[q]^T [\eta] = h_f [T_s - T_B] \quad \text{at } z = 0 (\text{surface 2}) \text{ and } z = w (\text{surface 3})$$

where  $[\eta]$  is the unit outward normal vector,  $h_f$  is the heat transfer coefficient and  $T_s$  and  $T_B$  are the surface temperature and bulk temperature of adjacent fluid, respectively.

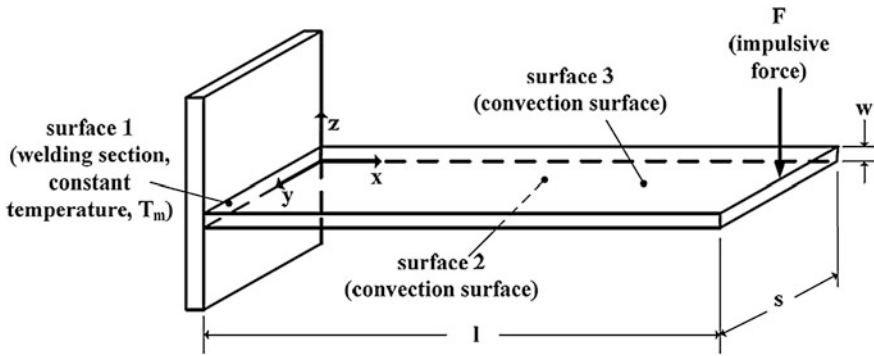


Fig. 2.39 Heating situation and coordinate system [28]

Initially the substrate material is assumed to be at a reference temperature,  $T_0$ , therefore, the initial condition becomes:

$$T = T_0 \quad \text{at } t = 0$$

The thermal properties of the bar material used are given as: 53 W/m K for thermal conductivity and 520 J/kg k for specific heat. In finite element domain the bar is divided into SOLID98 ANSYS elements. The coupled-filed 10-node tetrahedral element has a quadratic displacement behavior.

Each of the ten nodes has 3 structural translations and one thermal degrees of freedom at each node (temperature, T).

### 2.8.1.1 Flexural Motion Analysis

The finite element, in matrix form, description of the flexural motion of the bar is written as:

$$[M_e^s] [\ddot{U}_e] + [C_e^s] [\dot{U}_e] + [K_e^s] [U_e] = [F_e^{th}] + [F_e^{nd}] \quad (2.82)$$

where,

- $[M_e^s]$  = element mass matrix
- $[U_e]$  = nodal displacement vector of element
- $[C_e^s]$  = structural damping matrix
- $[K_e^s]$  = element stiffness matrix
- $[F_e^{th}]$  = element thermal load vector
- $[F_e^{nd}]$  = vector of nodal forces applied to the element

The structural boundary conditions of the bar are as follows: at the fixed end (at  $x = 0$ ), the displacement in all directions is always zero. It should be noted that in

laser cutting of sheet metals, the workpiece is clamped at both ends. However, in the present situation, high magnitude flexural motion is required during the laser pulse heating process (during the cavity formation). This can be achieved by using a cantilever arrangement of the workpiece where the load due to recoil pressure should be acting at the free end of the workpiece. Initially the displacements are set to zero for a cantilever arrangement. The structural material properties are given as:  $7,880 \text{ kg/m}^3$  for density, 0.015 for damping coefficient and  $1.5 \times 10^{-5} \text{ 1/K}$  for thermal expansion coefficient.

The grid size independency heat transfer and flexural studies were carried to determine the optimum grid size of the flat solid. For obtaining a maximum accuracy of results, it was decided to use a grid size of 438 elements. In carrying the grid independency studies, the time step size used for integration was taken as 0.0006 s, which was determined, based from studies that were carried to determine the required time step size.

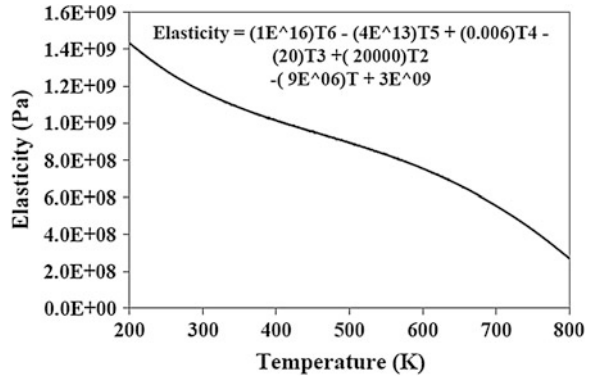
## 2.8.2 Results and Analysis

Heating of a bar resembling a welding situation is considered and temperature field is predicted. The bar is fixed at one end and heated at constant temperature at the fixed end. The temperature of the heat source is maintained at melting temperature of the bar material. (800 K). Since the elastic modulus changes with temperature (see Fig. 2.40), flexural motion of the bar when excited at the free end with an impulsive force as described in Fig. 2.41, is modeled. The impulse force is applied at different heating durations and displacements as well as frequency of the flexural motion of the bar are computed accordingly. Moreover, knowing the temperature distribution and the size of the heat affected zone, wave characteristics of the flexible motion are related to the temperature field in the bar.

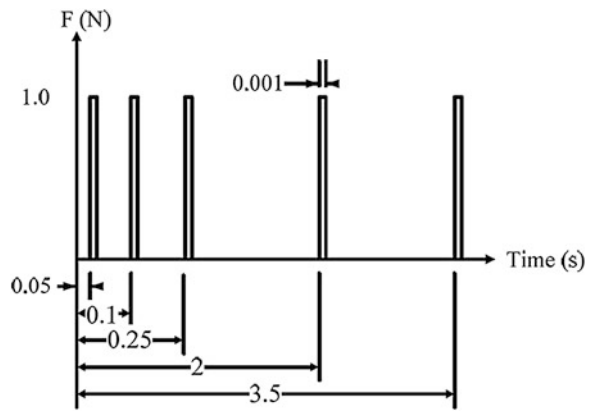
Figure 2.42 shows temperature distribution at the centerline for different heating durations. Temperature difference in region close to the heating section decays sharply and as the distance increases towards the bar free end, the temperature decays gradually. This is more pronounced in the early heating period. In this case, internal energy gain of the substrate material from the heat source increases and conduction losses towards bar free end becomes low in the early heating period. This results in sharp decay of the temperature in the vicinity of the heat source. However, as the time progresses temperature gradient remains high and heat diffusion from high temperature region to the bar end enhances, which lowers temperature decay in the region close to the heated zone. Since the modulus of elasticity varies with temperature, increasing temperature in the heated region of the bar lowers the modulus of elasticity. This becomes significant as the heating period progresses, i.e. the variation in the modulus of elasticity extends towards the free end of the bar with progressing heating period.

Figure 2.43 shows the wave behavior of flexural motion at different heating durations when the bar is excited by an impulsive force at different heating

**Fig. 2.40** Elastic modulus versus temperature curve [28]

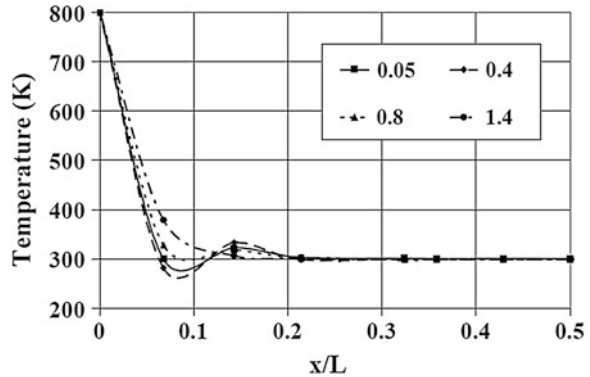


**Fig. 2.41** Description of the impulsive loads employed in the present study [28]



durations as well as when the bar is excited with no heating situation. The wave characteristics are computed at the free end of the flat solid where amplitude of flexural motion is the maximum. The characteristics of flexural waves (amplitude and frequency) due to heating and no heating situations is almost the same at time 0.05 s when the impulse force is applied, i.e. slight variation in amplitudes is observed for both flexural waves corresponding to heating and no heating conditions. The flexural wave amplitude is smaller for no heating situation than that of heating situation due to the change in the modulus of elasticity with temperature. However, difference in amplitude of both waves is more pronounced for heating periods of 0.1 and 0.25 s. this is because of the variation in modulus of elasticity, which results in change of flexural wave characteristics. Consequently, the wave characteristics are modified by the temperature field through change in modulus of elasticity. As the heating period progresses, the difference between both wave characteristics becomes small; in which case, the difference in wave amplitude due to heating and no heating situations becomes small. This is because of the reflected wave from the free end of the bar, which modifies the wave characteristics as well

**Fig. 2.42** Temperature distributions at bar center line during different heating durations [28]



as temperature field which extends into the bar with progressing time modifying the elastic module in the heated region. Consequently, change of the elastic modulus due to temperature field and the reflected wave from the free end of the bar modifies the wave characteristics during the long heating period.

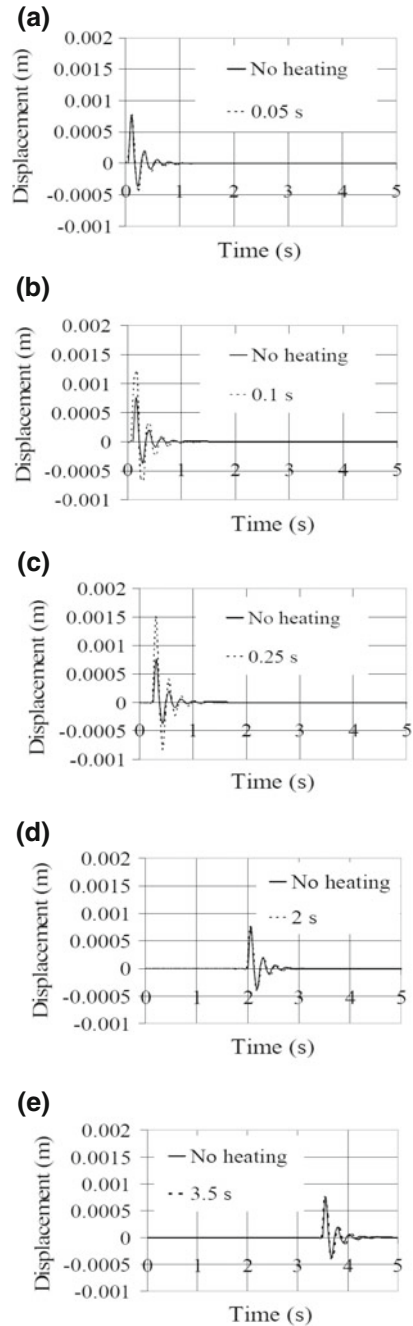
As the heating progresses, high temperature region extends into the bar with gradual temperature decay towards the bar end. This causes the modulus of elasticity decay gradually in this region. Consequently, the wave characteristics of the flexural motion are modified in such a way that the maximum amplitude difference in both waves becomes small. Therefore, the effect of temperature decay in the bar on the maximum amplitude is significant as similar to the time shift of both waves.

## 2.9 Local Heating of a Bar: Effect of Heat Source Location

In the current analysis of the flexural characteristics of the bar, the formulation and findings of the previous study [29] are considered. The flexural behavior of a uniform rectangular bar considered in this case has a  $w$  width, a  $l$  length and  $h$  thickness with cantilever arrangement, as shown in Fig. 2.44. The effects of the local heat source, resembling the immediately after the electric resistance welding process, on the wave characteristics are examined when an impulsive load is applied at the tip of the bar. The heat source is introduced along the width of the bar and the location of the heat source is changed along the length of the bar (at  $x = 0, 0.25, 0.5$  and  $0.75l$ ). Since the elastic modulus of the bar is considered as temperature dependent, the change of the location of the heat source modifies the wave characteristics. This enables examination of the change of heat source location and corresponding variation of the magnitude and frequency of the flexural wave.

**Fig. 2.43** Flexural motion at different heating durations when the bar is excited by an impulsive force at different heating durations [28].

- a** Impulsive load applied at heating time = 0.05 s.
- b** Impulsive load applied at heating time = 0.1 s.
- c** Impulsive load applied at heating time = 0.25 s.
- d** Impulsive load applied at heating time = 2.0 s.
- e** Impulsive load applied at heating time = 3.5 s.



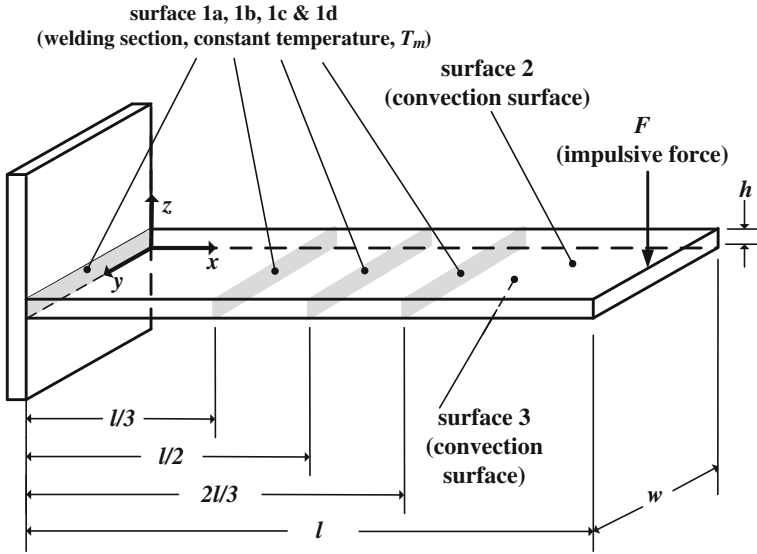


Fig. 2.44 The plate coordinate system and locations of heating load [29]

### 2.9.1 Mathematical Modeling Numerical Solution

The transient diffusion equation based on the Fourier heating model can be written in the Cartesian coordinates as:

$$\rho c_p \frac{\partial T}{\partial t} = k \left( \frac{\partial^2 T}{\partial x^2} + \frac{\partial^2 T}{\partial y^2} + \frac{\partial^2 T}{\partial z^2} \right) \quad (2.83)$$

where  $\rho$  is the density,  $c_p$  is the specific heat capacity and  $k$  is the thermal conductivity. The thermal boundary conditions of the flat solid are as follows:

A constant temperature heat source is assumed at one of the following locations: 1a or 1b or 1c or 1d, as shown in Fig. 2.44, of the uniform bar, i.e.,

$$T = T_m \quad \text{at } 0 \leq y \leq h, \quad 0 \leq z \leq w$$

where  $T_m$  is the melting temperature of the flat solid material.

At the free surfaces (surfaces 2 and 3) (in  $x$ - $y$  plane at  $z = 0$  and  $z = h$ ) a convective boundary is assumed, therefore, the corresponding boundary condition is:

$$[q]^T [\eta] = h_f [T_s - T_B] \quad \text{at } z = 0 \text{ (surface 2) and } z = h \text{ (surface 3)}$$

where  $[\eta]$  is the unit outward normal vector,  $h_f$  is the heat transfer coefficient and  $T_s$  and  $T_B$  are the surface temperature and bulk temperature of adjacent fluid, respectively.

Initially the substrate material is assumed to be at a reference temperature,  $T_o$ , therefore, the initial condition becomes:

$$T = T_o \quad \text{at } t = 0$$

The properties of the uniform bar material used are given in Table 2.11. In finite element domain the uniform bar is divided into SOLID98 ANSYS elements. The coupled-filed 10-node tetrahedral element has a quadratic displacement behavior. Each of the ten nodes has 3 structural translations and one thermal degrees of freedom at each node (temperature, T) [27].

To compare the numerical predictions with the analytical solution presented in the open literature for the no heating situation, the analytical formulation is introduced. In this case, the differential equation describing the flexural motion of a bar with no heating condition is given as [30]:

$$\frac{d^4 z}{dx^4} - \left( \frac{\omega^2 m}{EI} \right) y = 0 \quad (2.84)$$

where  $\omega$  represents the natural frequency values satisfying solution of Eq. (2.84) for certain boundary conditions. E is the modulus of elasticity of the bar material, I is the mass moment of inertia and m is the mass per unit length of the bar. The general solution of Eq. (2.84) is presented as follows:

$$\begin{aligned} z = & A \cosh \left( \left( \frac{m\omega^2}{EI} \right)^{1/4} x \right) + B \sinh \left( \left( \frac{m\omega^2}{EI} \right)^{1/4} x \right) \\ & + C \cos \left( \left( \frac{m\omega^2}{EI} \right)^{1/4} x \right) + D \sin \left( \left( \frac{m\omega^2}{EI} \right)^{1/4} x \right) \end{aligned} \quad (2.85)$$

where A, B, C and D are the integration constants and can be found after substituting the following boundary conditions in Eq. (2.85): at the clamped end of the uniform bar ( $x = 0$ ):

$$y|_{x=0} = 0 \quad \text{and} \quad \left. \frac{dy(x)}{dx} \right|_{x=0} = 0$$

at the free end ( $x = l$ ):

$$\left. \frac{d^2 y(x)}{dx^2} \right|_{x=l} = 0 \quad \text{and} \quad \left. \frac{d^3 y(x)}{dx^3} \right|_{x=l} = 0,$$

which reduces Eq. (2.85) into:

**Table 2.11** The thermal properties of the flat solid material used in the simulations

Thermal conductivity, $k$ (W/m K)	53
Specific heat, $c_p$ (J/kg K)	520
Poisson's ratio, $\nu$	0.29
Thermal expansion coefficient, $\alpha$ (1/K)	$1.5 \times 10^{-5}$
Density, $\rho$ (kg/m <sup>3</sup> )	7,880
Damping coefficient, $\zeta$	0.015

$$\cosh \left( \left( \frac{m\omega^2}{EI} \right)^{1/4} l \right) \cos \left( \left( \frac{m\omega^2}{EI} \right)^{1/4} l \right) + 1 = 0 \quad (2.86)$$

According to [30, 31], the resulting fundamental natural frequency corresponding to the first mode of motion for the uniform bar is:

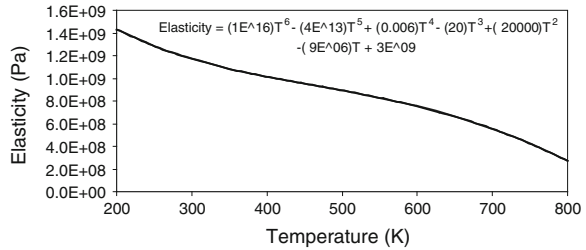
$$\omega_{fundamental} = 1.875^2 \sqrt{\frac{EI}{ml^4}} \quad (2.87)$$

Figure 2.45 presents the elastic modulus (E) versus temperature (T). The impulsive force exciting the free end of bar is as described in Table 2.12. The grid size independency heat transfer and flexural studies were carried to determine the optimum grid size of the bar. It was found that 572 elements are required to simulate accurately the flexural behavior of the bar; however, for the purpose of producing a better presentation for the temperature contours of the bar, when subjected to welding at different locations, a higher number of elements were used. The numbers of elements used for finding the results when the bar is heated at  $x = 0, 0.25, 0.5$  and  $0.75l$  were respectively 572, 1,002, 994 and 983 elements. The integration time step independency tests were as well conducted and the value of 0.0006 s was used in the study for performing the time integrations. The Newmark ANSYS time integration method for implicit transient analysis was employed [27]. The dimensions for the uniform bar are as follows: 0.15 m for length,  $l$ , 0.05 m for width,  $w$ , and 0.0015 m for thickness,  $h$ . The fundamental natural frequency was calculated according to Eq. (2.87) and found to be equal to 26.436 rad/s. The damped natural frequency is calculated according to the following formula [30]:

$$\omega_d = \omega_{fundamental} \sqrt{1 - \zeta^2} \quad (2.88)$$

where  $\zeta$  is the damping coefficient of the uniform bar and taken as 0.015 for the uniform bar. The resulting damped natural frequency is 26.433 rad/s. For the sake of validating the numerical results, the damped natural frequency was calculated for the case when the bar was simulated under no heating conditions (when the temperature is equal to 300 K and the corresponding elasticity is equal to 1.2 GPa), The resulting damped time period was found as 0.238 s and the corresponding damped natural frequency ( $\omega_{d, \text{numerical}} = 2 \times \pi / \text{damped time period}$ ) is

**Fig. 2.45** Elastic modulus versus temperature curve [29]



**Table 2.12** Description of the impulsive loads employed in the present study

Location of heating source	Heating time at which impulsive load is applied (s)	Amplitude of impulsive load, F (N)	Duration of impulsive load (s)
0l	2.5	1	0.001
1/3	2.5	1	0.001
1/2	2.5	1	0.001
2l/3	2.5	1	0.001

calculated to be 26.363 rad/s. The percentage difference between the results of the analytical solution and the numerical damped natural frequencies, obtained from ANSYS simulation, for the uniform bar is found to be 0.07 %.

### 2.9.2 Results and Discussion

Heating of a bar, resembling the situation immediately after the electric resistance welding process and the effect of the location of the heated region on the flexural motion of the bar are examined. It should be noted that in a simulation, a heat source, resembling immediately after the welding process is applied at a particular x-axis location and along the y-axis of the plate. The location subjected to welding is treated as one of the boundary conditions, by fixing the temperature of the welding location to the metal melting temperature,  $T_m$ , at all the nodes of the welding location. In ANSYS, this can be done by defining a thermal load function at all the time points of the desired solution and the value of the thermal load function will always be equal to the melting temperature of the metal. The transient effects across the plate due to the welding process in the y and z directions are incorporated in solving the heat conduction equation [Eq. (2.83)]. Figure 2.46 shows temperature distribution at different locations in the plate, while Fig. 2.47 shows temperature variation along the dimensionless axial length ( $x/l$ ) at different locations in the plate. Since the temperature heat source is considered, temperature attains high values at the locations of the heat source and decays sharply as the distance in the vicinity of the heat source increases in the axial direction (along the x-axis). Although convection boundary is considered at the top and bottom

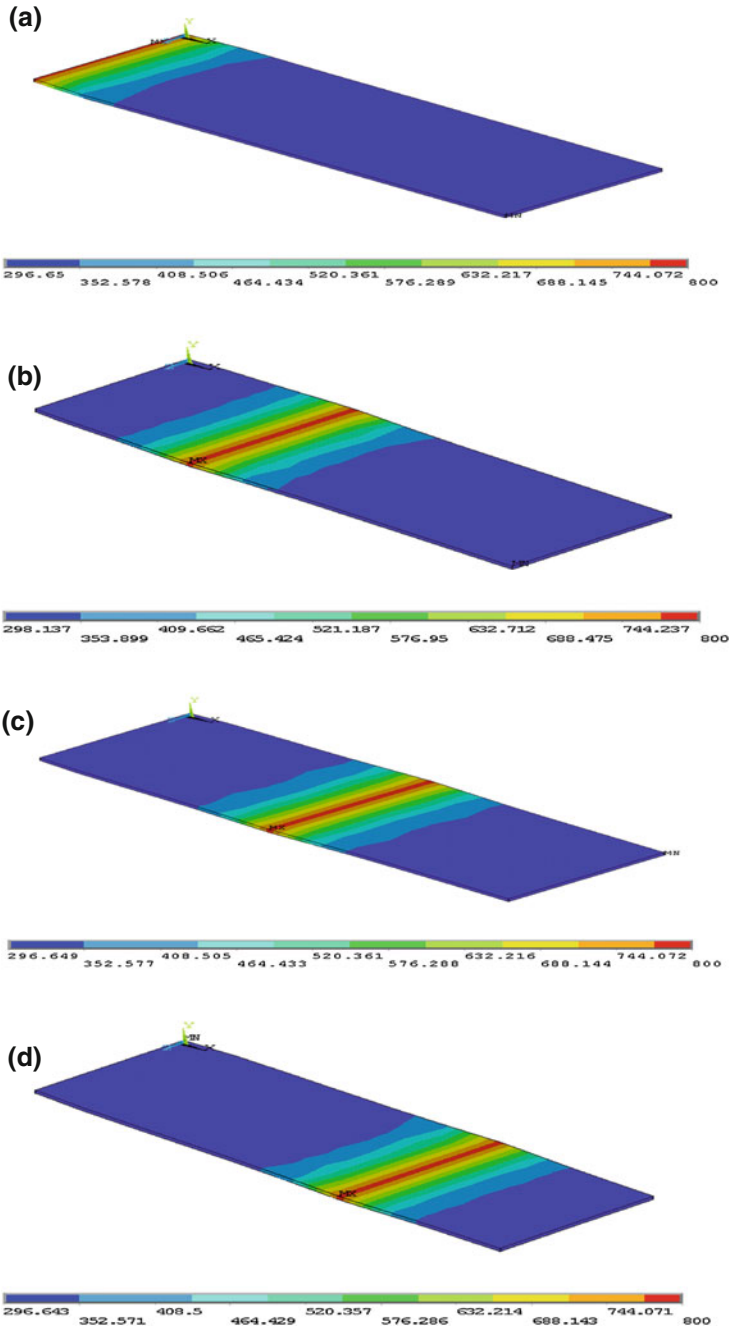


**Fig. 2.46** Temperature contours of plate for different heating locations [29]. **a** Heating location at  $x = 0l$ . **b** Heating location at  $x = 1/3$ . **c** Heating location at  $x = 1/2$ . **d** Heating location at  $x = 2l/3$

**Fig. 2.47** Spatial variations of temperature at plate mid-plane ( $y = 0.5 w, z = 0.5 h$ ) for different locations of heating [29]

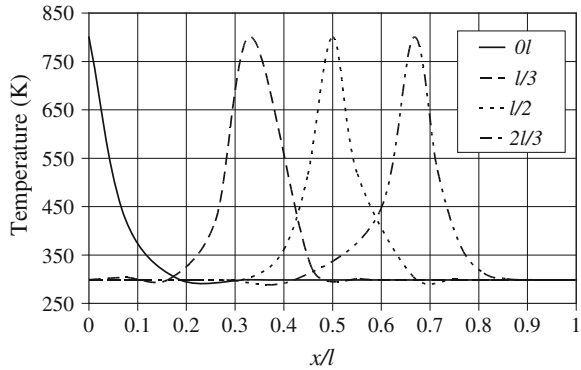
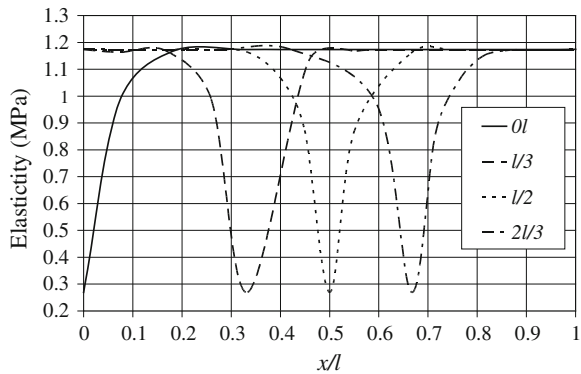


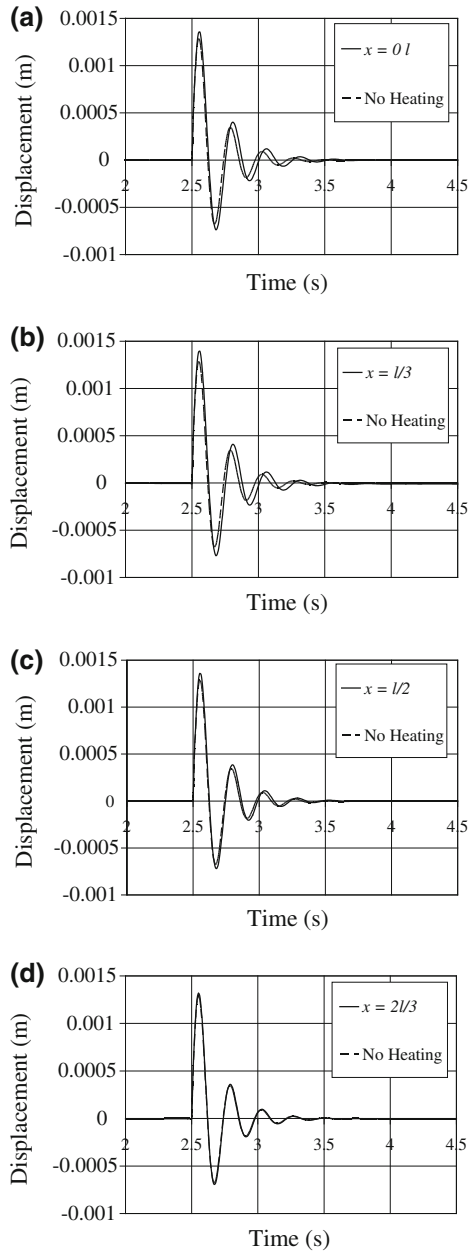
**Fig. 2.48** Spatial variations of elasticity at plate mid-plane ( $y = 0.5 w, z = 0.5 h$ ) for different locations of heating [29]



surfaces of the plate, heat transfer through diffusion in the plate is dominant. This is because of the magnitude of the heat transfer coefficient at the surface, which is low, i.e. in the order of  $10 \text{ W/m}^2 \text{ K}$  due to the natural convection. Since the heat source is considered to be at constant temperature, the temperature gradient becomes the same in the region front and back of the heat source. This results in similar elastic modulus variation around the heat source. This situation is seen from Fig. 2.48, in which elastic modulus of the substrate material is shown in the axial direction (along the x-axis). It should be noted that the elastic modulus is considered to be temperature dependent. Moreover, the location of the heat source is changed along the axial distance for the each case simulated. Consequently, for each case, elastic distribution varies similarly along the x-axis, provided that the location of the maximum elastic modulus changes along the x-axis for the each case.

Figure 2.49 shows tip displacement of the plate (at  $x = 1$ ) due to the flexural motion resulted through the applied force. It should be noted that for each case, where the location of the heat source is changed along the axial distance, with heating and no-heating situations are considered. The resulting displacements for no-heating and heating situations are plotted in each figure. Since the cantilever

**Fig. 2.49** Flexural motion of plate tip (at  $x = l$ ) for different sizes of constant heat source [29]. **a** Heating location at  $x = 0l$ . **b** Heating location at  $x = 1/3$ . **c** Heating location at  $x = 1/2$ . **d** Heating location at  $x = 2/3$



arrangement of the plate is considered and the load is applied at the free end of the plate, the flexural displacement is the maximum at the free end of the plate. The small difference in the displacement is observed with heating and no-heating

situations. This difference diminishes where location of the heat source is moved to  $x = 2l/3$ . In addition, small shift in the frequency of the flexural displacement is observed. It also diminishes for the heat source locations at  $x = 2l/3$ . This indicates that the location of the heat source in the plate modifies the flexural wave characteristics of the plate due to change of elastic modulus with temperature.

## 2.10 Laser Welding of Cantilever Plate: Influence of Speed of the Heating Source

The mathematical analysis and the findings for laser welding of cantilever plate are presented below in line with the previous study [32]. Consider the flexural characteristics of the cantilever plate, which is heated by a moving source at fixed end. The influence of the moving heat source speed, located at the fixed end, on the flexural characteristics of the cantilever plate is computed using the finite element method. The plate is excited by an impulsive force at the free end. In the analysis, temperature dependent Young's modulus is accommodated to simulate the nonlinear effect of the Young's modulus on the amplitude and the time shift of the flexural motion of the plate. The simulations are repeated for three heat source speeds.

### 2.10.1 Mathematical Modeling and Numerical Solution

In the analysis, a flat plate with cantilever arrangement (length,  $L = 0.075$  m, height,  $H = 0.00075$  m, and width,  $W = 0.025$  m), as shown in Fig. 2.50, is considered. The flexural impulsive load at the free end of the plate is introduced.

In finite element domain the flat solid is divided into SOLID98 ANSYS elements, which is a coupled-field 10-node tetrahedral element. It has quadratic displacement behavior, is introduced. Each of the ten nodes has 3 structural (translations:  $u_x$ ,  $u_y$  and  $u_z$ ), and one thermal degrees of freedom at each node (temperature,  $T$ ) [27]. The transient diffusion equation based on the Fourier heating model can be written in the Cartesian coordinates as:

$$\rho c_p \frac{\partial T}{\partial t} = k \left( \frac{\partial^2 T}{\partial x^2} + \frac{\partial^2 T}{\partial y^2} + \frac{\partial^2 T}{\partial z^2} \right) \quad (2.89)$$

where  $\rho$  is the density,  $c_p$  is the specific heat capacity and  $k$  is the thermal conductivity. The finite element, in matrix form, description of the flexural motion of the flat solid is written as:

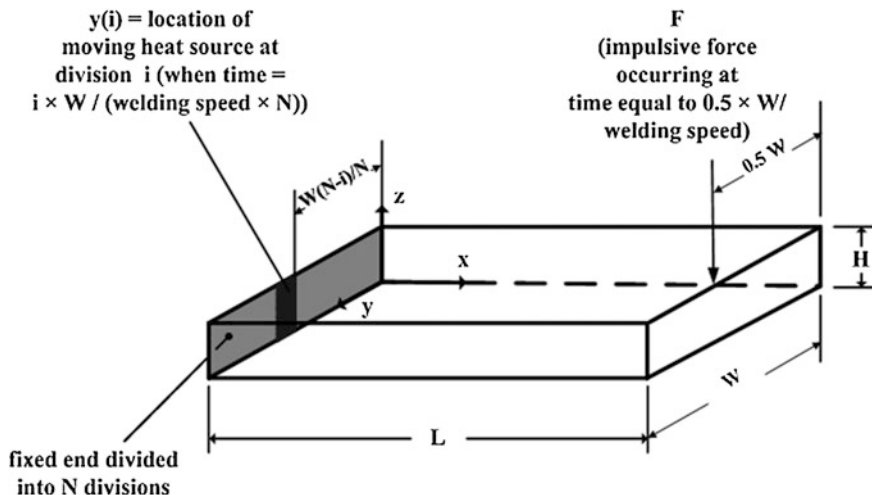


Fig. 2.50 The cantilever plate [32]

$$[M_e^s] [\ddot{U}_e] + [C_e^s] [\dot{U}_e] + [K_e^s] [U_e] = [F_e^{th}] + [F_e^{nd}] \tag{2.90}$$

where,

- $[M_e^s]$  = element mass matrix
- $[U_e]$  = nodal displacement vector of element
- $[C_e^s]$  = structural damping matrix
- $[K_e^s]$  = element stiffness matrix
- $[F_e^{th}]$  = element thermal load vector
- $[F_e^{nd}]$  = vector of nodal forces applied to the element

The modulus of elasticity of the cantilever plate material varies with temperature and is given as follows:

$$E = (10^{16} \times T^6) - (4 \times 10^{13} \times T^5) + (0.006 \times T^4) - (20 \times T^3) + (20,000 \times T^2) - (9 \times 10^6 \times T) + 3 \times 10^9 \tag{2.91}$$

where  $E$  is in Pascal and  $T$  in Kelvin.

At the free surfaces of the cantilever, a convective boundary is assumed. Initially the substrate material is assumed to be at a reference temperature equal to the room temperature. The moving heat source along the width of the plate (in the  $y$ -direction) at the fixed end, where the heating action due to the welding process takes place, is simulated as follows:

The width of the plate at the fixed end,  $W$ , is divided into equal number of divisions,  $N$ , where the area of each division is equal to  $H \times W/N$ .

An index is assigned to each of the divisions i.e.;  $i = 1, 2, \dots, N$ , where the starting location for each of the divisions in the y-direction is  $y(i) = (W/N) \times (N - i)$ .

The overall heating time is divided into equal number of time steps, each of is equal to  $W/(\text{welding speed} \times N)$ . When the moving heat source reaches to a division at a time equal to  $i \times W/(\text{welding speed} \times N)$ , as shown in Fig. 2.50, the temperature of all the finite element nodes at the surface of the division (at  $x = 0$ ) is fixed to a temperature equal to the melting temperature of the metal (800 K) for a time duration equal to a single time step ( $W/(\text{welding speed} \times N)$ ).

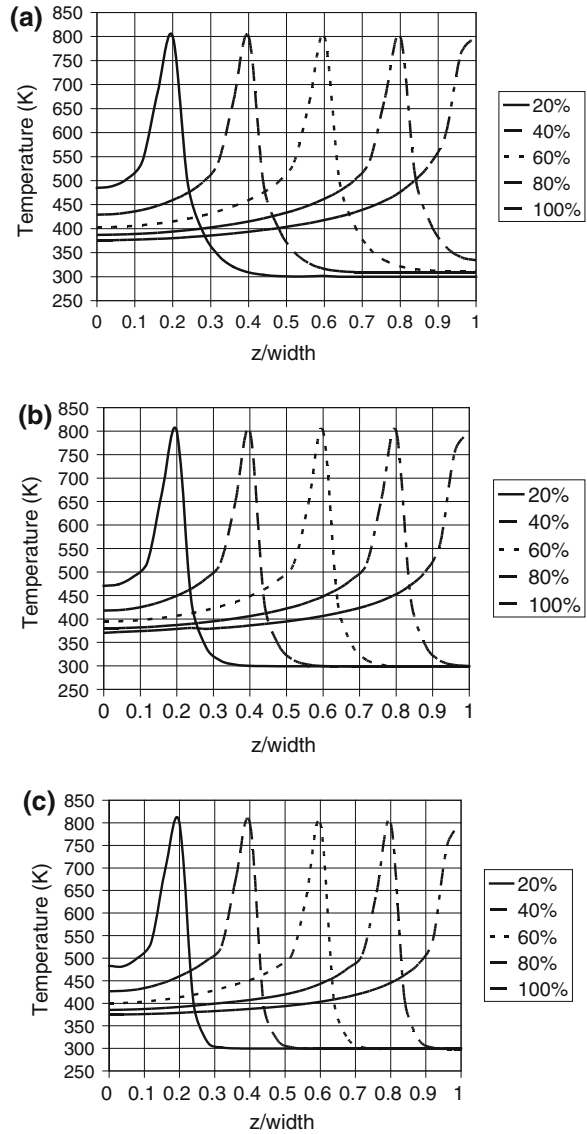
The plate material has the following properties: 53 W/m K for thermal conductivity, 520 J/kg K for specific heat,  $1.5 \times 10^{-5}$  for thermal expansion coefficient, 7,880 kg/m<sup>3</sup> for density and 0.01 for damping coefficient. At the fixed end, the displacement in all directions is always zero. The impulsive load duration is 0.01 s and was applied at a time equal to 50 % of total heating time ( $= 0.5 \times W/(\text{welding speed})$ ) after starting the heating process (Fig. 2.50).

## 2.10.2 Results and Discussion

In this case the flexural motion of the one side-heated cantilever plate is considered. A moving heat source is considered to resemble the laser heating situations in relation to welding. The influence of the heated zone on the resulting temperature field and the dynamic motion of the plate excited by an impulsive force from the free end are examined.

Figure 2.51 shows temperature distribution along the z-axis, where the heat source movement takes place, for different heating periods and moving heat source speeds, while Fig. 2.52 shows the contour plots of temperature for the same time periods and heat source speeds. Temperature rises to reach its maximum and decays sharply for all time periods and heat source speeds. However, the temperature gradient changes from low to high at temperature about 500 K. This change is more pronounced for the low speed when the heating is completed (heat source reaches to the other end along the plate width). This is because of the initial heating of the distance along the width during the movement of the heat source. Moreover, the temperature gradient in the region before the attainment of the maximum temperature is different than in the region during the decay of temperature from its maximum. This is because of the unheated region in front of the moving heat source. In this case, heat diffusion for the moving heat source to the area in front of the source is not considerable due to short time period. Consequently, temperature decays sharply in front of the moving heat source resulting in the high temperature gradient in this region. This situation is the same for all moving heat source speeds. It should be noted that in the frontal region of the moving source, gradual decay of temperature is observed, which starts at about 400 K. However, this decay changes with the heat source speed; in which case,

**Fig. 2.51** Temperature variation in the welding direction ( $z$ ) at different stages of the total welding time [32]. **a** Welding speed = 1 cm/s. **b** Welding speed = 2 cm/s. **c** Welding speed = 3 cm/s



increasing moving heat source speed enhances temperature rise and decay along the  $z$ -axis.

Figure 2.53 shows the displacement at the free end of cantilever for three moving heat source speeds. It should be noted that the displacements with and without heating situations are given for the comparison reason. The time shift between the flexural responses with heating and without heating situations is due to the time for the impacting force applied at the free end of the plate. In this case, when heat source reaches to half of the plate width the impact force was applied.

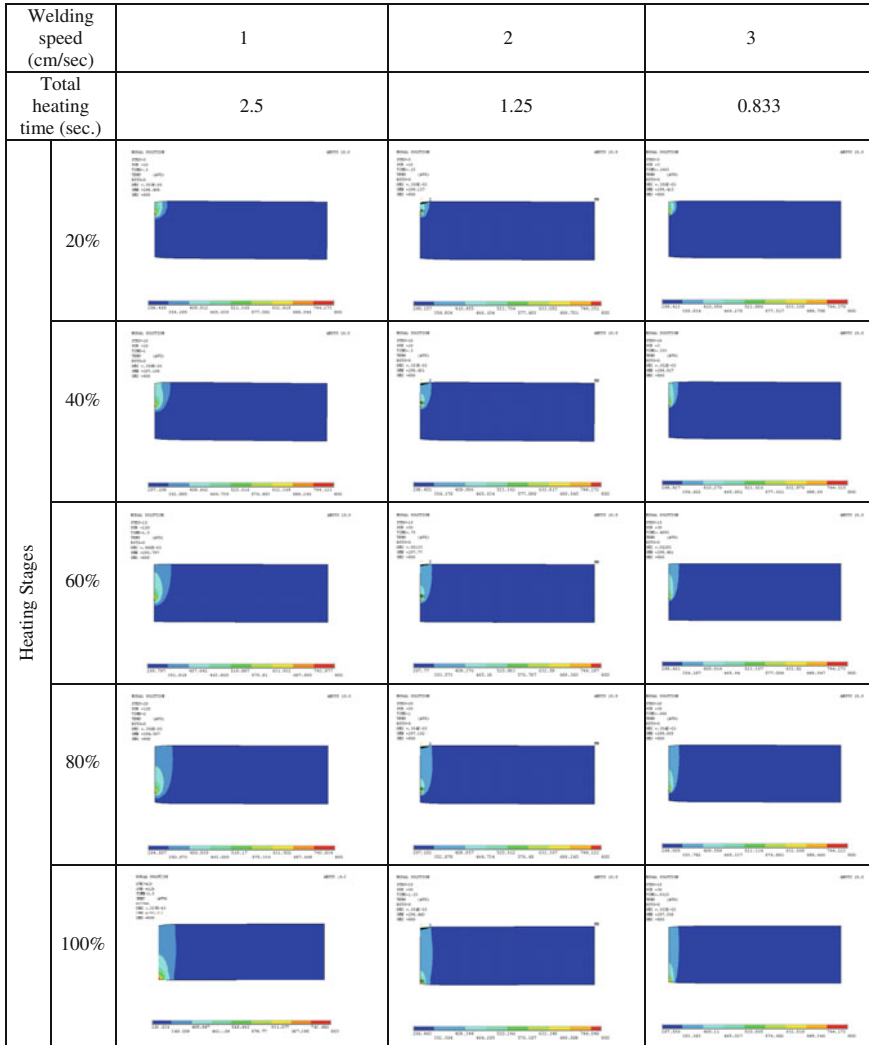
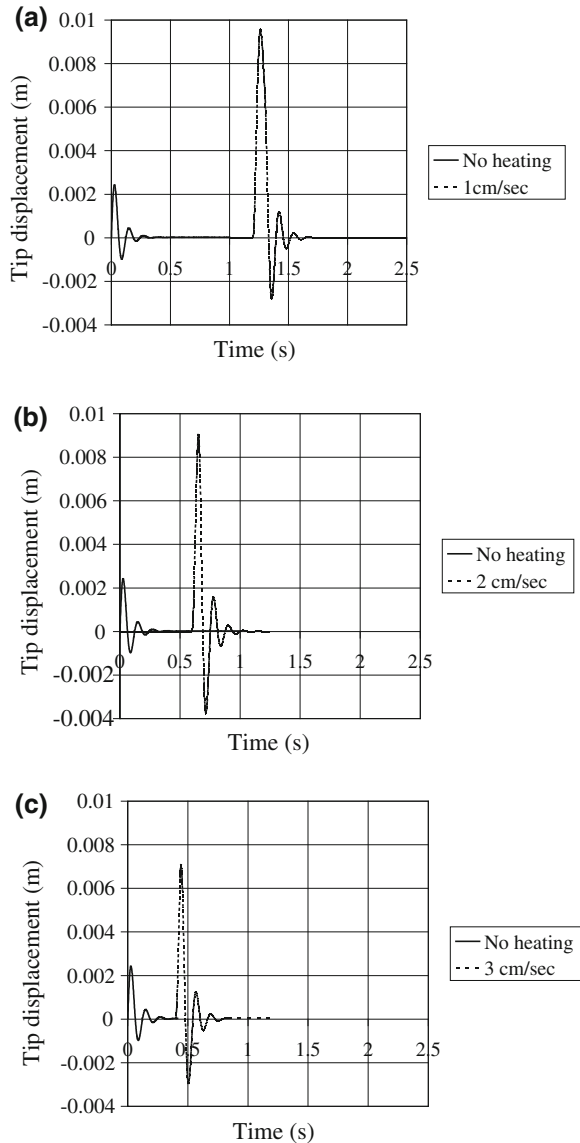


**Fig. 2.52** Temperature contours of the heated plate at different heating stages according to three welding speeds [32]

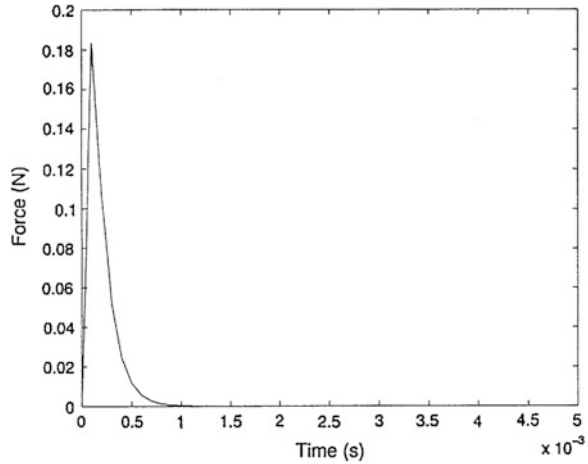
Moreover, the displacement corresponding to the heating situation is significantly larger than the without heating situation. This is because of the elastic modulus of the plate material, which changes with temperature. Once the speed of the heating source is increased, the time difference between displacements due to heating and without heating situations becomes less. This is because of the time taken for the heat source reaching at the mid of the plate width becomes less. The magnitude of the displacement reduces with increasing heat source speed. This can be explained in terms of the temperature field. In this case, heat diffusion to the solid bulk

**Fig. 2.53** Flexural response of the plate tip when the plate is heated according to different welding speeds [32].  
**a** Welding speed = 1 cm/s.  
**b** Welding speed = 2 cm/s.  
**c** Welding speed = 3 cm/s



enhances with low heat source speed due to increased time for the energy transfer via conduction from the moving heat source for the solid bulk in the plate becomes smaller for the high heat source speeds. Consequently, high temperature region extends into the solid bulk for low heat source speed. This, in turn, modifies the elastic modulus of the plate material in a large region where temperature is high. Therefore, the magnitude of displacement increases for low heat source speed due to modification of the elastic modulus in a large region of the plate.

**Fig. 2.54** Force input applied on the workpiece [33]



## 2.11 Laser Pulse Heating of Two-Layer Assembly

In the following analysis of the flexural characteristics of the two-layer assembly, the formulation and findings of the previous study [33] are considered. In this case laser evaporative heating of the cantilever workpiece consisting of two layers is considered. The first layer is Inconel 625 alloy, which can be formed by the high-velocity oxygen fuel (HVOF) coating with thicknesses in the range of 200  $\mu\text{m}$ , and the second layer is 1 mm thick stainless steel. The recoil pressure and the loading force are formulated analytically. The flexural motion of the workpiece is modelled and wave motion is predicted numerically. The simulations are repeated for four thicknesses of the first layer. The influence of the thickness layer on the displacement of the resulting flexural motion is discussed.

### 2.11.1 Heat Transfer Analysis

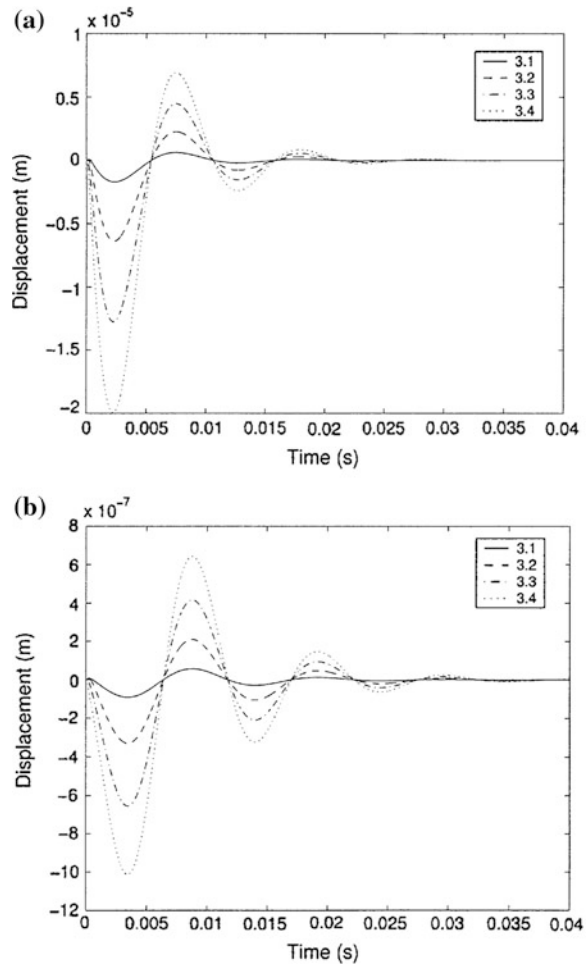
Figure 2.54 shows the normal pressure force of laser power intensity distribution. The heat transfer analysis is given above in Eqs. (2.20)–(2.24).

The pressure force acting normal to the substrate surface can be written as

$$F_0 = \int_0^{r_e} 2\pi r P dr \quad (2.92)$$

where  $r_e$  is the Radius of evaporated surface ( $r_e = 0.4 \text{ mm}$ ). The variation of normal pressure force with time is assumed to be exponential, i.e.

**Fig. 2.55** **a** Displacement response of the cantilever beam for a top layer thickness of 180  $\mu\text{m}$ . **b** Difference in displacement response of the cantilever beam for a top layer thickness of 180  $\mu\text{m}$  [33]



$$F(t) = F_0[\exp(-\beta t) - \exp(-\gamma t)]$$

where  $\beta$  and  $\gamma$  are constants.

### 2.11.2 Flexural Wave Analysis

The finite element method (FEM) is applied as a numerical tool for the analysis of flexural wave behavior for a workpiece as shown in Fig. 2.55. The rectangular finite elements for the workpieces contain pseudo-internal degrees of freedom (DOF). The internal DOF are for better representation of bending moments

generated by the external actuators and are condensed into the physical DOF using Guyan reduction technique [12].

Hamilton's principle is given by

$$\delta \int_{t_1}^{t_2} (K_i - \Pi) dt = 0 \quad (2.93)$$

$K_i$  in the above equation is the kinetic energy defined as

$$K_i = \frac{1}{2} \int_V \rho \dot{\mathbf{u}}^T \dot{\mathbf{u}} dV \quad (2.94)$$

In Eq. (2.93), the potential energy  $\Pi$  is given by

$$\Pi = - \int_V \mathbf{u}^T \mathbf{P}_b dV - \int_S \mathbf{u}^T \mathbf{P}_s dS - \mathbf{u}^T \mathbf{P}_c \quad (2.95)$$

$\mathbf{P}_b$  is the vector of body forces applied to volume  $V$ ,  $\mathbf{P}_s$  is the vector of surface force and  $\mathbf{P}_c$  is the concentrated load vector.

The following relations are defined for the finite element formulation:

$$\mathbf{u}_e = N_u \mathbf{u}_i$$

where  $N_u$  is the shape function matrix and  $\mathbf{u}_i$  is the vector of nodal displacement. The subscript 'e' in the equations stands for the element. Relating strain to displacement

$$S_e = L_u \mathbf{u}_e = [L_u N_u] \mathbf{u}_i = B_u \mathbf{u}_i$$

where  $S_e$  is the elemental strain and  $L_u$  is the differential operator which is given by

$$L_u = \begin{bmatrix} \frac{\partial}{\partial x} & 0 & 0 \\ 0 & \frac{\partial}{\partial y} & 0 \\ 0 & 0 & \frac{\partial}{\partial z} \\ \frac{\partial}{\partial y} & \frac{\partial}{\partial x} & 0 \\ 0 & \frac{\partial}{\partial z} & \frac{\partial}{\partial y} \\ \frac{\partial}{\partial z} & 0 & \frac{\partial}{\partial x} \end{bmatrix} \quad (2.96)$$

Substituting the above equations in (2.93) gives

$$M_{uu}\ddot{\mathbf{u}} + K_{uu}\mathbf{u} = \mathbf{F} \quad (2.97)$$

where the element matrices and vectors are given by

$$M_{uu} = \int_{V_e} \rho N_u^T N_u dV : K_{uu} = \int_{V_e} B_u^T c B_u dV$$

$$\mathbf{F}_e = \int_{V_e} N_u^T \mathbf{P}_b dV + \int_{S_e} N_u^T \mathbf{P}_s dS + N_u^T \mathbf{P}_c$$

For a rectangular element of size ( $2a \times 2b \times 2c$ ), the shape functions are given as

$$N_1 = \frac{1}{8} \left(1 - \frac{x}{a}\right) \left(1 - \frac{y}{b}\right) \left(1 + \frac{z}{c}\right) \quad N_2 = \frac{1}{8} \left(1 + \frac{x}{a}\right) \left(1 - \frac{y}{b}\right) \left(1 + \frac{z}{c}\right)$$

$$N_3 = \frac{1}{8} \left(1 + \frac{x}{a}\right) \left(1 + \frac{y}{b}\right) \left(1 + \frac{z}{c}\right) \quad N_4 = \frac{1}{8} \left(1 - \frac{x}{a}\right) \left(1 + \frac{y}{b}\right) \left(1 + \frac{z}{c}\right)$$

$$N_5 = \frac{1}{8} \left(1 - \frac{x}{a}\right) \left(1 - \frac{y}{b}\right) \left(1 - \frac{z}{c}\right) \quad N_6 = \frac{1}{8} \left(1 + \frac{x}{a}\right) \left(1 - \frac{y}{b}\right) \left(1 - \frac{z}{c}\right)$$

$$N_7 = \frac{1}{8} \left(1 + \frac{x}{a}\right) \left(1 + \frac{y}{b}\right) \left(1 - \frac{z}{c}\right) \quad N_8 = \frac{1}{8} \left(1 - \frac{x}{a}\right) \left(1 + \frac{y}{b}\right) \left(1 - \frac{z}{c}\right)$$

Internal DOF are added to the element to give a better representation to the bending moments caused by the piezoelectric effects. Two shape functions are defined for this purpose, which are given as follows:

$$N_9 = \frac{a^2 - x^2}{a^2} \quad N_{10} = \frac{b^2 - y^2}{b^2} \quad N_{11} = \frac{c^2 - z^2}{c^2}$$

The shape functions vanish at the element boundaries when  $x = \pm a$  and  $y = \pm b$ . The displacement vector,  $\mathbf{u}_e$ , is now expressed as

$$\mathbf{u}_e = N_u \mathbf{u}_i + X \mathbf{a}_j \quad (2.98)$$

The strain vector,  $\mathbf{S}_e$ , is now written as

$$\mathbf{S}_e = B_u \mathbf{u}_i + Y \mathbf{a}_j \quad (2.99)$$

where  $\mathbf{a}_j$  is the added generalized coordinate vector and  $X$  and  $Y$  in the above equations are given by

$$X = \begin{bmatrix} 0 & 0 & 0 \\ 0 & 0 & 0 \\ N_9 & N_{10} & N_{11} \end{bmatrix} \quad \text{and} \quad Y = L_u X = \begin{bmatrix} 0 & 0 & 0 \\ 0 & 0 & 0 \\ 0 & 0 & \frac{-2z}{c^2} \\ 0 & 0 & 0 \\ 0 & \frac{-2y}{b^2} & 0 \\ \frac{-2x}{a^2} & 0 & 0 \end{bmatrix} \quad (2.100)$$

The new matrix,  $K_{uu}^*$  is the global elastic stiffness matrix which is composed of  $[K_{uu}]_e^*$  and given by

$$[K_{uu}]_e^* = [K_{uu}]_e - [K_{ua}]_e [K_{aa}]_e^{-1} [K_{au}]_e \quad (2.101)$$

where  $[K_{ua}]_e$  and  $[K_{aa}]_e$  are partitioned stiffness matrices which is given by

$$[K_{ua}]_e = \int_V B_u^T c Y dV \quad \text{and} \quad [K_{aa}]_e = \int_V Y^T c Y dV \quad (2.102)$$

where C is a constant matrix. Hence the final equation becomes

$$M_{uu} \ddot{u} + K_{uu}^* u = F \quad (2.103)$$

### 2.11.2.1 Initial and Boundary Conditions

Initially, the displacements are set to zero for the cantilever case. Also, at  $x = 0$ , i.e. at the fixed end, the displacement is always zero, which is given as at  $x = 0$ ,  $u = 0$ .

### 2.11.2.2 Method of Solution

In the finite element analysis, the workpiece is divided into 16 elements where the number of divisions are uniform in both  $x$  and  $z$  directions and the thickness is considered to be uniform. The elemental stiffness and mass matrices are determined, which are then assembled to yield the global matrices.

### 2.11.2.3 State-Space Method

The equation of motion is converted into state-space form. For a deterministic system, it is given as

$$\dot{z} = Az + BF \quad (2.104)$$

$$u = Cz \quad (2.105)$$

where  $z$  is the complete state vector and  $u$  is the required displacement.  $A$ ,  $B$  and  $C$  are the system, input and output matrices respectively, given as

$$A = \begin{bmatrix} 0 & I \\ -M_{uu}^{-1}K_{uu} & -M_{uu}^{-1}C_{uu} \end{bmatrix} \quad \text{and} \quad B = \begin{bmatrix} 0 \\ -M_{uu}^{-1}F \end{bmatrix} \quad (2.106)$$

where  $C_{uu}$  is the proportional damping introduced through the following equations:

$$C_{uu} = \alpha M_{uu} + \beta K_{uu}$$

$\alpha$  and  $\beta$  in the above equation are the damping coefficients.  $C$  in Eq. (2.105) is a matrix defining the location where displacement is required.

These matrices are introduced through Matlab code and simulated for a given force and time interval to obtain the displacement  $u$  at various locations.

#### 2.11.2.4 Determination of Stresses

The strain for a given element is given by  $S_e = B_u u_e$ , where  $B_u = L_u N_u$  and  $N_u$  is given by

$$N_u = \begin{bmatrix} N_1 & 0 & 0 & N_2 & 0 & 0 & N_3 & 0 & 0 & N_4 & 0 & 0 & N_5 & 0 & 0 & N_6 & 0 & 0 & N_7 & 0 & 0 & N_8 & 0 & 0 \\ 0 & N_1 & 0 & 0 & N_2 & 0 & 0 & N_3 & 0 & 0 & N_4 & 0 & 0 & N_5 & 0 & 0 & N_6 & 0 & 0 & N_7 & 0 & 0 & N_8 & 0 & 0 \\ 0 & 0 & N_1 & 0 & 0 & N_2 & 0 & 0 & N_3 & 0 & 0 & N_4 & 0 & 0 & N_5 & 0 & 0 & N_6 & 0 & 0 & N_7 & 0 & 0 & N_8 & 0 \end{bmatrix}$$

The stress is obtained using the stress-strain relationship which is given by  $\sigma_e = ES_e$ . These elemental stresses are properly mapped with respect to global node numbering to obtain the global stress. The so obtained global stress  $\sigma$  is given by

$$\sigma = \begin{bmatrix} \sigma_x \\ \sigma_y \\ \tau_{xy} \\ \tau_{yz} \\ \tau_{xz} \end{bmatrix} \quad (2.107)$$

Hence, the equivalent stress is given by

$$\sigma_{eq} = \sqrt{0.5 [(\sigma_x - \sigma_y)^2 + (\sigma_y - \sigma_z)^2 + (\sigma_x - \sigma_z)^2]} \quad (2.108)$$

**Table 2.13** Mechanical properties of steel and Inconel 625 used in simulations

	Steel	Inconel 625
E (Pa)	$2.068 \times 10^{11}$	$205.5 \times 10^9$
$\rho$ (kg/m <sup>3</sup> )	7,830	8,440
$\nu$	0.3	0.312

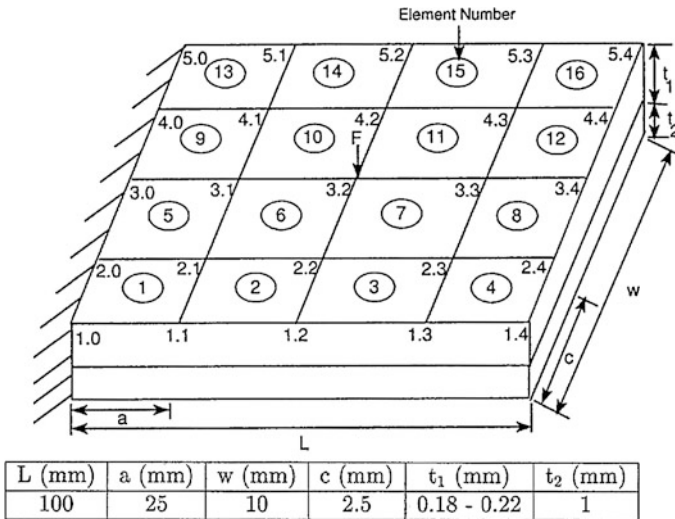
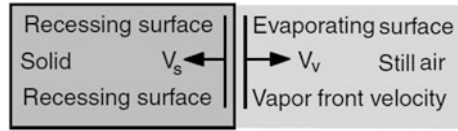


**Fig. 2.56** Layout and dimensions of the workpiece employed in simulations [33]

### 2.11.3 Results and Discussions

In this case laser ablation of the substrate surface and recoil pressure generation across the vapor front and the workpiece surface are presented. The flexural motion of the workpiece with a cantilever arrangement is modelled and frequency as well as magnitude of the wave are predicted. The workpiece is considered as consisting of two layers. The first layer is Inconel 625 alloy with thicknesses of about 200 nm, which resembles the coating formed by HVOF, while the second layer is stainless steel with 1 mm thickness. The simulations are repeated with different thicknesses of the first layer. This provides information on the variation of the flexural wave characteristics with layer thickness and enables a prediction to be made of the coating thickness without destructive testing. Since the laboratory facilities are limited at present, the authors could not conduct the experiment in this regard. However, a high-speed laser velocimeter based on the reflection of the coated surface may be used to collect the beam data for the frequency and amplitude measurements of the workpiece oscillation; i.e. predictions may be validated using the measurement. Table 2.13 gives the properties of the layers employed in the simulations. Figure 2.54 shows the temporal variation of the

**Fig. 2.57** Schematic view of interface [34]



pressure force (loading force) determined from the recoil pressure and used in the analysis. The peak value of the load is in the order of 0.19 N.

Figure 2.55a shows displacement of the workpiece with time at different locations on the workpiece (where Fig. 2.56 shows the location and dimensions of the elements on the workpiece) while Fig. 2.55b shows the displacement difference for the first layer thickness of 180  $\mu\text{m}$ . The displacement difference corresponds to the displacement difference due to the workpiece with and without a first layer. The magnitude of displacement at different location changes; i.e. displacement corresponding to the location close to the free end of the workpiece (location 3.4 in Fig. 2.56) is higher than that corresponding to the fixed end (location 3.1). The displacement decays with time due to the cantilever arrangement of the workpiece. The maximum magnitude of displacement is of the order of 2 mm and the period of the wave motion is of the order of 0.012 s. The displacement difference (Fig. 2.55b) has a slightly higher period than that of the displacement, but its maximum magnitude is less than 1 mm. Consequently, the first layer, which is 180  $\mu\text{m}$  thick, results in a slight increase in frequency but a substantial increase in magnitude of the wave motion; i.e. the value increases to almost twice.

## 2.12 3D Analysis of Laser Evaporative Heated Cantilever Workpiece

The mathematical analysis and the findings for the 3D analysis of laser evaporative heated cantilever workpiece are presented below in line with the previous study [34]. The present case consider modeling the flexural motion and stress field inside the substrate material. The recoil pressure is integrated over an irradiated area to obtain a normal force, which initiates the flexural motion of the workpiece. When solving the wave and stress equations finite element method (FEM) is adopted. Steel plate is selected as a workpiece material while copper element is introduced in the workpiece to examine its influence on the flexural motion and stress field. In the analysis, cantilever arrangement of the workpiece is considered.

### 2.12.1 Heat Transfer Analysis

The irradiated surface due to receding surface is shown in Fig. 2.57. The heat transfer analysis is given above in Eqs. (2.20)–(2.24).

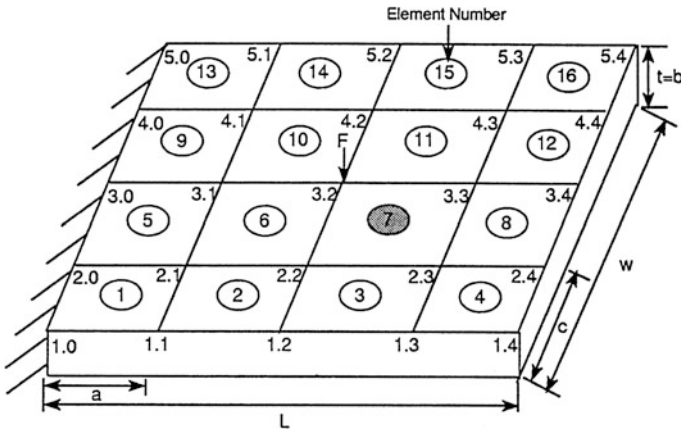
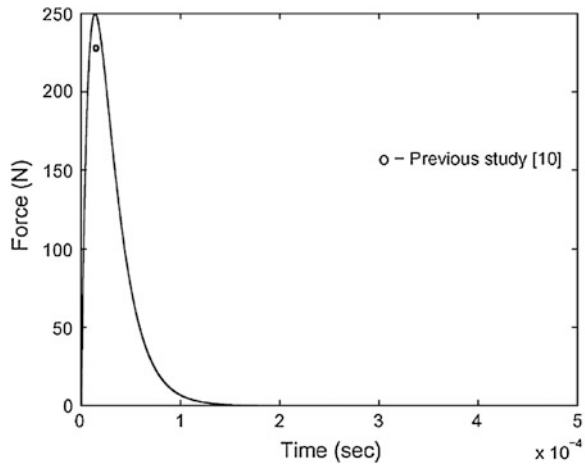


**Fig. 2.58** Schematic view of cantilever workpiece showing the seventh element as copper.  $a = 0.025$  m,  $c = 0.0025$  m;  $L = 0.1$  m,  $t = 0.002$  m,  $w = 0.01$  m [34]

**Table 2.14** Mechanical properties of steel and copper used in simulations

	Steel	Copper
E (Pa)	$2.068 \times 10^{11}$	$1.3 \times 10^{11}$
$\rho$ (kg/m <sup>3</sup> )	7,830	8,920
$\nu$	0.3	0.34

**Fig. 2.59** Force response [34]



The pressure predicted is given in the previous study [6]

$$P_v = 1.82 \times 10^{-3} \frac{\sqrt{C_p T_s I_0}}{[C_p(T_s - T_0) + L_{ev}]} \quad (2.109)$$

The unit in Eq. (2.109) is bar.

**Fig. 2.60** Displacement response of the cantilever beam [34]

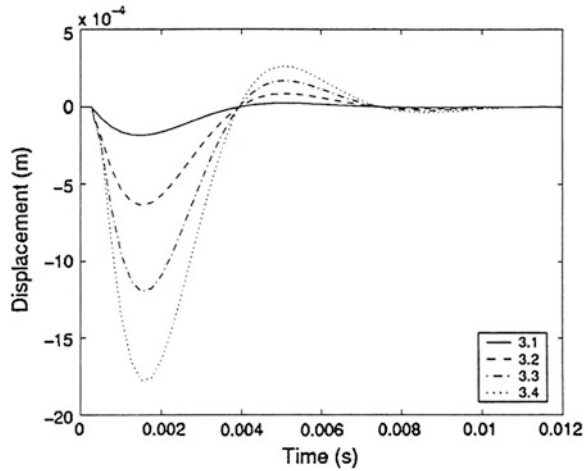
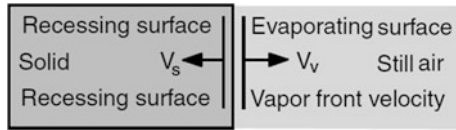


**Fig. 2.61** Schematic view of interface [35]



### 2.12.2 Flexural Wave Analysis

FEM is applied as a numerical tool for the analysis of flexural wave behavior for a workpiece as shown in Fig. 2.58. Flexural wave analysis is given above in Eqs. (2.93)–(2.108).

### 2.12.3 Results and Discussions

Laser induced flexural motion in cantilever steel plate is analyzed. Pressure force is considered to initiate the flexural motion of the workpiece. Table 2.14 gives the material properties used in the simulations. Figure 2.59 shows the variation of pressure force with time. The peak pressure force is in the order of 250 N, which acts normal to the surface of the workpiece. Since the evaporation process is time dependent, variation of pressure force with time is assumed as exponential. Figure 2.60 shows the temporal variation of displacement at different locations in the workpiece (elements) due to flexural motion while Fig. 2.58 shows the location of the elements. The magnitude of displacement is high at the free end of the workpiece and it is lowest close to the fixed end. This is due to the cantilever arrangement of the workpiece. Moreover, the frequency of oscillation is in the

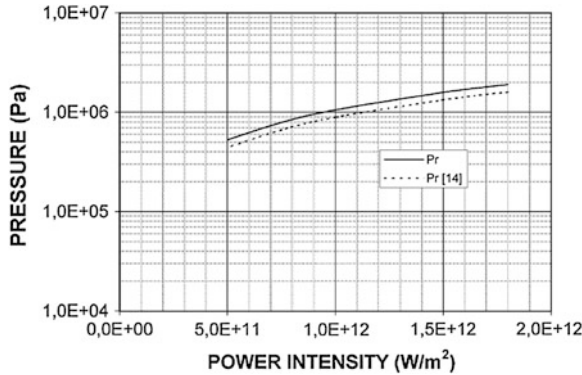


Fig. 2.62 Interface pressure with power intensity [35]

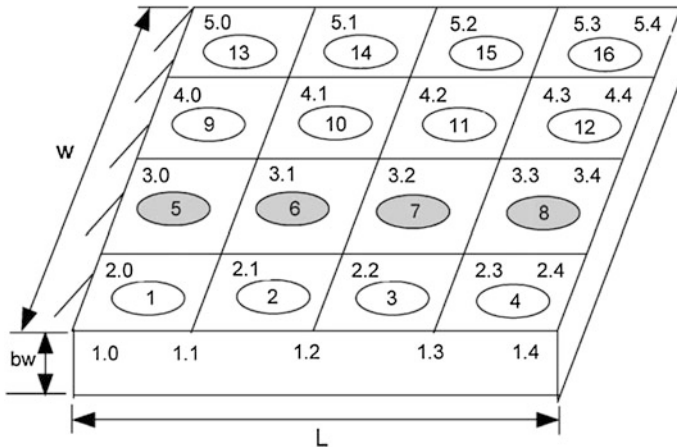


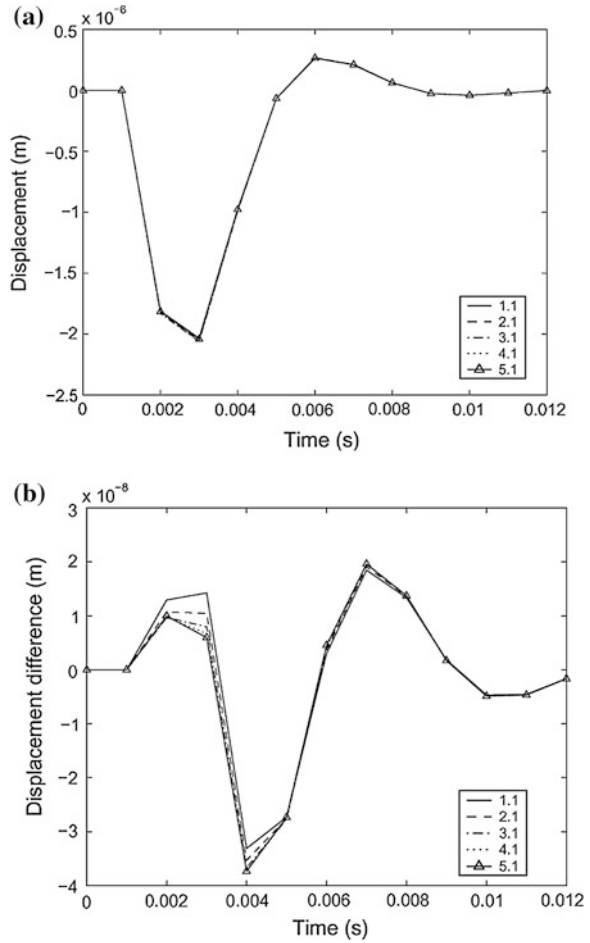
Fig. 2.63 Cantilever workpiece finite element model [35]

order of 0.2 kHz, provided that the oscillation dies out as the time progresses to 12 ms. The maximum displacement in the order of 20 μm is resulted at around 3 ms. Due to the flexural motion of the workpiece, the stresses are developed.

### 2.13 Laser Induced Flexural Wave: Aluminum in Steel Substrate

In the following analysis of the flexural characteristics of the beam, the formulation and findings of the previous study [35] are considered. Laser induced flexural wave generation is considered in this case. The evaporation of the surface

**Fig. 2.64** **a** Displacement response in the transverse direction when aluminum is in the sixth position for the first points. **b** Difference in transverse displacement when aluminum is in the sixth position for the first points [35]



is modeled and the interface pressure acting at the vapor–solid interface is formulated. The flexural wave analysis is carried out in three-dimensional domain and resulting surface displacement is obtained for cantilever arrangement. The simulations are carried out for steel substrate with existence of locally imbedded single aluminum cell in the substrate material. In order to investigate the effect of aluminum cell on the resulting flexural wave displacement, the location of the cell is varied in the substrate material.

### 2.13.1 Heat Transfer Analysis

The schematic view of the interface is shown in Fig. 2.61. The heat transfer analysis is given above in Eqs. (2.20)–(2.24).

The irradiated surface due to receding surface is shown in Fig. 2.61.

The pressure predicted is given in the previous study [6].

$$P_v = 1.82 \times 10^{-3} \frac{\sqrt{C_p T_s I_0}}{[C_p(T_s - T_0) + L_{ev}]} \quad (2.110)$$

The unit in Eq. (2.110) is bar.

### 2.13.2 Flexural Wave Analysis

Flexural wave analysis is given above in Eqs. (2.93)–(2.108).

### 2.13.3 Results and Discussions

The flexural wave analysis during laser evaporation of the steel surface is considered. The interface pressure is formulated and the pressure force acting normal to the workpiece is employed as a loading force for the flexural wave generation. The geometric arrangement of the workpiece is a cantilever arrangement. The effect of locally imbedded aluminum element on the workpiece displacement is investigated. In order to comprehend the influence of the aluminum element on the temporal and spatial resolution of the displacement of the workpiece, the differences in the surface displacements corresponding to with and without additional element (aluminum cell) is considered, i.e.,

$$D_{\text{difference}} = D_{\text{without add. element}} - D_{\text{with add. element}}$$

where  $D_{\text{difference}}$  is the displacement difference of the surface,  $D_{\text{without add. element}}$  the displacement of the surface when there is no additional aluminum element imbedded in the workpiece and  $D_{\text{with add. element}}$  the displacement of the surface when the additional element is locally added in the substrate material.

Figure 2.62 shows the pressure predicted from the present and the previous studies [14]. The equation derived previously predicts the interface zone pressure as high as 500 kPa. The values of the pressure predicted from the present study agree well with the previous results. The finite element model of the cantilever workpiece is shown in Fig. 2.63.

Figure 2.64a shows the temporal variation of the surface displacement due to flexural wave motion at different mesh points and the differential element is at sixth location (Fig. 2.63). The displacement attains high values at certain periods, provided that it reaches its peak value at about 3 ms after the laser pulse ends. Moreover, as the time progresses, the magnitude of displacement reduces. The displacement corresponding to different locations in the transverse direction does not vary considerably. This indicates that the flexural motion of the surface at each

location along the transverse direction is almost identical. The displacement difference due to with and without aluminum element is shown in Fig. 2.64b for the same condition of Fig. 2.64a. The displacement difference reaches its peak value almost 4 ms after the laser pulse ends. Consequently, the time at which the peak values of displacement and displacement difference occur does not coincide. This is because of the aluminum element, which modifies slightly the mode of flexural motion of the surface.

## References

1. B.S. Yilbas, F. Mahmood, Flexural waves generated due to pressure force during the laser induced evaporation process. *J. Laser Appl.* **13**(3), 118–124 (2001)
2. B.S. Yilbas, A.Z. Sahin, R. Davies, Laser heating mechanism including evaporation process initiating laser drilling. *Int. J. Mach. Tools Manuf.* **35**, 1047–1062 (1995)
3. Y.V. Afanasev, O.N. Krokhin, Vaporization of matter exposed to laser emission. *Sov. Phys. JETP* **25**, 639–647 (1967)
4. B.S. Yilbas, Z. Yilbas, Some aspects of laser-metal vapour interaction. *Pramana J. Phys.* **31**, 365–381 (1988)
5. B.S. Yilbas, A.F.M. Arif, Laser short pulse heating and elastic–plastic wave generation. *Jpn. J. Appl. Phys.* **39**, 5879–5888 (2000)
6. M. Hugenschmidt, R. Schmitt, Pulsed laser-targets effects and high resolution process diagnostics. *Opt. Quantum Electron.* **27**, 1231–1242 (1995)
7. J.F. Doyle, *Wave Propagation in Structures* (Springer, New York, 1989)
8. F. Mahmood, Transient response of varying thickness Timoshenko beam under point load. M.Sc. thesis, Mechanical Engineering Department, KFUPM, Dhahran, 1999
9. B.S. Yilbas, S.J. Hyder, S.Z. Shuja, Flexural wave generation and stress analysis during laser evaporative heating of steel. *Proc. Inst. Mech. Eng. [C]* **216**, 531–542 (2002)
10. B.S. Yilbas, M. Sami, A. Al-Ferayedhi, Closed form and numerical solutions to the laser heating process. *Proc. Inst. Mech. Eng. [C]* **212**(C2), 141–151 (1998)
11. B.G. Loh, P.I. Ro, Changing the propagation direction of flexural ultrasonic progressive waves by modulating excitation frequency. *J. Sound Vib.* **238**, 171–178 (2000)
12. R.J. Guyan, Reduction of stiffness and mass matrices. *Am. Inst. Aeronaut. Astronaut. J.* **3**, 380–386 (1965)
13. B.S. Yilbas, M. Faisal, S.Z. Shuja, A.F.M. Arif, Laser pulse heating of steel surface and flexural wave analysis. *Opt. Lasers Eng.* **37**, 63–83 (2002)
14. S.Z. Shuja, B.S. Yilbas, Gas-assisted repetitive pulsed heating of a steel surface. *Proc. Inst. Mech. Eng. [C]* **212**, 741–757 (1998)
15. T.B. Gotski, M.Y. Hussaini, J.L. Lumley, *Simulation and Modeling of Turbulent Flows* (Oxford University Press, New York, 1996)
16. C.B. Scruby, L.E. Drain, *Laser Ultrasonics: Techniques and Applications* (Adam Hilger, Bristol, 1990)
17. F.P. Incropera, D.P. Dewitt, *Introduction to Heat Transfer F Appendix* (Wiley, New York, 1985), pp. 667–696
18. H.K. Versteeg, W. Malalasekera, *An Introduction to Computational Fluid Dynamics: The Finite Volume Method* (Longman Scientific and Technical, New York, 1995)
19. S.Z. Shuja, Simulation of three-dimensional gas-assisted heating of solid substance. Ph.D. thesis, Mechanical Engineering Department, KFUPM, Dhahran, 1998
20. B.S. Yilbas, Laser heating process and experimental validation. *Int. J. Heat Mass Transf.* **40**(5), 1131–1143 (1997)

21. S.V. Patankar, *Computer Analysis of Fluid Flow and Heat Transfer* (Swansea, Pinridge, 1981), pp. 223–252 (Chap. 8)
22. K.J. Bathe, *Finite Element Procedures* (Englewood Cliffs, NJ, Prentice-Hall, 1996), pp. 148–192 (Chap. 6)
23. B.S. Yilbas, S.J. Hyder, Laser pulse heating and flexural wave generation during treatment of metallic surfaces. *J. Mater. Process. Technol.* **141**, 1–8 (2003)
24. B.S. Yilbas, J. Hyder, Flexural motion due to laser ablation: influence of force location on the flexural motion. *Proc. Inst. Mech. Eng. [C]* **218**(12), 1411–1420 (2004)
25. B.S. Yilbas, J. Hyder, Influence of layers on flexural motion of multilayer assembly due to laser ablation process. *Proc. Inst. Mech. Eng. [C]* **217**, 945–954 (2003)
26. T. Al-Zaharnah, B.S. Yilbas, Effect of heat transfer on the flexural characteristics of cantilever plate heated at fixed end. *J. Mech.* **25**(1), 1–8 (2009)
27. ANSYS, Inc., Theory Reference, Release 10.0
28. I.T. Alzaharnah, S. Al-Kaabi, B.S. Yilbas, Effect of temperature field on flexural wave characteristics of a bar resembling welding to rigid body. *Adv. Mater. Res.* **83–86**, 1212–1219 (2010)
29. I.T. Alzaharnah, B. S Yilbas, Investigation into flexural characteristics of a bar subjected to local heating: the effect of heat source location. *Proc. IMechE. [B]* **222**, 1355–1362 (2008)
30. W.T. Thomson, M.D. Dahleh, *Theory of Vibration with Applications*, 5th edn. (Prentice Hall, Englewood Cliffs, NJ, 1998)
31. A. Meirovitch, *Elements of Vibration Analysis*, 2nd edn (McGraw-Hill Book Company, 1986)
32. I.T. Alzaharnah, B.S. Yilbas, S.A. Al-Kaabi, Flexural characteristics of a laser welded cantilever plate: influence of speed of the heating source. *Lasers Eng.* **18**, 337–350 (2008)
33. B.S. Yilbas, S.J. Hyder, Analysis of flexural wave due to laser heating pulse: two-layer assembly case. *Proc Inst. Mech. Eng. [C]* **216**, 1165–1174 (2002)
34. S.J. Hyder, B.S. Yilbas, S.Z. Shuja, Flexural Motion in laser evaporative heated cantilever workpiece: three-dimensional analysis. *Opt. Quant. Electron.* **35**, 111–128 (2003)
35. S.J. Hyder, B.S. Yilbas, S.Z. Shuja, Laser induced flexural wave analysis: an aluminum element in steel substrate. *J. Mater. Process. Technol.* **136**, 24–34 (2003)

## Chapter 3

# HVOF Coating and Characterization

**Abstract** HVOF Coating is one of the thermal barrier coatings to protect surfaces from high temperature, corrosion, and erosion environments. Coating characteristics including thickness, metallurgy, elemental composition, and morphology play an important role in practical applications. In this chapter, a brief description of HVOF coating process and coating characteristics is presented. The practical applications of HVOF coating and coating properties are also included in detail.

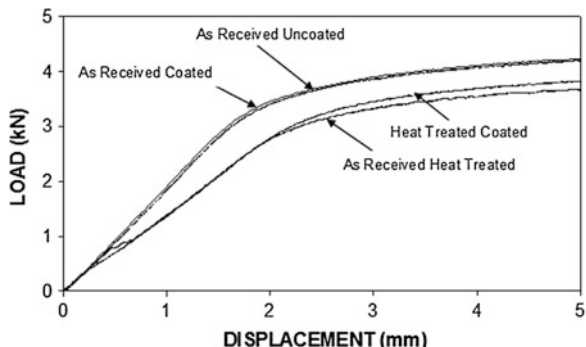
**Keywords** HVOF coating · Microstructure · Morphology · Mechanical properties

### 3.1 Single Layer HVOF Coating and Characterization

High Velocity Oxy-Fuel (HVOF) coatings find wide application in industry. HVOF process protective coating of metallic surface from the harsh environment such as high temperature, corrosion and wear environments. HVOF process is involved in thermal spraying of powder onto the surface through which the coating is resulted. The mechanical anchoring is the only process to bond the coating to the base material; consequently, a care is taken to improve the bonding strength between the coating and the base material during the HVOF process. The powders with carbide content are favorable for wear applications and nickel base powders are used for the corrosion protection. In the case of the wear applications, carbide and molybdenum base alloys are demanding.

The results and discussions are classified according to the mechanical tests carried out in the present work. Therefore, the discussions of the findings are given under the appropriate headings in line with the previous studies [1–4].

**Fig. 3.1** Load and displacement characteristics of the workpiece after three-point bend tests [1]



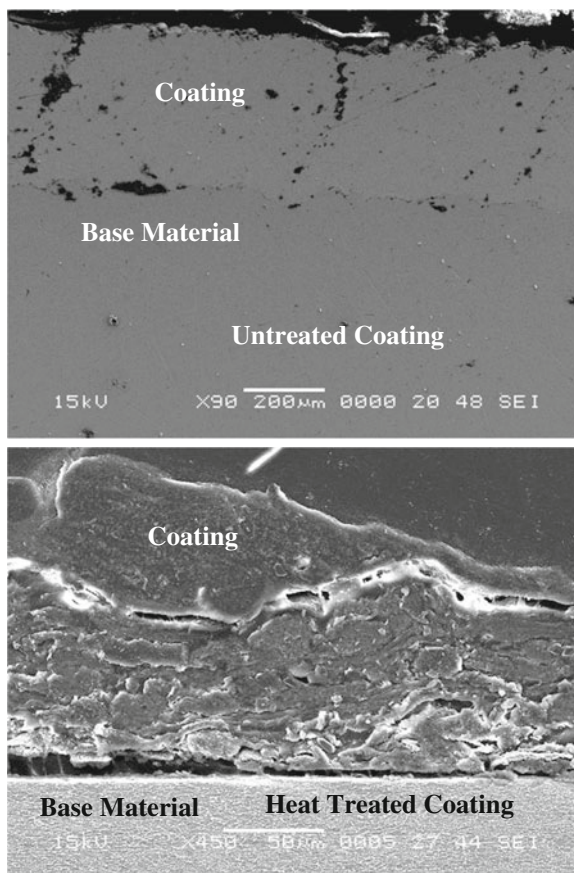
### 3.1.1 The Point Bending Tests

The results presented for three-point bending tests cover HVOF coating of AM-DRY 9954 powders on Ti-6Al-4V alloy. The some of the HVOF coated surfaces are subjected to the heat treatment prior to the tests to resemble the gas turbine applications. The data obtained from the finite element analysis are also provided in the discussions in line with the previous study [5].

The elastic-plastic behavior of the workpiece with coating and without coating as well as with heat treatment is demonstrated in Fig. 3.1. The data for three-point bend tests are obtained under the constant strain rate bending. As-received uncoated and heat treated uncoated workpieces show similar elastic-plastic behavior while coated workpieces behaves slightly different in such a way that the formation of the plastic region takes place at low load levels for heat treated coated samples for the same flexural displacement. This indicates that heat treatment has an effect on the coating, since the heat treated uncoated and as-received uncoated workpieces behave similarly, i.e., toughness of the coating changes slightly after the heat treatment. The gradual deformation at interface of the substrate material could relieve the stress levels while contributing to the stress relaxation during the tests. The compressive stress generated at the top surface does not give rise to the coating such as peeling due to elastic strain energy stored in the coating.

Since the coated surface is placed at the bottom surface of the workpiece, where the three-point bend indented is applied, the coating is subjected to tensile-shear force only. Therefore, the main failure in the coating occurs because of the tensile-shear deformation, particularly coating-substrate material interface. The cracks in the coating is formed due to the tensile load and initiated at the free surface of the coating as well as oxide sites in the coatings. Under the tensile-shear loading, delamination above the plastically deformed region is occurred. It should be noted that during the thermal spraying process, formation of oxidation is expectedly high in the free surface of the coating. This, in turn, results in differences in the coating stiffness. Consequently, high oxide content in the surface region of the coating triggers early crack initiation and propagation along the coating and the substrate material interface. Development of internal stress, due to tensile-shearing force,

**Fig. 3.2** Coating cross-section prior and after the heat treatment process [1]



creates local stress concentrations, particularly at the defect sites in the region of coating-substrate interface. In this case, the defect site has a significant effect on the failure mechanism. It should be noted that stress concentrations at the defect sites are, in general, higher than the mean internal stresses. When the critical stress for crack propagation is reached in the defect sites, particularly at the interface, the entire coating fails and peels off from the workpiece surface. If the crack propagation is limited within the local region, the fracture of the coating is resulted; in which case, internal stress in the coating is relaxed around the crack sites. If the energy used for the crack propagation is dissipated, the crack cannot spread into the substrate material.

Figure 3.2 shows SEM micrographs of coating prior and after the heat treatment process. The coating consists of lamellar structure with existence of some small voids between the splats. Some voids are distributed randomly in the coating while resulting in overall 3 % porosity in the coating. Oxides around some splats are evident due to the oxidation of the sprayed powders during in-flight prior to

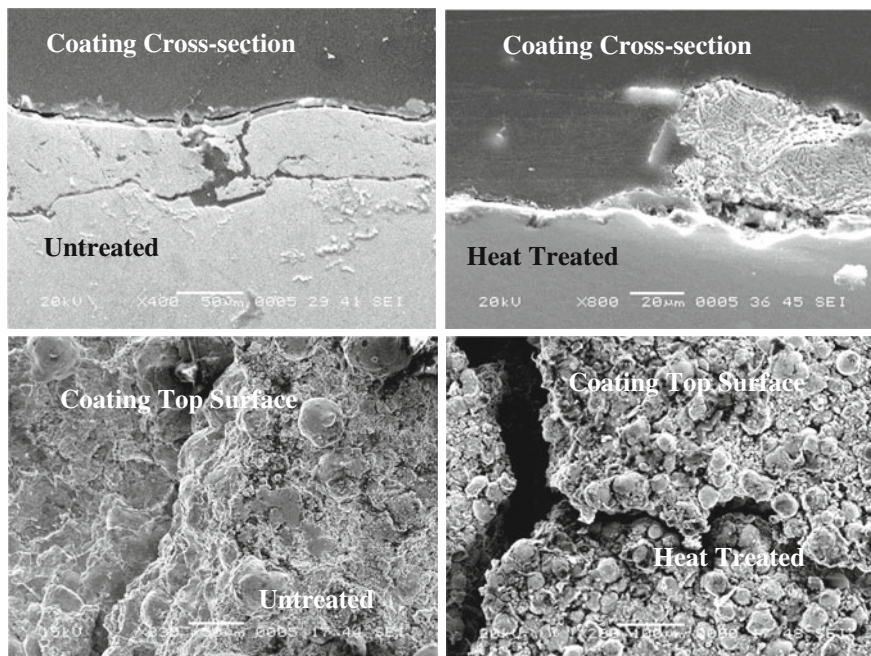


**Fig. 3.3** Coat cross-section and *top* view of coated surface after three-point bending tests [1]

their impact at the substrate surface. In addition, some stringers like dark inclusions are also observed, which compose of brittle oxide particles in the coating.

Figure 3.3 shows SEM micrographs of the tensile surface as well as the cross-section of the workpiece after the three-point bending tests. Multi-crack deformation in the coating occurs, which demonstrates that coating does not conform to the plastic deformation in the substrate material. In some regions, crack spacing is small because of the sliding and splitting deformation taking place in the coating. However, when the crack spacing is large, total elimination of coating is resulted (peeling off from the substrate surface) due to shear deformation at coating-substrate interface. In addition, the coating structure is brittle and no sign of plastification is observed. The metallic particles (splats) de-bond mainly through their oxide interfaces. The elongated particles, particularly oxide brittle particles, promote a high stress concentration and crack initiation. The adhesion failure is also observed resulting in separation of the substrate surface from the coating. In the case of heat treated workpieces, thermal stress generated along the coating-substrate interface, owing to differences in thermal expansion of both materials, influences significantly adherence of coating to the substrate material, despite the fact that gradual cooling in air ambient is adopted in the cooling cycle of the heat treatment process. Figure 3.4 shows load-displacement curves obtained from the experiment and simulation. It can be observed that both curves are in agreement, which in turn lead to realistic results for stress and strain predictions.

**Fig. 3.4** Force versus displacement behavior obtained from three point experiments and used in the FEM (ANSYS) simulations [1]

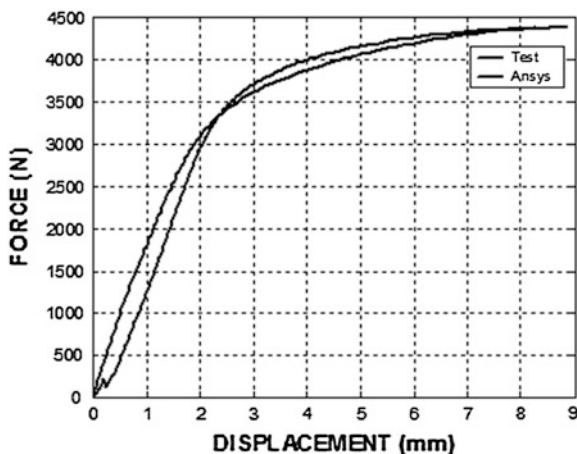
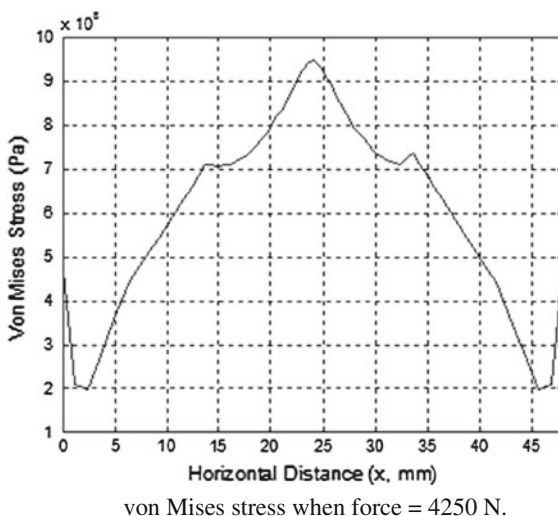
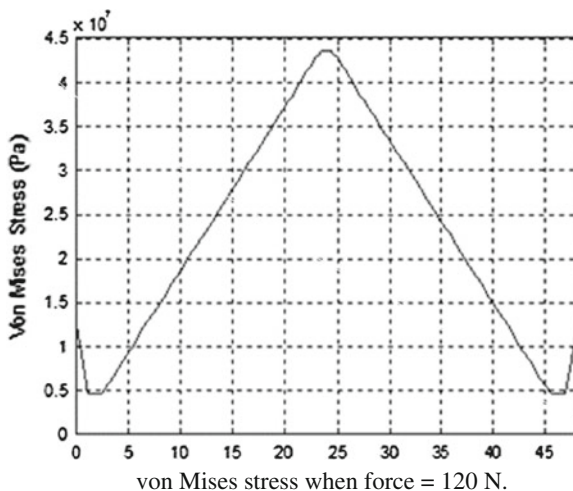


Figure 3.5 shows three von-Mises stresses corresponding to three load conditions at coating substrate interface. The first load condition corresponding to the elastic region while second and third load levels are in the elasto-plastic and plastic regions. In the elastic region, von-Mises stress is the maximum at the point of maximum workpiece deflection. The magnitude of von-Mises stress is considerably less than the elastic limit of the coating and the substrate material. In the case of high load levels, the maximum magnitude of von-Mises stress extends along the horizontal direction with its magnitude exceeding the elastic limit of the coating and base material. This, in turn, results in multi-cracking of the coating within the region of the maximum deflection. This situation can also be observed from Fig. 3.2. As the load level increases, von-Mises stress increases sharply in the region of the maximum deflection. The extension of high magnitude of von-Mises stress continues at the coating interface. This causes elongated cracks to be formed in the deflection region of the coating. Although stress realization at coating interface is resulted due to elongated cracks, continuation of bending load results in severe damage in the coatings such that partial peeling of the coating from the base material surface is resulted.

### 3.1.2 Fatigue Tests

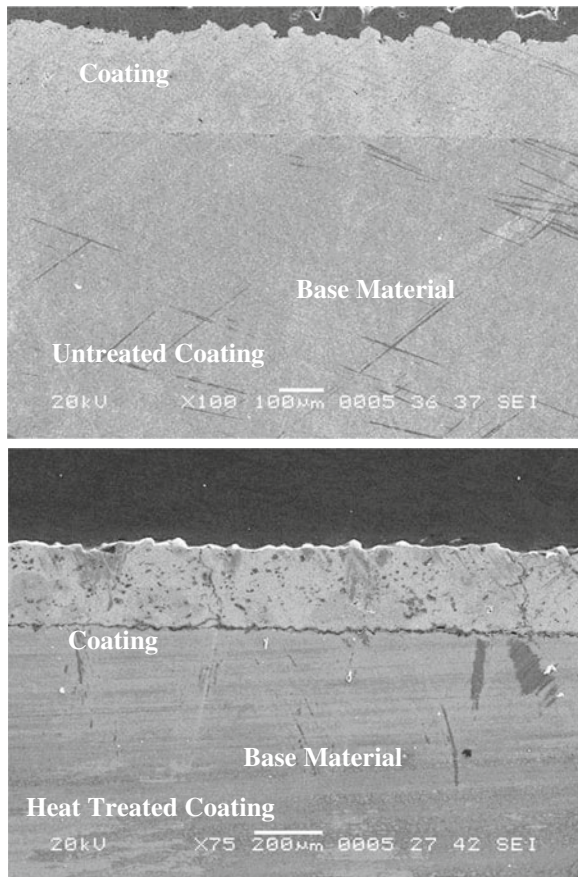
Fatigue properties of HVOF AMDRY 9954 on to the titanium alloy (Ti-6Al-4V) prior and after heat treatment are presented in line with the previous study [5]. Figure 3.6 shows SEM micrograph of coating cross-section. The coating thickness within the range of 250  $\mu\text{m}$  is achieved. Lamella structure is observed due to multi-pass spraying process. Partially melted particles are evident appearing as rounded shapes and their distribution is random in the coating. Moreover, partially scattered small pores are observed and the porosity of the coating varies within

**Fig. 3.5** von Mises stress at different load conditions [1]



2–4 %. Due to high temperature spraying process, oxidation of some splats occurs in-flight to impacting to surface. This is because of the content of the powder particles which contain chromium. Dark inclusions in the coating are the oxide compounds and, particularly, stringers like oxides are observed in between the splats. High oxygen content causes the scattered oxide particles de-bond through their interfaces in the coating. This situation occurs mainly in chromium oxides. Consequently, elongated brittle oxides (stringers like oxides) enhance stress concentration and crack initiation [6]. Since the coated workpieces are annealed in the furnace at 735 °C, small thickness of the oxide scale is formed at the free surface of the coating.

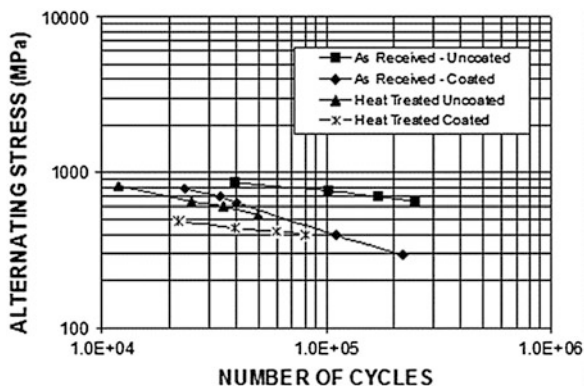
**Fig. 3.6** SEM micrograph of coating cross-section prior and after heat treatment [2]



To perform the fatigue test, initially it is ramped to mean load level and then a sinusoidal loading with a frequency of 20 Hz at a stress ratio  $R = 0.1$ . The maximum cyclic stress ranged approximately from 50 to 90 % of tensile strength of the material. As received and coated as well as heat treated and coated heat treated samples were tested at different maximum alternating stresses, which depend upon the yield strength of the workpieces. Therefore, 80, 70, 65, 40 % of the ultimate tensile stress was used as maximum alternating stress in the fatigue tests. In this case, the maximum stresses for as received workpieces ranged 859–553 MPa, for as received and coated workpieces ranged 788–394 MPa, for as received heat treated ranged 805–537 MPa, and for coated and heat treated ranged 493–394 MPa. It should be noted that tensile stress is determined from load over the cross-sectional area of the workpiece, in which coating area was included.

However, Alternating stress ( $S$ ) and cycle of failure ( $N$ ) can be related through Basquin relation, i.e.:

**Fig. 3.7** Logarithmic scale of alternating stress with number of cycles for different fatigue tested workpieces [2]



$$S = AN^{-m} \quad (3.1)$$

where  $A$  and  $m$  are constants for each workpiece material.

Equation (3.1) can be used to estimate the percentage of reduction fatigue life. In this case, equation determining the fatigue life reduction in percentage is:

$$R = \frac{N^{coated} - N^{substrate}}{N^{substrate}} \quad (3.2)$$

where  $N^{coated}$  is the cycle of failure of coated workpieces (whether heat treated coated or coated only) and  $N^{substrate}$  is the cycle of failure of substrate material. Equations (3.1) and (3.2) are used to determine the fatigue life reduction in percentage for heat treated and untreated coated workpieces.

Figure 3.7 shows S–N curve, alternating stress with number of cycles prior to fracture, for coated and uncoated as well as heat-treated coated and uncoated workpieces. Annealing heat treatment of Ti-6 Al-4V alloy results in low strength and high ductility and some improvement in fracture toughness occurs after the heat treatment [7]. The life cycle of the heat-treated and uncoated workpiece is less than its counterpart corresponding to as-received workpiece. In this case, oxide formation in the surface vicinity of the annealed workpiece gives rise to brittle structures in the surface region. In addition, due to differences in thermal expansion coefficient of coating and the base substrate, thermally induced residual stress is formed at coating-base substrate interface. These are the main sources for early failure of the annealed workpiece. In general, the coating on the surface of the alloy enhances the fatigue life of the workpiece. Any cracking and coating failure due to local delamination results in reduction in the area of load carrying segments. This situation enhances the low fatigue life of the heat treated workpieces. As-received and coated workpiece results in highest fatigue strengths. This may be attributed to strong bonding between the coating and the substrate material; in which case, grit blasting modifies the substrate surface such that surface hardness improves due to the plastic deformation that takes place in the substrate surface

**Table 3.1** Slope and coefficient obtained from Eqs. (3.1) and (3.2) for each workpiece

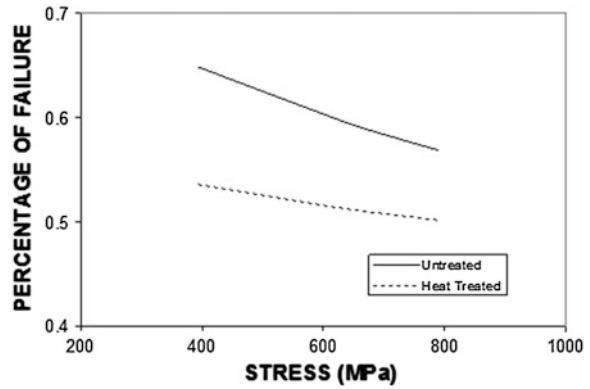
Variables	A (GPa)	m
As received—uncoated	4.261981	0.1515
As received—coated	0.070845	0.4458
Heat treated—coated	2.669081	0.169
Heat treated—uncoated	11.24287	0.2809

vicinity. Similar observation was reported in the early studies [6, 8]. Moreover, the particle impacting force and particle size most likely result in locally distributed compressive residual stresses concentrations in the surface region. Since the substrate surface was cleaned prior to the spraying process, impurities, which are left over after grit blasting, are removed. Therefore, the effect of impurities, captured between the coating and the substrate material, on the fatigue response of the coated workpiece is minimized. As-received material is an  $\alpha$ -phase colony structure composed of prime  $\beta$  grains. After annealing, the transformation results in the formation of  $\beta$ -phase and precipitation of  $\alpha$ -phase. However, the fatigue cracking starts at prior  $\beta$ -grain boundaries and/or colony boundaries as well as  $\alpha/\beta$  interface [9]. The fatigue crack propagation rate of the annealed substrate having fine prior  $\beta$ -grains is faster than that of coarse  $\beta$ -grains (as as-received substrate). Consequently, fatigue failure of heat-treated workpiece is expected to be faster than the as-received workpieces. In addition due to the differences in thermal expansion coefficient of the coating and the substrate material, high concentration of residual stresses are develop at the interface of the substrate material and coating after the heat treatment process. This gives rise to total failure of coating through delaminating or peeling from the substrate surface during fatigue testing.

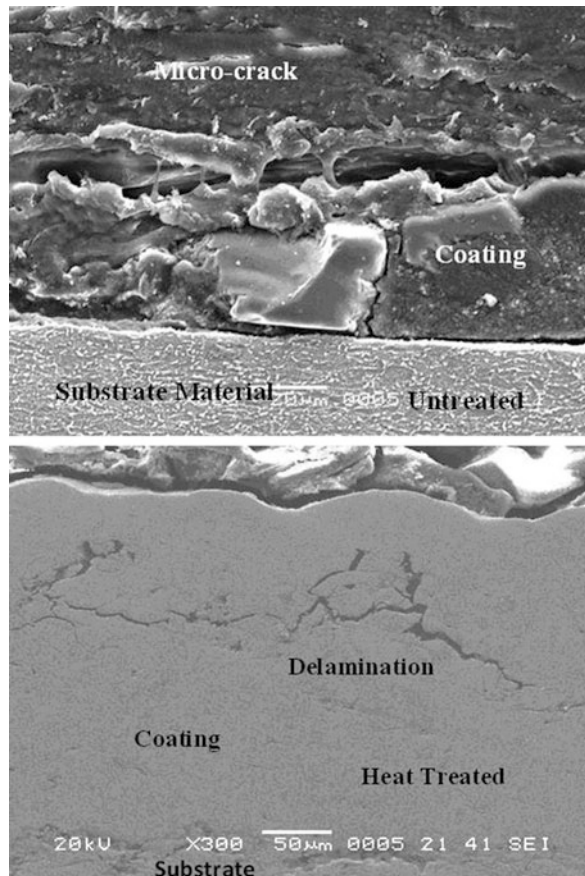
Table 3.1 gives the values of A and m, which are determined from Eq. (3.1). The values of A is related to the fatigue strength coefficient of the workpiece while m represents fatigue strength component. It should be noted that A is associated with the true fracture stress due to static tensile test while m is the slope of the fatigue curve, which is associated with the fatigue life of the workpiece. Figure 3.8 shows the percentage of reduction in fatigue life for as received coated and coated heat treated workpieces as obtained from Eq. (3.2). It is evident that heat treatment lowers significantly the fatigue life of the workpieces.

Figure 3.9 shows SEM micrographs of cross-section of fractured surface of coating while Fig. 3.10 shows optical photographs of top view of fractured workpieces. It is evident from SEM micrographs that partial elongated crack occurs at fractured surface; in which case, coating is partially delaminated from the surface. This may be caused due to the presence of  $\text{Cr}_2\text{O}_3$  in the coating, particularly in the surface region. The delamination of the coating takes place particularly in the surface region where oxide compounds locally scattered. In the case of heat-treated workpieces, multiple fracturing of coating as well as total failure of coating through peeling off from the substrate surface is evident. Therefore, heat treatment lowers the coating adherence to substrate material because of the

**Fig. 3.8** Percentage of fatigue failure with alternating stress for heat treated and untreated coated workpieces [2]



**Fig. 3.9** SEM micrograph of cross-section of fractured coating after fatigue testing of untreated and heat treated workpieces [2]



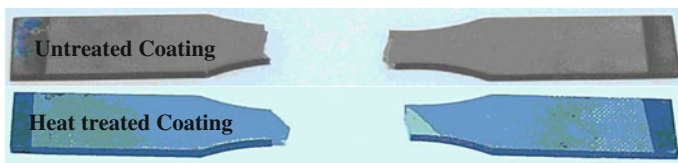


**Fig. 3.10** Optical photographs of fatigue tested workpieces [2]

residual thermal stresses developed due to mismatching of thermal expansion coefficients of coating and underneath substrate material. Cracks formed in the coating do not conform to the base material. Once the cracking is formed, the internal stresses are relaxed and the region of failure becomes limited. These results in the crack propagation in lateral direction normal to the direction of load applied during the tests. Moreover, oxygen diffusion in the free surface of coating during the heat treatment process results in high oxygen content in the surface region, which acts like a barrier preventing diffusion of oxygen further into the coating. Consequently, brittle structure mainly occurs in the region of the free surface of the coating. Therefore, once the crack is initiated at the surface, it expands in the coating through splitting separation of brittle plates containing oxygen rich compounds. Once the crack is formed within the coating, crack extends towards the free surface of the coating due to previously formed oxygen rich brittle structure in this region.

### 3.1.3 Tensile Tests

Figure 3.11 shows tensile test results for coated workpieces as well as heat treated ones. In general, stiffness increases slightly and elastic limit reduces for the workpieces subjected to the heat treatment. This is more pronounced for coated workpieces. In this case, heated and coated workpieces result in short elongation at high load. It should be noted that small increase of oxygen content in the surface region after heat treatment results in modifying the elastic modulus of the coating; in which case, coating structure becomes brittle in the surface region. Consequently, coating failure occurs at high applied tensile loads. The smooth appearance of the curves indicate that no crack initiation within the elastic limit of the coating occurs, i.e., local stress relieving due to poor coating, loose substrate interface, or coating defects in the surface region do not occur. It should be noted that when coating is fractured under the tensile load, internal stresses in the coating and at coating workpiece interface relaxes. If the energy for crack formation is totally dissipated during the first crack formation, secondary crack initiation and crack propagation cease. This, in turn, enhances the magnitude of rupture stress. Figure 3.12 shows micrographs of fractured workpiece cross-sections after the tensile tests. Delamination of coating from the crack site with partially attachment to the workpiece surface is observed. This indicates that tensile stress in the

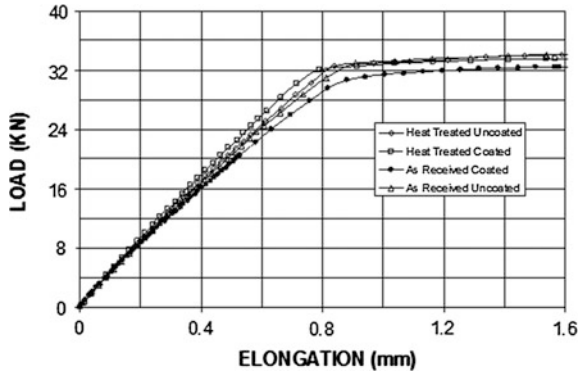


**Fig. 3.11** Tensile test results for as received uncoated, as received coated, heat treated uncoated and heat treated coated workpieces [4]

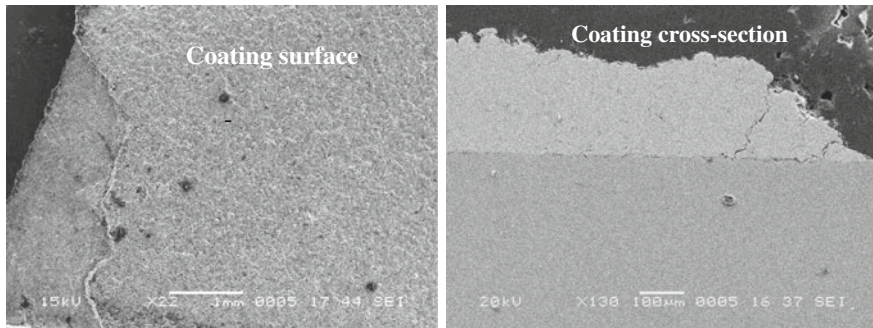
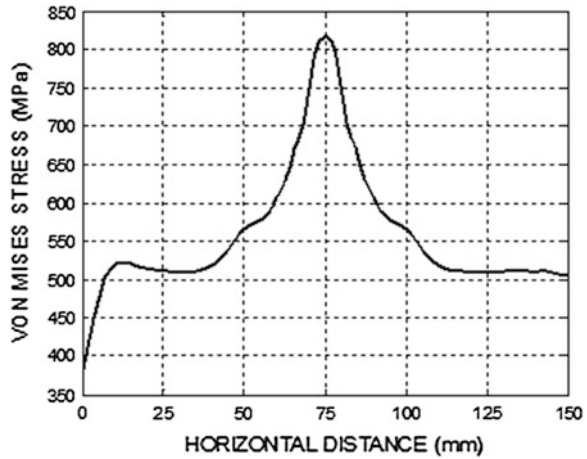


**Fig. 3.12** View of fractured untreated coating after the tensile tests [4]

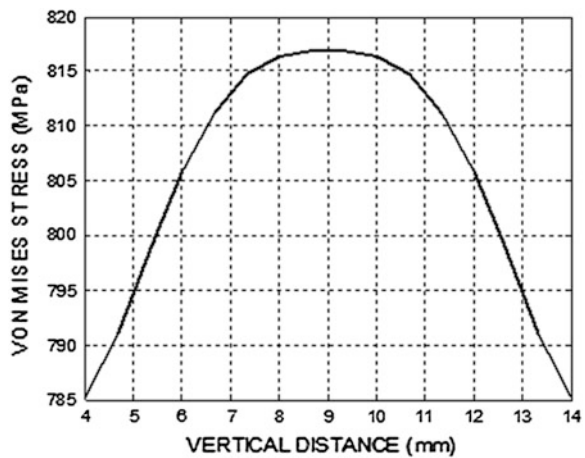
surface region of coating results in crack formation and delamination of the coating in this region. Since the oxygen content of the coating is high in this region, brittleness of this region is responsible for crack initiation and delamination. In the case of heat-treated workpiece, total failure of coating is observed. This is mainly due to the differences between the coating and substrate material elastic modules, which are modified by the heat treatment process. Consequently, coat peels off from the surface once the elastic limit of the coating is reached during the tensile testing. Moreover, if coating is fractured and failed, internal stresses are relaxed and the region of failure does not extend into the coating in the direction of load applied in the tests. The multiple local crack formation in the vicinity of the coating surface is observed for some workpiece. This indicates that the coating splitting separation between layered columns in the coating occurs due to non-conforming the plastic deformation produced along the crack sites.

Figure 3.13 shows von-Mises stress along x-axis (horizontal distance), y-location is centerline and z-location is at the workpiece-coating interface. von-

**Fig. 3.13** von Mises stress along the x-axis (*horizontal distance*) at coating workpiece interface (Force = 30,400 N) [4]



**Fig. 3.14** von Mises stress along the y-axis (*vertical distance*) at coating workpiece interface (Force = 30,400 N) [4]



Mises stress reaches maximum at the central region of the workpiece and decays sharply in the region next to the workpiece center. The maximum magnitude of von-Mises stress reaches close to the elastic limit of the substrate material. The flat top of the stress is evident of plastic deformation of the substrate material. Figure 3.14 shows von-Mises stress along the y-axis, x-axis location is workpiece center ( $x = 75 \text{ mm}$ ) and z-axis location is workpiece-coating interface. Similarly, flat top of von-Mises stress is evident of plastic deformation of the workpiece. Figure 3.15 shows von-Mises stress along z-axis (along thickness), x- and y-axes locations are the center of the workpiece. von-Mises stress rises sharply across the workpiece-coating interface, although the magnitude of stress is slightly less than that corresponding to workpiece. This results in rapid change of total strain in this region. Therefore, any residual stress formed during the coating process results in failure of the coating. This situation is observed during the tensile tests.

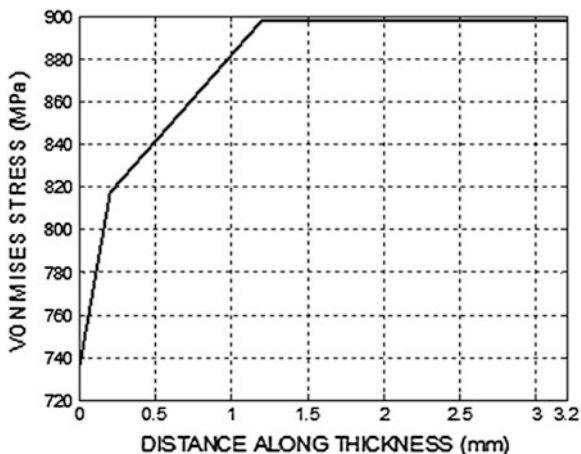


Fig. 3.15 von Mises stress along the z-axis (distance along thickness) across the coating and workpiece (Force = 30,400 N) [4]

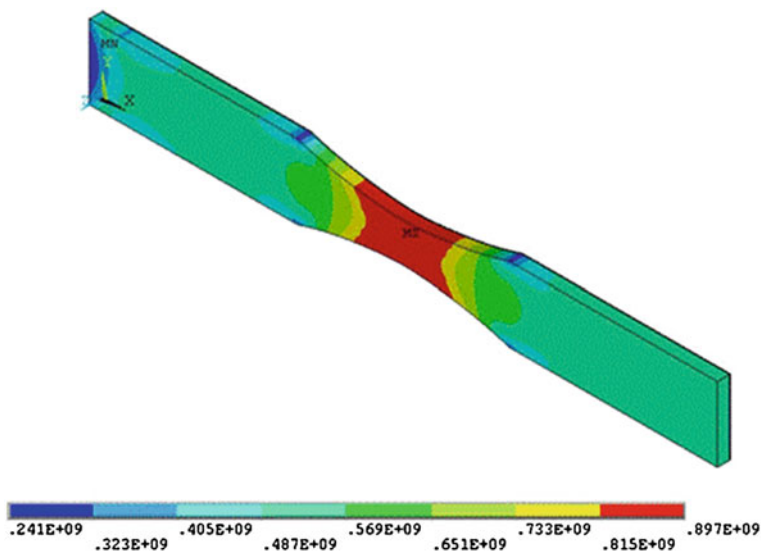
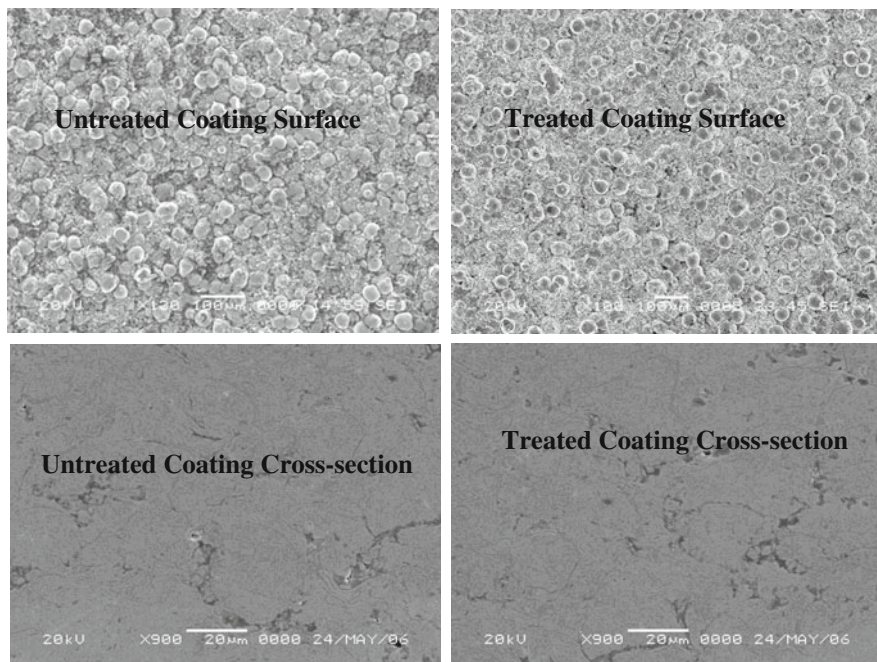


Fig. 3.16 Three-dimensional contour plot of von-Mises stress in the workpiece (Force = 30,400 N) [4]

Figure 3.16 shows contour plots of von-Mises stress in the workpiece. It is evident that magnitude of von-Mises stress and total strain are maximum in the central region of the workpiece. In this case, early initiation of plastic deformation of the coating and workpiece material are unavoidable in this region.



**Fig. 3.17** *Top and cross-sectional views of coating before and after heat treatment [3]*

### **3.1.4 Fracture Toughness Measurement**

HVOF coating of AMDRY 995 on Ti-6Al-4V alloy is carried out and Young's modulus as well as fracture toughness of coating is measured using three point bending and indentation tests. The workpieces coated was heat treated at annealing temperature of the base material for 1 h prior to indenting tests.

Figure 3.17 shows the micrographs of coating before and after the heat treatment process. In general, lamella-like structure is observed and existence of some round shaped splats in coating indicates that some of the splats are in partial molten state prior to impacting at the surface. Oxidation of splats is evident particularly at the location close to the surface region of the coating, which is more pronounced for heat treated surface. Elemental composition of the coating can be observed Fig. 3.18. In this case, oxygen diffusion enhances the oxygen content in the coating. Moreover, once the oxygen content in the coating surface region becomes high, then, oxygen diffusion further into the coating reduces due to saturation of oxygen content in the surface region. EDS line scan around the splat boundary (Fig. 3.18) shows that enrichment of oxygen, chromium, and aluminum occurs within the splat boundary. Consequently, oxidation mainly takes place within the surface region of the splat which was also indicated in the previous

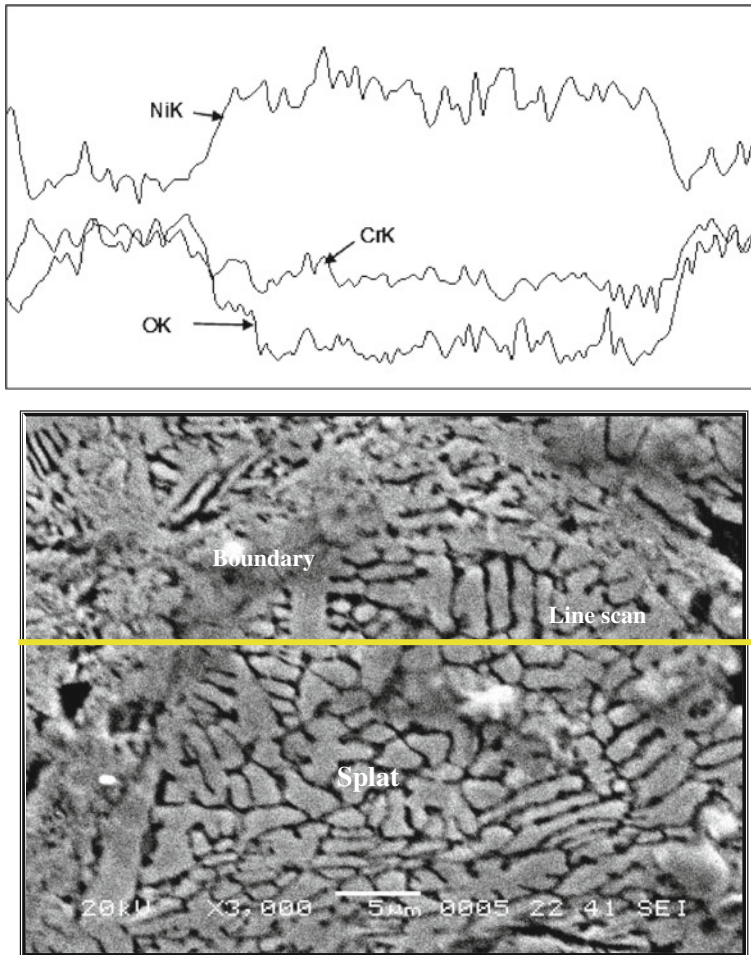


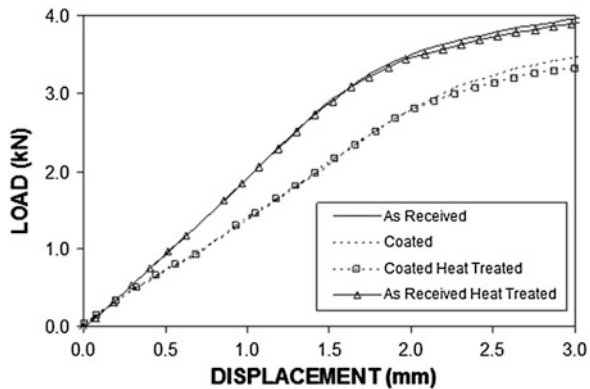
**Fig. 3.18** EDS line scan across the splat and its boundary [3]

study [10]. Chromium and aluminum enrichment at splat boundary indicates the formation of chromium and aluminum oxides.

Table 3.2 gives the Young's modulus and fracture toughness of the coatings prior and after the heat treatment. The Young's modulus obtained from three-point bending tests for uncoated substrate and data obtained from literature [11] are in good agreement. Moreover, Young's modulus determined from three-point bending tests and indentation tests are in good agreement. However, heat treatment modifies the Young's modulus, in which case it reduces. Untreated substrate material (Ti-6Al-4V), is an  $\alpha$ -phase structure composed of prime  $\beta$  grains. However,  $\beta$ -phase formation and  $\alpha$ -phase precipitation is resulted due to the annealing process. In bending tests,  $\beta$ -phase transformation lowers the toughness of the

**Table 3.2** Young's modulus obtained from three point bending and indentation tests

Variables	Three point bending tests (GPa)	Indentation tests (Pa)	Fracture toughness ( $\text{N/m}^{1.5}$ )
As received	138	141	$2.1 \times 10^7$
Heat treated	249	261	$0.9 \times 10^7$

**Fig. 3.19** Load and displacement characteristics obtained from three-point bending tests [3]

workpiece and load displacement characteristics, which is different than that of the untreated material. This situation is seen from Fig. 3.19, in which the three-point bending test results are shown. In addition, thermal stresses developed during the heat treatment process results in brittle structure in the surface region of the coating due to high rate of oxygen diffusion taking place in this region. Consequently, the crack formation initiates in the surface region and extends towards the coating. However, the multiple crack initiation in the surface region of the coating relaxes the stresses in this region. Once the crack formed extends in the coating, particularly, reaching the interface of coating-base material, the coating integrity fails and it peels off from the base material surface, i.e., total failure is resulted. This is because of the high oxide content in the surface region of the coating, which in turn results in a brittle structure. In addition, low Young's modulus of the coating is also responsible for less fracture toughness of heat treated workpieces.

### 3.2 Two Layer HVOF Coating and Characterization

Depending on the coating powder properties, the resulting coating can be resistive to erosion, corrosion and wear. Some of the powders, such as Diamalloy 4010 which is iron/chrome blend, are resistive to corrosion and wear. The combination of these powders in layered structure may offer advantages over the individual powders; in which case, the mechanical properties of the resulting layered structure can be improved. However, mechanical properties of coating produced from

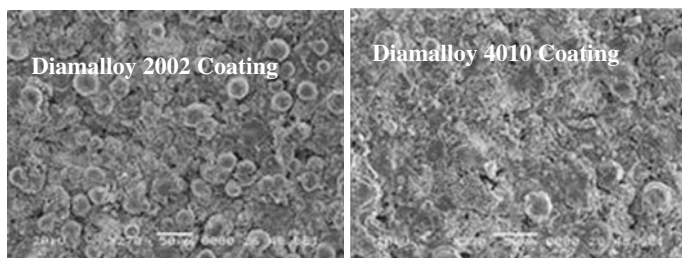


**Fig. 3.20** SEM micrographs of *top view* of coatings produced from Diamalloy 2002 and Diamalloy 4010 powders [12]

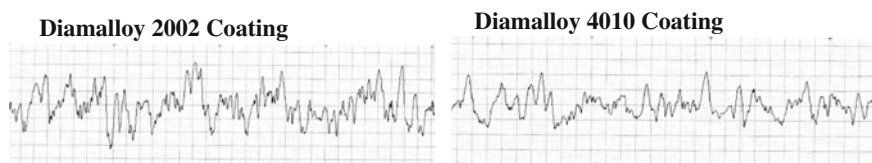
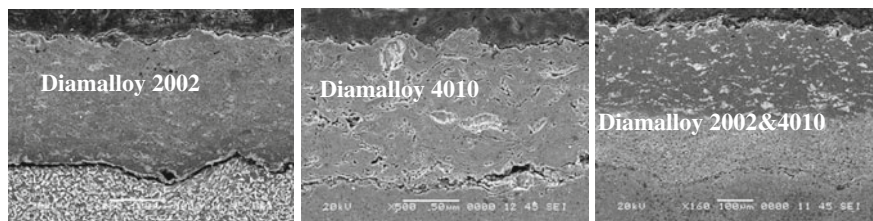


**Fig. 3.21** Roughness of the coating surfaces [12]

carbide blended powders also need to be investigated in details. In addition, coating consists of combination of the layers produced by these powders are of interest for the practical applications. Consequently, investigation into mechanical and metallurgical properties of the resulting structure becomes necessary.

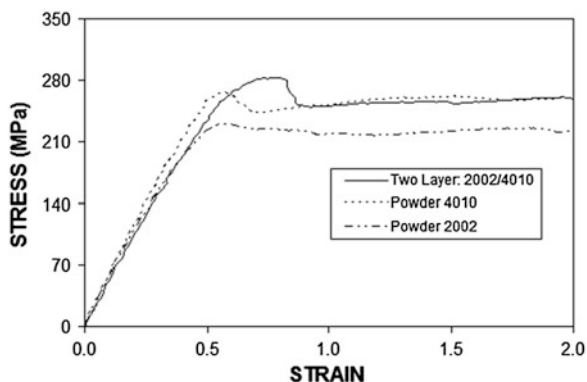
In the present section, HVOF coating of Diamalloy 2002 and Diamalloy 4010 onto carbon sell is presented in line with the previous studies [12–14]. Therefore, the discussions cover the findings of a single and two layers of coating (Diamalloy 4010 at the bottom and Diamalloy 2002 at the top HVOF coating). The mechanical properties of the resulting coatings are presented through the findings of tensile, three-point bending, and fracture toughness tests.

Figure 3.20 shows optical and SEM micrographs of the top surface of the coatings, while Fig. 3.21 shows the surface roughness of the coatings. It is evident from the SEM micrograph that no loose splats or surface asperities such as cavities or cracks are observed at the top surface of the coating. The micrographs for cross-section of the coating (Fig. 3.22) shows that lamella like structure is formed due to the presence of molten state of splats on set of impacting the surface. However, locally scattered spherical splats are also evident. This indicates the presence of semi-molten state of some splats. However, they appear to be few in number. Moreover, the presence of the dark inclusions (stringers) in the surface region of the coating is evident. This indicates the presence of oxide particles with small size, which is attributed to oxidation of small particles during in-flight. However oxidation of the splats at coating surface after the impacting also contributes to the oxidation state of the coatings. The splat size has significant effect on the oxidation process, in which case, oxygen content increases as the particle size reduces. The



**Fig. 3.22** SEM micrographs of cross-sections of single and two layered coatings with two different powders [12]

**Fig. 3.23** Stress-strain curve resulted from tensile tests [13]



splat size changes for Diamalloy 2002 due to the presence of WC, which is 12 %, in the coating. The porosity of Diamalloy 2002 coatings is higher than that of Diamalloy 4010. This is because of the presence of solid phase WC particles, which does not integrate with neighboring splats in molten state.

Figure 3.23 shows tensile test results for coating produced from Diamalloy 2002 and Diamalloy 4010 for single as well as for two layers. In general, stiffness increases slightly for coating produced Diamalloy 4010. The elastic limit of the coating increases for Diamalloy 4010 and two layered coating. It should be noted that oxide formation around the splats contributes to the stiffness and elastic limit of the coatings. However, coating produced Diamalloy 2002 powders and two layered structure have similar stress-strain behavior almost up to the elastic limit. This indicates that the influence of Diamalloy 2002 on the tensile behavior is more pronounced. Moreover, the smooth variation of stress-strain curve up to the elastic limit indicates that tensile loading does not produce excessive number of cracks affecting the tensile behavior of the coated workpiece. However in the region of the elastic limit, irregularities in the form of broken lines in the tensile curve indicate the formation of cracks in the coating. This is particularly true for two-layered coating. In this case, the stress developed at interface of first and second layers in the coating initiates the cracks in the coating. When the coating is fractured under the tensile load, the stress relaxation occurs in the coating; in

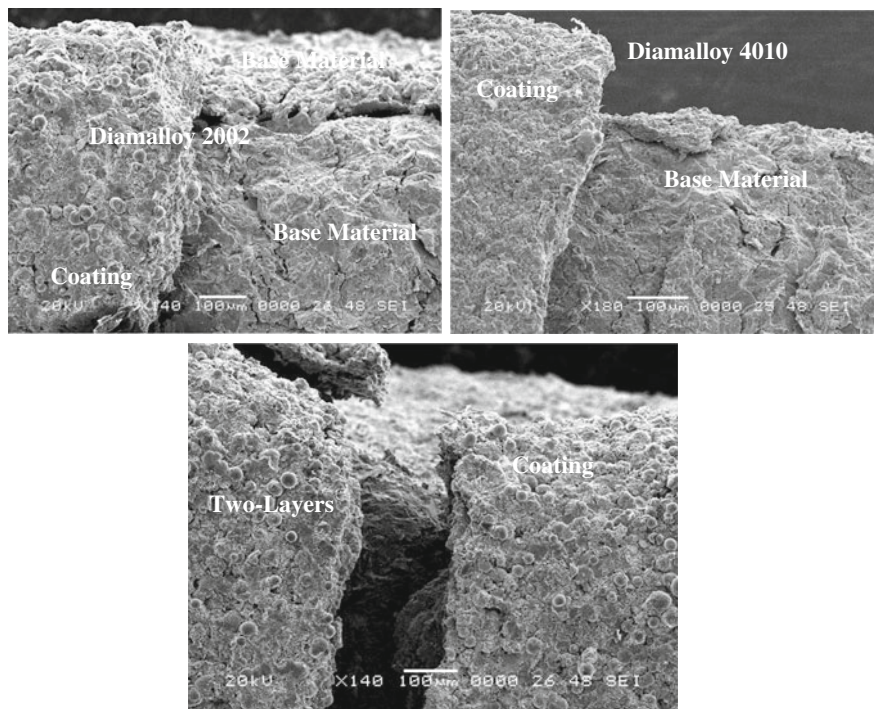


**Fig. 3.24** SEM micrographs of coating surfaces after tensile tests [13]

which case, the energy is dissipated through the cracks and secondary cracking with increasing tensile load cease.

Figure 3.24 shows SEM micrographs of tensile test workpieces. The micrographs reveal that multi-cracks are formed in the coatings. This is particularly true for Diamalloy 2002 coating, which contains 12 % WC. In this case, the crack size is larger than those observed for Diamalloy 4010 coatings. The close examination of micrographs reveals that some section of the coating is peeled off while some other section adheres to the workpieces surface. This shows that cracks could not propagate to the coating and base material interface, so that coating dose not conform the plastic deformation in the base material. This is more pronounced for two-layered coating. In this case, shear deformation at the interface of two coating layers in responsible for peeling of the coating. In the case of small cracks, the sliding and splitting deformation take place in the coating under the tensile load. The close examination of fracture surfaces shows that fracture is brittle and takes place through the splats boundary. This may be explained the oxide layer formed around some of the splats; in which case, splats de-bound through their oxide interfaces. The stringers, which are the oxide particles, act as stress centers promoting the stress concentration in the coating. Consequently, during the tensile loading, these centers contribute significantly to the crack initiation and propagation in the coating. Moreover, at coating-base material interface adhesion failure

**Fig. 3.25** Load-displacement characteristics obtained from three-point bending tests [13]

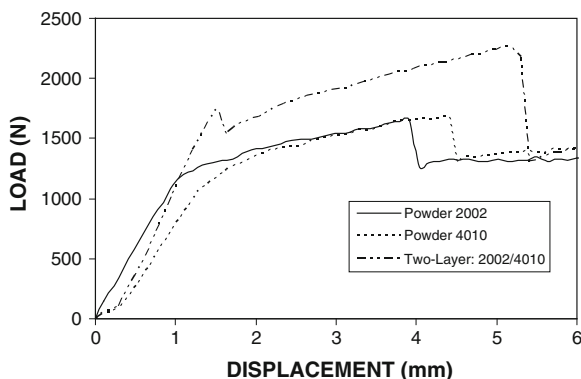


**Table 3.3** Elastic modulus determined from three-point bending tests

Diamalloy 4010 (GPa)	Diamalloy 2002 (GPa)
135	240

is also observed, which occurs locally due to the presence of interface impurities in this region.

Figure 3.25 shows load-displacement curve obtained from the three-point bending tests. It should be noted that three point bending is carried out at constant stress rate. The elastic-plastic behavior of the coatings, due to Diamalloy 2002 and Diamalloy 4010 as well as two layered structure, are different. The flexural displacement increases at low load levels for coating produced from Diamalloy 4010 powder while it is low for Diamalloy 2002 coating. This is attributed to the presence of WC content in the coatings, which makes the coating stiffer and harder. The sudden drop in flexural displacement reveals the failure of the coating during the bending tests. This occurs after the long flexural displacement for Diamalloy 2002 coating and two-layered structure. This suggests that the gradual deformation takes place, which relieve the stress levels in the coating while contributing to the stress relaxation during the bending tests. Table 3.3 gives the elastic modulus determined from the three-point bending tests. It is evident that Diamalloy 2002 has the highest elastic modulus because of the presence of 12 % WC in the coating.

Figure 3.26 shows SEM micrograph of fractured surface after three-point bending tests. Since the coating was applied at the top and bottom surface of the workpieces, coating failure is due to compression and tensile-shear. The extended crack formation at the bottom surface, where tensile-shear failure takes place, is evident. However, in some region, the delimitation of coating occurs because of excessive shear stress developed in the coating during the bending test. In addition, the presences of oxide particles contribute to the shear failure, particularly in the surface region of the coating. The tensile-shearing force enhances the internal stresses while creating local stress concentrations in the coating. This is more

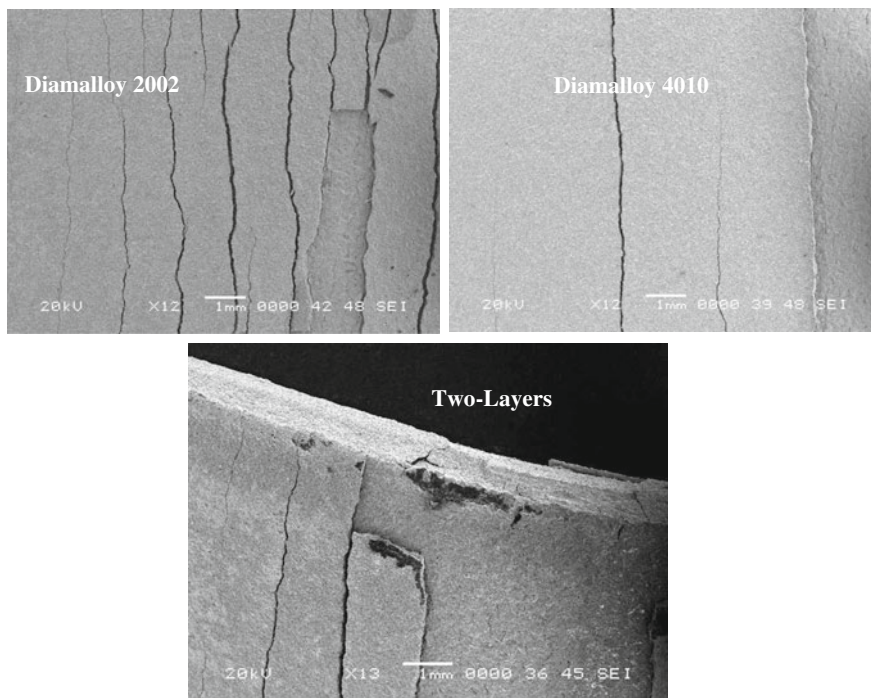


**Fig. 3.26** SEM micrographs of coating surfaces after three-point bending tests [13]

**Table 3.4** Data obtained after indenting tests

	E (GPa)	E* (GPa)	H (HV)	P (N)	R ( $\mu\text{m}$ )	h ( $\mu\text{m}$ )
Diamalloy 4010	114	46.5	540	20	60	10
Diamalloy 2002	214	66	690	20	40	9

\* represents the apparent Elastic modulus

pronounced at defect sites such as oxide particles in the coating. Consequently, stress concentrations at defect sites become higher than that of the mean internal stress. As bending progresses, a critical stress levels is reached at the defect sites. This triggers the large crack formation. However, the presence of defect sites at coating-base material interface results in the total failure of the coating, i.e., coating peels of form the base material surface. In the surface region, the crack propagation is limited with this region; in which case, small cracks are formed during the bending. However, if the energy dissipated during micro cracks formation, the crack propagation ceases and the microcracks are formed in the surface region. In addition the compressive stress developed at the top surface of the workpiece resulted in partial peeling of the coating in the surface region.

Table 3.4 gives the elastic modulus determined from the indentation tests for all the coatings. It is evident that the elastic modules for the coating produced from

Diamalloy 2002 powders is higher than that corresponding to Diamalloy 4010. This is because of the high surface hardness of Diamalloy 2002 coating. It should be noted that the error related to the measurement is in the order of 8 %. Since the elastic modulus measurement is limited with the surface, two layers coating resulted the surface elastic modulus similar to that of Diamalloy 2002. This is because of the top layer in the coating, which is Diamalloy 2002. In addition, the stress developed in two layer coating is compressive because of its large thickness. Consequently, for proper assessment of the elastic modulus, further tests are needed, such as three point bending and tensile tests.

### 3.3 Residual Stress Analysis HVOF Coating

The powder emerging from the spray gun reaches almost the melting temperature of the constituting substrate material. Since the stand-off-distance between the gun exit and the base material surface is short, the splats change from the round shape to the oval shape upon impacting onto the surface due to their elevated temperatures. Once the coating is built on to the base material surface, the coating temperature remains high while the substrate bulk temperature is low. During the cooling period, the thermal stresses are developed in the coating. Once the temperature equilibrium is achieved between the base material and the coating during the cooling period, the residual stress field is developed in the coating. Depending on the coating thickness, the residual stresses can be compressive or tensile. The residual stress in the coating influences the mechanical performance of the coating; consequently, investigation into the residual stress developed in the coating after the spraying process becomes necessary.

In this chapter, the analysis and findings are presented in line with the previous study [15].

#### 3.3.1 Experimental

HVOF spraying parameters were selected based on the optimum spraying conditions, which are given in Table 3.5. The optimum coating conditions were assessed through microstructure. In this case, the low porosity and oxidation levels, judged by SEM and EDS, in the coating were considered. Therefore, coating conditions resulting in less porosity and oxidation levels in the coating as well as high tensile strength of coating were selected as the optimum coating conditions.

Nickel based alloy Diamalloy Powder 1005, which was equivalent to Inconel 625, was sprayed onto the sand blasted and cleaned Ti-6Al-4V alloy surface. The powder sprayed had a particle distribution between 25 and 40  $\mu\text{m}$  with mainly spherical morphology. The K type thermocouples were located on the top and

**Table 3.5** Process parameters of HVOF thermal spray

Oxygen pressure (kPa)	Fuel pressure (kPa)	Air pressure (kPa)	Powder feed rate (m <sup>3</sup> /h)	Spray rate (kg/h)	Spray distance (m)
1023	580	710	0.82	6.3	0.28

bottom surfaces of the specimens to monitor the temperature rise during the spraying process.

JEOL JDX-3530 scanning electron microscope (SEM) and EDS are used to obtain photomicrographs of the cross-section and surface of the workpieces after the tests. The Bruker D8 Advance having Cu-K $\alpha$  radiation is used for XRD analysis. A typical setting of XRD was 40 kV and 30 mA. It should be noted that the residual stress measured using the XRD technique provides the data in the surface region of the specimens. This is because of the penetration depth of Mo-K $\alpha$  radiation into the coating, i.e., the penetration depth is in the order of 10–20  $\mu$ m.

### 3.3.2 Heat Transfer Analysis

The transient diffusion equation based on the Fourier heating model can be written in the Cartesian coordinates as:

$$\rho \frac{\partial(C_p T)}{\partial t} = \left( \frac{\partial}{\partial x} \left( k \frac{\partial T}{\partial x} \right) + \frac{\partial}{\partial y} \left( k \frac{\partial T}{\partial y} \right) + \frac{\partial}{\partial z} \left( k \frac{\partial T}{\partial z} \right) \right) \quad (3.3)$$

where  $x$ ,  $y$  and  $z$  are the axes (Fig. 3.27),  $\rho$  is the density,  $C_p$  is the specific heat capacity, and  $k$  is the thermal conductivity. It should be noted that the coating is initially assumed to be at uniform temperature of 1,000 K. This assumption satisfies the actual coating temperature as measured by the thermocouples. The base material temperature is assumed to be uniform at 560 K during the coating process. It should be noted that the specimens were preheated prior to coating; therefore, the assumption is verified through the actual temperature measurement of the base material.

At the free surfaces of the coated specimen (Fig. 3.27) the convective boundary is assumed, therefore, the corresponding boundary condition is:

$$\begin{aligned} \text{At the free surfaces} \rightarrow \frac{\partial T}{\partial x} = \frac{h}{k}(T_s - T_{amb}) : \frac{\partial T}{\partial y} = \frac{h}{k}(T_s - T_{amb}) : \frac{\partial T}{\partial z} \\ = \frac{h}{k}(T_s - T_{amb}) \end{aligned}$$

where  $h$  is the heat transfer coefficient due to natural convection, and  $T_s$  and  $T_{amb}$  are the surface and ambient temperatures, respectively.

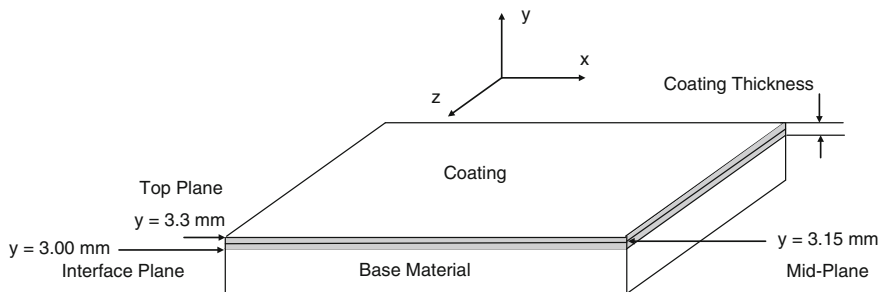


**Fig. 3.27** A schematic view of the coated base material and the coordinate system [15]

### 3.3.3 Modeling of Thermal Stresses

From the principle of virtual work (PVW), a virtual (very small) change of the internal strain energy ( $\delta U$ ) must be offset by an identical change in external work due to the applied loads ( $\delta V$ ). Considering the strain energy due to thermal stresses resulting from the constrained motion of a body during a temperature change, PVW yields:

$$\begin{aligned} & \{\delta u\}^T \int_{vol} [B]^T [D] [B] dv \{u\} - \{\delta u\}^T \int_{vol} [B]^T [D] \{\varepsilon^{th}\} dv \\ & = \{\delta u\}^T \int_{Area} [N_s]^T \{p\} dS + \{\delta u\}^T \{F_N\} \end{aligned} \quad (3.4)$$

Noting that the  $\{\delta u\}^T$  vector is a set of arbitrary virtual displacements common in all of the above terms, the condition required to satisfy above equation reduces to:

$$[K] \{u\} = \{F^{th}\} + \{F^{pr}\} + \{F^n\} \quad (3.5)$$

where

$$\begin{aligned} [K] &= \int_{vol} [B]^T [D] [B] dv = \text{Element stiffness matrix} \\ \{F^{th}\} &= \int_{vol} [B]^T [D] \{\varepsilon^{th}\} dv = \text{Element thermal load vector} \\ \{\varepsilon^{th}\} &= \{\alpha\} \Delta T = \text{Thermal strain vector} \\ \{\alpha\} &= \text{vector of coefficients of thermal expansion} \\ \{F^{pr}\} &= \int_{Area} [N_s]^T \{p\} dS = \text{Element pressure vector} \\ \{F^n\} &= \text{Nodal force vector} \end{aligned} \quad (3.6)$$

**Table 3.6** Mechanical and thermal properties of Ti-6Al-4V alloy used in the simulations

Temp (K)	373	478	588	698	813	923		
$\alpha \times 10^{-6}(1/K)$	8.6	9.0	9.2	9.4	9.5	9.7		
$\nu$	0.342							
E (GPa)	113.6							
$\rho$ (kg/m <sup>3</sup> )	4,430							
Temp (K)	373	473	673	873	1,073	1,273	1,473	1,773
K (W/mK)	30.5	24.5	20.4	19.4	19.7	20.7	22.0	24.5
Cp (J/Kg K)	300	465	551	591	633	675	620	686

In the current work, the effect of mechanical deformation on heat flow has been ignored and the thermo-mechanical phenomenon of melting is idealized as a sequentially-coupled unidirectional problem. For thermal analysis, the given structure is modeled using thermal element (SOLID70). SOLID70 has a 3-D thermal conduction capability. The element has eight nodes with a single degree of freedom, temperature, at each node. The element is applicable to a 3-D, steady-state or transient thermal analysis. Since the model containing the conducting solid element is also to be analyzed structurally, the element is replaced by an equivalent structural element (such as SOLID45) for the structural analysis. SOLID45 is used for the 3-D modeling of solid structures. The element is defined by eight nodes having three degrees of freedom at each node: translations in the nodal x, y, and z directions. The element has plasticity, creep, swelling, stress stiffening, large deflection, and large strain capabilities.

The thermal and structural properties used in the current simulations are given in the Tables 3.6 and 3.7. It should be noted that the conditions for the current simulations resemble the actual experiments carried out in the present study.

### 3.3.4 Residual Stress Measurements

The XRD and curvature measurement techniques are introduced. The method for each measurement technique is adopted in according to the previous studies.

*XRD Technique:* The measurement relies on the stresses in fine grained polycrystalline structure. The position of the diffraction peak undergoes shifting as the specimen is rotated by an angle  $\psi$ . The magnitude of the shift is related to the magnitude of the residual stress. The relationship between the peak shift and the residual stress ( $\sigma$ ) is given [16]:

$$\sigma = \frac{E}{(1 + \nu)\sin^2\psi} \frac{(d_n - d_o)}{d_o} \quad (3.7)$$

**Table 3.7** Mechanical and thermal properties of Inconel 625 alloy used in the simulations

Temp (K)	303	366	477	589	700	1,273	1,473	1,673	1,873	2,073
E (GPa)	208	201	199	191	184	176	168	157	146	129
Temp (K)	447	589	700	811	922	1,033	1,144	1,255		
$\alpha \times 10^{-6}(1/K)$	13.1	13.5	13.9	14.4	15.1	15.7	16.6	17.3		
$\nu$	0.36									
$\rho$ (kg/m <sup>3</sup> )	8,440									
Temp (K)	300	373	473	573	673	773	873			
K (W/mK)	9.8	11.4	13.4	15.5	17.6	19.6	21.3			
Cp (J/Kg K)	429	446	463	480	496	513	560			

**Table 3.8** Data used in Eq. (3.8)

$E_c$ (GPa)	$E_s$ (GPa)	$t_s$ (m)	$t_c$ (m)	$\alpha_c$ (1/K) $\times 10^{-6}$	$\alpha_s$ (1/K) $\times 10^{-6}$	$T_R$ (K)
227	113.6	$3 \times 10^{-3}$	$3 \times 10^{-4}$	13.1	9	300

where E is Young's modulus,  $\nu$  is Poisson's ratio,  $\psi$  is the tilt angle, and  $d_i$  are the  $d$  spacing measured at each tilt angle. If there are no shear strains present in the specimen, the  $d$  spacing changes linearly with  $\sin^2\psi$ .

*Analytical expression for the residual stress:* The analytical expression for the residual stress was developed previously is used [17]. The previous expression is based on the thermal expansion mismatched between the coating and the base material. Therefore, the residual stress is:

$$\sigma = \frac{[E_c(T_f - T_R)(\alpha_c - \alpha_s)]}{1 + 2\left(\frac{E_c t_c}{E_s t_s}\right)} \quad (3.8)$$

where  $E_c$  and  $E_s$  are the elastic modules of the coating and the base material,  $t_c$  and  $t_s$  are the coating and base material thicknesses,  $T_f$  is the maximum temperature during laser heating and  $T_R$  is the room temperature after the cooling period is over,  $\alpha_c$  and  $\alpha_s$  are the thermal expansion coefficient of the coating and the base material, respectively. Table 3.8 gives the data used for the residual stress calculation using Eq. (3.8).

### 3.3.5 Findings and Discussion

Thermal stress developed in the HVOF coating is considered and the residual stress developed in the coating is predicted using the Finite Element Model (FEM) and it is measured using the XRD technique and the curvature method. The study is extended to include the residual stress calculations based on the early formulation [17].

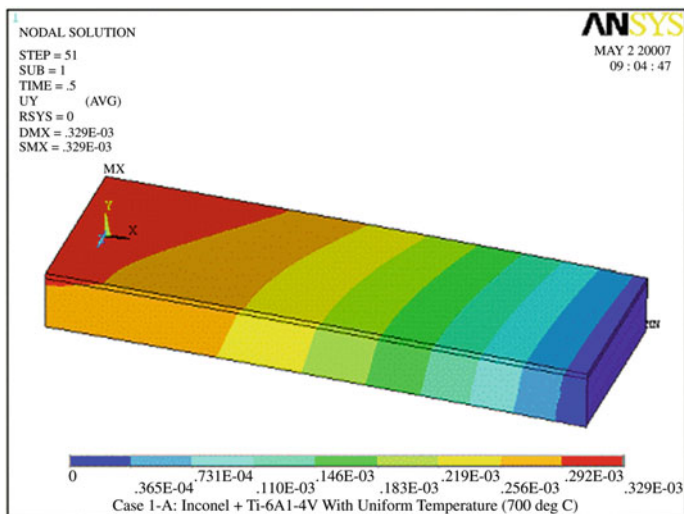


**Fig. 3.28** The displacement of the coating and the base material after cooling to 300 K. The unit of the displacement is in meters [15]

**Fig. 3.29** Displacement of the coating at the central point of the surface along the axial distance [15]

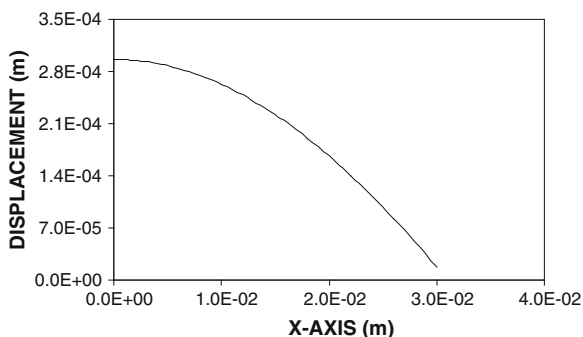
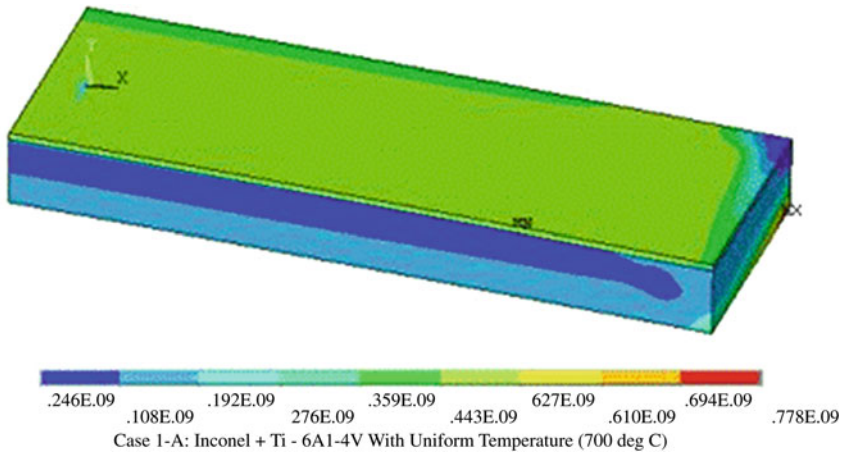


Figure 3.28 shows three-dimensional view of the y-axis displacement predicted from the FEM simulations. It should be noted that 1/4 of the view of the coated specimen is shown in the Fig. 3.28. Moreover, in the simulations, the free surface of the coating is assumed to be free from any mechanical load or other constraints. The y-axis expansion is purely due to the temperature field. In addition, the displacement of the surface is shown after the end of the cooling cycle. Initially, the coating is at 1,000 K (as measured during the spraying process) and once the spraying terminates, the cooling cycle initiates. The cooling cycle ends when temperature in the coating reduces to 300 K. The displacement is maximum at the x-axis location of  $x = 0$  where it is at the mid-point of the coated specimen. The maximum displacement is in the order of 0.329 mm upwards. This indicates that the residual stress developed in the coating is compressive. Figure 3.29 shows the



**Fig. 3.30** von Mises stress at top of the coating. Stress unit is GPa [15]

displacement of the coating surface along the  $x$ -axis at the end of the cooling cycle. It is evident that the displacement reaches the maximum at the center-point of the specimen; however, as the distance along the  $x$ -axis increases, displacement reduces in a non-linear form. It should be noted that in the simulations, the both ends of the specimen are fixed, which resemble the actual experimental conditions; i.e., during the spraying process, the both ends of the specimen are fixed. Since the base material is at 460 K (as measured during the coating process), the contribution of the base material temperature to the displacement is not significant.

Figure 3.30 shows three-dimensional view of the von Mises stress at the top plane (in the vicinity of the free surface of the coating, Fig. 3.27) at the mid-plane (plane at the half thickness of the coating, and the base material) after the end of the cooling cycle. The stresses are associated with the residual stresses developed after the cooling cycle. The maximum magnitude of the residual stress is in the order of 531 MPa, which is locally distributed with a limited region in the coating. The von Mises stress distribution remains almost the same in the top and mid-plane while it differs in the interface plane. The similar distribution of the von Mises stress is attributed to the cooling of the coating, i.e., a uniform elevated temperature (1,000 K) is considered in the coating prior to the cooling and the heat transfer coefficient at all the free surfaces is assumed to be the same due to natural convection from the free surface. This results in almost similar von Mises stress distribution in the surface region and in the mid-plane. This situation can also be seen from Fig. 3.31, in which the von Mises stress distribution along the  $x$ -axis is shown in three planes at different  $y$ -axis locations after the cooling period. However, the average value of the von Mises stress (averaged based on the surface area) in the surface region is 531 MPa. The von Mises stress remains the same in the vicinity of the upper surface and the mid-plane. The magnitude of the von Mises stress is in the order of 500 MPa. Moreover, in the interface plane, the magnitude of the von Mises stress reduces significantly. This is because of the heat

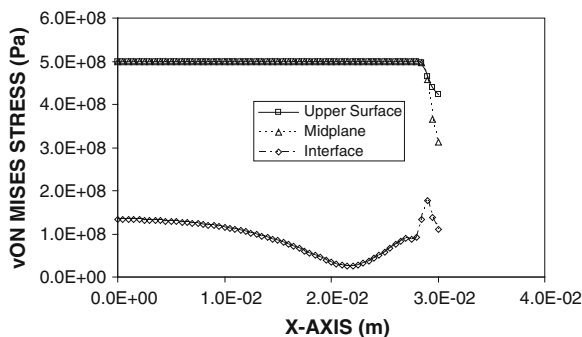


Fig. 3.31 von Mises stress along the axial direction at three planes in the coating [15]

transfer from coating to the base material. Since the cooling rate is relatively smaller at the interface plane than the free surface of the substrate material, temperature gradient across the interface becomes small. This, in turn, lowers the von Mises stress levels. The conduction heat transfer from the coating to the base material during the cooling cycle increases the temperature gradient in the base material. This, in turn, results in high stress levels developed in the base material after the cooling period ends. However, the stress levels in the substrate material are smaller than that of in the coating.

Figure 3.32 shows three-dimensional view of the plastic strain in the substrate material at the top and at the mid-planes. The plastic strain attains higher values in the top plane than that of the mid-plane, provided that the plastic strain distribution is almost similar in the two planes. The attainment of plastic strain in the surface region is because of the convection cooling of the coating at the free surface. However, the natural convection results in almost a uniform heat transfer coefficient at the free surface so that the spatial distribution of plastic strain becomes almost similar in both planes. Figure 3.33 shows the plastic strain along the  $x$ -axis at all planes. The plastic strain attains high values in the surface region and it becomes low at the interface plane. This is because of the cooling rates, which is relatively lower at the interface plane than that of in the top plane. Consequently, the convection cooling from the free surface enhances the temperature gradient and the plastic strain in this region becomes high after the cooling period ends.

Figure 3.34 shows optical micrograph of the coating cross-section. The Lamella-like structure is evident, provided that some round shaped splats reveals the presence of the partially solid and partially molten particles in the spraying jet before the impacting onto the base material surface. The impacting of some semi-molten and unmelted powder particles results in the residual stress sites in the coating, particularly at the coating-base material interface. Some small scattered porosity is observed, which is in the order of 3 %. The close examination of the SEM micrograph (Fig. 3.35) shows the dark and light regions due to the oxide and the metallic phases in the coating. Moreover, the oxide stringers are visible, in particular, in the surface region of the coating. The oxide components are formed

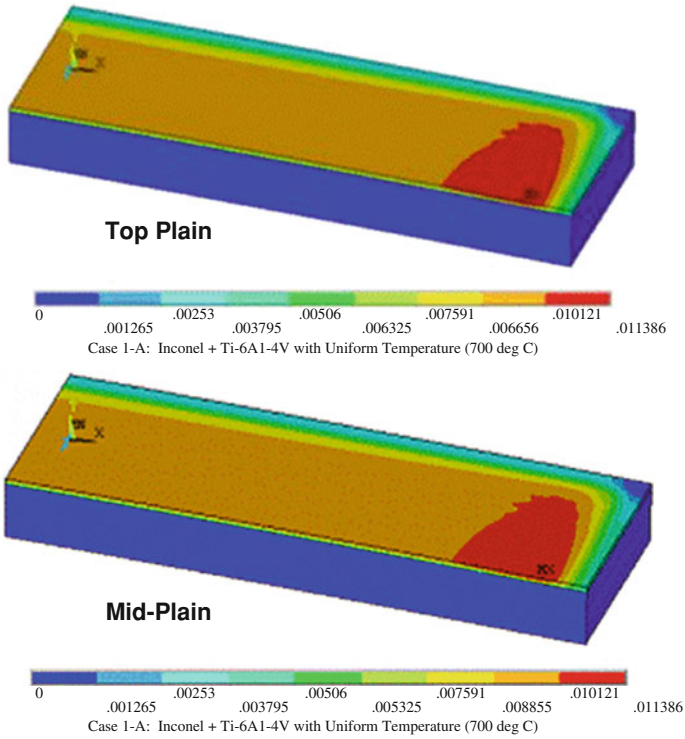


Fig. 3.32 Equivalent plastic strain at three planes in the coating [15]

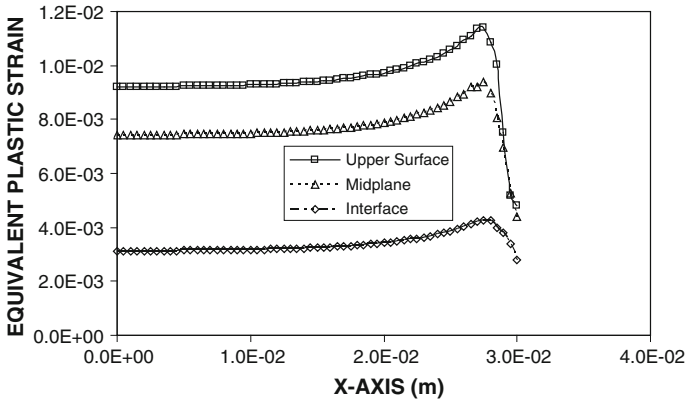
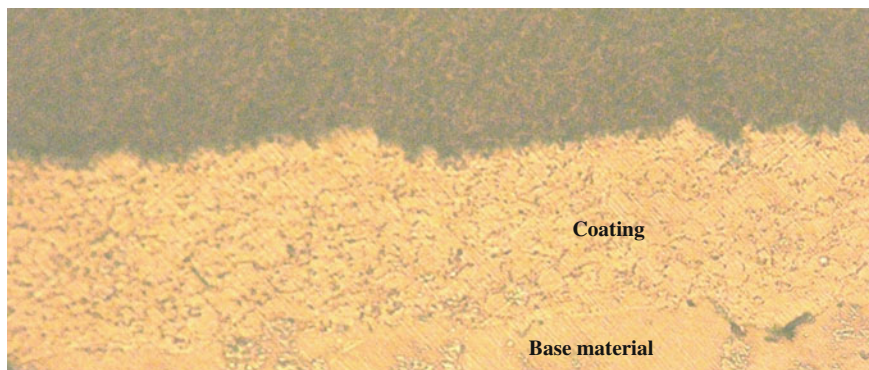


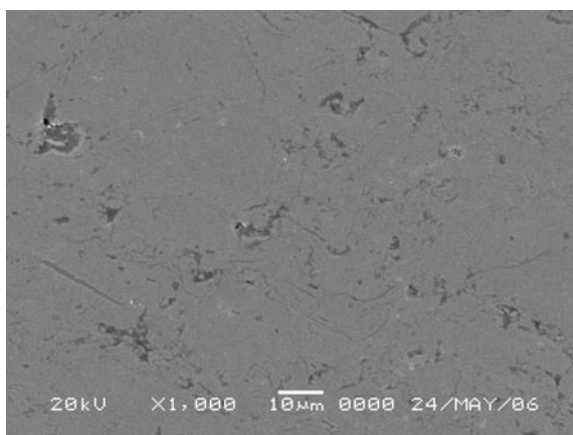
Fig. 3.33 Equivalent plastic strain along the axial direction at three planes in the coating [15]

during the in-flight of splats and they form the brittle structure sites in the coating. In addition, the cooling rates of the powder particles in the coating are modified by the presence of the oxygen compounds in the coating. This, in turn, results in the



**Fig. 3.34** Optical micrograph of the cross section of the coating [15]

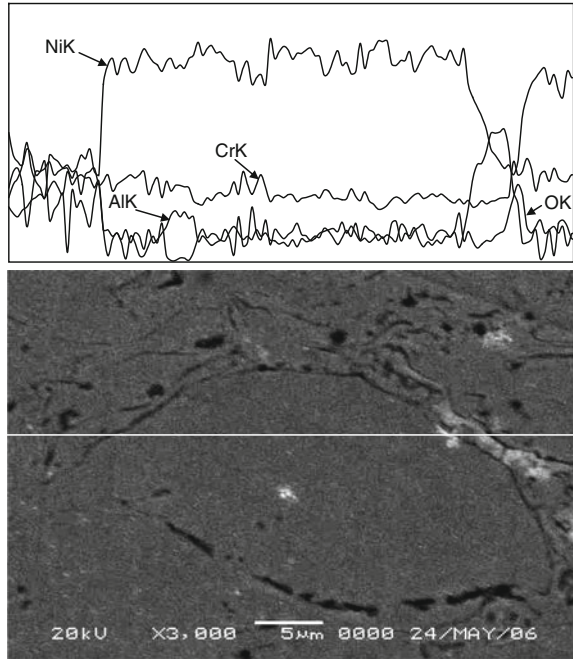
**Fig. 3.35** SEM micrograph of the coating [15]



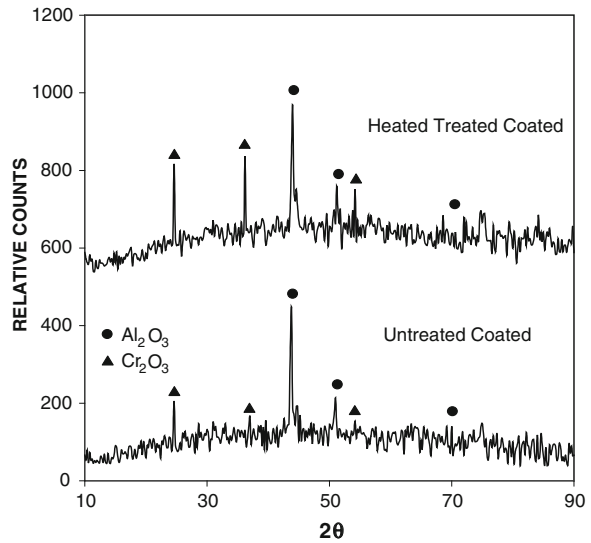
multi-directional cooling at different cooling rates. Consequently, the resulting thermal stress field in the coating varies significantly because of the variation in the cooling rates. However, the oxide compounds are formed around the splat boundary. This situation is seen from EDS line scan around the splat boundary (Fig. 3.36). In this case, enrichment of oxygen chromium and aluminum at the splat boundary is evident. This situation can also be seen from Fig. 3.37, in which XRD result is shown. The formation of chromium and aluminum oxide is evident.

Table 3.9 lists the maximum residual stress predicted in the coating and calculated from Eqs. (3.7) and (3.8). The maximum residual stress predicted remains almost the same at the top and mid-planes. Consequently, the residual stress measured using the XRD technique has merit base to compare with the predictions, despite the fact that XRD measurements provide the data in the surface region of the coating, i.e., the highest residual stress predicted is in the top plane (in the surface region) and the XRD measurement provides the data in the surface

**Fig. 3.36** Line scan of the splat in the coating [15]



**Fig. 3.37** XRD results obtained for the coating [15]



region. It should be noted that the curvature ( $k$ ) is determined from the simulation and from the experiment. The residual stress measured using the XRD technique is also given in Table 3.9. When comparing the results obtained from the XRD

**Table 3.9** Comparison of the residual stress obtained from the FEM predictions, measurements, and previous analytical formulation [17]

Predictions (MPa)	XRD technique (MPa)	Curvature method (MPa)	Analytical formulation (MPa)
531	495	480	436

It should be noted that the predictions of the residual stress is based on the maximum value in the coating

technique, the curvature measurement method, the analytical formulation, and the present predictions, it can be observed that the residual stress measured from the experiment agrees reasonably well with the analytical results and the predictions of the present simulations. Moreover, the present simulations give closer results to the results obtained from the XRD method as compared to that of the analytical formulation. Consequently, the residual stress simulations have sound base to determine the stress levels in the coating.

### 3.4 Laser Re-melting of Inconel HVOF Coating

Inhomogeneous structure in HVOF coating occurs because of the presence semi-molten state and oxidation of some splats in the coating. In this case, some of the splats remain as round solid structure in the coating. However, thermal integration in the coating through control melting provides the coating homogeneity and improved the bonding strength at the coating-base material interface. The laser heating process is one of the alternatives for the thermal integration of the HVOF coating through control melting. However, the stress levels in the coating upon the solidification become important. In the present section, in line with the previous study [18], laser melting of HVOF coating sprayed onto Ti-6Al-4V alloy is considered and the residual stress levels in the coating and coating-base material interface are predicted using the finite element method (FEM). The data used in the simulation resemble the experimental conditions. The residual stress developed in the coating after the laser treatment process is measured using the XRD technique. SEM and EDS are carried out to examine the morphological and the metallurgical changes in the coating prior and after the laser treatment process.

#### 3.4.1 Mathematical Analysis

Since the laser scans at the workpiece surface during the treatment, the heat transfer can be modelled after considering a three-dimensional situation. The transient diffusion equation based on the Fourier heating model can be written in the three-dimensional Cartesian coordinates as:

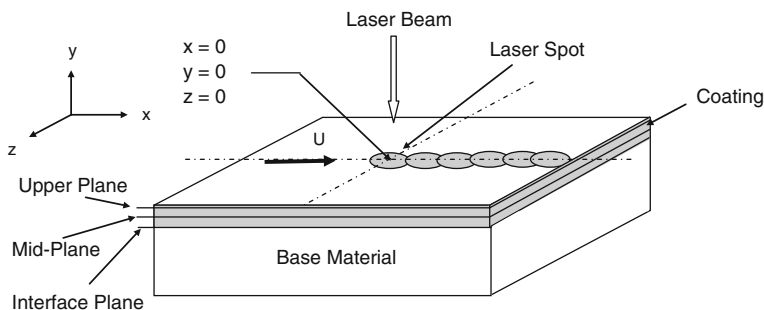


**Fig. 3.38** Cross-section of the laser heating situation and coordinate system [18]

$$\rho C_p \frac{\partial T}{\partial t} = k \left( \frac{\partial^2 T}{\partial x^2} + \frac{\partial^2 T}{\partial y^2} + \frac{\partial^2 T}{\partial z^2} \right) + u \rho C_p \frac{\partial T}{\partial y} + S_0 \quad (3.9)$$

where  $x$ ,  $y$  and  $z$  are the axes (Fig. 3.38),  $u$  is the scanning speed of the laser beam,  $\rho$  is the density,  $C_p$  is the specific heat capacity,  $k$  is the thermal conductivity. It should be noted that the laser heating situation is considered to be a constant temperature heat source at the workpiece surface  $S_0 = I_o(1 - r_f) \left( e^{-\frac{(x^2+y^2)}{a^2}} \right)$  with a radius  $a$  (laser beam radius at focused surface) in the  $x$ - $y$  plane,  $I_o$  is the peak power intensity,  $r_f$  is the surface reflectivity, and a depth of melt layer is limited with the thickness of the coating along the  $y$ -axis. These conditions represent the situation such that the coating temperature does not reach the evaporation temperature of the substrate material along the  $z$ -axis in the  $x$ - $y$  plane where laser beam is located (Fig. 3.38). At the free surface (in  $x$ - $y$  plane at  $z = 0$ ) a convective boundary is assumed, therefore, the corresponding boundary condition is:

$$\text{At } z = 0 \text{ (at the surface)} \rightarrow \frac{\partial T}{\partial y} = \frac{h}{k} (T_s - T_o)$$

where  $h$  is the heat transfer coefficient and  $T_s$  and  $T_o$  are the surface and reference temperatures, respectively. In addition, at a distance far away from the surface in the  $x$ - $y$  plane temperature becomes the same as the reference temperature. This yields the boundary condition of:

$$\text{At } x \text{ and } y = \infty \rightarrow T = T_\infty \quad (T_o, \text{ Specified})$$

Initially the substrate material is assumed to be at a reference temperature ( $T_o$ ), therefore, the initial condition becomes:

$$\text{At } t = 0 \rightarrow T = T_\infty \quad (T_o, \text{ Specified})$$

To solve Eq. (3.9) an explicit scheme is employed. The details of the numerical scheme are given in [10]. The stability criteria due to time increment are considered for a stable solution; therefore, the time increment is limited by:

$$\left( \frac{2k}{\rho c_p \Delta x^2} + \frac{2k}{\rho c_p \Delta y^2} + \frac{2k}{\rho c_p \Delta z^2} \right) \Delta t \leq 1 \quad (3.10)$$

The calculation domain is divided into grids and grid independence test is being performed for different grid size and orientation. The material properties and simulation conditions for Eq. (3.9) are given in Tables 3.6 and 3.7.

Finite Element Method is one of the most accepted and widely used tool for the solution of non-linear partial differential equations which rise during the mathematical modeling of various processes. The modeling of laser heating involving phase change of substrate material is a highly non-linear coupled thermo-mechanical phenomenon. The modeling of such a process is very involved as various physical phenomena's are interacting e.g., heat flow, complicated molten metal dynamics, microstructure evolution and overall thermo-mechanical response of the structure. It is indeed very cumbersome to account for all the couplings that exist. In computational mechanics, high degree of simplification is used and most of these couplings are ignored based on their weak nature. The moving heat source results in localized heat generation and large thermal gradients. The non-uniform temperature distribution results in thermal stresses and distortions. The basic theory describing the behavior of continuum combines the theory of heat transfer through conduction and convection and Elasto-Plasticity. To analyze the phase change problem, a nonlinear transient thermal analysis is performed employing enthalpy method. To account for latent heat evolution during phase change, the enthalpy of the material as a function of temperature is incorporated in the energy equation.

For structural response, the finite element formulation is based on the principle of virtual work. From PVW, a virtual (very small) change of the internal strain energy ( $\delta U$ ) must be offset by an identical change in external work due to the applied loads ( $\delta V$ ). Considering the strain energy due to thermal stresses resulting from the constrained motion of a body during a temperature change, PVW yields:

$$\{\delta u\}^T \int_{vol} [B]^T [D] [B] dv \{u\} = \{\delta u\}^T \int_{vol} [B]^T [D] \{\varepsilon^{th}\} dv \quad (3.11)$$

Noting that the  $\{\delta u\}^T$  vector is a set of arbitrary virtual displacements common in all of the above terms, the condition required to satisfy above equation reduces to:

$$[K] \{u\} = \{F^{th}\} \quad (3.12)$$

where

$$\begin{aligned}
[K] &= \int_{vol} [B]^T [D] [B] dv = \text{Element stiffness matrix} \\
\{F^{th}\} &= \int_{vol} [B]^T [D] \{\varepsilon^{th}\} dv = \text{Element thermal load vector} \\
\{\varepsilon^{th}\} &= \{\alpha\} \Delta T = \text{Thermal strain vector} \\
\{\alpha\} &= \text{vector of coefficients of thermal expansion}
\end{aligned} \tag{3.13}$$

In the analysis, the effect of mechanical deformation on heat flow has been ignored and the thermo-mechanical phenomenon of melting is idealized as a sequentially-coupled unidirectional problem. According to this simplified approach a fully coupled thermal-metallurgical analysis is performed first which is followed by a structural analysis. During the thermal analysis, microstructure evolution can be modeled through either more sophisticated direct calculation procedure or by relatively simpler but common method of indirect incorporation of microstructure aspects into the material model. During the structure analysis, temperature and microstructure dependence of stresses and deformations are accommodated by invoking the results of thermal-metallurgical analysis into the stress analysis.

For thermal analysis, the given structure is modeled using thermal element (SOLID70). SOLID70 has a 3-D thermal conduction capability. The element has eight nodes with a single degree of freedom, temperature, at each node. The element is applicable to a 3-D, steady-state or transient thermal analysis. Since the model containing the conducting solid element is also to be analyzed structurally, the element is replaced by an equivalent structural element (such as SOLID45) for the structural analysis. SOLID45 is used for the 3-D modeling of solid structures. The element is defined by eight nodes having three degrees of freedom at each node: translations in the nodal x, y, and z directions. The element has plasticity, creep, swelling, stress stiffening, large deflection, and large strain capabilities.

*Material Model:* An accurate modeling of temperature dependent material properties is a key parameter to the accuracy of computational mechanics and has been a challenging job due to scarcity of material data at elevated temperature. In the computational mechanics microstructure evolution is addressed either by direct calculations from thermal history, various phase fraction, properties of each constituent and deformation history or indirectly by considering the micro-structural dependency on the thermal and mechanical history. Although the indirect approach is relatively crude but widely used in the simulation due to its relative ease.

The thermal and structural properties used in the current simulations are given in the Tables 3.6 and 3.7. It should be noted that the conditions for the current simulations resemble the actual experiments carried out in the present study; the thickness of coating is 250  $\mu\text{m}$  and thickness of the workpiece is 3 mm. Since the coating is melted by a laser beam during the simulations, no initial residual stress is considered due to the HVOF spraying process, i.e., during the melting, residual stress is relaxed in the coating.

**Table 3.10** Laser assisted surface treatment conditions

Scanning speed (mm/min)	Power (W)	Peak power (W)	Frequency (Hz)	Nozzle gap (mm)	Nozzle diameter (mm)	Gaussian parameter (mm)	Focus setting (mm)	N <sub>2</sub> pressure (kPa)
100	160–180	2,000	200	1.5	1.5	0.55	127	300

### 3.4.2 Experimental

The CO<sub>2</sub> laser (LC-ALPHAIII) delivering nominal output power of 2 kW at pulse mode with different frequencies is used to irradiate the workpiece surface. The nominal focal length of the focusing lens is 127 mm. Nitrogen assisting gas emerging from the conical nozzle and co-axially with the laser beam is used. The workpiece surface was scanned at a constant speed by a laser beam. Laser treatment conditions are given in Table 3.10. An aluminum substrate is used as the workpiece material.

JEOL JDX-3530 scanning electron microscope (SEM) and EDS are used to obtain photomicrographs of the cross-section and surface of the workpieces after the tests. The Bruker D8 Advance having Cu-K $\alpha$  radiation is used for XRD analysis. A typical setting of XRD was 40 kV and 30 mA. It should be noted that the residual stress measured using the XRD technique provides the data in the surface region of the specimens. This is because of the penetration depth of Mo-K $\alpha$  radiation into the coating, i.e., the penetration depth is in the order of 10–20  $\mu$ m.

The residual stress measurement using the XRD technique relies on the stresses in fine grained polycrystalline structure. The position of the diffraction peak undergoes shifting as the specimen is rotated by an angle  $\psi$ . The magnitude of the shift is related to the magnitude of the residual stress. Consequently, the precise measurement of this shift in a certain peak position in a diffraction pattern allows calculating the degree of strain within the coating. The relationship between the peak shift and the residual stress ( $\sigma$ ) is given [16].

If there are no shear strains present in the specimen, the  $d$  spacing changes linearly with  $\sin^2 \psi$ . Figure 3.39 shows the  $d$ -spacing with  $\sin^2 \psi$ . It can be observed that the variation is linear and no splitting in the curve occurs; therefore, the presence of shear strain is not notable. In addition, the slope is negative indicating that the stress is compressive.

### 3.4.3 Findings and Discussion

The findings of the simulation and the experiment are presented below in line with the previous study [18]. In this case, laser treatment of the HVOF coating is under taken and the residual stress developed in the coating after the laser treatment

**Fig. 3.39** d-Spacing with  $\sin^2(\psi)$  obtained from the XRD data [18]

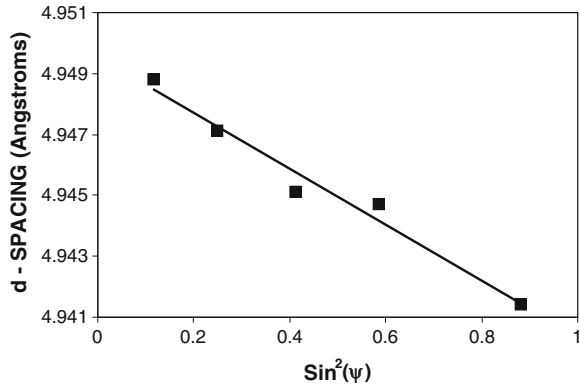
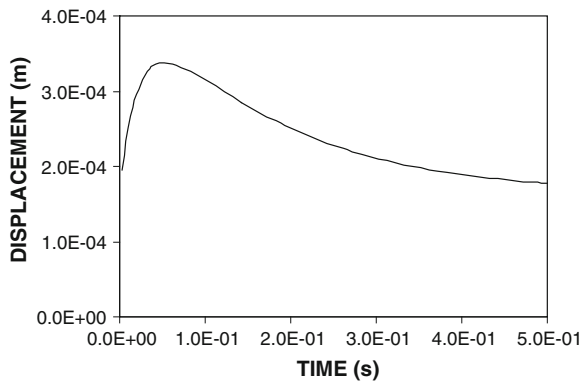


**Fig. 3.40** Temporal variation of displacement at the mid-point of the specimen during the cooling cycle [18]



process is presented. An experiment is carried out to melt the HVOF coating and the XRD technique is used to measure the residual stress in the coating.

Figure 3.40 shows the temporal variation of the displacement of the surface and along the y-axis as predicted from the simulation while Fig. 3.41 shows three-dimensional view of the y-axis displacement. It should be noted that the cooling cycle is assumed to start at  $t = 0$ , i.e., initial heating phase (heating cycle) is not considered and at  $t = 0$  coating is assumed to be at the melting temperature of the substrate material (Inconel 625). Moreover, temperature of the base material (Ti-6Al-4V) is kept 460 K, which is lower than that of cooling at time  $t = 0$ . Although initially assumed that the displacement of the coating and the base material is zero at  $t = 0$ , because of the heat transfer from coating to the base material through the conduction as well as the heat transfer from coating to the surrounding environment by convection enable the base material and the coating to bend outwards along the y-axis. This results in the displacement of the surface along the y-axis. Once the temperature gradient reaches to a critical value, the surface displacement becomes the maximum and prolonging the cooling results in decreasing of the surface displacement. In this case, the temperature gradient reduces and the

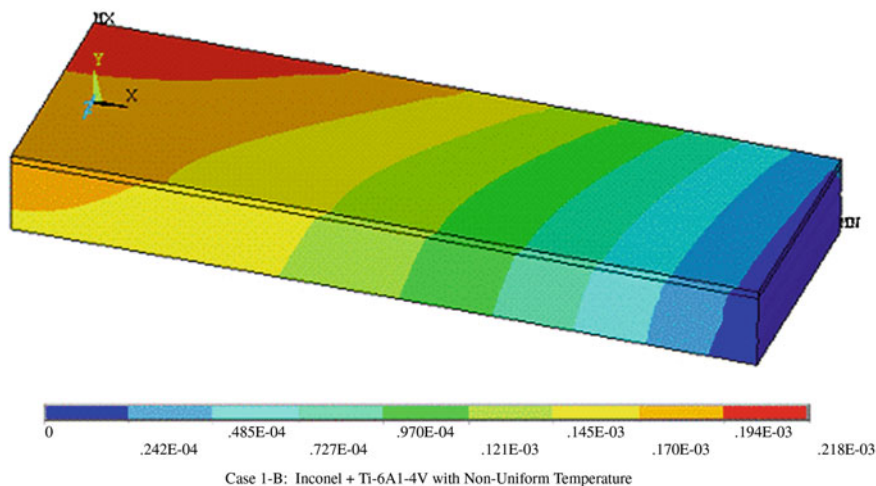


**Fig. 3.41** Dimensional view of displacement after ending the cooling cycle ( $t = 0.5$  s) [18]

displacement along the y-axis reduces, accordingly. As the cooling period progresses further the displacement reduces gradually; however, it never reaches to zero due to the residual stress developed in the coating during the cooling cycle. This situation is also be seen from Fig. 3.41. This is because of the corresponding time, which is long enough for temperature to reduce to the room temperature i.e., at the end of the cooling period.

Figure 3.42 shows temporal variation of von-Mises stress at three planes in the coating (reference to Fig. 3.38). von-Mises stress rises rapidly in the surface region (upper line) and remains the same with progressing time. The rapid rise of von-Mises stress is associated with the cooling rates in the surface region, which is high because of the convective heat transfer from the free surface to the surround ambient. However, as the time progresses further change in von-Mises stress is negligible and cannot be observed from the figure. In the case of the mid-plane, von-Mises stress attains almost the same value as that of in the surface region von-Mises stress attains high values in the early heating period and decreases rapidly at the interface plane. This is because of the temperature gradient at the interface, which differs significantly from its counterpart in the surface region of the coating. The conduction heat transfer from the coating to the base material lowers temperature at the interface plane, since base material temperature is lower than that of the coating. As the time progresses, temperature of the base material increases at the interface plane because of the heat diffusion from the coating to its environment. This increases von-Mises stress with progressing time at the interface. During the cooling cycle, the cooling rate changes because of the temperature gradient developed at the interface during the heating cycle. This modifies the residual stress levels once the cooling cycle is completed. It should be noted that for time period of 0.5 s, temperature of the coating reduces to about 530 K, which

**Fig. 3.42** Temporal variation of von-Mises stress at three planes (shown in Fig. 3.40) in the coating during the cooling cycle [18]

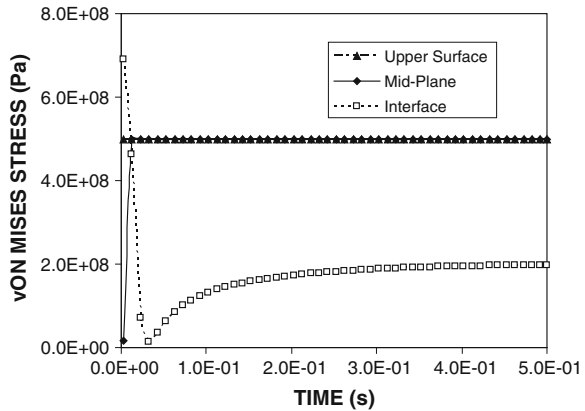


**Table 3.11** Residual stress predicted in the top plane and measured using the XRD technique

Residual stress predicted (MPa)	Residual stress measured (MPa)
350	330

is considerably low and von-Mises stress after this time period can be considered as the residual stress in the coating and at the interface plane between the coating and the base material. Consequently, the residual stress at the coating-base material interface attains different values than that of in the coating. This can be observed from Fig. 3.42. Table 3.11 gives the residual stress predicted from FEM simulations and XRD measurements. It can be seen that von-Mises stress predicted agrees with the measurements result. It should be noted that von-Mises predicted in the top plane is given in the table for the comparison. This is because of the fact that XRD measurement provides data with the 20 μm depth below the surface due to penetration limit of the Cu-Kα radiation. However, when comparing von-Mises stress at different planes in the coating, it can be observed that von-Mises stress attain minimum at the coating-base material interface. Other locations in the coating, it remains almost the same.

Figure 3.43 shows the top and cross-sectional view of HVOF coated samples prior and after the laser treatment. The top view of the coating reveals that some of the splats de-bond in the surface region where the oxygen concentration is high (Table 3.12, in which EDS analysis is given). The de-bonding is mainly through the oxide interfaces. In addition, some small elongated splats are also observed. Despite the fact that the oxide particles promote high stress concentration in the surface region, no crack is evident in the surface region. In case of HVOF coating cross-section, lamellar structure and locally and randomly distributed voids in between the splats are observed. In the coating, the regions around the splats boundary reveal the existence of the oxidation during in-flight before impacting the coating surface. Moreover, some stringers like inclusions are also evident in the coating. These are

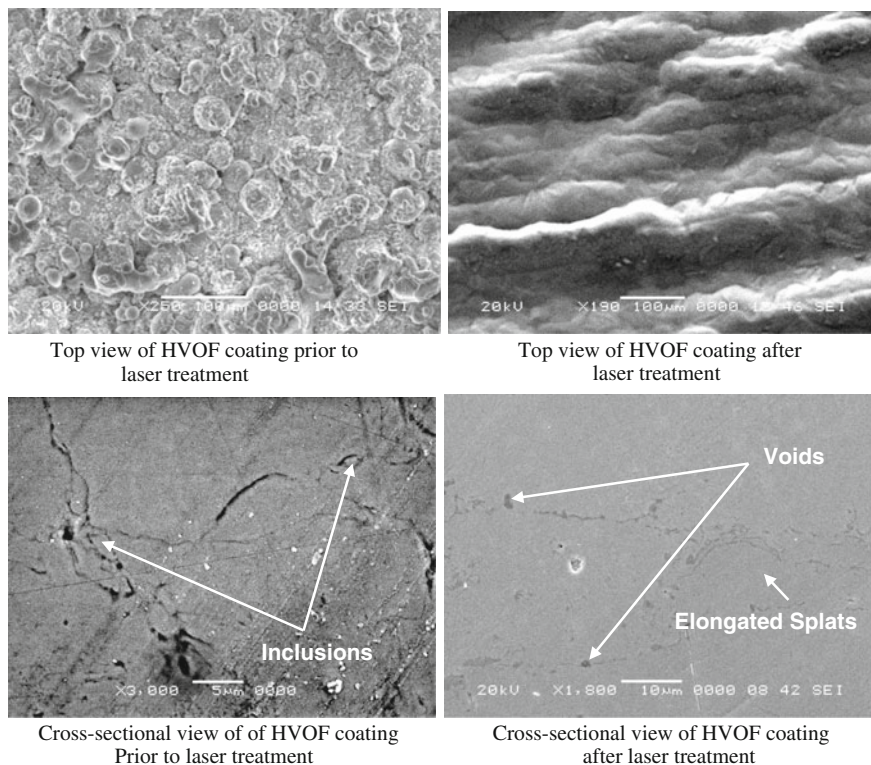


**Fig. 3.43** SEM macrographs as-received HVOF coating and laser treated coatings [18]

**Table 3.12** EDS results after the laser treatment process

Location below surface ( $\mu\text{m}$ )	O	Al	Cr	Ni	Fe
5	11.87	0.21	16.98	30.28	Balance
20	7.23	0.32	16.18	31.60	Balance

highly oxide particles in the coating. In the case of the laser treated specimens, the complete melting of the coating is evident from the micrographs. In addition, the micro-holes, formed due to the gasification and the bubbles formed during the melting, is not evident in the melt region. This is mainly because of the low scanning speed of the laser beam; consequently, bubbles formed during the laser melting coalesces and escape during the melting and voids formed by the bubbles are filled with the liquid metal due to the surface tension force. The oxide formed around the splats are partially disappears due to the melting and mixing in the coating. Moreover, the laser melted region is compact and sealing effect of the melt layer at the coating surface is evident, i.e., the spreading or partially melted splats at the surface

are not observed. Although the cooling rate at the surface is high, upon solidification no micro-crack is observed from the micrographs. During the laser melting of coating, the residual stress developed in the coating during the HVOF spraying process is relaxed. However, changing in the cooling rate as well as the effects of high cooling rate on the solidification process in the coating during the cooling cycle result in the residual stresses development in the coating as well as at the coating-base material interface.

### 3.4.4 Laser Control Melting HVOF Coating

The laser melting of HVOF coating has several advantages over the conventional melting methods. The local heating resulting in small heat affected zone, precise of operation, and fast processing time are the main advantages. The thermal strain developed during the heating and cooling cycles differs significantly in the coating. This, in turn, results in the development of the excessive stress field in the coating leading to the crack formation at the stress centers in the coating. Therefore, in the present section, laser re-melting of HVOF coating is introduced and the micro-structural analysis prior and post re-melting is carried out. Inconel is used as the spraying powder while stainless steel (SS 316 L) is accommodated as the based material for spraying. EDS, optical microscopy and SEM are conducted for material characterization and microstructural analyses. Laser heating situation is modeled using the lump parameter analysis and predications are compared with experimental findings in line with the previous study [19–21].

In modeling the laser induced melting process, the lumped parameter technique is used. This enables to formulate the liquid layer thickness during the laser heating process. In the analysis, it is assumed that the melt layer developed on the solid surface during laser irradiation flows steadily in the direction of the assisting gas due to the drag force developed at the assisting gas-liquid interface. Consider a small fraction ( $\beta$ ) of molten metal evaporates from the melt surface during the laser heating process. Since the liquid layer thickness ( $\delta_L$ ) is formulated previously [21], the resulting equation is presented below:

$$\delta_L = \mu_L \frac{\sqrt{\frac{C_1}{C_5} s - \frac{5}{4} \frac{(C_4 + 2U_e^2)s}{C_5}}}{\frac{1}{2} C_f \rho_g U_e^2} \quad (3.14)$$

where

$$C_1 = \frac{1}{\rho_L} \frac{\frac{P_o}{A} + \dot{q}_c - h(T_m - T_{oi})}{[Cp_s(T_m - T_i) + L_m + \beta L_{ev} + 1.65 Cp_m(T_{ev} - T_m)]} \quad (3.15)$$

and

$$C_2 = \rho_L [C_{p_s}(T_m - T_i) + L_m + \beta L_{ev} + 1.65 C_{p_m}(T_{ev} - T_m)] \quad (3.16)$$

and

$$C_4 = \rho_g U_e C_H [C_{p_g}(T_{ev} - T_{oe})] \quad (3.17)$$

and

$$C_5 = \frac{s}{2C_2} - \frac{1}{2} \mu_L \frac{1}{C_f \rho_g} \frac{2}{U_e^2} \quad (3.18)$$

where  $A$  is the area ( $m^2$ ),  $C_p$  is the specific heat capacity of gas ( $J/kg K$ ),  $C_{p_m}$  is the specific heat capacity of liquid ( $J/kg K$ ),  $C_{p_s}$  is the specific heat capacity of solid ( $J/kg K$ ),  $C_H$  is the heat transfer parameter,  $C_f$  is the skin friction coefficient,  $D$  is the diffusion coefficient ( $m^2/s$ ),  $E_{in}$  is the laser power available at liquid surface ( $W$ ),  $E_{conduction}$  is the rate of energy conducted ( $W$ ),  $E_{convection}$  is the rate of energy convected ( $W$ ),  $E_{req}$  is the rate of energy required for melting ( $W$ ),  $h$  is the heat transfer coefficient ( $W/m^2 K$ ),  $h_o$  is total enthalpy of gas at the edge of the boundary layer ( $J/kg K$ ),  $h_g$  is the total enthalpy of gas at the melt surface ( $J/kg K$ ),  $k$  is thermal conductivity ( $W/m K$ ),  $L_m$  is the latent heat of melting ( $J/kg$ ),  $L_{ev}$  is the latent heat of evaporation ( $J/kg$ ),  $m_g$  is the assisting gas mass flow rate ( $kg/s$ ),  $m_L$  is the liquid mass flow rate ( $kg/s$ ),  $Pr$  is the Prandtl number,  $P_o$  is the laser output power reaching the melt surface after reflection ( $W$ ),  $Re_L$  is the liquid layer Reynolds number,  $s$  is the distance along the workpiece surface ( $m$ ),  $Sc$  is the Schmidt number,  $T_{ev}$  is the boiling temperature ( $K$ ),  $T_m$  is the melting temperature ( $K$ ),  $T_o$  is the initial temperature of the workpiece ( $K$ ),  $T_{oe}$  is the gas temperature at the edge of the boundary layer ( $K$ ),  $T_{ref}$  is the reference temperature,  $U_e$  is the gas velocity at the edge of the gas boundary layer ( $m/s$ ),  $U_L$  is the melt velocity ( $m/s$ ),  $U_{LS}$  is the melt velocity at the melt surface ( $m/s$ ),  $V_L$  is the melt velocity normal to the surface ( $m/s$ ),  $y$  is the distance normal to the workpiece surface ( $m$ ),  $\beta$  is the evaporation factor and  $<1$ ,  $\eta$  is the thermal efficiency,  $\rho_g$  is the density of assisting gas ( $kg/m^3$ ),  $\rho_L$  is the density of molten metal ( $kg/m^3$ ),  $\rho_s$  is the density of workpiece material ( $kg/m^3$ ).

A computer program is developed to compute the liquid layer thickness. Table 3.13 is used to simulate the liquid layer thickness ( $\delta_L$ ) from Eq. (3.14) for various laser power settings.

### 3.4.5 Experimental

In the line with the previous study [19, 20], the HVOF coating was carried out by (Applied Surface Technology Ltd.) using Diamond Jet Hybrid (DJ2600) of layer thickness of approximately 300  $\mu m$  in which were sectioned, mounted in resin and polished. The  $CO_2$  laser equipment used was Rofin DC 020 (Diffusion-cooled Slab

**Table 3.13** Thermal properties used in the simulations for inconel 625 powder

Source of variation	Value	Units
Boiling temperature	3,133	K
Melting temperature	1,910	K
Density of assisting gas	1.97 at 150 kPa	kg/m <sup>3</sup>
Density of workpiece	8,440	kg/m <sup>3</sup>
Fraction of evaporation contribution ( $\beta$ )	0.1	–
Specific heat capacity of solid	429	J/kg K
Specific heat capacity of melt	560	J/kg K
Specific heat capacity of gas	918	J/kg K
Thermal conductivity of molten metal	21.3	W/mK
Thermal conductivity of solid	9.8	W/mK
Latent heat of melting	$10^5 \times 2.72$	J/kg
Latent heat of boiling	$10^6 \times 6.10$	J/kg

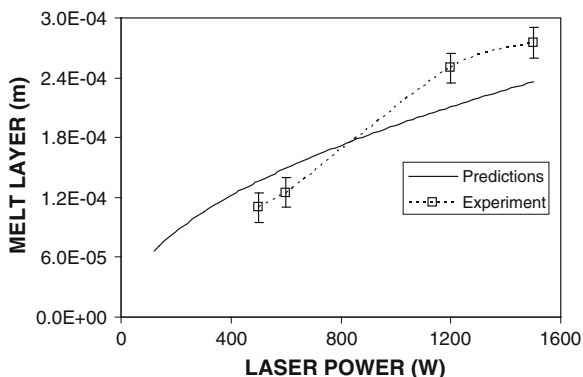
CO<sub>2</sub>). It does have the properties of HF excitations with output power of 2,000 W of power range from 200 to 2,000 W. The beam quality factor for this equipment is to be considered as  $k > 0.9$  and the pulse frequency is 0 or 2 up to 5,000 Hz; cw. The overlap tracks were performed on SS 316L sample plates through scanning the laser beam. The traverse speed of the samples varied from 10 to 150 mm/s. The spot size was changed from 1.2 to 0.6 mm. The mixture was pre-placed into the surface by means of thermal spray HVOF system. An overlap ratio of 0.4 was used to cover large areas. Argon was used as a shielding gas during processing to reduce oxidation of the Inconel 625 powder.

### 3.4.6 Findings and Discussion

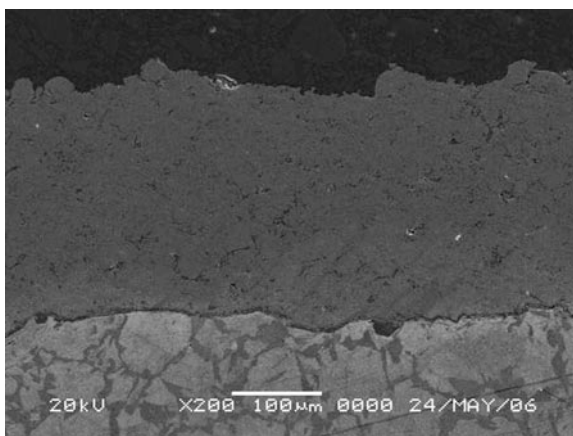
In line with the previous study [19, 20], the findings are given below. Laser melting of HVOF sprayed Inconel 625 coating is carried out and the melt layer thickness and microstructural changes in the laser re-melted zone are examined. The melt layer thickness is formulated using the lump parameter analysis and compared with the experimental results.

Figure 3.44 shows melt layers thickness with laser output power for predictions and experimental data. The melt layer thickness increases almost in a parabolic form with increasing laser output power. In the analysis laser scanning speed and beam spot size at the workpiece surface are kept constant to resemble the experimental conditions. The non-linearity in the melt layer variation occurs for the laser power intensity  $\leq 400$  W. This is because of the heating situation during the formation of the melt layer at low laser power intensities. In this case, conduction and convection losses from the melt region are almost comparable to the laser power at low intensities. The increase in the conduction and convection losses from the melt site is incremental as the laser power increases. Consequently, increase in the melt size mostly depends on the increase in the laser irradiated

**Fig. 3.44** Melt layer thickness with laser power predicted from the lump parameter analysis and obtained from the experiment [19]



**Fig. 3.45** SEM micrograph of HVOF coating cross-section prior to laser melting [19]



power. This provides almost linear variation of melt layers thickness with increasing laser irradiated power beyond 400 W. When comparing the experimental results and predictions of melt layer thickness, it is evident that both results are in good agreement. Some small discrepancies between both results are because of the assumptions of the structural homogeneity and porous free consideration, as well as constant thermal properties used in the analysis. Although the porosity level in the coating is almost 2–3 %, which is small, the oxide formation in the coating as a result of spraying process alters the thermal properties. In addition, thermal properties vary with temperature, provided that this variation is not significant. Consequently, the effects of structural changes such as oxide formation, and temperature dependent properties are responsible for the discrepancies between the experimental results and the predictions of the melt layer thickness.

Figure 3.45 shows SEM micrographs of HVOF coating prior to laser melting. It can be observed that the coating consists of lamellar structure. The voids are scattered randomly provided that overall porosity is within 2–3 %. Moreover, some oxidation around the splats is evident, which occurs during the in-flight prior

**Fig. 3.46** SEM micrograph of laser HVOF coating cross-section after the laser treatment. The cellular structure is clearly observed [19]

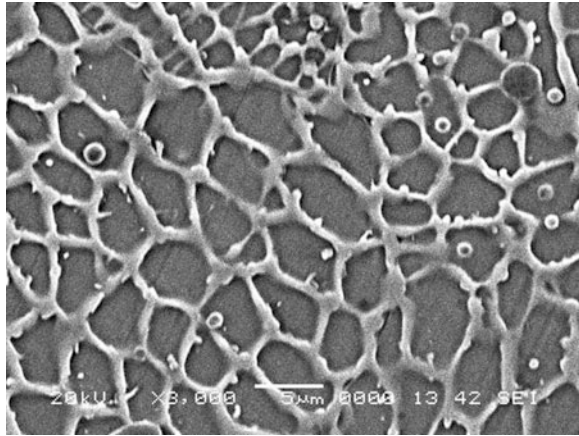


**Table 3.14** EDS results for the laser melted region

Spectrum	C	Al	Cr	Fe	Ni	Au	Total
Spectrum 1		0.25	16.98	52.49	30.28		100.00
Spectrum 2	0.67		16.18	45.17	26.60	11.38	100.00
Spectrum 3	0.37		16.24	45.96	26.55	10.87	100.00
Spectrum 4	0.50		15.60	46.36	25.65	11.89	100.00
Spectrum 5	0.79		15.70	45.95	25.32	12.25	100.00
Spectrum 6	0.62		16.50	45.22	26.82	10.84	100.00
Spectrum 7	0.59		17.60	44.48	26.36	10.97	100.00
Spectrum 8	0.59		14.33	46.64	26.56	11.88	100.00
Spectrum 9	0.60		15.29	46.68	25.31	12.11	100.00
Max.	0.79	0.25	17.60	52.49	30.28	12.25	
Min.	0.37	0.25	14.33	44.48	25.31	10.84	

Each spectrum represents the different points across the cross-section of the coating after the laser treatment. The existing of gold in the spectrums is because of the gold coating of the samples prior to the EDS analysis

to impacting the base material surface. Some dark inclusions around the splats are the evidence of brittle oxide particles. Figure 3.46 shows SEM micrographs of the cross-section of laser melted and re-solidified coating structure. The coating material is Inconel 625 without WC inclusion. The cellular structure is observed upon solidification and the size of grain changes across the cross-section of the laser re-melted region. This is because of the non-uniform cooling at high rates. In this case, the liquid solution upon melting is solidified progressively while the composition of the solid is not uniform. The distribution of the solute in the solid after the completion of the solidification becomes different than from that in liquid. This situation is also observed from the EDS results (Table 3.14); in which case, non-uniformity of the elemental composition in the coating post laser re-melting is evident. Moreover, the development of transverse periodicity in the solidification process is also evident. This is attributed to the instability during the super-cooling

**Fig. 3.47** SEM micrograph of laser HVOF coating cross-section after the laser treatment. The corrugations of the cellular structure are observed [19]

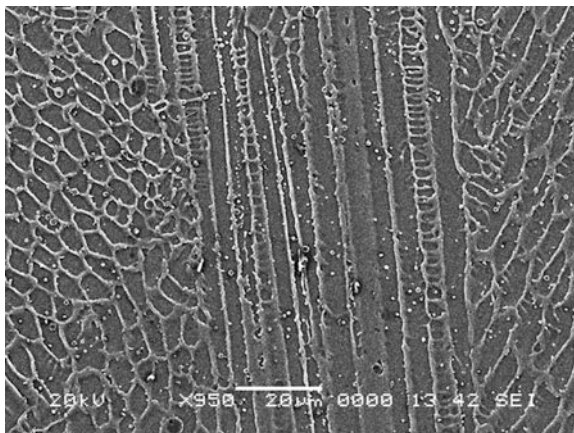
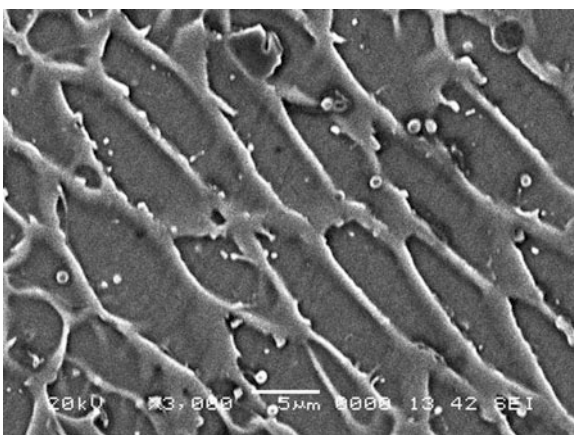
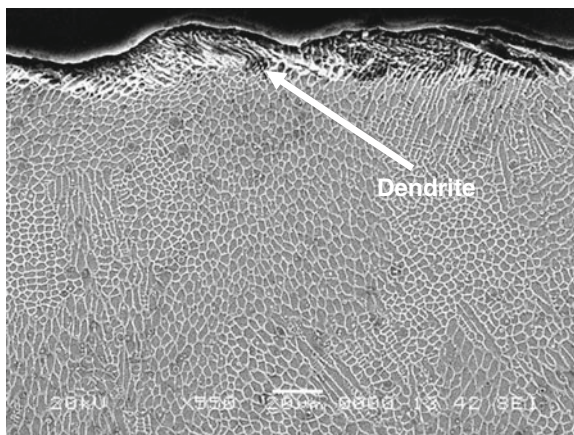


**Fig. 3.48** SEM micrograph of laser HVOF coating cross-section after the laser treatment. The differences in the cell sizes are observed due to non-uniform cooling rates [19]



process. In this case, cellular sub-structures are formed and then fine regular corrugated structures are developed extending along the regular cellular boundary. The corrugations are roughly parallel to the direction of growth of the crystal (Fig. 3.47). Furthermore, the formation of the cellular structure (Fig. 3.48) is because of the liquid, which is rapidly decanted exposing the solid-liquid interface. The cell size increases with decreasing rate of growth and the growth direction depends on the impurity content, speed of growth, and the inclination of the dendrite direction to the growth direction. The heat flow and cooling rate are related to the asymmetry in the shape of the cells, which in turn results in anisotropy of the growth rate of the cells. The segregation occurs at the grain boundaries during the process of solidification, i.e., two crystals grow side-by-side and the boundary between them forms a groove. It should be noted that cellular segregation occurs when super-cooling takes place during the solidification. However, segregation decreases as a result of diffusion during the cooling after the

**Fig. 3.49** SEM micrograph of laser HVOF coating cross-section after the laser treatment. The dendritic structure is observed in the surface region of the coating [19]



solidification. In the cooling process, if the temperature gradient is reduced, then the zone of super-cooling extends. Consequently, the cells change to characteristic of dendrites forming cellular dendrites as seen from Fig. 3.49. This appearance is distinct from the cellular structure and free dendritic growth. One of the causes for this type of morphology is that the cellular dendritic type of growth occurs when the temperature gradient is small in the liquid phase providing the heat rejection into the solid at a low rate. Alignment of dendrites forms webs, which enhances conducting path for heat flow from the liquid to the crystals. It should be noted that the cellular-dendritic growth differs from cellular growth; in which case, the depth of super-cooled zone is greater for cellular growth.

## 3.5 Nanoparticles Blended Wires Deposition

Coating of metallic surfaces via welding deposition finds wide applications in repairing parts. The development of nanotechnology enables to reinforce and/or improves the metallurgical and mechanical properties of the deposited layer. Moreover, depending upon the nanoparticles blended in the wire material and processing parameters, the properties of the resulting coating change. Consequently, in the present section coating produced by nanoparticles blended wires is presented in the light of the previous study [22, 23].

### 3.5.1 Experimental

To deposit the nanostructured wire feed arc welding equipment was used in accordance with the American National Standards for Arc Welding Equipment (ANS/IEC 60974-2009). Welding Equipment EnDOTEc continuous electrodes are

**Table 3.15** Coating parameters

Wire diameter (mm)	Voltage (V)	Current (A)
1.6	23–34	170–300

**Table 3.16** Chemical composition of wire material [wt.%]

C	Si	Mn	Cr	Mo	Nb	W	B	Fe
1.34	0.46	0.22	15.43	3.71	4.18	7.84	4.18	Balance

compatible with most conventional, constant voltage power sources [24]. Models with programmable, pulsed arc, metal transfer modes offer optimal performance. The coating was realized using the electrode at an angle of 70–80°. This provided clean, spatter-free, high profile coating deposits. To achieve sufficient weld deposition at the surface of the workpiece, the multi-passes of coatings were carried out while the initially deposited coating was still hot. The shielding gas mixture was used during the deposition (S 97.5 % Ar and 2.5 % CO<sub>2</sub>). Coating parameters are given in Table 3.15.

The nanostructured wire (DO\*390 N) is ideal for maintenance and repair applications or batch manufacturing where highest integrity welding, efficiency and productivity are required. It provides outstanding abrasion and erosion resistance performance like tungsten carbide without using scarce exotic elements. The elemental composition of wire material is given in Table 3.16.

The slag-free deposit contains a high volume fraction of ultra-hard, complex borocarbides uniformly distributed within an iron alloy matrix. The nanoscale type microstructure improves wear resistance of the surface, subjected to the severe abrasion and erosion, retaining elevated bulk hardness properties to 750 °C. Coating deposit exhibits stress relieving micro-fissures. Low heat input for minimal dilution ensuring best possible coating layer properties.

Carbon steel sheets with 15 mm thicknesses were used as workpieces. JEOL JDX-3530 scanning electron microscope (SEM) was utilized to obtain photomicrographs of the coating deposited sections (coating). The standard test method for Vickers indentation hardness of advanced ceramics (ASTM C1327-99) was adopted. Microhardness was measured at the workpiece surface after the laser treatment process. The measurements were repeated five times at each location for the consistency of the results.

### 3.5.2 Results and Findings

Figure 3.50 shows optical micrographs of top surface of the workpiece. It is evident that no surface crack due to thermal effects is observed. In addition, no cavitation and voids are formed due to excessive heating during the multi-passes

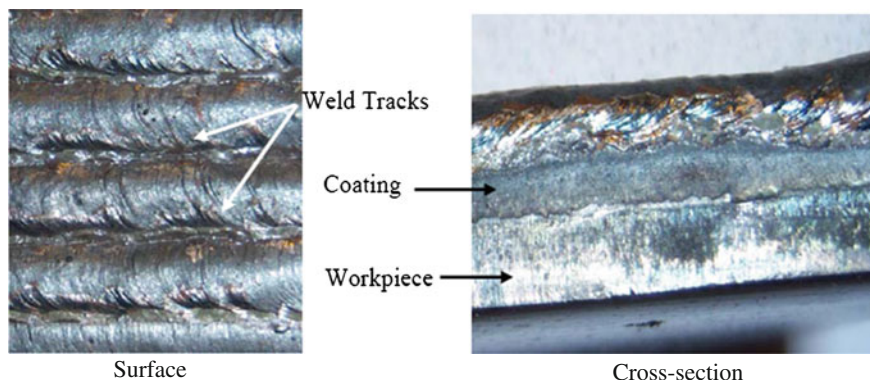


**Fig. 3.50** Optical micrographs of coating surface and cross-section [22]

deposition. The melt tracks reveal that the overlapping ratio is about 90 %, which provides a continuous melt deposition at the surface. However, the melt tracks are set slightly apart during the deposition process. This provides smooth deposition without irregular surface texturing while avoiding excessive temperature rise during the deposition process. The nominal thickness of the coating layer is in the order of 5 mm, which is usually the case for the repair applications. The oxide formation at the surface is evident through the coloration of the coating. The oxide formation is associated with the initial oxidation of the sample surface prior to the deposition process. In this case, during the deposition process, oxygen may release from the workpiece at high temperature and undergoes an exothermic reaction at the melt surface. Since the amount of oxygen is less, the degree of oxidation is also less at the surface, i.e., no loose debris is observed during and after the process.

Figure 3.51 shows SEM micrographs for the cross-sections of both coatings produced by conventional and the nano-particle blended electrodes. It is evident from SEM micrographs that there is no discontinuity in terms of cavitations at the interface between the coating and the base material. This is true for coatings produced by nano-structured and standard electrodes. In addition, no microcracks due to high temperature gradients in the vicinity of the interface are observed. This shows that the coating rate is not significantly high causing the excessive thermal stresses in this region. However, the microstructure developed in the coating is completely different than that of the base material. This is particularly true for nano-particle blended coating. In this case, the nano-particles remain almost undissolved in the metallic matrix. In some regions, small grains are observed where the nano-particles are concentrated. This may occur during the deposition process, in which case, some of nano-particles, such as WC remains in solid phase and these particles may agglomerate locally. It should be noted that nano-structured zones act as crack arrests. The crack tends to propagate through the coatings weakest link and cracks propagating and reaching these well-embedded regions tend to be arrested by the nano-structured zones.

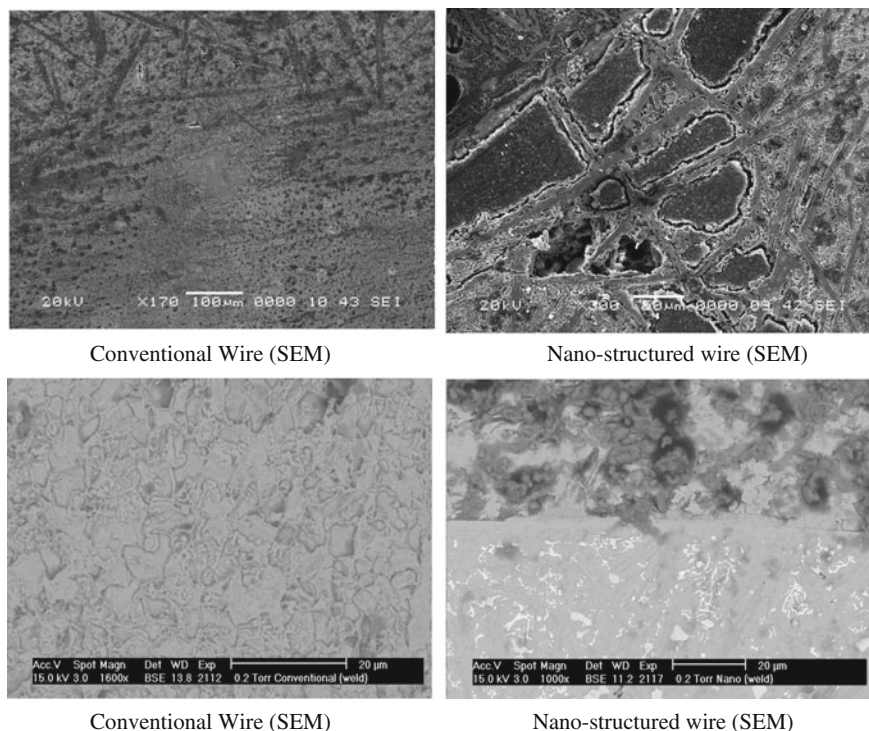


**Fig. 3.51** SEM micrographs of conventional and nano-structured coating cross-sections [22]

Figure 3.52 shows close view for the cross-sections of the nano-structured coatings. The structure involving small grains and crystalline materials. In this case nano-particle interacts with the grain boundary to reduce the energy of the boundary particle system and restrains the boundary movement [25]. Moreover, during the grain growth the area for the nano-particles is reduced. This results in enhancement of nano-particles concentration locally in the metal matrix. This is true for nano-particles having high melting temperatures. Moreover, the presence of conventional nano-particles in the matrix can prevent grain growth through slow down the growth kinetics via reducing the boundary free energy or the grain boundary mobility. Moreover, the clustered nano-particles act as inclusion in the matrix suppressing the grain growth nearby until the particles dissolve or become mobile in the molten state of the matrix. The nano-structures, composing of nano-particles, generate large number of internal interfaces in the liquid matrix causing the formation of small grains. This occurs locally while resulting randomly distributed fine grains in the structure.

Table 3.17 shows microhardness measurement results. Microhardness measurements reveal that hardness of the coating increased slightly as compared to the base material, which is carbon steel. The slight increase in the hardness is because

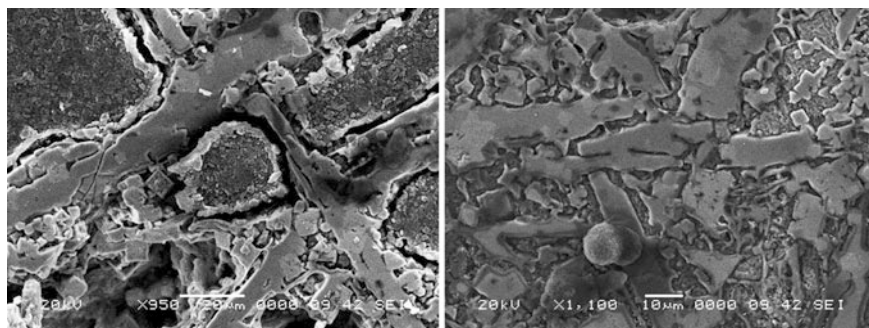


**Fig. 3.52** SEM micrographs of cross-sectional views of nano-structured coating [22]

**Table 3.17** Microhardness of the coating and the base material

	Nano-structured coating	Standard coating	Base material
Microhardness (HV)	950	450	130

of the melting and resolidification processes during the coating deposition. In this case, fine grain structures are responsible for increase in hardness. In the case of nano-structured electrode, microhardness increases significantly in the coating. In this case, the hardness ratio of coating to base material is in the order of 5.5. This is because of the fine grain structured formed in the coating due to presence of the nano-particles. Consequently, grain refinement and compact structured due to nano-particles concentration at grain boundaries are responsible for increased hardness in the coating. In the case of interface between the coating and the base material, hardness gradually decreases in the coating towards the interface while it increases towards the interface in the base material. This indicates that the variation in the coating due to differences in the thermal conductivities of coating and the base material is responsible for this behavior.

## References

1. D. Al-Anazi, M.S.J. Hashmi, B.S. Yilbas, M. Sunar, Three-point bend testing of HVOF AMDRY 9954 coating on Ti-6Al-4V alloy. *J. Mater. Proc. Technol.* **174**(1-3), 204-210 (2006)
2. D. Al-Anazi, M.S.J. Hashmi, B.S. Yilbas, HVOF thermally sprayed CoNiCrAlY coatings on Ti-6Al-4V alloy: High cycle fatigue properties of coating. *Proc. Inst. Mech. Eng. Part B J. Eng. Manuf.* **221**(4), 647-654 (2007)
3. D. Al-Anazi, M.S.J. Hashmi, B.S. Yilbas, HVOF coating of AMDRY 9954 onto Ti-6Al-4V alloy: Fracture toughness measurement. *Proc. Inst. Mech. Eng. Part B J. Eng. Manuf.* **221**(4), 617-623 (2007)
4. D. Al-Anazi, M.S.J. Hashmi, B.S. Yilbas, M. Sunar, HVOF sprayed AMDRY 995 powders onto Ti-6 Al-4V alloy: tensile properties, in Conference on Advances in Material Processing Technology, AMPT06, Las Vegas, 30 July-2 Aug 2006

5. D.M. Al-Anazi, Study of the mechanical and metallurgical properties of AMDRY 9954 HVOF coated Ti-6Al-4V Alloy, Ph.D. thesis, School of Mechanical and Manufacturing Engineering, Dublin City University, Ireland, 2007
6. S. Watanabe, T. Tajiri, N. Sakoda, J. Amano, Fatigue cracks in HVOF thermally sprayed WC-Co coatings. *J. Therm. Spray Technol.* **7**(1), 93–96 (1998)
7. K. Padilla, A. Velázquez, J.A. Berrios, E.S. Puchi Cabera, Fatigue behavior of a 4140 steel coated with a NiMoAl deposit applied by HVOF thermal spray. *Surf. Coat. Technol.* **150**, 151–162 (2002)
8. O.C. Brandt, Mechanical properties of HVOF coatings. *J. Therm. Spray Technol.* **4**(2), 147–152 (1995)
9. D. Eylon, J. Hall, Fatigue behavior of beta processed titanium alloy, IMI 685. *Metall. Trans. A* **8A**, 981–990 (1977)
10. C.-J. Li, W.-Y. Li, Effect of sprayed powder particle size on the oxidation behavior of MCrAlY materials during high velocity oxygen-fuel deposition. *Surf. Coat. Technol.* **162**, 31–41 (2002)
11. C. Rinaldi, L. Ferravante, F. Uberti Paci, P. Bianchi, Extensive characterization of dense and corrosion resistant coatings produced by improved shrouded techniques, in *Proceedings of the International Thermal Spray Conference*, pp. 1185–1193 (2001)
12. Y.A. Al-Shehri, M.S.J. Hashmi, B.S. Yilbas, HVOF coating of diamalloy 2002 and 4010 on carbon steel sheets: Microstructure examination (AMPT 2009, Kuala Lumpur, Malaysia, 26–29 Oct 2009). *Adv. Mater. Res.* **264–265**, 1482–1486 (2011)
13. Y.A. Al-Shehri, M.S.J. Hashmi, B.S. Yilbas, HVOF coatings of diamalloy 2002 and diamalloy 4010 onto steel: Tensile and bending response of coatings, in *Proceedings of AIP Conference on Advances in Materials and Processing Technologies Conference: AMPT 2010* in Paris, France, vol. 1315, pp. 1347–1352, 24–27 Oct 2010
14. Y.A. Al-Shehri, M.S.J. Hashmi, B.S. Yilbas, HVOF coating of metallic surfaces using different powders: fracture toughness measurement of resulting surfaces. *Adv. Mater. Res.* **445**, 621–626, 2012, in *AMPT 2011 14th International Conference on Advances in Materials and Processing technologies*, Istanbul, Turkey, 13–16 July 2011
15. B.S. Yilbas, A.F.M. Arif, Residual stress analysis for HVOF Diamalloy 1005 on Ti-6Al-4V alloy. *Surf. Coat. Technol.* **202**, 559–568 (2007)
16. Z.A. Khan, M. Hadfield, S. Tobe, Y. Wang, Ceramic rolling elements with ring crack defects—a residual stress approach. *Mater. Sci. Eng. A* **404**, 221–226 (2005)
17. J. Stokes, L. Looney, Residual stress in HVOF thermally sprayed thick deposits. *Surf. Coat. Technol.* **117–118**, 18–23 (2004)
18. A.F.M. Arif, B.S. Yilbas, Laser treatment of HVOF coating: modeling and measurement of residual stress in coating. *J. Mater. Eng. Perform.* **17**(5), 644–650 (2008)
19. Z.Y. Taha-al, M.S.J. Hashmi, B.S. Yilbas, Laser treatment of HVOF coating: model study and characterization. *J. Mech. Sci. Technol.* **21**, 1439–1444 (2007)
20. Z.Y. Taha-al, M.S.J. Hashmi, B.S. Yilbas, Effect of WC on the residual stress in the laser treated HVOF coating. *J. Mater. Process. Technol.* **209**(7), 3172–3181 (2009)
21. B.S. Yilbas, B.J.A. Aleem, Dross formation during laser cutting process. *J. Appl. Phys. Part D* **39**, 1451–1461 (2006)
22. A. Al Askandarani, M.S.J. Hashmi, B.S. Yilbas, Coating produced by deposition of nanoparticles blended wires (AMPT 2009, Kuala Lumpur, Malaysia, 26–29 Oct 2009). *Adv. Mater. Res.* **264–265**, 1476–1481 (2011)
23. A. Al Askandarani, S.J. Hashmi, B.S. Yilbas, Arc spraying of nanostructured wires on steel surfaces: influence of coating thickness on microstructure and fracture toughness. *Adv. Mater. Res.* **445**, 803–808 (2012), in *AMPT 2011 14th International Conference on Advances in Materials and Processing technologies*, Istanbul, Turkey, 13–16 July 2011
24. [www.castolin.com/wCastolin\\_com/products/welding/endotec.php](http://www.castolin.com/wCastolin_com/products/welding/endotec.php)
25. P. Miao, G.R. Odette, J. Gould, J. Bernath, R. Miller, M. Alinger, C. Zanis, The microstructure and strength properties of MA957 nanostructured ferritic alloy joints produced by friction stir and electro-spark deposition welding. *J. Nucl. Mater.* **367–370**, 1197–1202 (2007)

## Chapter 4

# Concluding Remarks

**Abstract** Flexural characteristics of cantilever beam when subjected to laser heating pulse are presented in detail. High Velocity Oxy-Fuel Coating is presented and its practical applications are given in detail. In this chapter, the findings of the flexural motion and HVOF coatings are presented in detail.

**Keywords** Flexural motion · HVOF coating · Mechanical characteristics · Morphology

Findings of the analysis in relation to the flexural motion of cantilever beams, resembling plates, and characteristics of high velocity oxy-coating are presented in line with the previous findings [1–23]. Therefore, findings are presented under the appropriate sub-headings including flexural analysis and coating characteristics.

### 4.1 Findings from the Flexural Analysis

The findings from laser non-conduction limited heating of multiplayer assembly consisting of steel and Inconel alloy reveal that the recoil pressure, obtained through vapor pressure integrated over the irradiated, which acts as an impacting load generating the flexural motion of the workpiece. The displacement of the cantilever beam occurs as high as  $10^{-4}$  m while the maximum equivalent stress is in the order of 20 MPa is resulted. In addition, two layer assembly results in considerably higher magnitude of displacement as compared three and four layers assemblies despite the fact that the additional layers (Inconel alloy) have considerably small thickness, which is in the order of 200  $\mu\text{m}$ . Equivalent stress is higher when the displacement is larger. Moreover, the maximum magnitude of shear stress is higher than that corresponding to equivalent stress.

It is found from the study of the flexural waves generated due to pressure force during the laser induced evaporation process that the pressure generated in the interface zone reaches on the order of 700 MPa. The amplitude of the flexural waves at a location of workpiece center demonstrates an irregular pattern with time.

This occurs because of one or all of the following reasons: (1) the dispersion effect of the workpiece material, (2) partially overlapping of the wave modes, and (3) the interference of the reflected waves from the free ends of the workpiece with the traveling wave. The flexural wave pattern changes at different locations of the workpiece. However, the regular pattern is observed as the location moves toward the workpiece end. The time shift occurs for the regular pattern to develop as the location at the surface moves toward the workpiece end. The regular pattern in the traveling wave is observed after introducing the radiating element in the analysis. The amplitude of the traveling wave in the radiating element case is less than that corresponding to the workpiece with the free supported case. This indicates the significant effect of the reflected waves on the traveling wave characteristics.

The findings of laser pulse heating of steel surface and flexural wave analysis show that the normal component of the thermal stress in the surface vicinity is tensile and no unique pattern of the flexural wave is obtained at different locations on the surface of the workpiece. This is due to the dispersion effect of the workpiece material, overlapping of two modes, and interference of the reflected waves emanating from the free ends of the workpiece. During the laser heating, the temperature rises rapidly at the surface in the early heating period and the rate of temperature rise reduces as the heating progresses. Temperature decay rate in the beginning of the cooling cycle is higher than that corresponding to high cooling periods. This is because the temperature gradient in the surface vicinity of the workpiece reduces at a slow rate as the cooling period progresses. The normal component of the thermal stress is tensile in the surface vicinity and it varies with time such that two peaks are observed, one in the heating cycle and the other in the cooling cycle. The strain continues to increase in the early cooling period provided that it reduces rapidly as the cooling period progresses further. The amplitude of the travelling wave reduces as the location at the workpiece surface moves towards the free end of the workpiece. This is because of the damping and dispersion effects of the workpiece material and interference of the reflected waves from the free ends of the workpiece. The pattern of the travelling wave changes towards the workpiece end and the wave amplitude breaks into high frequency peaks. This is because of the reflected waves and the partial overlapping of the two modes of the travelling wave. The throw-off analysis indicates that the reflected waves have significant effect on the travelling wave, since the time required for the reflected wave to reach the center of the irradiated spot is in the order of  $0.16 \times 10^{-3}$  s; which is considerably less than the time domain considered in the present study. Moreover, a certain pattern is identified in the travelling wave at locations close to the center of the irradiated spot when throw-off element is introduced at the free end of the workpiece. This pattern is shifted in time domain as the location moves away from the irradiated spot center. This is because of the effect of the second mode on the travelling wave; in which case, the second mode travels faster than the first mode and the partial overlapping of two modes occurs, which modifies the wave pattern.

It is observed from the flexural wave generation and stress analysis during laser evaporative heating of steel that the surface displacement of the order of 2 mm

occurs, which in turn results in equivalent stress and shear stress levels of the order of 104 and 105 Pa. It should be noted that two geometric arrangements of the workpiece are considered, namely cantilever and with both ends simply supported. In addition, to investigate the influence of an additional element on the stress levels, aluminum is considered as the additional element in steel. The additional aluminum reduces the stress levels in the substrate material. The displacement due to the normal pressure force damps out earlier for a workpiece with both ends simply supported as compared with that corresponding to a cantilever arrangement. The magnitude of displacement is higher in the case of a cantilever arrangement than that which occurs when both ends are simply supported. The equivalent stress oscillates with time, and the resulting stress level oscillation for the cantilever arrangement shows a non-regular pattern. Moreover, the stress level for workpieces with both geometric arrangements is lower than the yield stress of the substrate material. In the case of a workpiece with both ends simply supported, the equivalent stress decreases with time. The additional aluminum in steel reduces the stress level, and in this case the stress level difference is higher in the early period. The shear stress developed in the workpiece is higher than the equivalent stress level. This is due to the bending of the workpiece during flexural motion. The shear stress attains a zero value when the displacement becomes zero. The shear stress behavior at locations 1.2 and 1.3 in the workpiece is out of phase. The addition of aluminum reduces the magnitude of the shear stress.

The findings of laser pulse heating and flexural wave generation during treatment of metallic surfaces indicate that the peak value of recoil pressure predicted agrees well with the previous result. The flexural wave characteristics change considerably as workpiece configuration is varied. In this case, flexural wave damps out at a fast rate for both ends fixed workpieces, i.e. the damping frequency increases while amplitude decreases. The wave amplitude in the order of 20 mm is predicted at the center of the workpiece. Moreover, in the case of location close to the workpiece ends, the amplitude reduces considerably for all workpiece configurations, except for the cantilever configuration.

Three-dimensional analysis of flexural motion due to laser evaporative heated cantilever workpiece demonstrates that the maximum displacement in the order of 20  $\mu\text{m}$  occurs due to the flexural motion of the workpiece. It should be noted that the governing equations of motion are solved numerically using a FEM. In order to investigate the influence of additional element on the displacement and stress field, copper is added as a seventh element position in the workpiece. The maximum equivalent stress levels in the order of 60 MPa is resulted. The influence of addition copper element on the stress levels is considerable, i.e. it lowers as well as enhances the stress levels with time. The displacement dies out as time progresses and maximum displacement occurs at the last element of the workpiece. This is because of the cantilever arrangement of the plate. The frequency of displacement is in the order of 0.2 kHz. Temporal behavior of equivalent stress is similar to temporal behavior of displacement, i.e. higher displacement results in higher equivalent stress. The influence of copper additional element on equivalent stress is considerable; in this case, equivalent stress reduces and increases with

progressing time. The shear stress difference in the transverse direction is almost negative, which in turn indicates that the additional copper element reduces the shear stress in this direction.

It is found from laser induced flexural wave analysis due to the presence of an aluminum element in steel substrate that the surface displacement in the order of 10 mm range is resulted. The temporal behavior of the surface displacement and displacement difference depend on the location of the additional element in the workpiece. However, in the analysis, an additional element of different properties is locally imbedded in the substrate material. This enables to examine the surface displacement due to the flexural wave response to the additional element in the workpiece. Moreover, the magnitude of the displacement difference is high at some periods. The temporal behavior of the displacement difference is influenced considerably by the axial locations of the additional element, provided that the small changes in temporal behavior of displacement difference is observed when the additional element is located close to the free end of the workpiece. The magnitude and temporal behavior of displacement difference does not change considerably for different mesh points along the transverse direction when the location of additional element changes. In this case, the temporal behavior of displacement difference corresponding to different mesh points in the transverse direction becomes identical for different axial locations of aluminum element.

The results associated with the influence of force location on the flexural motion of the cantilever beam due to laser ablation demonstrate that the magnitude of flexural displacement is highest when the pressure force location is at the free end of the cantilever assembly. Moreover, time occurrence of the maximum flexural displacement is independent of the pressure force location at the assembly surface. The normal stress component reaches its maximum when the pressure force location is at the free end of the cantilever assembly, provided that the maximum normal stress level is less than the yielding limit of the substrate material. The temporal behavior of the shear stress follows almost the temporal behavior of the flexural displacement. The magnitude of the shear stress is about three times the maximum normal stress. Consequently, ablation of the assembly surface by a laser beam in the region close to the free end of the cantilever assembly results in high magnitude of the flexural displacement at the free end; however, the maximum stress levels are well below the yielding limit of the substrate material.

The study related to the flexural behavior of a laser welded cantilever plate due to variation of welding speed of the heating source shows that temperature decay along and normal to the plate changes with the heat source speed. This is more pronounced for the low heat source speeds (1 cm/s). However, change in temperature distribution modifies the elastic modulus in the substrate material. This alters the flexural characteristics of the plate when subjected to the heating the heating situations. Lowering the heat source speed enhances the displacement difference and the time shift between the peak displacements. However, increasing heat source speed to 3 cm/s reduces drastically the amplitude difference and the time shift. This is associated with the large change in the elastic modulus at high temperatures. Moreover, the influence of non-linear effect on of the elastic

modulus, due to high temperature, is more pronounced on the time shift; in which case, the time shift reduces significantly as the heat source speed increases from 1 to 2 cm/s. The drastic change in the time shift is related to the location of the heat source, which moves forward along the plate width with increasing heat source speed. Consequently, the amplitude difference changes slightly at low speeds. However, the time shift changes drastically with small change in the heat source speed, in which case the magnitude of the time shift reduces almost 50 % once the heat source speed increases from 1 to 2 cm/s.

The findings of flexural characteristics of a bar subjected to local heating and the effect of heat source location indicate that the maximum amplitude difference changes for the different locations of the heat source. This is attributed to the changes of the elastic modulus of the bar material with temperature; in which case, elastic modulus reduces with increasing temperature. Since this variation is non-linear, the amplitude difference variation with heat source locations is not in a simple form. The similar argument can apply for the time period difference due to heating and no-heating situations. However, the amplitude and time period difference can be related with the locations of the heat source. This relation can form the base to determine the locations of the local heat source through analyzing the flexural motion characteristics.

The study associated with the effect of temperature field on flexural wave characteristics of a bar resembling welding to rigid body concludes that temperature decays rapidly in the region next to the heated zone in the early heating period. As the heating progresses, temperature decay in the region next to the heated zone becomes gradual. In this case, the modulus of elasticity of the bar material is modified in according with the temperature field in the bar material. The wave characteristics of the flexural motion due to heating and no heating situations change with time. In this case, the difference in time period of the flexural wave with and without heating situations becomes significant in the early heating period when temperature decays rapidly in the region next to the heated zone. This is true for the maximum difference of the amplitude of both waves corresponding to the heating and the no heating situations. In this case, the shift in the time period as well as the maximum amplitudes of flexural waves becomes small due to gradual variation of the modulus of elasticity in the bar.

It is observed from the study pertinent to the effect of heat transfer on the flexural characteristics of cantilever plate heated at fixed end that temperature rises rapidly in the early heating period and this rise becomes gradually as the heating period increases. This is because of the temperature gradient across the heat source and its neighborhood, which is high in the early periods. Temperature gradient becomes high for the small heat source size in the vicinity of the heat source. This is associated with the radial heat diffusion suppressing temperature rise in the plate. The maximum amplitude difference increases with the size of the heat source at the fixed end of the plate. This increase is high for the small heat source size and it becomes gradual as the heat source size increases. This situation is associated with the temperature field in the plate during the heating period; in which case, the elastic modulus of the plate is modified in the region subjected to

high temperature. The time shift in the flexural response of the plate, due heating and no heating situations, increases with the size of the heat source at the fixed end of the plate. This increase is notably high so that it can be related to the size of the heat source and high temperature region in the plate.

The flexural behavior of tapered cantilevered bar is investigated and influence of the taper angle on the amplitude and frequency of the tapered bar oscillation is examined. The taper angle of the cantilever bar includes positive and negative slopes through adjusting the cantilever bar taper aspect ratios. The analysis related to the flexural characteristics of tapered bar in relation to taper angle measurements indicates that taper angle has significant effect on the flexural behavior of the cantilever bar. In this case, increasing taper (negative slope) and reducing taper (positive slope) has an adverse effect on the maximum amplitude difference with progressing time, i.e. the maximum amplitude difference is the maximum for low aspect ratios and reduces with increasing aspect ratios. This is attributed to the damping behavior of the tapered cantilever bar as well as the mass change of the bar due to change in the aspect ratios. Time period corresponding to the first peak of the cantilever bar reduces with increasing taper from negative to positive taper. Findings of the time period and the peak amplitude reveals that measuring the flexural properties of the tapered cantilevered bar and it is possible to identify the taper angle of the bar as well as monitor the faulted tapered bars in the production line.

## 4.2 Findings from High Velocity Oxy-Fuel Coating Characterization

The findings of the analysis related to HVOF can be classified according to mechanical, metallurgical and morphological characteristics of the coating with and without laser treatment. Therefore, the findings are given below in line with the previous studies [14–23] under the appropriate sub-headings.

*Three-Point Bending Tests:* Three-point bending tests are carried out to examine the tensile-shear response of the coating under the bending load. The findings revealed that coating with small porosity and voids is achieved. Elongated cracks are developed in the coating in the region of deflection of the workpiece during the bending tests. This, in turn, results in partial attachment of the coat onto the base material without complete peeling off from the substrate surface due to stress relaxation at coating interface. Coating with severe crack formation and total peeling off from the substrate surface are also observed, which is more pronounced for heat treated workpieces. von-Mises stress excess of elastic limit at coating-base material interface extends in the horizontal direction, which indicates that the crack formation in coating is unavoidable. As the load level increases, elongated cracks are formed in the coating, particularly in the region of maximum deflection. Once the cracks are formed, stress relaxation at coating interface occurs, which

reduces the strain in this region and the cracks do not propagate into the base material.

*Fatigue Test:* Fatigue testing is carried out prior and after heat treatment process. The results show that coated workpieces without heat treatment result in higher fatigue life than heat treated workpieces without coating. This is attributed to the strong adherence of coating to the substrate material and grit blasting prior to coating. In this case, grit blasting cause local residual stress centers which improve the fatigue strength of the workpiece. It should be noted that HVOF coating does not always enhance the fatigue life. Moreover, heat treatment process lowers the fatigue strength of both as-received and coated workpieces. This is mainly because of the formation of  $\beta$ -phase and precipitation of  $\alpha$ -phase inside the  $\beta$ -phase; in which case, fatigue crack initiation and propagation start early periods of testing. Heat treatment process enhances oxygen content in the surface vicinity of coating, which in turn increases the brittleness of coating in this region. Consequently, failure of coating initiates either at oxide compounds boundaries in the coating or  $\text{Al}_2\text{O}_3$  particles left over from the grit blasting at coating-substrate interface prior to coating. Due to the differences in thermal expansion coefficients of coating and the underneath substrate material, thermally-induced residual stresses are developed at coating-substrate interface after the heat treatment process. This situation causes total failure of coating through peeling and spalling of coatings from the substrate surface during the testing. In the case of coated workpieces, without heat treatment, cracks are initiated in the brittle sites, such as  $\text{Cr}_2\text{O}_3$  within the coating. This, in turn, results in partial delamination of coating; in which case part of the coating remains on the substrate surface.

*Tensile Test:* Tensile properties of the coated workpieces is examined and in order to simulate the working conditions of gas turbine, some of the coated workpieces are heat treated at  $730\text{ }^\circ\text{C}$  prior to tensile tests. The results reveal that coating with small scattered porosity is achieved. Lamellae structure in coating suggests the almost molten state of power is reached prior to impacting onto substrate surface. Oxygen content in the coating changes after the heat treatment. In this case, oxygen content in the surface region of the coating enhances due to oxygen diffusion during the heat treatment. However, oxygen content in the coating in the region close to the coating workpiece interface does not change significantly after the heat treatment process. Tensile test results reveal that stiffness of heat treated workpieces increases slightly resulting in high load and short elongation in the elastic limit. Early crack initiation is not observed from tensile response of the coating. Since the oxygen content is high in the region of coating surface, delamination of coating with some coating adherence to workpiece surface is observed. In the case of heat treated workpieces total failure of coating is resulted despite the fact that the oxygen content at coating substrate material interface is not influenced by the heat treatment process. Consequently, heat treatment modifies the elastic modulus of the coating and the base material so that total internal stress developed at coating workpiece interface results in total failure of the coating after the tensile tests. The results of ANSYS simulations reveal that stress level changes drastically across the workpiece-coating interface,

which in turn results in failure of coating at interface. This situation is also observed during the tensile experiments.

*Fracture Toughness Measurements:* Indentation and three-point bending tests are carried out to determine the fracture toughness of the coatings prior and after the heat treatment process. The results show that the heat treatment influences significantly the load-displacement characteristics of the coated workpieces. In this case,  $\beta$ -phase transformation and  $\alpha$ -phase precipitation in the base material after the heat treatment lowers the Young's modulus. Young's modulus determined from bending tests and indentation tests are in good agreement. In addition, oxygen diffusion in the surface region of coating after the heat treatment enhances chromium and aluminum oxide formations in this region. The brittle oxides act as the crack initiation sites under the bending load. Consequently, multiple crack initiation at the surface is resulted and once the crack reaches the interface of coating-base material, total failure occurs. Fracture toughness of coating reduces after the heat treatment process due to high level of oxidation in the surface region of the coating.

*Residual Stress Analysis:* The finite element model is introduced to predict the residual stress developed after the cooling period of the thermally sprayed coating and XRD technique is incorporated to measure the residual stress levels in the coating. In addition, the analytical expression developed in the early study is used to compare the predictions of residual stress levels in the coating. The findings indicate that the predictions of the residual stress agrees well with the experimental results obtained using the XRD method. The difference of about 5 % in the stress level is attributed to the assumption of the homogeneous structure in finite element modeling. The heat transfer rate across the interface is different than that of from the free surface. This modifies the stress levels in the coating, particularly lowering the residual stress at the coating interface. Moreover, the locally scattered oxide formation around the splats in the coating modifies the cooling rates of the splats in the coating. This introduces the non-uniformity in the thermal stress levels in the coating. This situation is more pronounced in the surface region where the oxygen content is high. The results obtained from the analytical solution for the residual stress is reasonably comparable to finite element predictions. In addition, the residual stresses measured from the XRD technique and the curvature method are similar and both results are comparable to finite element predictions. Consequently, the residual stress modeling using finite element has a sound base to predict the residual stress in the coating after the cooling period ends.

*Morphological and Stress Analysis:* The morphological and thermal stress analysis reveal that the residual stress predicted in the surface region is in the order of 350 MPa and it reduces to 150 MPa at coating-base material interface. The attainment of low residual stress at the interface plane is associated with the heat diffusion from the coating to the base material, which modifies the temperature gradient in this region. Consequently, temperature gradients in the coating and across the interface plane differ significantly. This agrees well with the XRD measurements of the residual stress. The surface displacement predicted remains positive, which agrees with the experimental observations. This indicates that the

residual stress field is compressive. The melting modifies the coating structure, in which case, a compact coating with excellent sealing at the surface is observed. Although the cooling rates are high at the surface due to convective boundary, no cracks or spreading of splats are observed. In addition, oxide formation around the splat boundary almost disappears due to the melting and mixing in the coating. The voids in the coating disappears and the bubble sites formed during the melting, due to initial capture of air in HVOF coating process, replace with the molten metal through the surface effect. This lowers the porosity during the melting and solidification process.

*Metallurgical and Microhardness Analyses:* The findings of HVOF coating of Diamalloy 2002 and 4010 powders onto the carbon steel surface is presented herein. Two layered coatings, consisting of Diamalloy 4010 bottom layer and Diamalloy 2002 top layer, is realized. The results show that coatings produced from the Diamalloy 2002 and Diamalloy 4010 give similar surface textures, provided that some scattered protruded splats are observed at the surface for Diamalloy 2002 coating. This can be related to the presence of contains WC, which has a high melting temperature. Coatings produced from both powders formed lamellar structures with the porosity of the order of 3 %. No large cavities or irregularities are observed at the coating-base material interface, except Diamalloy 2002 coating. In this case, a locally extended line of discontinuous gap is observed. Oxidation of the some splat surface appears as black inclusions in the coatings; however, the oxide layer does not cover all the surface of the splats. The microhardness measurement reveals that the coating formed by using Diamalloy 2002 has higher hardness than that corresponding to Diamalloy 4010. This is attributed to the presence of WC in the splats. The elastic modulus determined from the indentation tests shows that the elastic modulus of the coating formed from Diamalloy 2002 is higher than that of Diamalloy 4010.

*Nanoparticles Blended Wires Deposition:* The coating is realized using two types of wires, namely standard and nano-structured wires. The resulting coating was free from microcracks and voids. The presence of nano-particles in the coating suppresses the growth of grains during the solidification process. The dense structures with fine grains are resulted in the coating. In addition, the regions with high concentration of nano-particles act as crack arresting centers. Therefore, high stress levels developed in the cooling cycle may not result in cracks due to the presence of nano-sized particles in the coating. Nano-particles concentrated in some regions in the coatings; however, the concentrated regions are randomly distributed. This, in turn, results in large number of interfaces in the liquid matrix while suppressing the grain growth in this region. The microhardness tests reveal that microhardness of coating increases substantially for coating deposited using the nano-structured wires. This is because of the grain refinement in the coating. The variation in the thermal properties across the coating base material interface causes variation in the hardness in this region. In this case, microhardness reduces towards the interface for nano-structured coating while microhardness increases towards the interface for the base material.

## References

1. B.S. Yilbas, F. Mahmood, Flexural waves generated due to pressure force during the laser induced evaporation process. *J. Laser Appl.* **13**(3) (2001)
2. B.S. Yilbas, S.J. Hyder, S.Z. Shuja, Flexural wave generation and stress analysis during laser evaporative heating of steel, in *Proceedings of the Institution of Mechanical Engineers, Part C: Journal of Mechanical Engineering Science*, vol. 216, pp. 531–542, 2002
3. B.S. Yilbas, M. Faisal, S.Z. Shuja, A.F.M. Arif, Laser pulse heating of steel surface and flexural wave analysis. *Opt. Lasers Eng.* **37**, 63–83 (2002)
4. B.S. Yilbas, S.J. Hyder, Laser pulse heating and flexural wave generation during treatment of metallic surfaces. *J. Mater. Process. Technol.* **141**, 1–8 (2003)
5. B.S. Yilbas, J. Hyder, Flexural motion due to laser ablation: influence of force location on the flexural motion, in *ImechE Proceedings Part C: Journal of Mechanical Engineering Science*, vol. 218(12), pp. 1411–1420, 2004
6. B.S. Yilbas, J. Hyder, Influence of layers on flexural motion of multilayer assembly due to laser ablation process, in *Proceedings of the Institution of Mechanical Engineers, Part C: Journal of Mechanical Engineering Science*, vol. 217, pp. 945–954, 2003
7. T. Al-Zaharnah, B.S. Yilbas, Effect of heat transfer on the flexural characteristics of cantilever plate heated at fixed end. *J. Mech.* **25**, 1–8 (2009)
8. I.T. Alzaharnah, S. Al-Kaabi, B.S. Yilbas, Effect of temperature field on flexural wave characteristics of a bar resembling welding to rigid body. *Adv. Mater. Res.* **83–86**, 1212–1219 (2010)
9. I.T. Alzaharnah, B.S. Yilbas, Investigation into flexural characteristics of a bar subjected to local heating: the effect of heat source location, in *Proceedings of the Institution of Mechanical Engineers, Part B: Journal of Engineering Manufacture*, vol. 222, pp. 1355–1362, 2008
10. I.T. Alzaharnah, B.S. Yilbas, S.A. Al-Kaabi, Flexural characteristics of a laser welded cantilever plate: influence of speed of the heating source. *Lasers Eng.* **18**, 337–350 (2008)
11. B.S. Yilbas, S.J. Hyder, Analysis of flexural wave due to laser heating pulse: two-layer assembly case, in *Proceedings of the Institution of Mechanical Engineers, Part C: Journal of Mechanical Engineering Science*, vol. 216, pp. 1165–1174, 2002
12. S.J. Hyder, B.S. Yilbas, S.Z. Shuja, Flexural motion in laser evaporative heated cantilever workpiece: three-dimensional analysis. *Opt. Quant. Electron.* **35**, 111–128 (2003)
13. S.J. Hyder, B.S. Yilbas, S.Z. Shuja, Laser induced flexural wave analysis: an aluminum element in steel substrate. *J. Mater. Process. Technol.* **136**, 24–34 (2003)
14. D. Al-Anazi, M.S.J. Hashmi, B.S. Yilbas, M. Sunar, Three-point bend testing of HVOF AMDRY 9954 coating on Ti-6Al-4 V alloy. *J. Mater. Process. Technol.* **174**(1–3), 204–210, 2006
15. D. Al-Anazi, M.S.J. Hashmi, B.S. Yilbas, HVOF thermally sprayed CoNiCrAlY coatings on Ti-6Al-4 V alloy: high cycle fatigue properties of coating, in *Proceedings of the Institution of Mechanical Engineers, Part B: Journal of Engineering Manufacture*, vol. 221(4), pp. 647–654, 2007
16. D. Al-Anazi, M.S.J. Hashmi, B.S. Yilbas, M. Sunar, in *HVOF Sprayed AMDRY 995 Powders onto Ti-6 Al-4 V Alloy: Tensile Properties*. Conference on Advances in Material Processing Technology, AMPT06, Las Vegas, July 30–August 2, 2006
17. D. Al-Anazi, M.S.J. Hashmi, B.S. Yilbas, HVOF coating of AMDRY 9954 onto Ti-6Al-4 V alloy: fracture toughness measurement, in *Proceedings of the Institution of Mechanical Engineers, Part B: Journal of Engineering Manufacture*, vol. 221(4), pp. 617–623, 2007
18. Y.A. Al-Shehri, M.S.J. Hashmi, B.S. Yilbas, HVOF coating of diamalloy 2002 and 4010 on carbon steel sheets: microstructure examination. *Adv. Mater. Res.* **264–265**, 1482–1486, (2011) (AMPT 2009, Kuala Lumpur, Malaysia, 26–29 October 2009)
19. Y.A. Al-Shehri, M.S.J. Hashmi, B.S. Yilbas, in *HVOF Coatings of Diamalloy 2002 and Diamalloy 4010 onto Steel: Tensile and Bending Response of Coatings*. AMPT 2010,

- Advances in Materials and Processing Technologies Conference, 24–27 October 2010 in Paris, France. AIP Conference Proceedings, vol. 1315, pp. 1347–1352, 2010
20. B.S. Yilbas, and A.F.M. Arif, Residual stress analysis for HVOF diamalloy 1005 on Ti-6Al-4 V alloy. *Surf. Coat. Technol.* **202**, 559–568 (2007)
  21. A.F.M. Arif, B.S. Yilbas, Laser treatment of HVOF coating: modeling and measurement of residual stress in coating. *J. Mater. Eng. Perform.* **17**(5), 644–650 (2008)
  22. Z.Y. Taha-al, M.S.J. Hashmi, B.S. Yilbas, Laser treatment of HVOF coating: model study and characterization. *J. Mech. Sci. Technol.* **21**, 1439–1444 (2007)
  23. A. Al Askandarani, M.S.J. Hashmi, B.S. Yilbas, Coating produced by deposition of nanoparticles blended wires. *Adv. Mater. Res.* **264–265**, 1476–1481 (2011) (AMPT 2009, Kuala Lumpur, Malaysia, 26–29 October 2009)